Isogeometric analysis of anisotropic mechanical and electromechanical higher-gradient continua

von der Fakultät Maschinenbau
der Technischen Universität Dortmund
zur Erlangung des akademischen Grades

Doktor-Ingenieurin (Dr.-Ing.)

genehmigte Dissertation

von

Carina Victoria Witt

aus Ahaus

Vorsitz:	Prof. Dr.-Ing. M. Schulze Darup
Referent:	Prof. Dr.-Ing. habil. A. Menzel
Korreferenten:	Prof. A. McBride
	Prof. Dr.-Ing. habil. D. Balzani
Tag der Einreichung:	02.04.2024
Tag der mündlichen Prüfung:	11.10.2024

Bibliografische Information Der Deutschen Bibliothek
Die Deutsche Bibliothek verzeichnet diese Publikation in der Deutschen Nationalbibliografie; detaillierte bibliografische Daten sind im Internet über **http://dnb.ddb.de** abrufbar.

Bibliographic information published by Die Deutsche Bibliothek
Die Deutsche Bibliothek lists this publication in the Deutsche Nationalbibliografie; detailed bibliographic data is available in the Internet at **http://dnb.ddb.de**.

Schriftenreihe des Instituts für Mechanik

Herausgeber: Institut für Mechanik
Fakultät Maschinenbau
Technische Universität Dortmund
Leonhard-Euler-Str. 5
D-44227 Dortmund

Druck: Koffler DruckManagement GmbH

© by Carina Victoria Witt 2024

This work is subject to copyright. All rights are reserved, whether the whole or part of the material is concerned, specifically the rights of translation, reprinting, reuse of illustrations, recitation, broadcasting, reproduction on microfilm or in any other way, and storage in data banks. Duplication of this publication or parts thereof is permitted in connection with reviews or scholarly analysis. Permission for use must always be obtained from the author.

Alle Rechte vorbehalten, auch das des auszugsweisen Nachdrucks, der auszugsweisen oder vollständigen Wiedergabe (Photographie, Mikroskopie), der Speicherung in Datenverarbeitungsanlagen und das der Übersetzung.

Als Manuskript gedruckt. Printed in Germany.

ISSN 2191-0022
ISBN 978-3-947323-50-0

"Nothing in life is to be feared, it is only to be understood.
Now is the time to understand more, so that we may fear less."

Marie Curie (1867–1934)

Acknowledgements

The work presented in this thesis is the result of my research at the Institute of Mechanics at TU Dortmund University, conducted during my time as research assistant between 2020 and 2024. Throughout these years, I have been supported by many people in both personal as well as scientific aspects and I would like to hereby express my sincere gratitude to all of them.

First and foremost, I wish to thank my doctoral advisor Prof. Andreas Menzel for his great support and for the opportunity to work and graduate in his exceptional research group. Thank you for all the rewarding discussions and for encouraging me to pursue my own ideas. It was a pleasure to learn from your scientific experience and expertise.

Moreover, I would like to thank the members of my examination committee for their engagement with my work. In particular, I want to thank Prof. Andrew McBride for accepting to act as the co-referee, Prof. Daniel Balzani for serving as the third referee and Prof. Moritz Schulze Darup for agreeing to chair the committee.

I would also like to express my gratitude to the entire team at the Institute of Mechanics. I truly appreciated the friendly working atmosphere and enriching scientific discussions, and enjoyed the memorable social activities and team events after work. It was a pleasure to be part of this group and I will always cherish this special time. Of all my colleagues I want to especially thank PD Dr.-Ing. Tobias Kaiser for his guidance throughout my PhD and earlier during my graduate studies. Thank you for your unwavering support and for sharing your experience and knowledge both scientifically and personally. In addition, I would like to acknowledge Christina McDonagh for carefully proofreading manuscripts, Christina McDonagh and Kerstin Walter for their kind assistance in all administrative and organisational aspects, and Matthias Weiss for maintaining the hardware and software resources that were essential for completing this thesis. Beyond the team at the Institute of Mechanics I would also like to thank the members of the GAMM Juniors for the valuable interdisciplinary exchange.

Lastly, and most importantly, I am profoundly grateful to my friends and especially my family for their endless support and encouragement over the past years. Thank you for always believing in me and for standing by my side through every challenge.

Dortmund, October 2024 Carina Witt

Zusammenfassung

Die vorliegende Arbeit behandelt die Modellierung und numerische Simulation von *anisotropen Materialien*, deren mechanisches bzw. elektromechanisches Verhalten maßgeblich von ihrer Mikrostruktur beeinflusst wird. Um solche mikrostrukturellen Effekte zu berücksichtigen werden *generalisierte Kontinuumsansätze* sowie die *isogeometrische Analyse* verwendet. Die isogeometrische Analyse wird im ersten Teil dieser Arbeit mit besonderem Fokus auf ihre Anwendung auf Gradientenkontinua behandelt. Im zweiten Teil wird eine gradientenerweiterte Elastizitätstheorie für die Simulation von faserverstärkten Verbundwerkstoffen untersucht, bei der die *Biegesteifigkeit der Fasern* durch die Einbeziehung des Gradienten des Faservektors in die zugrunde liegende Energiedichtefunktion berücksichtigt wird. Dabei werden sowohl infinitesimal kleine als auch finite Deformationen untersucht. Im letzten Teil der Arbeit wird ein Modellierungsansatz für das gradientenbasierte elektromechanische Phänomen der *Flexoelektrizität* vorgestellt, um flexoelektrisch induzierte Knochenumbauprozesse sowie Heilungsprozesse von Mikrorissen in kortikalem Knochen zu analysieren. Unter Berücksichtigung von chemo-elektro-mechanischer Kopplung wird Flexoelektrizität zusammen mit *anisotropen Zelldiffusionsprozessen* und *Oberflächenwachstum* behandelt.

Abstract

This thesis deals with the modelling and numerical simulation of *anisotropic materials* whose mechanical, respectively electromechanical behaviour is significantly influenced by their microstructure. From a modelling point of view, *generalised continuum approaches* are adopted in order to account for these microstructural effects and *isogeometric analysis* is employed for their numerical treatment. Accordingly, isogeometric analysis is addressed in the first part of this work with special focus on the application to gradient continua. In the second part, a gradient elasticity approach for the modelling and simulation of fibre-reinforced composites is investigated in which the *fibre bending stiffness* is accounted for by incorporation of the gradient of the fibre vector in the underlying stored energy density function. An isogeometric analysis framework is established for a small strain as well as finite strain setting. In the last part of this thesis, a modelling approach for the gradient-based electromechanical phenomenon *flexoelectricity* is proposed for the simulation of flexoelectricity-induced bone remodelling processes and microcrack healing in cortical bone. Accordingly, chemo-electro-mechanical coupling is considered and a computational framework which captures flexoelectricity together with *anisotropic cell diffusion processes* and *surface growth* is established.

Publications

The contents of this thesis are based on peer-reviewed journal articles which have been published during the progress of this work. For these articles, the author of this thesis contributed essential aspects regarding the outline of the theory, carried out all of the numerical implementations, evaluated the simulations and prepared the journal articles. Some contents and figures of the original articles have been modified in this thesis whenever considered valid, e.g. to avoid repetitions and to provide a meaningful structure. The mentioned journal articles are listed in the following:

1. C. Witt, T. Kaiser, A. Menzel: *An isogeometric finite element approach to fibre-reinforced composites with fibre bending stiffness*, Archive of Applied Mechanics, 91(2):643–672, 2021, [170].

2. C. Witt, T. Kaiser, A. Menzel: *A finite deformation isogeometric finite element approach to fibre-reinforced composites with fibre bending stiffness*, Journal of Engineering Mathematics, 128(1):15, 2021, [171].

3. C. Witt, T. Kaiser, A. Menzel: *On the incorporation of curvature effects into the isogeometric analysis of fibre-reinforced solids*, Proceedings in Applied Mathematics and Mechanics, 21(1):e202100185, 2021, [173].

4. C. Witt, T. Kaiser, A. Menzel: *Modelling and numerical simulation of remodelling processes in cortical bone: An IGA approach to flexoelectricity-induced osteocyte apoptosis and subsequent bone cell diffusion*, Journal of the Mechanics and Physics of Solids, 173:105194, 2023, [174].

5. C. Witt, T. Kaiser, A. Menzel: *An IGA-FEA model for flexoelectricity-induced healing of microcracks in cortical bone*, Computer Methods in Applied Mechanics and Engineering, 425:116919, 2024, [175].

Moreover, the author of this thesis contributed to the following peer-reviewed journal articles:

6. A. Menzel, C. Witt: *Extremal states and coupling properties in electroelasticity*, Philosophical Transactions of the Royal Society A: Mathematical, Physical and Engineering Sciences, 380(2234):20210330, 2022, [105].

7. C. Hergl, C. Witt, B. Nsonga, A. Menzel, G. Scheuermann: *Electromechanical Coupling in Electroactive Polymers - a Visual Analysis of a Third-Order Tensor Field*, IEEE Transactions on Visualization and Computer Graphics, 29(12):5357-5371, 2023, [78]. Supplementary material to this journal article is available under the DOI: 10.1109/TVCG.2022.3209328/mm1.

For the articles 6-7, the author of this thesis carried out the numerical implementations and simulations and contributed to the evaluation of simulation results as well as to the preparation of the journal articles.

Contents

Notation

In this thesis, the meaning of any employed scalar-valued or tensor-valued variable is generally described in the corresponding sections. However, the notation conventions used throughout this work are provided in the following for the reader's convenience.

Tensors For the three-dimensional Euclidean space $\mathbb{R}^3$ which is spanned by the Cartesian basis vectors $\{\boldsymbol{e}_i\}$ with $i \in \{1, 2, 3\}$, first-order tensors, respectively vectors, are expressed as

$$\boldsymbol{u} = u_i \, \boldsymbol{e}_i$$

following Einstein's summation convention. Tensors of higher order follow analogously as

$$\begin{aligned}
\boldsymbol{T} &= T_{ij} \, \boldsymbol{e}_i \otimes \boldsymbol{e}_j, \\
\boldsymbol{R} &= R_{ijk} \, \boldsymbol{e}_i \otimes \boldsymbol{e}_j \otimes \boldsymbol{e}_k, \\
\mathsf{S} &= \mathsf{S}_{ijkl} \, \boldsymbol{e}_i \otimes \boldsymbol{e}_j \otimes \boldsymbol{e}_k \otimes \boldsymbol{e}_l, \\
\mathsf{C} &= \mathsf{C}_{ijklm} \, \boldsymbol{e}_i \otimes \boldsymbol{e}_j \otimes \boldsymbol{e}_k \otimes \boldsymbol{e}_l \otimes \boldsymbol{e}_m,
\end{aligned}$$

including tensors of up to fifth order, in particular. Accordingly, non-bold letters are used for scalars, bold-face lower-case italic letters for vectors and bold-face upper-case italic letters are employed for second-order and third-order tensors. Bold-face upper-case sans-serif letters represent tensors of fourth or higher order. Besides, tensors are also represented by bold-face lower-case italic letters in this thesis when Greek symbols are employed.

Tensor transpositions Different kinds of transpositions of tensors are used throughout this work depending on the order of the tensor. As tensors of any order can be constructed by dyadic products of first-order tensors, respectively vectors, the transpositions are defined in the following under the use of arbitrary vectors $\boldsymbol{a}, \boldsymbol{b}, \boldsymbol{c}$ and $\boldsymbol{d}$. The transposition of a second-order tensor $\boldsymbol{T}$ accordingly reads

$$\boldsymbol{T}^{\mathrm{t}} := [\boldsymbol{a} \otimes \boldsymbol{b}]^{\mathrm{t}} = [\boldsymbol{b} \otimes \boldsymbol{a}] \, . \tag{0.1}$$

For a fourth-order tensor S, minor and major transpositions can be distinguished. In this work, they are defined as

$$\mathsf{S}^{\mathrm{t}} := [\boldsymbol{a} \otimes \boldsymbol{b} \otimes \boldsymbol{c} \otimes \boldsymbol{d}]^{\mathrm{t}} = [\boldsymbol{b} \otimes \boldsymbol{a} \otimes \boldsymbol{c} \otimes \boldsymbol{d}] \,, \tag{0.2}$$

$$\mathsf{S}^{\mathrm{T}} := [\boldsymbol{a} \otimes \boldsymbol{b} \otimes \boldsymbol{c} \otimes \boldsymbol{d}]^{\mathrm{T}} = [\boldsymbol{c} \otimes \boldsymbol{d} \otimes \boldsymbol{a} \otimes \boldsymbol{b}] \,. \tag{0.3}$$

Additionally, a special type of transposition for fourth-order tensors is used in this work, i.e.

$$\mathsf{S}^{\mathrm{T}*} := [\boldsymbol{a} \otimes \boldsymbol{b} \otimes \boldsymbol{c} \otimes \boldsymbol{d}]^{\mathrm{T}*} = [\boldsymbol{d} \otimes \boldsymbol{a} \otimes \boldsymbol{b} \otimes \boldsymbol{c}] \,. \tag{0.4}$$

Similarly, for a third-order tensor $\boldsymbol{R}$, additional non-standard transpositions are introduced as

$$\boldsymbol{R}^{\mathrm{t}} := [\boldsymbol{a} \otimes \boldsymbol{b} \otimes \boldsymbol{c}]^{\mathrm{t}} = [\boldsymbol{b} \otimes \boldsymbol{a} \otimes \boldsymbol{c}] \,, \tag{0.5}$$

$${}^{\mathrm{t}}\boldsymbol{R} := {}^{\mathrm{t}}[\boldsymbol{a} \otimes \boldsymbol{b} \otimes \boldsymbol{c}] = [\boldsymbol{a} \otimes \boldsymbol{c} \otimes \boldsymbol{b}] \,, \tag{0.6}$$

$$\boldsymbol{R}^{\mathrm{T}} := [\boldsymbol{a} \otimes \boldsymbol{b} \otimes \boldsymbol{c}]^{\mathrm{T}} = [\boldsymbol{c} \otimes \boldsymbol{a} \otimes \boldsymbol{b}] \,, \tag{0.7}$$

$${}^{\mathrm{T}}\boldsymbol{R} :=^{\mathrm{T}} [\boldsymbol{a} \otimes \boldsymbol{b} \otimes \boldsymbol{c}] = [\boldsymbol{b} \otimes \boldsymbol{c} \otimes \boldsymbol{a}] \,. \tag{0.8}$$

Inner tensor products Let $\boldsymbol{\mathcal{A}}$ and $\boldsymbol{\mathcal{B}}$ denote tensor-valued quantities of arbitrary order in the Cartesian basis system. The inner tensor products between the tensors are denoted by dots, i.e.

$$\begin{aligned} \boldsymbol{\mathcal{A}} \cdot \boldsymbol{\mathcal{B}} &= [\mathcal{A}_{ij\ldots kl}\, \boldsymbol{e}_i \otimes \boldsymbol{e}_j \cdots \otimes \boldsymbol{e}_k \otimes \boldsymbol{e}_l] \cdot [\mathcal{B}_{mn\ldots op}\, \boldsymbol{e}_m \otimes \boldsymbol{e}_n \cdots \otimes \boldsymbol{e}_o \otimes \boldsymbol{e}_p] \\ &= \mathcal{A}_{ij\ldots kl}\, \mathcal{B}_{ln\ldots op}\, \boldsymbol{e}_i \otimes \boldsymbol{e}_j \cdots \otimes \boldsymbol{e}_k \otimes \boldsymbol{e}_n \cdots \otimes \boldsymbol{e}_o \otimes \boldsymbol{e}_p, \end{aligned} \tag{0.9}$$

$$\begin{aligned} \boldsymbol{\mathcal{A}} : \boldsymbol{\mathcal{B}} &= [\mathcal{A}_{ij\ldots kl}\, \boldsymbol{e}_i \otimes \boldsymbol{e}_j \cdots \otimes \boldsymbol{e}_k \otimes \boldsymbol{e}_l] : [\mathcal{B}_{mn\ldots op}\, \boldsymbol{e}_m \otimes \boldsymbol{e}_n \cdots \otimes \boldsymbol{e}_o \otimes \boldsymbol{e}_p] \\ &= \mathcal{A}_{ij\ldots kl}\, \mathcal{B}_{kl\ldots op}\, \boldsymbol{e}_i \otimes \boldsymbol{e}_j \cdots \otimes \boldsymbol{e}_o \otimes \boldsymbol{e}_p, \end{aligned} \tag{0.10}$$

$$\begin{aligned} \boldsymbol{\mathcal{A}} :\cdot \boldsymbol{\mathcal{B}} &= [\mathcal{A}_{ij\ldots klm}\, \boldsymbol{e}_i \otimes \boldsymbol{e}_j \cdots \otimes \boldsymbol{e}_k \otimes \boldsymbol{e}_l \otimes \boldsymbol{e}_m] :\cdot [\mathcal{B}_{nop\ldots qr}\, \boldsymbol{e}_n \otimes \boldsymbol{e}_o \otimes \boldsymbol{e}_p \cdots \otimes \boldsymbol{e}_q \otimes \boldsymbol{e}_r] \\ &= \mathcal{A}_{ij\ldots klm}\, \mathcal{B}_{klm\ldots qr}\, \boldsymbol{e}_i \otimes \boldsymbol{e}_j \cdots \otimes \boldsymbol{e}_q \otimes \boldsymbol{e}_r, \end{aligned} \tag{0.11}$$

where the number of dots clearly corresponds to the number of contractions. For the double and triple contraction, tensors $\boldsymbol{\mathcal{A}}$ and $\boldsymbol{\mathcal{B}}$ need to be of at least second, respectively third order. The inner tensor products also give rise to the definition of the norm, i.e.

$$\|\boldsymbol{u}\| = \sqrt{\boldsymbol{u} \cdot \boldsymbol{u}}, \quad \|\boldsymbol{T}\| = \sqrt{\boldsymbol{T} : \boldsymbol{T}} \tag{0.12}$$

for first-order and second-order tensors, respectively.

Outer tensor products The standard outer product of two tensors $\boldsymbol{\mathcal{A}}$ and $\boldsymbol{\mathcal{B}}$ of suitable order is defined as

$$\begin{aligned}\boldsymbol{\mathcal{A}} \otimes \boldsymbol{\mathcal{B}} &= [\mathcal{A}_{ij\ldots kl}\, \boldsymbol{e}_i \otimes \boldsymbol{e}_j \cdots \otimes \boldsymbol{e}_k \otimes \boldsymbol{e}_l] \otimes [\mathcal{B}_{mn\ldots op}\, \boldsymbol{e}_m \otimes \boldsymbol{e}_n \cdots \otimes \boldsymbol{e}_o \otimes \boldsymbol{e}_p] \\ &= \mathcal{A}_{ij\ldots kl}\, \mathcal{B}_{mn\ldots op}\, \boldsymbol{e}_i \otimes \boldsymbol{e}_j \cdots \otimes \boldsymbol{e}_k \otimes \boldsymbol{e}_l \otimes \boldsymbol{e}_m \otimes \boldsymbol{e}_n \cdots \otimes \boldsymbol{e}_o \otimes \boldsymbol{e}_p. \end{aligned} \tag{0.13}$$

Additionally, two non-standard dyadic products are introduced, accordingly

$$\begin{aligned}\boldsymbol{\mathcal{A}} \mathbin{\overline{\otimes}} \boldsymbol{\mathcal{B}} &= [\mathcal{A}_{ij\ldots kl}\, \boldsymbol{e}_i \otimes \boldsymbol{e}_j \cdots \otimes \boldsymbol{e}_k \otimes \boldsymbol{e}_l] \mathbin{\overline{\otimes}} [\mathcal{B}_{mn\ldots op}\, \boldsymbol{e}_m \otimes \boldsymbol{e}_n \ldots \boldsymbol{e}_o \otimes \boldsymbol{e}_p] \\ &= \mathcal{A}_{ij\ldots km}\, \mathcal{B}_{ln\ldots op}\, \boldsymbol{e}_i \otimes \boldsymbol{e}_j \cdots \otimes \boldsymbol{e}_k \otimes \boldsymbol{e}_l \otimes \boldsymbol{e}_m \otimes \boldsymbol{e}_n \cdots \otimes \boldsymbol{e}_o \otimes \boldsymbol{e}_p, \end{aligned} \tag{0.14}$$

$$\begin{aligned}\boldsymbol{\mathcal{A}} \mathbin{\underline{\otimes}} \boldsymbol{\mathcal{B}} &= [\mathcal{A}_{ij\ldots kl}\, \boldsymbol{e}_i \otimes \boldsymbol{e}_j \cdots \otimes \boldsymbol{e}_k \otimes \boldsymbol{e}_l] \mathbin{\underline{\otimes}} [\mathcal{B}_{mn\ldots op}\, \boldsymbol{e}_m \otimes \boldsymbol{e}_n \ldots \boldsymbol{e}_o \otimes \boldsymbol{e}_p] \\ &= \mathcal{A}_{ij\ldots kn}\, \mathcal{B}_{lm\ldots op}\, \boldsymbol{e}_i \otimes \boldsymbol{e}_j \cdots \otimes \boldsymbol{e}_k \otimes \boldsymbol{e}_l \otimes \boldsymbol{e}_m \otimes \boldsymbol{e}_n \cdots \otimes \boldsymbol{e}_o \otimes \boldsymbol{e}_p. \end{aligned} \tag{0.15}$$

Identity tensor The Kronecker delta symbol δ_{ij} gives rise to the second-order identity tensor

$$\boldsymbol{I} = \delta_{ij}\, \boldsymbol{e}_i \otimes \boldsymbol{e}_j \quad \text{with} \quad \delta_{ij} = \boldsymbol{e}_i \cdot \boldsymbol{e}_j = \begin{cases} 1 & \text{if } i = j, \\ 0 & \text{if } i \neq j. \end{cases} \tag{0.16}$$

Permutation tensor The third-order permutation tensor, also referred to as Levi-Civita symbol, is defined as

$$\boldsymbol{\epsilon} = \epsilon_{ijk}\, \boldsymbol{e}_i \otimes \boldsymbol{e}_j \otimes \boldsymbol{e}_k \quad \text{with} \quad \epsilon_{ijk} = \begin{cases} 1 & \text{if } (ijk) \text{ is even permutation of (123)}, \\ -1 & \text{if } (ijk) \text{ is odd permutation of (123)}, \\ 0 & \text{if at least two indices are identical.} \end{cases} \tag{0.17}$$

Vector products For first-order tensors $\boldsymbol{u}$ and $\boldsymbol{v}$, the vector product is denoted under the use of the permutation tensor so that

$$\boldsymbol{u} \times \boldsymbol{v} = u_i\, v_j\, \epsilon_{ijk}\, \boldsymbol{e}_k. \tag{0.18}$$

For a second-order tensor $\boldsymbol{T}$, the product reads

$$\boldsymbol{T} \times \boldsymbol{v} = T_{ij}\, v_k\, \epsilon_{jkl}\, \boldsymbol{e}_i \otimes \boldsymbol{e}_l. \tag{0.19}$$

Gradient operations Gradient operations are denoted as $\nabla_{\boldsymbol{x}} \bullet$ or $\nabla_{\boldsymbol{X}} \bullet$, depending on whether the gradient operation is performed with respect to the spatial or reference configuration. In this thesis, the gradient and corresponding derived operations are right-gradients. Accordingly, the gradient of a tensor $\boldsymbol{\mathcal{A}}$ of arbitrary order yields

$$\nabla_{\boldsymbol{x}} \boldsymbol{\mathcal{A}} = \frac{\partial \mathcal{A}_{ij\ldots kl}}{\partial x_m}\, \boldsymbol{e}_i \otimes \boldsymbol{e}_j \cdots \otimes \boldsymbol{e}_k \otimes \boldsymbol{e}_l \otimes \boldsymbol{e}_m. \tag{0.20}$$

The divergence and curl operators can be written in terms of the gradient operator and result in

$$\nabla_{\boldsymbol{x}} \cdot \boldsymbol{\mathcal{A}} = \nabla_{\boldsymbol{x}} \boldsymbol{\mathcal{A}} : \boldsymbol{I} = \frac{\partial \mathcal{A}_{ij\ldots kl}}{\partial x_l}\, \boldsymbol{e}_i \otimes \boldsymbol{e}_j \cdots \otimes \boldsymbol{e}_k, \tag{0.21}$$

$$\nabla_{\boldsymbol{x}} \times \boldsymbol{u} = \epsilon_{ijk} \frac{\partial u_k}{\partial x_j}\, \boldsymbol{e}_i. \tag{0.22}$$

Taking both the gradient and divergence operator into account, the Laplace operator with respect to the spatial configuration is defined as $\Delta_{\boldsymbol{x}} \bullet = \nabla_{\boldsymbol{x}} \cdot \nabla_{\boldsymbol{x}} \bullet$ and includes second-order derivatives of a tensorial quantity $\bullet$.

For the application of the gradient and divergence operators in a polar coordinate system in the two-dimensional space, the derivatives of the basis vectors $\boldsymbol{e}_r, \boldsymbol{e}_\varphi$ must be considered. For a scalar field $\Phi(r, \varphi)$ and a vector field $\boldsymbol{\Psi}(r, \varphi)$, the operations yield

$$\nabla_{\boldsymbol{x}} \Phi(r, \varphi) = \frac{\partial \Phi}{\partial r} \boldsymbol{e}_r + \frac{1}{r} \frac{\partial \Phi}{\partial \varphi} \boldsymbol{e}_\varphi, \tag{0.23}$$

$$\begin{aligned} \nabla_{\boldsymbol{x}} \boldsymbol{\Psi}(r, \varphi) = {} & \frac{\partial \Psi_r}{\partial r} \boldsymbol{e}_r \otimes \boldsymbol{e}_r + \left[\frac{1}{r} \frac{\partial \Psi_\varphi}{\partial \varphi} + \frac{\Psi_r}{r} \right] \boldsymbol{e}_\varphi \otimes \boldsymbol{e}_\varphi \\ & + \left[\frac{1}{r} \frac{\partial \Psi_r}{\partial \varphi} - \frac{\Psi_\varphi}{r} \right] \boldsymbol{e}_r \otimes \boldsymbol{e}_\varphi + \frac{\partial \Psi_\varphi}{\partial r} \boldsymbol{e}_\varphi \otimes \boldsymbol{e}_r, \end{aligned} \tag{0.24}$$

$$\nabla_{\boldsymbol{x}} \cdot \boldsymbol{\Psi}(r, \varphi) = \frac{1}{r} \frac{\partial \left[r\, \Psi_r \right]}{\partial r} + \frac{1}{r} \frac{\partial \Psi_\varphi}{\partial \varphi}. \tag{0.25}$$

Application of the Laplace operator to the scalar and vector fields Φ and $\boldsymbol{\Psi}$ in polar coordinates results in

$$\Delta_{\boldsymbol{x}} \Phi(r, \varphi) = \frac{\partial^2 \Phi}{\partial r^2} + \frac{1}{r} \frac{\partial \Phi}{\partial r} + \frac{1}{r^2} \frac{\partial^2 \Phi}{\partial \varphi^2}, \tag{0.26}$$

$$\Delta_{\boldsymbol{x}} \boldsymbol{\Psi}(r, \varphi) = \left[\Delta_{\boldsymbol{x}} \Psi_r - \frac{\Psi_r}{r^2} - \frac{2}{r^2} \frac{\partial \Psi_\varphi}{\partial \varphi} \right] \boldsymbol{e}_r + \left[\Delta_{\boldsymbol{x}} \Psi_\varphi - \frac{\Psi_\varphi}{r^2} + \frac{2}{r^2} \frac{\partial \Psi_r}{\partial \varphi} \right] \boldsymbol{e}_\varphi. \tag{0.27}$$

1 Introduction

1.1 Motivation and state of the art

Within the field of material modelling, the overall objective is to establish models which most accurately capture the behaviour of real materials. This thesis particularly deals with the modelling of materials possessing a characteristic microstructure which contributes to the macroscopic mechanical or electromechanical material response and introduces size effects. The following sections present the state of the art in the realm of such advanced modelling approaches including continuum theories as well as analytical and numerical solution methods along with the underlying experimental findings. Sect. 1.1.1 provides a general basis on the modelling of materials with microstructure, whereas the subsequent sections focus on specific (anisotropic) materials in particular. To be precise, Sect. 1.1.2 deals with fibre-reinforced solids under consideration of the fibre bending stiffness, and Sect. 1.1.3 addresses flexoelectricity in dielectric materials and its particular role in the cortical bone remodelling process.

1.1.1 Materials with microstructure

Many materials and structures show a behaviour as described by a classic continuum theory. There are, however, several classes of materials which yield a different response upon loading, meaning that they behave stiffer, respectively softer than classically expected. This is particularly the case when the size of the loaded structure is on a similar scale as the microstructural elements of the material it is made of. Since such a behaviour can be beneficial in many applications, research on artificial materials with microstructures designed to exhibit these effects has become increasingly relevant in the last years. Moreover, size effects have also been observed in naturally occurring materials such as bones so that appropriate modelling approaches are required in order to correctly describe their physical behaviour.

Experimental findings The experimental investigation of microstructural effects in solids is a challenging task since these effects are only observable on small scales. This

not only makes the experimental setup more difficult but might also promote inaccuracies in measurements by, e.g., surface damage induced while preparing specimens or applying loads. In [87], these challenges are discussed in detail and different experimental methods for generalised continua are proposed. In the so-called *Method of size effects* in particular, specimens of different dimensions are analysed experimentally in order to study the size-dependent rigidity response.

In [32], cortical bone specimens are investigated by such a procedure. More specifically speaking, 88 specimens of varying heights ranging from 100 µm to 550 µm but with constant height-to-length-ratio are studied in terms of three-point bending tests on a microscope stage. From the slope of the resulting load-displacement curve, the elastic modulus is calculated by using a Timoshenko beam theory. Fig. 1.1a presents the corresponding results in dependence on the ratio between surface area and volume which is directly related to the specimen size. A "smaller is stiffer"-type size effect is clearly observable for small samples, whereas a convergence to a constant value is obtained for larger specimens.

In contrast to this behaviour, Fig. 1.1b reveals a "smaller is softer"-type size effect resulting from the compression of aluminium cell foams [9]. Both open-cell and closed-cell foams are investigated in terms of mm-sized samples with a constant ratio of height to cross sectional diameter, respectively edge length. Multiple samples of different sizes are loaded on a testing machine with a compressive load. In order to disregard effects of localised plasticity, the unloading modulus is calculated from the slope of the unloading stress-strain curve. In Fig. 1.1b, the modulus is normalised with respect to the Young's modulus of the bulk material and plotted over the ratio between specimen size and cell size. With decreasing dimensions, the observed modulus takes smaller values for both open-cell and closed-cell foams. In [158], the size-dependent behaviour of metallic foams is discussed in more detail for different loading conditions. It is concluded that for bending and uniaxial compression, foams exhibit a softening effect with decreasing ratio between specimen size and cell size, whereas a stiffening effect is observed in shear and indentation tests.

Generalised continuum approaches In order to account for the experimentally observed size effects in continuum models, several distinct theories have been proposed which can be divided into *higher-order* theories and *higher-gradient* theories. Within higher-order theories, additional degrees of freedom are introduced which are associated with the microstructure. The most general approach in this regard is the *micromorphic theory* [56, 106, 157] in which a microdeformation tensor is attached to each material point. Accordingly, nine degrees of freedom are introduced in addition to the three translational degrees of freedom accounted for in a classic Cauchy continuum. The micromorphic theory can be reduced to other generalised continuum theories which only consider specific parts of the microdeformation tensor. Accordingly, *Cosserat continua* [39] are obtained by including three rotational and three translational degrees of freedom at each material point. An extension of this approach with respect to micro-inertia terms

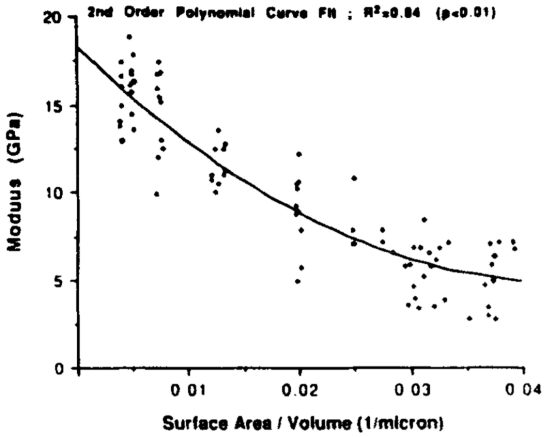

(a) Size effects of "smaller is stiffer"-type experimentally observed in three-point-bending tests on cortical bone samples. Reprinted from [32], copyright (1990), with permission from Elsevier.

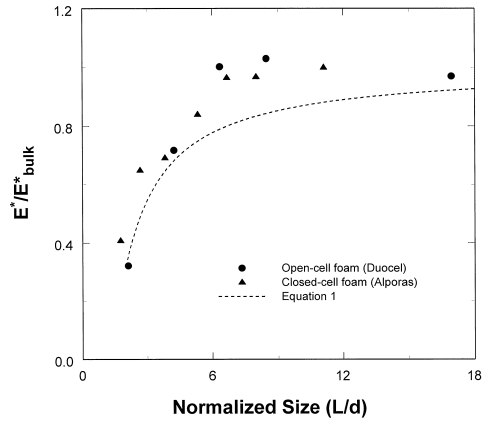

(b) Size effects of "smaller is softer"-type experimentally observed in compression tests on aluminium foams. Reprinted from [9], copyright (2000), with permission from Elsevier.

Figure 1.1: Experimentally observed size effects in materials with different microstructure.

yields *micropolar continua* [54], whereas for the static case both terms are used interchangeably. Moreover, *microstretch continua* [55] are obtained by considering not only microrotations and translations but also a stretch-related degree of freedom, whereas *dilatational continua* account for a single dilatational degree of freedom [119] in addition to the translations at each material point.

By coupling the microdeformation to the macrodeformation of the continuum under investigation, gradient theories can also be derived from the micromorphic theory. Gradient theories are, accordingly, not based on additional degrees of freedom but on the incorporation of higher gradients of existing fields. In elasticity, second gradients of the displacement vector are typically employed. More specifically speaking, the *strain-gradient theory* is based on the gradient of the strain tensor [106], whereas the *couple-stress theory* in the form proposed in [108] incorporates the gradient of the rotation vector, i.e. the gradient of the curl of the displacement field. In [106, 161], a more general form of these gradient approaches is additionally addressed which includes all components of the second displacement gradient, respectively the material gradient of the deformation gradient when finite deformations are considered. For linear elasticity, the relation between these different gradient approaches is discussed in detail in [109]. In the context of coupled problems, gradients of other field variables can similarly be incorporated such as polarisation gradients in the case of electromechanical coupling [107]. The introduction of gradients of stresses, however, leads to a different continuum approach which has been introduced in [61, 136]. This *stress gradient theory* accounts for negative size effects in the sense "smaller is softer", whereas classic (strain) gradient theories are associated with positive size effects of "smaller is stiffer"-type.

Numerical approaches to gradient continua Various numerical frameworks have been proposed in order to study generalised continua and the related size effects. Within the scope of this thesis, the focus lies on gradient continua in particular. When dealing with gradient continua, a numerical challenge is the treatment of the fourth-order partial differential equations (PDEs) which result from the incorporation of higher gradients in the underlying energy functions. More specifically speaking, the basis functions used within finite element discretisations must exhibit square integrable second-order derivatives.

There are generally two options to deal with this issue, which are either choosing higher-order elements which satisfy this condition or avoiding the higher-continuity requirements by dividing the fourth-order PDE into two PDEs of second order. The latter can be achieved by introducing additional kinematic variables. In, e.g., [7] the displacements and displacement gradients are used as independent degrees of freedom, and Lagrange multipliers are incorporated in order to enforce their kinematic relation by side constraints. A similar procedure is employed in [59] by treating the gradient continuum as a constrained micromorphic continuum.

In order to deal with fourth-order PDEs directly, mesh free methods can be adopted since they can be formulated on the basis of highly continuous basis functions, see, e.g., [11]. Discontinuous Galerkin methods are another possible choice in the context of gradient continua. In, e.g., [50, 51] these are employed in the context of gradient plasticity, in particular. Alternatively, higher-order finite elements can be used such as Hermite elements as proposed in [17] or other specific C^1-continuous elements as introduced in, e.g., [123] for three-dimensional gradient elasticity problems. Another method which has been employed in order to deal with the higher continuity requirements on the basis functions is isogeometric analysis (IGA). This approach is based on highly continuous non-uniform rational B-splines (NURBS) basis functions. In, e.g., [60, 167] an isogeometric analysis framework for gradient elasticity has been proposed. Isogeometric analysis is also the basis for the investigations of gradient continua and related applications in this thesis.

1.1.2 Fibre-reinforced solids with fibre-bending stiffness

Fibre-reinforced solids In many industrial applications, fibre-reinforced composites are in high demand because of their advantageous properties compared to non-reinforced materials. Specifically speaking, a reinforcement by certain types of fibres can enhance the stiffness, durability and strength-to-weight ratio of materials to name only a few benefits [34, 73, 85, 131]. Apart from these mechanical characteristics of fibre-reinforced composites, the electrical and thermal properties of solids can also be manipulated through the use of specific fibre reinforcements [5, 169]. This high level of flexibility leads to a broad spectrum of materials being reinforced, or used as reinforcement, as illustrated by the scanning electron microscope (SEM) images in Fig. 1.2, showcasing diverse engineering applications. To be precise, Fig. 1.2a presents a steel fibre-reinforced concrete material with a fibre diameter of 220 µm used in construction, whereas in Fig. 1.2b a brittle

ceramic-matrix composite (CMC) for high temperature applications is shown which is reinforced with short fibres of 13 µm diameter. In Fig. 1.2c, the microstructure of a structural capacitor is revealed. In this particular application, carbon fibres of a few µm thickness serve as electrodes and are separated by glass fibres. Finally, Fig. 1.2d presents a carbon fibre-reinforced polymer with an additional reinforcement by silver nanowires which enhances the electrical conductivity of the material and thereby makes it attractive for the use in electronic devices [75].

(a) Steel fibre-reinforced reactive powder concrete (RPC). Reprinted from [179], copyright (2013), with permission from Elsevier.

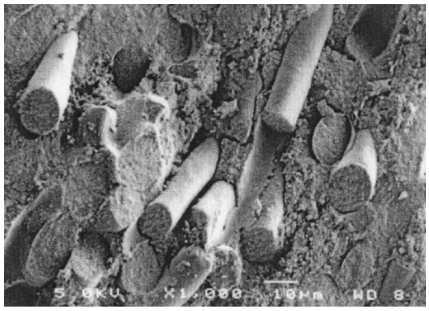

(b) Short fibre-reinforced ceramic-matrix composite (CMC). Reprinted from [156], copyright (2001), with permission from Elsevier.

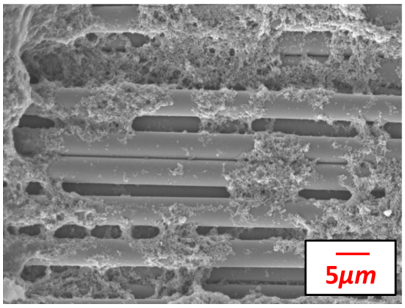

(c) Carbon fibres in a structural capacitor. Reprinted from [160] under the terms of the Creative Commons Attribution 4.0 International License (CC BY 4.0).

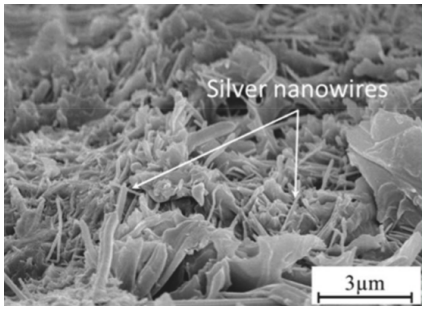

(d) Carbon fibre-reinforced polymer with silver nanowires. Reprinted from [142] under the terms of the Creative Commons Attribution License (CC BY).

Figure 1.2: Scanning electron microscope (SEM) images of fibre-reinforced materials on the micro and nano scale.

Classic modelling approaches Due to the high popularity of fibre-reinforced composites, efficient simulation methods are required to predict the behaviour of these materials. A broad range of modelling approaches already exists in which the fibres are assumed to be *perfectly flexible*. This implies that they solely exhibit a tensile stiffness, whereas a resistance of the fibres against bending or torsion is neglected. From a modelling point of view, this leads to a classic structural tensor approach as in, e.g., [25, 103, 104, 151, 152, 178]. Therein, the fibre direction vector is introduced as additional argument of the underlying energy function such that this originally anisotropic tensor function is reformulated as an isotropic tensor function in the extended list of

arguments. Accordingly, the energy function depends on five independent invariants, in general, assuming a constant structural tensor.

Although the concept of modelling fibre-reinforced solids by solely accounting for the fibre tensile stiffness yields accurate results for many applications, it cannot account for size effects that follow from particular fibre properties such as their diameter or spacing. Moreover, it does not exclude deformation patterns which yield fibre slope discontinuities since there is no energy contribution associated with a change in fibre direction from one material point to another [150].

Experimental findings on size effects and fibre-bending stiffness In contrast to the results obtained by classic modelling approaches for fibre-reinforced solids which consider the fibres to be perfectly flexible, i.e. infinitesimally thin, size effects which are related to the fibre dimensions have been observed in several experiments as presented in Fig. 1.3. In particular, Fig. 1.3a, shows the effective bending modulus obtained from three-point bending tests performed in [82] on silver nanowires which are, e.g., used as reinforcement in polymers as shown in Fig. 1.2d. By employing contact atomic force microscopy (C-AFM), a bending load is applied to nanowires with diameters ranging from $20 - 140\,\mathrm{nm}$, and the elastic modulus is calculated from the slope of the measured load deflection curves by means of a classic Euler-Bernoulli beam theory. As revealed in Fig. 1.3a, a significant size effect is obtained, i.e. wires of smaller size behave stiffer. In accordance with these results which have been observed for structurally isolated fibres, experiments on fibrous composites exhibit a similar size-dependency. Accordingly, several samples of ultra-high-performance hybrid fibre-reinforced concrete (UHP-HFRC) are studied in [116] in terms of four-point bending tests, whereas three different specimen sizes with equal fibre volume fractions and equal aspect ratios are considered. To be precise, the incorporated edge lengths of the samples with square cross section are $50\,\mathrm{mm}, 100\,\mathrm{mm}$ and $150\,\mathrm{mm}$. Fig. 1.3b presents the equivalent bending stress as a function of the observed deflection for all specimens. Focussing on the elastic regime before plastic deformation and cracking occur, the experimental results reveal generally higher stiffnesses for smaller-sized samples, i.e. for specimens in which the relative size of the fibres is rather large with respect to the macroscopic dimensions.

Extended modelling approach accounting for the fibre bending stiffness Motivated by the experimental findings on the size-dependent behaviour of fibre-reinforced composites, an extended approach for the modelling of such materials has been presented in [153]. It drops the assumption of perfectly flexible fibres and instead allows the incorporation of the *fibre bending stiffness* into the model. Amongst others, this new material parameter is associated with the gradient of the fibre direction vector which enters the energy function as additional argument and thereby introduces a length scale to the model. In a finite strain setting, the energy can be expressed as an isotropic tensor function of, e.g., the right Cauchy-Green tensor, the fibre direction vector and its gradient, accordingly. This leads to a dependence on, in general, 33 independent invariants. As

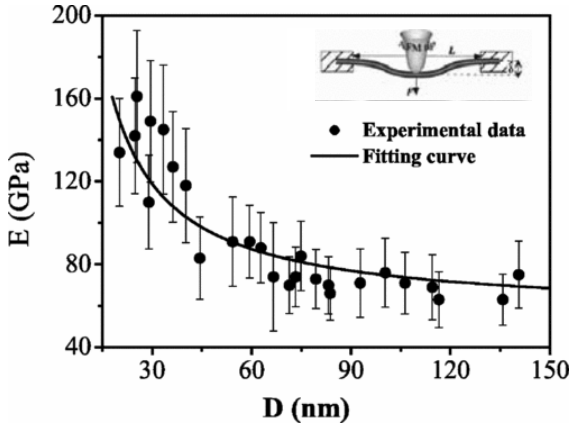

(a) Young modulus as a function of the diameters of silver nanowires obtained from three-point bending tests. Reproduced from [82], copyright (2006), with permission from American Physical Society.

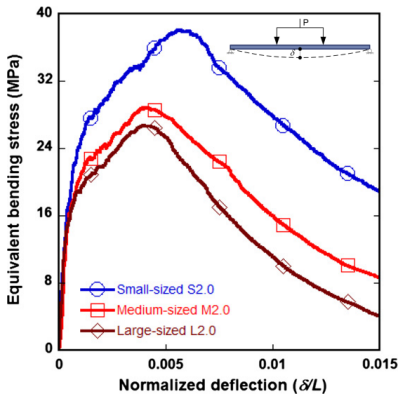

(b) Equivalent bending stress as a function of the normalised deflection of ultra-high-performance hybrid fibre-reinforced concrete (UHP-HFRC) obtained by four-point bending tests. Reproduced from [116], copyright (2012), with permission from Elsevier.

Figure 1.3: Experimentally observed size effects in individual fibres as well as in fibre-reinforced composites.

a special case, however, only the derivative of the fibre vector in the fibre direction is considered to exclusively account for *fibre curvature* and *fibre stretch gradient* effects. Effects from fibre twist or splay, on the other hand, are thereby excluded and the number of invariants reduces to eleven. In [153], a linear version of the proposed theory is additionally derived and a reduction to a plane strain state is presented. Overall, the modelling approach is based on the couple-stress theory introduced in [108] and thus leads to non-symmetric stresses and couple-stresses.

An alternative modelling approach for fibre-reinforced solids with fibre bending stiffness has been proposed in [154, 155] on the basis of a Cosserat continuum theory and accounts for *fibre twisting* in addition to stretching and bending. Therein, fibres are modelled in terms of continuously distributed Kirchhoff rods, and an orthonormal triad field is introduced which is associated with the unit tangent vector and cross section of the embedded fibres. The change in space of the triad field is accounted for by introduction of a rotation tensor and describes the fibre curvature and twist. Similar to the model proposed in [153], a length scale is introduced.

Analytical solutions The modelling approach proposed in [153] for fibre-reinforced composites with fibre bending stiffness has been used to derive analytical solutions to particular boundary value problems in which fibre bending is expected to have a significant impact on the material response. To be precise, a cylindrical tube subject to an azimuthal shear deformation has been studied in a two-dimensional, plane strain setting in [44] by employing the linear version of the modelling approach. For this particular boundary value problem, it can be shown that radial compression and azimuthal shear

become uncoupled deformations when the fibres are assumed to be initially straight and radially aligned. Accordingly, a pure azimuthal shear load would not yield any fibre resistance if perfectly flexible fibres were accounted for. By incorporation of a fibre bending stiffness, however, a resistance of the fibres against the shear deformation is observed leading to a physically more meaningful response for fibres with non-negligible thickness. The boundary value problem is studied under different assumptions on the compressibility of the bulk material and on the extensibility of the fibres. The results are shown to be identical in the linear framework with straight, radially aligned fibres due to the uncoupling of radial compression and azimuthal shear.

In [45, 150], the finite strain version of the modelling approach presented in [153] is adopted in order to investigate the same boundary value problem in a more general, non-linear setting. In contrast to the linearised version of the problem, pure azimuthal shear deformations are not applicable in this case when the tube is made of an ideal fibre-reinforced material, i.e. of an incompressible matrix material including inextensible fibres. Accordingly, extensible fibres are considered in [45], whereas in [150] area-preserving shear is instead investigated in combination with inextensible fibres which allows changes of the inner and outer tube radii.

Numerical approaches The modelling approach for fibre-reinforced solids with fibre bending stiffness proposed in [153] is based on the couple-stress continuum theory introduced in [108]. Accordingly, the theory poses higher continuity requirements on the basis functions when a finite element scheme is employed. In order to deal with this issue, a multi-field finite element approach with mixed elements has been proposed in [14]. Therein, the deformation map and the skew-symmetric part of the stress tensor are considered as independent fields together with an additional field variable coupled to the deformation gradient by a constraint equation. This finite element approach fulfils the continuity requirements in weak sense, accordingly. The framework is applied to two-dimensional as well as three-dimensional boundary value problems in order to study size effects and the influence of the fibre direction on the mechanical behaviour of beam-like structures. In [12], the framework is adopted for the azimuthal shear deformation of a cylindrical tube and the numerical results are compared to the analytical solutions provided in [44]. In addition, an application to nano composites is carried out in [13]. A mixed finite element formulation is also employed in [74] for the analysis of dynamically loaded, viscoelastic fibre bundles which possess a resistance against bending and twisting as proposed in [154, 155]. In this computational framework, rotational degrees of freedom are considered in order to account for the higher-order contributions, and micro inertia is incorporated. Accordingly, a constrained micropolar continuum theory is adopted.

An alternative numerical method used to account for fibre bending stiffness effects in fibre-reinforced solids is isogeometric analysis. A major advantage of this approach is the possibility of solving the underlying fourth-order partial differential equation directly as opposed to the multi-field method where the problem is split into two partial differential

equations of second order. Due to the omission of additional fields, the number of degrees of freedom can be significantly reduced in this way which, in general, lowers the computational effort. Moreover, the continuity requirements are fulfilled in a strong sense by using IGA. In this thesis, an isogeometric analysis framework is established for the modelling of fibre-reinforced solids with fibre bending stiffness on the basis of the derivations in [153] with restriction to one single family of fibres and on fibre bending and fibre stretching as active deformation modes. Besides taking one single family of fibres into account, woven fibre structures embedded in thin sheets of matrix material are elaborated by means of isogeometric analysis in [141]. Therein, a Kirchhoff-Love shell formulation is employed on the basis of [154, 155] for the investigation of in-plane and out-of-plane flexural fibre resistance in a hyperelastic regime. By comparison with experimental measurements, it is shown that the numerical calculations which account for fibre bending stiffness contributions yield more accurate results than those obtained by classic continuum approaches without the consideration of higher gradients.

1.1.3 Flexoelectricity-induced remodelling processes in cortical bone

Flexoelectricity in solids The phenomenon of flexoelectricity has gained increasing interest in the last decades in the context of electromechanical coupling. Although at first the effect was assumed to be related to a particular form of piezoelectricity, researchers later regarded flexoelectricity as an independent phenomenon with different coupling properties, see [16] and references cited therein. To be precise, the *direct flexoelectric effect* describes the coupling between strain gradient and electric polarisation. *Converse flexoelectricity*, on the other hand, accounts for (homogeneous) stresses induced by an external electric field gradient, whereas an inhomogeneous strain field induced by electric polarisation is captured by the *inverse flexoelectric effect* [49]. In contrast to piezoelectricity, flexoelectricity is a property of all dielectrics and not restricted to non-centrosymmetric structures. By exploiting the flexoelectric effect, the dependency on piezoelectric materials is consequently reduced which is a major advantage for the construction of electromechanical devices such as sensors and actuators. Fig. 1.4 shows such a flexoelectricity-based sensor developed in [91] for curvature measurements. A thin-film cantilever actuator, on the other hand, is presented in [23] on the basis of the inverse flexoelectric effect. Besides sensing and actuating, many different areas of application for flexoelectric devices have been revealed up to the current date such as energy harvesting, thin-film technology as well as biomedical applications to name but a few [49, 147, 163, 180].

Experimental findings on flexoelectricity in solids Since (direct) flexoelectricity occurs in the presence of strain gradients, experimental settings are designed in a way that inhomogeneous strain fields arise. This can be accomplished by either applying a load that results in non-uniform strains and stresses such as a bending load or by choosing a geometric structure which yields strain gradients for other load cases such as tension

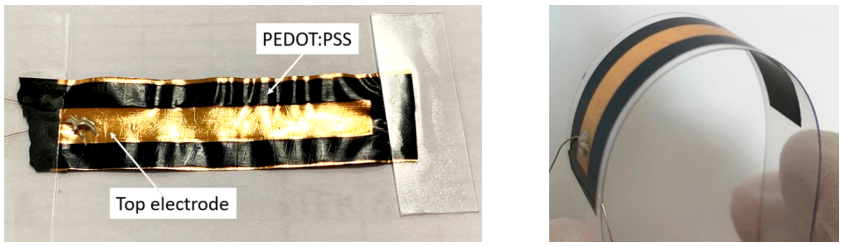

Figure 1.4: Flexoelectricity-based curvature sensor made of poly(3,4-ethylene dioxythiophene) polystyrene sulfonate (PEDOT:PSS) polymer films. Reproduced from [91], copyright (2023), with permission from American Chemical Society.

and compression as well. Typical examples are the bending of beam structures as well as the compression of truncated pyramids [42]. In Fig. 1.5, representative results are presented and the corresponding experimental setup is illustrated. In Fig. 1.5a, the bending-induced polarisation observed in polyvinylidene fluoride (PVDF) films is plotted over the corresponding strain gradient. In this experiment, 13.5 µm-thick PVDF films are glued to the top of a cantilever beam and an electrode is added to both the top and bottom surface of the PVDF films [16]. The bending deformation is induced by a dynamic loading tester (DLT) and the resulting strain and electric current are measured by using a MicroStrain DVRT probing sensor and a lock-in amplifier (LIA), respectively. The induced polarisation is calculated from the measured current and the effective flexoelectric coefficient finally results from the slope of the curve shown in Fig. 1.5a. In order to investigate other flexoelectric coefficients, experiments on a truncated pyramid have been carried out in [81]. Electrodes are attached to each side of the pyramid made of PVDF material. The compressive load is applied to the top surface by a material testing system. A charge amplifier measures the electric charge induced in the specimen by flexoelectricity and converts it to a voltage signal. The flexoelectric coefficients are calculated from the measured values and yield the fitting curves in Fig. 1.5b which are related to measurements in three different spatial directions.

Since large strain gradients can be also found in the vicinity of cracks, flexoelectricity measurements around defects in Rb-doped KTiOPO4 (RKTP) single crystals have been conducted in [38]. This ferroelectric material is studied in terms of indentation tests using an atomic force microscope (AFM), and the interplay between piezoelectricity and flexoelectricity is studied in the context of crack propagation. In addition to the experiments regarding the direct flexoelectric effect, experiments for converse flexoelectricity have been conducted in [2] by using piezoresponse force microscopy (PFM). A voltage is induced to the surface of SrTiO3 crystals via an atomic force microscope with an electrically conducting tip, and an effective piezoelectric response in the centrosymmetric, and thus non-piezoelectric material is observed.

Overall, experiments to characterise flexoelectricity are difficult to conduct since they have to be performed on very small scales due to the size dependency of this electromechanical phenomenon. Moreover, a clear distinction between bulk flexoelectricity and

other effects such as bulk and surface piezoelectricity can be challenging, and appropriate experimental setups must be found which allow the determination of particular flexoelectric coefficients [49]. Consequently, computational models in combination with appropriate analytical and numerical methods are highly relevant in order to study flexoelectricity in more detail.

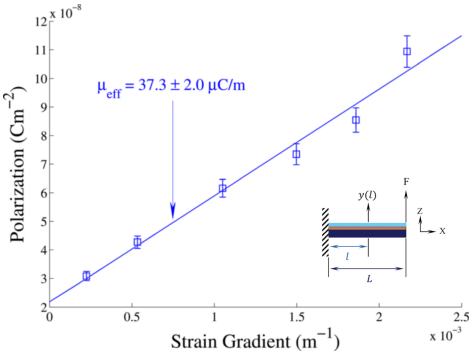

(a) Flexoelectricity-induced polarisation as a function of the strain gradient measured from bending tests on PVDF films. Reproduced from [16], copyright (2012), with permission from AIP Publishing.

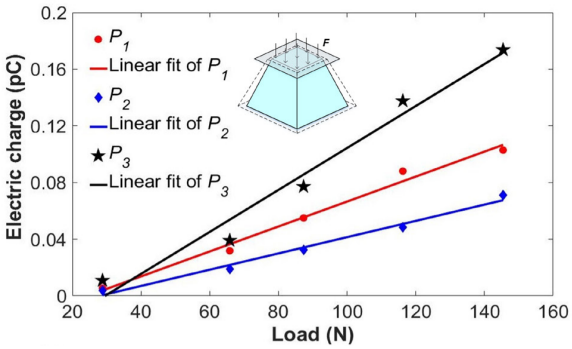

(b) Flexoelectricity-induced electric charge as a function of the compressive load applied on a PVDF pyramid structure. Results from measurements in three different directions are shown. Reprinted from [81], copyright (2020), with permission from IOP Publishing.

Figure 1.5: Experimentally observed polarisation, respectively electric charge due to flexoelectricity.

Modelling approaches Flexoelectricity in solid structures was first identified in a theoretical framework in [101] and the first phenomenological theory for this higher-order electromechanical effect was introduced in [84]. In the context of continuum theories, a model for converse flexoelectricity was proposed in [107] by extending the theory of linear dielectrics from [162]. Therein, the polarisation gradient is taken into account as additional argument of the energy function in order to account for electromechanical coupling in centrosymmetric dielectrics and, in particular, for crystals with cubic symmetry. More recently, several distinct modelling approaches have emerged based on different flexoelectric couplings. More specifically speaking, direct or converse flexoelectricity or both effects can be explicitly incorporated in the underlying energy function. In [36], these options are discussed in detail and it is shown that they yield the same equations of motion. Accordingly, both direct and converse contributions are generally included in the formulations, regardless of the choice of coupling which is explicitly incorporated in the energy function. However, different natural boundary conditions are obtained and the flexoelectric coefficients are, in general, not equal. Moreover, energy functions considering flexoelectricity can be formulated on the basis of different arguments. To be precise, the electric field or the dielectric displacements can be employed instead of the polarisation vector together with different flexoelectricity, respectively flexocoupling tensors. In most works, either the polarisation is employed as primary

variable [95, 98, 143] or the electric field is considered [1, 69, 115]. A relation between the distinct formulations can be made in terms of Legendre transforms [36, 143].

Analytical solutions An analytical solution to flexoelectricity in solids has been derived in [97] for a small strain setting and linear constitutive relations. By assuming an isotropic material, the fourth-order tensor characterising the direct flexoelectric effect is based on two independent constants in the proposed model. The underlying energy function is formulated in terms of the strain tensor and its gradient as well as on the electric polarisation vector. Apart from flexoelectricity, contributions from piezoelectricity and strain gradient elasticity (SGE) are additionally accounted for in this formulation. The governing set of equations which is based on the strain gradient theory [106] is solved for different boundary value problems in [97]. Amongst others, a cylindrical tube is analysed subject to in-plane pressure as well as to in-plane shear. Analytical solutions are derived by exploiting the axisymmetry of these boundary value problems and by employing modified Bessel functions of the first and second kind.

Moreover, the bending deformation of a flexoelectric, slender beam is studied in [97] based on the Euler-Bernoulli beam theory and on one effective flexoelectric coefficient which relates the beam curvature to the electric polarisation. By comparison of the results for two different sets of boundary conditions which invoke direct, respectively inverse flexoelectricity, the consistency between the two effects is shown. The bending deformation of a nano-sized slender beam is also discussed in [95] by considering flexoelectric and piezoelectric effects, and a comparison with atomistic simulations is carried out.

Another analytical approach to flexoelectricity in solids has been provided in [145] on the basis of Kirchhoff's plate theory. In particular, the electromechanical behaviour of thin hybrid graphene-reinforced piezoelectric composite (GRPC) plates subject to bending deformations is studied therein. The resulting fourth-order PDE is solved by means of a Fourier series expansion with respect to different mechanical loading conditions, and the influence of varying flexoelectric coefficients on the deflection of the mechanically loaded plate is studied. It can be observed that, with increasing flexoelectricity coefficients, the deflection decreases since a greater amount of elastic energy is transformed into electric energy. Accordingly, a flexoelectric stiffening effect is obtained.

Numerical approaches During the last two decades, various numerical approaches have been proposed for the investigation of flexoelectric effects in solids. Several researchers have investigated the flexoelectric effect in the context of small strains [1, 95, 98] and, especially for soft materials, by using a finite strain setting [35, 48, 115, 159, 177]. In order to deal with the incorporation of gradient contributions in the energy function and with the resulting PDE of, in general, fourth order, researchers have for example used mesh-free methods [1], B-spline immersed boundary approaches [37], C^0-interior penalty methods [165] or a finite element scheme on the basis of C^1 triangular Argyris

elements [177]. Moreover, isogeometric analysis is typically employed due to the underlying higher-order NURBS basis functions [69, 94, 115, 144, 159] and is also used in this thesis in order to deal with the flexoelectric coupling. Alternative numerical methods which avoid the treatment of the fourth-order PDE include mixed finite element methods [47, 98] and micromorphic approaches [102]. A compact overview on numerical frameworks in the context of flexoelectricity is also provided in recent review articles [49, 147, 163, 180].

Experimental findings on flexoelectricity-induced bone remodelling The process of bone remodelling is concerned with the healing of cracks that frequently occur in bones under cyclic mechanical load [77]. It is important for maintaining the structural integrity of bones and, accordingly, it has been investigated intensively in the literature such as in [53, 64, 83, 96]. One key aspect in this regard is the initiation of bone remodelling which is attributed to different phenomena. Apart from *streaming potentials* and *matrix piezoelectricity* which are investigated in, e.g., [130] and [65], it was recently found that *flexoelectricity* acts as a trigger for remodelling in cortical bone [120]. In their prior work, the authors have demonstrated the general capability of flexoelectricity to induce electric fields in bone, which are high enough to cause *osteocyte apoptosis* [164]. Based on this finding and by excluding other possible effects through an appropriate experimental setting, evidence is provided in [120] that flexoelectricity indeed causes osteocytes to undergo apoptosis and thus initiate bone remodelling. Fig. 1.6 shows the experimental results including the flexoelectricity-induced electric field in a pre-cracked specimen of bone mineral as well as the dead osteocytes in the vicinity of the crack.

The bone remodelling process itself has been analysed in many experimental studies in vivo as well as in vitro. In [18, 41], experimental findings on osteocyte-driven bone remodelling are discussed in particular. Studies in vivo enable the investigation of cellular processes in their natural environment. The regulation of bone formation by osteocytes is studied in, e.g., [93] by targeted deletion of the SOST gene in mice which produces the protein sclerostin. Sclerostin is expressed by osteocytes and possesses an inhibitory effect on bone formation [18]. Accordingly, an increased bone mass is observed in the experiments, whereas on the other hand, low bone mass is obtained in genetically modified mice with an overexpression of SOST [132]. In order to avoid animal testing, in vitro studies are also frequently performed for the investigation of the bone remodelling process and its regulating factors. In [86], an in vitro method is established in which osteocytes are locally damaged and their impact on the activation and differentiation of osteoclast precursors is analysed. More specifically speaking, osteocytes are cultured and subjected to local damage by scratching. A secretion of the macrophage colony stimulating factor (M-CSF) and the receptor activator of nuclear factor-κB ligand (RANKL) is obtained as a result of the induced damage. Moreover, by culturing osteoclast precursor cells on top of the damaged osteocytes, tartrate-resistant acid phosphatase (TRACP) is observed which is a marker of mature osteoclasts. Besides the cellular regulation, the spatial and temporal progression of the targeted remodelling process has been ex-

perimentally investigated in, e.g., [20, 64] and gives insight into the joint remodelling activity of the bone cells in form of *Basic Multicellular Units* (BMUs). A review on modern visualisation techniques such as micro-computed tomography (micro-CT) which can be used to investigate the BMU activity is provided in [76]. Fig. 1.7 shows a CT image of microcracks in a cortical bone specimen as well as a BMU travelling through cortical bone during the remodelling process.

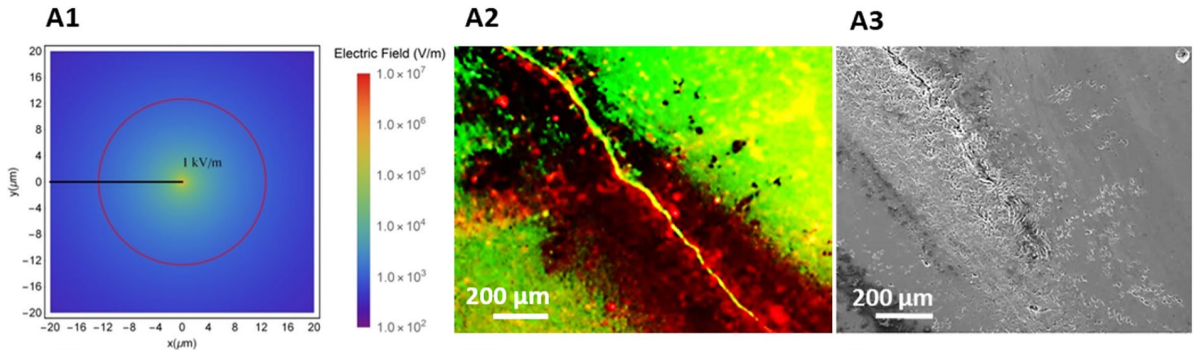

Figure 1.6: Impact of flexoelectricity in a pre-cracked sample of bone mineral, i.e. hydroxyapatite (HA). (A1) Flexoelectricity-induced electric field in the vicinity of the crack. (A2) Live/Dead staining of osteocytes cultured on the pre-cracked HA sample. (A3) Image of microcracks in the HA sample before cell culture. Reprinted from [120] under the terms of the Creative Commons Attribution 4.0 International License (CC BY 4.0).

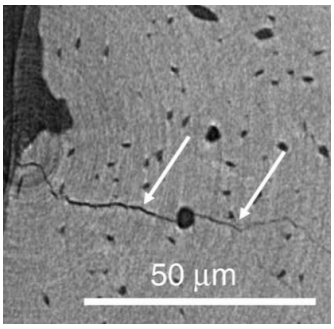

(a) CT image of microcracks in the mid-diaphyseal, cortical cross section of a mouse femur. The cracks occurred in consequence of compressive loading in an experimental setup in vitro. Reprinted from [166], copyright (2009), with permission from Elsevier.

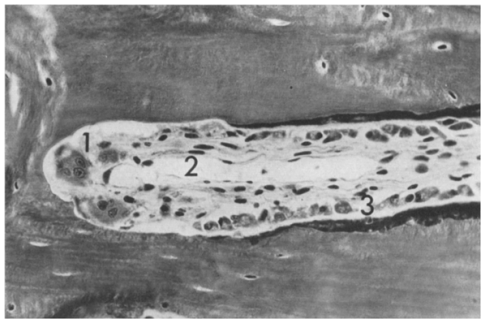

(b) Image of a BMU travelling through cortical bone. In front of the cutting cone, osteoclasts (1) resorb old bone. Around the central capillary (2), pre-osteoblasts and osteoblasts (3) follow and form new bone material. Reprinted from [138], copyright (1964), with permission from Springer.

Figure 1.7: Microcracks and the corresponding remodelling process in cortical bone.

Modelling approaches for bone remodelling Various numerical modelling approaches exist for the simulation of bone remodelling induced by streaming potentials and piezoelectricity. In [29, 127], Biot's theory of poroelasticity is employed within finite element

frameworks in order to study the fluid flow pattern and the induced streaming potentials in a remodelling osteon. In, e.g., [15, 57, 58] on the other hand, different finite element approaches for piezoelectricity in bones are proposed and reviewed in [111]. The impact of piezoelectricity-induced electric fields on bone resorption as well as formation is studied therein to predict bone density distributions after mechanical or electromechanical stimulation.

In contrast to streaming potentials and piezoelectricity, flexoelectricity as a possible trigger mechanism for bone remodelling has not been investigated quite as thoroughly due to the novelty of the underlying experimental findings. In [67], flexoelectricity has in fact been considered in a computational frame to predict growth processes in bone material. However, the approach is not embedded in a finite element context which would allow the simulation of complex bone structures, but simplified (rather academic) boundary value problems are studied for which analytical solutions can be derived. More specifically speaking, the flexoelectric effect is taken into account within a framework of Kirchhoff's plate theory and is employed to investigate bone density growth during the remodelling process. The authors also study combined volumetric and surface growth phenomena in bones based on Eshelby stresses as the main driving force for growth, whereas flexoelectric effects are not included in these works, see also [66, 70].

Regarding the cellular processes during bone remodelling and microcrack healing, mathematical models have been developed in, e.g., [27, 28, 72]. Therein, cells and signalling proteins are modelled as continuous populations which are connected by intercellular mechanisms. More specifically speaking, cells undergo production, apoptosis and differentiation in response to various signals and reactions between the chemical constituents. On this basis, the evolution of the chemical concentrations is investigated and the resulting changes in bone mass [72] respectively the formation of new bone material at the boundaries [27, 28] are evaluated. A two-dimensional model to account for the diffusion of bone cells and regulating species in addition to their temporal evolution has been proposed in [134, 135] by employing a set of spatio-temporal PDEs with time delay. The model is used to simulate the remodelling of microfractured bone tissues. In [10], an alternative model is introduced which includes simplified signalling mechanisms and an explicit incorporation of osteoclastic and osteoblastic precursor cells. A simulation of bone remodelling is carried out on the basis of an initially prescribed osteocyte apoptosis event.

In order to capture the cellular processes of bone remodelling in a unified framework with the mechanical behaviour of bone on the macroscale, multiscale approaches have been established [68, 126]. Accordingly, a distinction is made between organ level (whole bone), tissue level (cortical and trabecular structure), cell level (cells and intercellular connections) and molecular level (individual proteins). One key aspect therein is the connection between the different scales along with the transfer of variables and effective material properties among them.

1.2 Objective and outline of this thesis

The objective of this thesis is the modelling and numerical investigation of particular materials which exhibit size effects as a result of their underlying microstructure. In order to account for these microstructural effects in numerical simulations, a gradient continuum theory is considered and isogeometric analysis is employed in this work. Accordingly, isogeometric analysis will be introduced in Chapter 2 with special focus on the application to higher-gradient continua. Afterwards, the focus lies on materials with anisotropies and under electromechanical coupling. More specifically speaking, effects from the fibre bending stiffness in fibre-reinforced materials are studied in Chapter 3, whereas flexoelectric effects in dielectric solids are under investigation in Chapter 4 and, in particular, a modelling approach for flexoelectricity-induced bone remodelling is proposed. In the following, more details on the contents of each chapter are provided. Fig. 1.8 illustrates the connection between the individual topics.

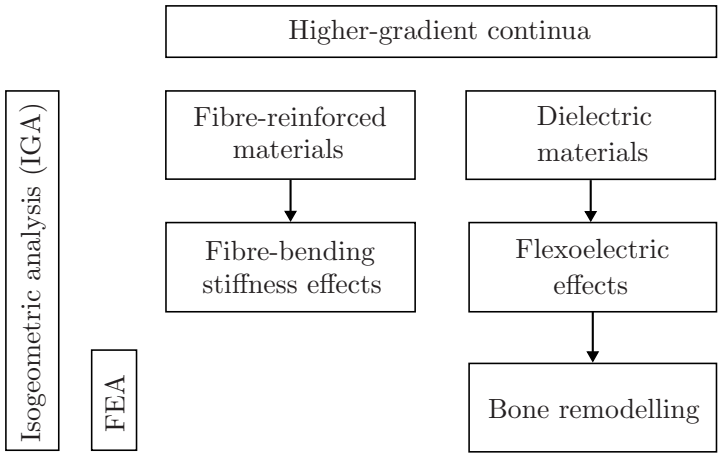

Figure 1.8: Overview of the contents of this thesis.

Chapter 2 Chapter 2 introduces the method of isogeometric analysis and thereby provides the basis for the numerical simulations in this work. In Sect. 2.1, the formulation of non-uniform rational B-splines which serve as basis functions in isogeometric analysis is presented as well as their derivatives up to arbitrary order. Moreover, characteristic properties of these basis functions are pointed out and a comparison to Lagrangian basis functions which are mostly used in classic finite element approaches is performed. Sect. 2.2 provides details on the isogeometric finite element framework including coordinate mappings, refinement techniques and the special treatment of inhomogeneous boundary conditions. In addition to this fundamental framework, several important procedures are presented in Sect. 2.3 which are relevant when dealing with higher-gradient continua

in particular. These include knot removal techniques as well as special procedures for the connection of multiple patches in order to ensure sufficient continuity within the isogeometric analysis framework. This chapter is supplemented by Appendix A.

Chapter 3 Chapter 3 deals with a computational framework for the modelling of fibre-reinforced composite materials in which effects from the bending stiffness of the fibres are accounted for. The modelling approach is based on the derivations in [153] including an extended energy formulation which takes the gradient of the fibre vector in fibre direction into account. The framework in [153] has been derived for the general case of finite deformations and the reduction to a linearised setting under the assumption of small strains has been presented therein. Accordingly, a computational framework to simulate the behaviour of fibre-reinforced materials with fibre-bending stiffness is presented in Sect. 3.1 for small strains, whereas the non-linear setting is studied in Sect. 3.2. In both cases, the kinematic relations as well as the balance equations in the context of the couple-stress theory are presented. Afterwards, a weak form of the governing equation is derived and discretised by using NURBS basis functions to obtain an isogeometric finite element formulation. The constitutive relations are obtained from a stored energy function which constitutes an isotropic part accounting for the bulk material and an anisotropic part containing the fibre contributions including, in particular, the higher-order terms stemming from the fibre bending stiffness. For validation purposes, an academic example is investigated by the presented computational frameworks. To be precise, a fibre-reinforced cylindrical tube subject to a pure azimuthal shear deformation is studied, whereas the fibres are assumed to exhibit a bending stiffness. The numerical results are compared to analytical solutions provided in [44]. In order to further analyse the influence of the fibre bending stiffness on the material behaviour, two additional boundary value problems are studied. In the small strain framework, the bending of a fibre-reinforced beam is investigated, whereas different values for the parameter characterising the fibre bending stiffness are employed and the orientation of the fibres within the beam is varied. Moreover, size effects are examined by comparing beams with different height-to-length-ratios. For the finite strain approach, a notched plate is analysed in terms of a uni-axial tensile test. In analogy to the bending beam, the influence of the fibre bending stiffness and of the initial fibre direction is studied in various numerical simulations. Supplementary material to this chapter is provided in Appendix B.

Chapter 4 Chapter 4 addresses flexoelectric effects in dielectric materials and, in particular, the role of such effects in the process of cortical bone remodelling. Accordingly, the working principle of flexoelectricity in dielectric solids is elaborated and the balance equations are derived for the electromechanical coupling. Moreover, different choices on thermodynamic potentials are discussed and accounted for in the formulation of the dissipation inequality in terms of Legendre-(Fenchel-)transformations. Subsequently, the governing set of balance equations is transferred into its weak form and the discretisation is carried out by employing NURBS basis functions within an isogeometric analysis

framework. A validation is performed by revisiting the cylindrical tube example from the previous chapter subject to a radial compressive load. An analytical solution is derived on the basis of [97] and compared to the numerical results obtained by the isogeometric analysis.

Since flexoelectricity has been found in [120, 164] to act as an initiating factor in the process of cortical bone remodelling, the fundamentals of this process are provided in Sect. 4.2. The focus lies on targeted remodelling of bone microcracks, in particular. In Sect. 4.3, a modelling approach for the initiation of bone remodelling by flexoelectricity is proposed. To this end, the electromechanical framework derived for flexoelectricity is extended towards chemical contributions accounting for the diffusion, production and apoptosis of bone cells included in the remodelling process, i.e. osteocytes, osteoclasts and osteoblasts as well as corresponding messenger substances. The resulting chemo-electro-mechanically coupled model is investigated within a globally C^1-continuous isogeometric finite element framework. The discretised weak forms of the governing equations are derived and a constitutive model is presented which considers different anisotropies in the mechanical as well as electromechanical material behaviour. Numerical simulations are carried out with respect to a pre-cracked cortical bone specimen, whereas the influence of flexoelectricity on the initiation of bone remodelling is studied and compared to piezoelectricity for different specimen sizes. In Sect. 4.4, the modelling approach is extended towards the entire remodelling process, from the previously investigated flexoelectric initiation up to the formation of new bone material by surface growth with the purpose of crack healing. In analogy to the previous section, the resulting chemo-electro-mechanical model is presented and all balance equations are derived. The specific modelling approach for surface growth is furthermore discussed. For the simulation of the bone remodelling process, a computational framework is proposed which includes isogeometric analysis for the simulation of the flexoelectric initiation of bone remodelling and a classic finite element scheme for the subsequent diffusion processes and the growth mechanism. Both frameworks as well as their coupling are elaborated in detail and the discretised weak forms of the governing equations are derived. Finally, a numerical simulation is carried out for the pre-cracked sample of cortical bone in order to investigate the flexoelectricity-induced crack healing process. This chapter is supplemented by Appendix C.

2 Isogeometric analysis for higher-gradient continua

Isogeometric analysis (IGA) was first introduced in 2005 [80] and serves as an alternative to classic finite element methods. It has been developed with the aim of closing the gap between the disciplines of geometric design and finite element analysis (FEA) which had, until then, evolved rather independently. In the subsequent years, several additional advantages of IGA over classic FEA approaches have been identified such as the exactness of geometric descriptions, the possibility of advanced refinement strategies, and the higher continuity of the underlying basis functions [40]. The latter is of particular importance in the context of higher-gradient continua which are the main focus of this thesis. In this chapter, the fundamentals of isogeometric analysis are presented and particular aspects regarding its application to higher-gradient continua are addressed. Accordingly, the main contents of this chapter are:

- higher-order derivatives of basis functions in IGA
- continuity properties of basis functions in IGA
- strategies to ensure global C^1-continuity in a (multi-patch) IGA framework

2.1 Fundamentals of isogeometric analysis

The fundamentals of isogeometric analysis are provided in [40, 80]. The most important feature of this method are the underlying basis functions which originate from the research field of computational geometry. Typically, non-uniform rational B-Splines (NURBS) are used, but also other functions such as T-Splines are suitable choices for basis functions in IGA. In this thesis, NURBS are employed which are discussed in detail in [129]. In the following sections, NURBS are addressed with a special focus on higher-order derivatives as well as on their continuity properties which are relevant within the analysis of higher-gradient continua.

2.1.1 Knot vectors, B-Splines and NURBS

B-Splines are defined on a parametric space which is spanned by knot vectors such as

$$\Xi = \{\xi_1 = \ldots = \xi_{p+1}, \xi_{p+2}, \ldots, \xi_{\mathrm{n}}, \xi_{\mathrm{n}+1} = \ldots = \xi_{\mathrm{n}+p+1}\}. \tag{2.1}$$

This format refers to a so-called *open knot vector*, since the first and last knot appear $p+1$ times, where p represents the polynomial degree of the corresponding basis functions. In the two-dimensional case, one knot vector is required for each of the two parametric directions ξ and η.

B-Spline basis functions are calculated from knot vectors in a recursive manner depending on their polynomial degree. For $p = 0$, the expression for the one-dimensional B-Spline functions reads

$$N_i^0(\xi) = \begin{cases} 1 & \text{for } \xi_i \leq \xi < \xi_{i+1}, \\ 0 & \text{otherwise.} \end{cases} \tag{2.2}$$

For all higher degrees, the basis functions are constructed recursively following

$$N_i^p(\xi) = \frac{\xi - \xi_i}{\xi_{i+p} - \xi_i} N_i^{p-1}(\xi) + \frac{\xi_{i+p+1} - \xi}{\xi_{i+p+1} - \xi_{i+1}} N_{i+1}^{p-1}(\xi), \tag{2.3}$$

whereas the fractions are set to zero if their denominator is zero, i.e. $\xi_{i+p} = \xi_i$ or $\xi_{i+p+1} = \xi_{i+1}$, respectively [40].

Although B-Splines could be employed as basis functions in a finite element framework, using their rational counterpart provides some advantages such as the possibility of accurately modelling circular structures. The difference between the two formulations is the consideration of weights w_i, so that the one-dimensional NURBS basis functions result in

$$R_i^p(\xi) = \frac{N_i^p(\xi)\, w_i}{\sum_{\hat{\imath}=1}^{\mathrm{n}} N_{\hat{\imath}}^p(\xi)\, w_{\hat{\imath}}} =: \frac{\widetilde{R}_i^p(\xi)}{W(\xi)} \tag{2.4}$$

and for the two-dimensional case the expression can be extended to

$$R_{i,j}^{p,q}(\xi,\eta) = \frac{N_i^p(\xi)\, M_j^q(\eta)\, w_{i,j}}{\sum_{\hat{\imath}=1}^{\mathrm{n}} \sum_{\hat{\jmath}=1}^{\mathrm{m}} N_{\hat{\imath}}^p(\xi)\, M_{\hat{\jmath}}^q(\eta)\, w_{\hat{\imath},\hat{\jmath}}} =: \frac{\widetilde{R}_{i,j}^{p,q}(\xi,\eta)}{W(\xi,\eta)}. \tag{2.5}$$

Therein, n and m denote the number of B-Spline basis functions N_i^p and M_j^q in the respective parametric directions ξ and η with polynomial degrees p and q. Following the tensor product structure that becomes apparent from (2.4) and (2.5), the basis functions for the three-dimensional case are obtained by further expansion towards a third

parametric direction ζ. Within the scope of this thesis, however, only two-dimensional examples are investigated.

With the NURBS basis functions (2.5) at hand, a NURBS surface can be constructed by taking a number of so-called *control points* into account. As there are $\mathrm{n_{cp}} = \mathrm{n}\cdot\mathrm{m}$ control points in the two-dimensional case, the control points can be stored in a matrix of dimension $[\mathrm{n_{cp}} \times \mathrm{n_{dm}}]$, i.e.

$$\boldsymbol{B} = \begin{bmatrix} \boldsymbol{B}^{\mathrm{t}}_{1,1} \\ \boldsymbol{B}^{\mathrm{t}}_{1,2} \\ \vdots \\ \boldsymbol{B}^{\mathrm{t}}_{\mathrm{n,m}} \end{bmatrix} \quad \text{with} \quad [\boldsymbol{B}_{i,j}] = \begin{bmatrix} B_1 \\ B_2 \end{bmatrix}_{i,j}, \quad i = 1, \ldots, \mathrm{n}, \quad j = 1, \ldots, \mathrm{m} \tag{2.6}$$

where B_1 and B_2 are the coefficients of the control point vector in Cartesian coordinates belonging to indices i and j. Analogously, the NURBS basis functions (2.5) are stored in a matrix $\boldsymbol{R}$ of dimension $[\mathrm{n_{cp}} \times 1]$. The spatial coordinates $\boldsymbol{x} = [x_1 \quad x_2]^{\mathrm{t}}$ of a point on the corresponding NURBS surface then follow as

$$\boldsymbol{x}(\xi, \eta) = \boldsymbol{B}^{\mathrm{t}} \cdot \boldsymbol{R}(\xi, \eta). \tag{2.7}$$

A NURBS surface in $\mathbb{R}^2$ can also be interpreted as the projective transformation of a B-Spline surface in $\mathbb{R}^3$. To this end, the *projective control points*

$$\left[\boldsymbol{B}^{w}_{i,j}\right] = w_{i,j} \begin{bmatrix} B_1 \\ B_2 \\ 1 \end{bmatrix}_{i,j} \tag{2.8}$$

are introduced in analogy to (2.6) and the coordinate vector of a point on the related NURBS surface can be expressed as

$$\boldsymbol{x}(\xi, \eta) = \frac{1}{W(\xi, \eta)} \begin{bmatrix} x^w_1 \\ x^w_2 \end{bmatrix} \quad \text{with} \quad \boldsymbol{x}^w(\xi, \eta) = \sum_{i=1}^{\mathrm{n}} \sum_{j=1}^{\mathrm{m}} N^p_i(\xi)\, M^q_j(\eta)\, \boldsymbol{B}^w_{i,j}. \tag{2.9}$$

Therein, the weighting function $W(\xi, \eta)$ introduced in (2.5) has been employed to obtain the projective transformation, cf. [40, 129]. This projective viewpoint is, e.g., important for the derivation of knot insertion in the context of mesh refinement which will be discussed in detail in Sect. 2.2.2.

2.1.2 Derivatives of NURBS basis functions

The derivatives of the two-dimensional NURBS basis functions (2.5) with respect to the parametric coordinates ξ and η are derived in [129] as

$$R_{i,j}^{(\mathrm{K,L})} = \frac{1}{W}\Bigg[\widetilde{R}_{i,j}^{(\mathrm{K,L})} - \sum_{k=1}^{\mathrm{K}} \binom{\mathrm{K}}{k} W^{(k,0)} R_{i,j}^{(\mathrm{K}-k,\mathrm{L})} - \sum_{l=1}^{\mathrm{L}} \binom{\mathrm{L}}{l} W^{(0,l)} R_{i,j}^{(\mathrm{K,L}-l)} - \sum_{k=1}^{\mathrm{K}} \binom{\mathrm{K}}{k} \sum_{l=1}^{\mathrm{L}} \binom{\mathrm{L}}{l} W^{(k,l)} R_{i,j}^{(\mathrm{K}-k,\mathrm{L}-l)}\Bigg]. \tag{2.10}$$

This general formulation yields the K^{th} (L^{th}) derivative with respect to ξ (η) and includes the expressions

$$\widetilde{R}_{i,j}^{(\mathrm{K,L})} = w_{i,j}\, \frac{\mathrm{d}^{\mathrm{K}}}{\mathrm{d}\xi^{\mathrm{K}}} N_i^p(\xi)\, \frac{\mathrm{d}^{\mathrm{L}}}{\mathrm{d}\eta^{\mathrm{L}}} M_j^q(\eta) \tag{2.11}$$

and

$$W^{(k,l)} = \sum_{i=1}^{\mathrm{n}} \sum_{j=1}^{\mathrm{m}} w_{i,j}\, \frac{\mathrm{d}^k}{\mathrm{d}\xi^k} N_i^p(\xi)\, \frac{\mathrm{d}^l}{\mathrm{d}\eta^l} M_j^q(\eta). \tag{2.12}$$

The derivatives of the one-dimensional B-Spline functions N_i^p therein follow from

$$\frac{\mathrm{d}^k}{\mathrm{d}\xi^k} N_i^p(\xi) = \frac{p!}{[p-k]!} \sum_{j=0}^{k} a_{k,j} N_{i+j}^{p-k}(\xi) \tag{2.13}$$

with the coefficients

$$\begin{aligned} &a_{0,0} = 1, \quad a_{k,0} = \frac{a_{k-1,0}}{\xi_{i+p-k+1} - \xi_i}, \quad a_{k,k} = \frac{-a_{k-1,k-1}}{\xi_{i+p+1} - \xi_{i+k}}, \\ &a_{k,j} = \frac{a_{k-1,j} - a_{k-1,j-1}}{\xi_{i+p+j-k+1} - \xi_{i+j}} \quad \text{for} \quad j = 1, \ldots, k-1 \end{aligned} \tag{2.14}$$

specified from the corresponding knot vector. For the B-Spline basis functions M_j^q, the derivatives with respect to the second parametric direction η are obtained analogously.

2.1.3 Properties of NURBS

NURBS basis functions possess several distinctive properties in comparison with classic Lagrangian basis functions which are traditionally used within the finite element method. These mostly originate from the properties of B-Splines from which NURBS are built and are especially important when dealing with higher-gradient continua. In Fig. 2.1, exemplary basis functions of NURBS as well as Lagrangian type are shown for a one-dimensional domain consisting of three elements. Lagrangian basis functions are defined individually on each element and fulfil the Kronecker delta property at the element edges. NURBS basis functions, on the other hand, are defined over the whole patch

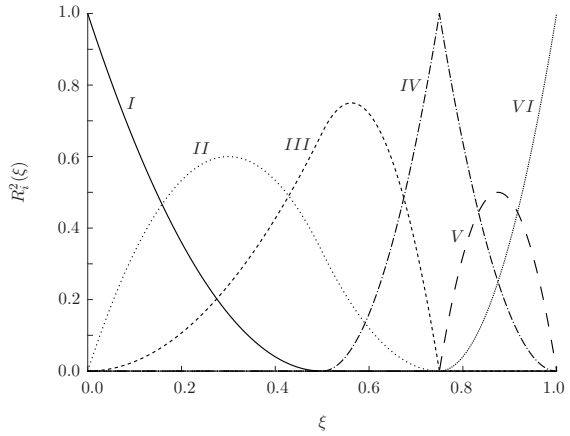

(a) Quadratic NURBS basis functions $R_i^2(\xi)$ for the knot vector $\Xi = \{0.0, 0.0, 0.0, 0.25, 0.5, 0.75, 0.75, 1.0, 1.0, 1.0\}$. The double knot at $\xi = 0.75$ leads to reduced continuity.

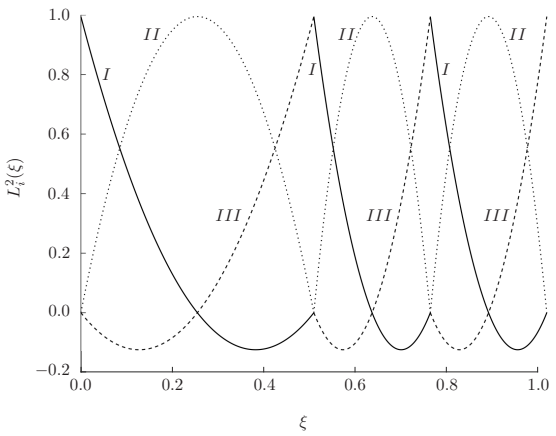

(b) Quadratic Lagrangian basis functions $L_i^2(\xi)$. The continuity is C^0 across all element boundaries.

Figure 2.1: Quadratic NURBS basis functions and quadratic Lagrangian basis function on the interval $[0.0, 1.0]$ spanning three finite elements in both cases.

which consists of multiple elements. The continuity between adjacent elements is C^{p-k} where k is the multiplicity of the knot which defines the respective element edge. NURBS are, accordingly, only interpolatory at the ends of the parameter interval spanned by their corresponding knot vectors, but, in general, not at interior knots. These continuity properties make NURBS excellent candidates for basis functions within the analysis of, e.g., second-gradient continua since the requirement of global C^1-continuity can, in general, be fulfilled by choosing at least quadratic NURBS as basis functions along with a multiplicity $k = 1$ for interior knots. Special techniques for maintaining C^1-continuity for higher knot multiplicities as well as over the boundaries of patches are discussed in detail in Sect. 2.3.

The support of NURBS basis functions is local to $p + 1$ knot spans which do not necessarily have to be non-zero. In the example presented in Fig. 2.1a, the quadratic basis functions are active over three knot spans, accordingly. In comparison to the Lagrangian basis functions presented in Fig. 2.1b, fewer functions are thus required for the discretisation of the domain with the same number of elements which may result in an increased computational efficiency. Fig. 2.1 also reveals that NURBS are pointwise non-negative which is a general property of NURBS in contrast to Lagrangian polynomials which can take negative values. Thereby, mass matrix entries are ensured to be positive a priori in the context of dynamic problems. The partition of unity property is fulfilled for both types of basis functions. For NURBS curves this attribute, together with the non-negativity and local support of the basis functions, yields a strong convex hull property which can analogously be deduced for NURBS surfaces and solids. Further details on the characteristics of NURBS, also in comparison with B-Splines, Bernstein polynomials and Lagrangian polynomials can be found in [4, 40, 80, 129].

2.2 Isogeometric analysis framework

Since isogeometric analysis can be regarded as a generalisation of classic FEA, cf. [40], the computational frameworks for both methods are similar to a large extent. The major differences, however, lie in the preprocessing and postprocessing procedures, i.e. construction of the geometry, mesh refinement, prescription of boundary conditions and output of nodal values, as well as in the incorporation of multiple patches and additional coordinate mappings which come along with the introduction of NURBS as basis functions. In the following, these distinct features of isogeometric analysis frameworks are addressed. Further implementation details are also discussed in [4].

2.2.1 Computational domains and coordinate mappings

Within the traditional finite element method, the geometry of the structure under investigation is contained by a so-called *physical space*, whereas numerical integration is performed on a *master element*, respectively *parent element*. Consequently, a mapping between the two domains is necessary. In isogeometric analysis, two different mappings are required for this purpose since an additional domain, denoted as *parameter space*, arises on which the underlying NURBS basis functions are defined. In addition, the mapping between the *control mesh* and the actual *physical mesh* needs to be taken into account [40, 80]. Fig. 2.2 visualises the different computational domains and corresponding mappings within the IGA framework.

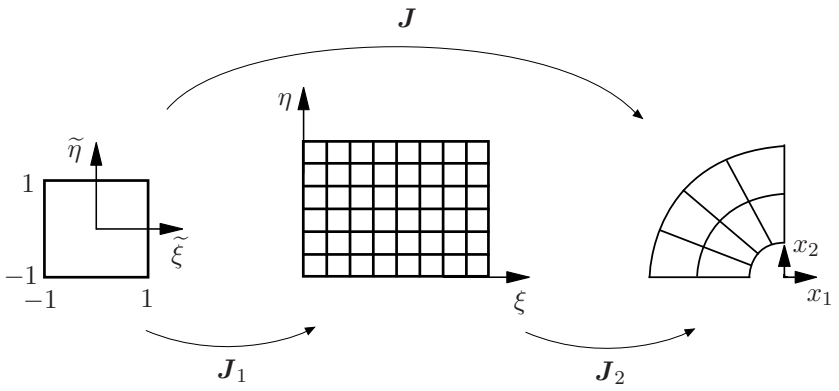

Figure 2.2: Computational domains and coordinate mappings within IGA. Reproduced from [170] under the terms of the Creative Commons Attribution 4.0 International License (CC BY 4.0).

In order to establish a relation between parent element and parameter space, an element $\Omega_e = [\xi_i, \xi_{i+1}] \otimes [\eta_j, \eta_{j+1}]$ of the latter is considered. Elements are, in general, defined by non-zero knot spans in the knot vectors and are represented by quadrilaterals

in the physical mesh. For the two-dimensional element under consideration, the Jacobian matrix $\boldsymbol{J}_1$ is obtained as

$$\boldsymbol{J}_1 = \begin{bmatrix} \frac{\partial \xi}{\partial \widetilde{\xi}} & 0 \\ 0 & \frac{\partial \eta}{\partial \widetilde{\eta}} \end{bmatrix} = \begin{bmatrix} \frac{1}{2}\left[\xi_{i+1} - \xi_i\right] & 0 \\ 0 & \frac{1}{2}\left[\eta_{j+1} - \eta_j\right] \end{bmatrix} \tag{2.15}$$

and relates the parametric coordinates $\boldsymbol{\xi} = [\xi \quad \eta]^{\mathrm{t}}$ to the coordinates $\widetilde{\boldsymbol{\xi}} = \left[\widetilde{\xi} \quad \widetilde{\eta}\right]^{\mathrm{t}}$ in the parent element. Secondly, a mapping between the parametric and the physical space is established by taking the relation between the control mesh and the physical mesh into account. From the definition of a NURBS surface in (2.7), the mapping between the coordinate vectors $\boldsymbol{x}$ and $\boldsymbol{\xi}$ can directly be obtained as

$$\boldsymbol{J}_2 = \frac{\partial \boldsymbol{x}}{\partial \boldsymbol{\xi}} = \boldsymbol{B}^{\mathrm{t}} \cdot \frac{\partial \boldsymbol{R}}{\partial \boldsymbol{\xi}}. \tag{2.16}$$

The final form of the Jacobian determinant, which is used to map between physical space and parent element within the IGA framework, includes the contributions of both (2.15) and (2.16) which yields

$$\det(\boldsymbol{J}) = \det(\boldsymbol{J}_1)\, \det(\boldsymbol{J}_2), \tag{2.17}$$

cf. [40].

Applying the mapping (2.16) to the derivatives of the NURBS basis functions determined in (2.10), the respective derivatives with respect to the physical domain can be computed. Applying the chain rule, the first-order and second-order derivatives of the NURBS basis functions with respect to the physical coordinates follow as

$$\frac{\partial \boldsymbol{R}}{\partial \boldsymbol{x}} = \frac{\partial \boldsymbol{R}}{\partial \boldsymbol{\xi}} \cdot \frac{\partial \boldsymbol{\xi}}{\partial \boldsymbol{x}} \tag{2.18}$$

and

$$\frac{\partial^2 \boldsymbol{R}}{\partial \boldsymbol{x} \partial \boldsymbol{x}} = \frac{\partial \boldsymbol{R}}{\partial \boldsymbol{\xi}} \cdot \frac{\partial^2 \boldsymbol{\xi}}{\partial \boldsymbol{x} \partial \boldsymbol{x}} + \left[\left[\frac{\partial \boldsymbol{\xi}}{\partial \boldsymbol{x}}\right]^{\mathrm{t}} \cdot \left[\frac{\partial^2 \boldsymbol{R}}{\partial \boldsymbol{\xi} \partial \boldsymbol{\xi}}\right]^{\mathrm{t}} \cdot \frac{\partial \boldsymbol{\xi}}{\partial \boldsymbol{x}}\right]^{\mathrm{t}}. \tag{2.19}$$

The expression for the third-order derivatives is obtained analogously and is denoted in Appendix A.1. In this thesis, the third-order derivatives are not directly necessary for the analysis but are employed for postprocessing purposes. In Appendix A.1, all derivatives included in (2.18)-(2.19) and not yet specified, are derived as well.

2.2.2 Refinement

As stated before, the number of non-zero knot spans in the knot vectors specifies the number of elements in the underlying finite element mesh. The multiplicity of reoccurring knots, on the other hand, affects the continuity of the basis functions at the corresponding inter-element locations. Consequently, the knot vectors need to be adjusted in order to obtain the desired mesh and basis function characteristics. In [129], different refinement procedures are presented for this purpose. In analogy to their counterparts in classic FEA, they are referred to as *knot insertion*, respectively h-refinement, *order elevation*, respectively p-refinement, and *k-refinement* which is unique for isogeometric analysis. The latter two methods aim at enhancing the order of the basis functions while either keeping the continuity fixed or increasing it at the same time. Within the scope of this thesis, these two procedures are not employed and, accordingly, will not be further elaborated. However, it shall be noted that especially k-refinement might be a useful tool in the context of analysing higher-gradient continua, in general.

In the following, knot insertion will be addressed in more detail. During knot insertion, new knots $\overline{\xi} \in [\xi_k, \xi_{k+1})$ are subsequently inserted into the knot vector Ξ, thus leading to an increased number of elements and possibly to more accurate analysis results. When a knot vector is expanded due to knot insertion, the control polygon has to be adjusted accordingly. To this end, each one-dimensional NURBS curve, e.g. as part of a two-dimensional surface, shall be treated individually. For the calculation of the new control points and weights of the j^{th} curve, the two-dimensional projective control points introduced in (2.8) are considered, whereas index j is omitted in the following for simplicity. The new set of projective control points is calculated on the basis of the updated knot vector according to

$$\overline{\boldsymbol{B}}_i^w = \alpha_i \boldsymbol{B}_i^w + [1 - \alpha_i]\, \boldsymbol{B}_{i-1}^w, \tag{2.20}$$

where

$$\alpha_i = \begin{cases} 1 & \text{for} \quad 1 \leq i \leq k-p, \\ \dfrac{\overline{\xi} - \xi_i}{\xi_{i+p} - \xi_i} & \text{for} \quad k-p+1 \leq i \leq k, \\ 0 & \text{for} \quad k+1 \leq i \leq \mathrm{n}+p+2. \end{cases} \tag{2.21}$$

For a two-dimensional NURBS surface, the algorithm is applied to each of the m NURBS curves. The same procedure is followed when inserting a knot into the knot vector for the second parametric direction η.

2.2.3 Inhomogeneous boundary conditions

Unlike Lagrange polynomials, NURBS basis functions are, in general, not interpolatory at the entire boundary of the computational domain. Accordingly, a specific technique is

required to accurately impose inhomogeneous boundary conditions. In [46], two possible ways of prescribing inhomogeneous Dirichlet boundary conditions have been introduced. The procedures are based on relation (2.7) between the control points and respective points of the physical mesh. Considering the $\mathrm{n_{bcp}}$ control points on the outer boundary of the control mesh only, and by choosing a number of $\mathrm{n_{bsp}}$ interpolating surface points on the boundary of the physical mesh, the relation is reformulated as

$$\widehat{\boldsymbol{x}} = \widehat{\boldsymbol{R}} \cdot \widehat{\boldsymbol{B}} \tag{2.22}$$

with matrices

$$\widehat{\boldsymbol{x}} = \begin{bmatrix} \boldsymbol{x}_1^{\mathrm{t}} \\ \boldsymbol{x}_2^{\mathrm{t}} \\ \vdots \\ \boldsymbol{x}_{\mathrm{n_{bsp}}}^{\mathrm{t}} \end{bmatrix}, \quad \widehat{\boldsymbol{B}} = \begin{bmatrix} \boldsymbol{B}_1^{\mathrm{t}} \\ \boldsymbol{B}_2^{\mathrm{t}} \\ \vdots \\ \boldsymbol{B}_{\mathrm{n_{bcp}}}^{\mathrm{t}} \end{bmatrix}, \quad \widehat{\boldsymbol{R}} = \begin{bmatrix} R_1^1 & \dots & R_1^{\mathrm{n_{bcp}}} \\ \vdots & \ddots & \vdots \\ R_{\mathrm{n_{bsp}}}^1 & \dots & R_{\mathrm{n_{bsp}}}^{\mathrm{n_{bcp}}} \end{bmatrix} \tag{2.23}$$

representing the chosen surface point coordinates, the control point coordinates on the corresponding boundary curve and the NURBS basis functions, respectively. Since isogeometric analysis traditionally comprises the isoparametric concept, the same structure holds for the displacements $\boldsymbol{u}$ that are associated with either the control points or the mesh points of the considered boundary, i.e.

$$\widehat{\boldsymbol{u}}_{\mathrm{bsp}} = \widehat{\boldsymbol{R}} \cdot \widehat{\boldsymbol{u}}_{\mathrm{bcp}}. \tag{2.24}$$

For the direct solution of equation system (2.24), matrix $\widehat{\boldsymbol{R}}$ must be quadratic and invertible. To this end, the number of interpolating points on the mesh must be chosen to be equal to the number of control points, and an adequate distribution of the mesh points has to be ensured [46]. The calculated displacement values $\widehat{\boldsymbol{u}}_{\mathrm{bcp}}$ are then imposed to the respective control points as inhomogeneous Dirichlet boundary conditions and will lead to the desired displacements $\widehat{\boldsymbol{u}}_{\mathrm{bsp}}$ of the actual boundary points of the body.

2.3 Isogeometric analysis for higher-gradient continua

In the context of (second-)gradient continua, second-order derivatives of the basis functions are required within the finite element framework. Consequently, global C^0-continuity, as possessed by traditional Lagrangian basis functions, is not sufficient from a mathematical point of view since square-integrability must be ensured not only for the first, but also for these second-order derivatives of the basis functions. Using NURBS as basis functions ensures continuity up to C^{p-1} across element boundaries. This motivates the use of isogeometric analysis for boundary value problems including higher-gradient contributions. In comparison to other established methods of dealing with fourth-order PDEs, such as multi-field methods or micromorphic approaches, IGA inherits the ad-

vantage that no additional degrees of freedom are introduced for the incorporation of higher-order derivatives of field variables. The C^{p-1}-continuity which makes NURBS excellent candidates for the approximation of such higher-order derivatives is, however, decreased at the location of knots with multiplicity $k > 1$ as well as at repeated control points, cf. Sect. 2.1.3. By additional procedures which are presented in the following sections, at least C^1-continuity is obtained at these locations which is sufficient for the solution of the problems under investigation in this thesis. Special focus also lies on the continuity between adjacent patches.

2.3.1 Knot removal

The issue of a decreased basis function continuity at the locations of repeated knots is addressed by the procedure of knot removal. In general, a knot of multiplicity k yields C^{p-k}-continuity of the underlying NURBS basis functions. The aim of knot removal is the re-increase of continuity by removing one or more repeated knots from the knot vector and thereby decreasing the multiplicity k.

The process of knot removal is derived in [129] by reversing the procedure of knot insertion which has been discussed in detail in Sect. 2.2.2. If a knot $\overline{\xi}$ being the rth knot in the knot vector, i.e. $\overline{\xi} = \xi_r \neq \xi_{r+1}$, of initial multiplicity s is removed t times, the new control points in the tth removal step can be found as

$$\begin{aligned} &\overline{\boldsymbol{B}}^{\boldsymbol{w}}_{i,t} = \frac{1}{\alpha_i}\left[\boldsymbol{B}^{\boldsymbol{w}}_{i,t-1} - (1-\alpha_i)\boldsymbol{B}^{\boldsymbol{w}}_{i-1,t}\right] \\ &\text{for} \quad r-p-t+1 \leq i \leq \tfrac{1}{2}\left[2r-p-s-t\right] \end{aligned} \tag{2.25}$$

and

$$\begin{aligned} &\overline{\boldsymbol{B}}^{\boldsymbol{w}}_{j,t} = \frac{1}{1-\alpha_j}\left[\boldsymbol{B}^{\boldsymbol{w}}_{j,t-1} - \alpha_j\boldsymbol{B}^{\boldsymbol{w}}_{j+1,t}\right] \\ &\text{for} \quad \tfrac{1}{2}\left[2r-p-s+t+1\right] \leq j \leq r-s+t-1 \end{aligned} \tag{2.26}$$

with the constant coefficients

$$\alpha_i = \frac{\overline{\xi} - \xi_i}{\xi_{i+p+t} - \xi_i}, \quad \alpha_j = \frac{\overline{\xi} - \xi_{j-t+1}}{\xi_{j+p+1} - \xi_{j-t+1}}. \tag{2.27}$$

Due to the local support of NURBS, the remaining control points are not affected by the removal process and do, as a consequence, not change.

Remark 2.1. It is, in general, not known a priori if a knot is removable from the knot vector without changing the geometry. In every step of the knot removal process, this has to be examined individually. Detailed information on this procedure is provided in [129, Sect. 5.4].

2.3.2 C^1-continuity over multiple patches

As open knot vectors are typically employed within IGA, this specifically means that the knot vectors are interpolatory at the ends of the parameter space interval where knots are repeated $p+1$ times. In the case of multiple patches, it is thus of particular importance to obtain the required C^1-continuity across the patch boundaries which naturally coincide with the ends of the parameter space intervals.

Various approaches for the enforcement of C^1-continuity across patches exist in literature. In [30], a strong multipatch C^1-coupling method is proposed which imposes constraints on the underlying basis functions and their derivatives. Other approaches, which result in a weak coupling between the patches, are mortar methods [26] or Nitsche's method [118]. On the other hand, continuity constraints are imposed on the vector of unknowns in the global system of equations in [40, 80]. In this thesis, the latter idea is employed so that C^1-constraints are directly applied to the field variables and a strong patch coupling is enforced as a consequence. In accordance with the detailed derivations in [129], the C^0 as well as C^1-condition are determined in terms of the control points of two connected patches. Assuming that these patches are connected in ξ-direction, these conditions are

$$\boldsymbol{B}_1^{\mathrm{B}} = \boldsymbol{B}_{\mathrm{n^A}}^{\mathrm{A}} \qquad \text{for } C^0\text{-continuity,} \tag{2.28}$$

$$\boldsymbol{B}_2^{\mathrm{B}} - \boldsymbol{B}_1^{\mathrm{B}} = k\left[\boldsymbol{B}_{\mathrm{n^A}}^{\mathrm{A}} - \boldsymbol{B}_{\mathrm{n^A}-1}^{\mathrm{A}}\right] \qquad \text{for } C^1\text{-continuity,} \tag{2.29}$$

and hold for the control points $\boldsymbol{B}_i^{\mathrm{A}} \in \{\boldsymbol{B}_1^{\mathrm{A}}, \boldsymbol{B}_2^{\mathrm{A}}, ..., \boldsymbol{B}_{\mathrm{n^A}}^{\mathrm{A}}\}$ and $\boldsymbol{B}_i^{\mathrm{B}} \in \{\boldsymbol{B}_1^{\mathrm{B}}, \boldsymbol{B}_2^{\mathrm{B}}, ..., \boldsymbol{B}_{\mathrm{n^B}}^{\mathrm{B}}\}$ of each curve in η-direction of connected patches A and B, see also [60] and Fig. 2.3. Therein, scalar k is dependent on the knot vectors Ξ^{A} and Ξ^{B}, on the corresponding polynomial degrees p^{A} and p^{B} as well as on the control point weights w_i^{A} and w_i^{B}. To be precise, the scalar is calculated according to

$$k = \frac{p^{\mathrm{A}}}{p^{\mathrm{B}}} \frac{\xi_{p^{\mathrm{B}}+2}}{1-\xi_{\mathrm{n^A}}} \frac{w_1^{\mathrm{B}}\, w_{\mathrm{n^A}-1}^{\mathrm{A}}}{w_2^{\mathrm{B}}\, w_{\mathrm{n^A}}^{\mathrm{A}}} \tag{2.30}$$

when considering normalised and open knot vectors of the form $\Xi = \{0, 0, \ldots, 0, \xi_{p+2}, \ldots, \xi_{\mathrm{n}}, 1, \ldots, 1, 1\}$. Constant k as defined in (2.30) ensures equality of the derivatives of the boundary NURBS curves belonging to the connected patches with respect to parametric direction ξ, see [129, (4.9)-(4.10)]. It is assumed in this regard that patch A is located on the left of patch B as illustrated in Fig. 2.3. For the special scenario in which the two patches contain basis functions of the same polynomial degree, i.e. $p^{\mathrm{A}} = p^{\mathrm{B}}$, knot vectors which are symmetric over the interface in the sense $\xi_{p^{\mathrm{B}}+2} - 0 = 1 - \xi_{\mathrm{n^A}}$, and control point weights which are as well symmetric over the interface, i.e. $w_1^{\mathrm{B}} = w_{\mathrm{n^A}}^{\mathrm{A}}$ and $w_2^{\mathrm{B}} = w_{\mathrm{n^A}-1}^{\mathrm{A}}$, the parameter takes the value $k = 1$. Following the isoparametric concept, constraints (2.28) and (2.29) can straightforwardly be applied to the field variables, such as displacement vector $\boldsymbol{u}$, so that combining both

conditions yields

$$\boldsymbol{u}_1^{\mathrm{B}} = \frac{1}{1+k}\left[\boldsymbol{u}_2^{\mathrm{B}} + k\,\boldsymbol{u}_{\mathrm{n^A}-1}^{\mathrm{A}}\right]. \tag{2.31}$$

The relations in this form are incorporated into the global system of equations in terms of linear constraints following the procedure established in [168].

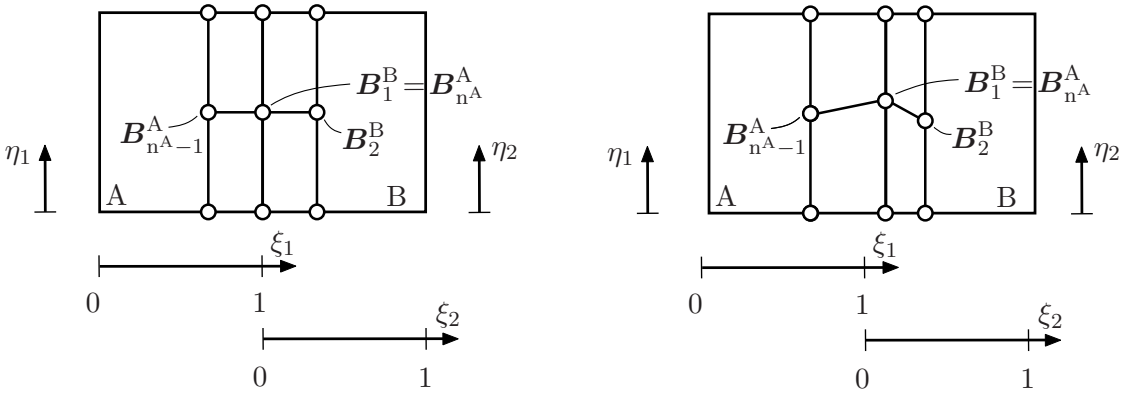

(a) In this example, the C^1-continuity condition (2.29) with $k = 1$ is directly fulfilled with respect to the control points.

(b) In this example, the C^1-continuity condition (2.29) with $k = 1$ is not fulfilled with respect to the control points since they are neither collinear nor equally spaced over the patch boundary.

Figure 2.3: Multipatch domain including two patches A and B with one connecting boundary. C^1-continuity shall be enforced with respect to the ξ_i-direction. Reproduced from [174] under the terms of the Creative Commons Attribution License (CC BY).

A Appendix

A.1 Higher-order NURBS derivatives

The first-order and second-order derivatives of NURBS basis functions with respect to the physical coordinates have been derived in Sect. 2.2.1 by employing the corresponding coordinate mappings. The third-order derivative of a NURBS basis function R analogously follows as

$$\begin{aligned}\frac{\partial^3 R}{\partial \boldsymbol{x}\partial \boldsymbol{x}\partial \boldsymbol{x}} = \frac{\partial R}{\partial \boldsymbol{\xi}} \cdot \frac{\partial^3 \boldsymbol{\xi}}{\partial \boldsymbol{x}\partial \boldsymbol{x}\partial \boldsymbol{x}} + \left[\frac{\partial \boldsymbol{\xi}}{\partial \boldsymbol{x}}\right]^{\mathrm{t}} \cdot \frac{\partial^2 R}{\partial \boldsymbol{\xi}\partial \boldsymbol{\xi}} \cdot \frac{\partial^2 \boldsymbol{\xi}}{\partial \boldsymbol{x}\partial \boldsymbol{x}} + \left[\left[\frac{\partial \boldsymbol{\xi}}{\partial \boldsymbol{x}}\right]^{\mathrm{t}} \cdot \frac{\partial^2 R}{\partial \boldsymbol{\xi}\partial \boldsymbol{\xi}} \cdot \frac{\partial^2 \boldsymbol{\xi}}{\partial \boldsymbol{x}\partial \boldsymbol{x}}\right]^{\mathrm{t}} \\ + \left[\left[\frac{\partial \boldsymbol{\xi}}{\partial \boldsymbol{x}}\right]^{\mathrm{t}} \cdot \frac{\partial^2 R}{\partial \boldsymbol{\xi}\partial \boldsymbol{\xi}} \cdot \frac{\partial^2 \boldsymbol{\xi}}{\partial \boldsymbol{x}\partial \boldsymbol{x}}\right]^{\mathrm{T}} + \left[\frac{\partial \boldsymbol{\xi}}{\partial \boldsymbol{x}}\right]^{\mathrm{t}} \cdot \frac{\partial^3 R}{\partial \boldsymbol{\xi}\partial \boldsymbol{\xi}\partial \boldsymbol{\xi}} : \left[\frac{\partial \boldsymbol{\xi}}{\partial \boldsymbol{x}} \overline{\otimes} \frac{\partial \boldsymbol{\xi}}{\partial \boldsymbol{x}}\right]. \end{aligned} \tag{2.32}$$

Therein, the mapping between the physical coordinates $\boldsymbol{x}$ and the parametric coordinates $\boldsymbol{\xi}$ is required. The first-order mapping $\partial\boldsymbol{\xi}/\partial\boldsymbol{x}$ is obtained by inversion of the Jacobian matrix $\boldsymbol{J}_2$ specified in (2.16). The second-order mapping can be derived as

$$\frac{\partial^2 \boldsymbol{\xi}}{\partial \boldsymbol{x}\partial \boldsymbol{x}} = \frac{\partial}{\partial \boldsymbol{x}}\left[\frac{\partial \boldsymbol{\xi}}{\partial \boldsymbol{x}}\right] = \frac{\partial}{\partial \boldsymbol{x}} \boldsymbol{J}_2^{-1} = \frac{\partial \boldsymbol{J}_2^{-1}}{\partial \boldsymbol{J}_2} : \frac{\partial \boldsymbol{J}_2}{\partial \boldsymbol{x}} \tag{2.33}$$

with

$$\frac{\partial \boldsymbol{J}_2^{-1}}{\partial \boldsymbol{J}_2} = -\boldsymbol{J}_2^{-1} \overline{\otimes} \boldsymbol{J}_2^{-\mathrm{t}}, \quad \frac{\partial \boldsymbol{J}_2}{\partial \boldsymbol{x}} = \frac{\partial^2 \boldsymbol{x}}{\partial \boldsymbol{\xi}\partial \boldsymbol{\xi}} \cdot \boldsymbol{J}_2^{-1}. \tag{2.34}$$

Similarly, the third-order mapping follows as

$$\frac{\partial^3 \boldsymbol{\xi}}{\partial \boldsymbol{x}\partial \boldsymbol{x}\partial \boldsymbol{x}} = \frac{\partial^2}{\partial \boldsymbol{x}\partial \boldsymbol{x}}\left[\frac{\partial \boldsymbol{\xi}}{\partial \boldsymbol{x}}\right] = \frac{\partial^2 \boldsymbol{J}_2^{-1}}{\partial \boldsymbol{x}\partial \boldsymbol{x}} = \frac{\partial \boldsymbol{J}_2^{-1}}{\partial \boldsymbol{\xi}} \cdot \frac{\partial^2 \boldsymbol{\xi}}{\partial \boldsymbol{x}\partial \boldsymbol{x}} + \frac{\partial^2 \boldsymbol{J}_2^{-1}}{\partial \boldsymbol{\xi}\partial \boldsymbol{\xi}} : \left[\frac{\partial \boldsymbol{\xi}}{\partial \boldsymbol{x}} \overline{\otimes} \frac{\partial \boldsymbol{\xi}}{\partial \boldsymbol{x}}\right] \tag{2.35}$$

with

$$\frac{\partial \boldsymbol{J}_2^{-1}}{\partial \boldsymbol{\xi}} = \frac{\partial \boldsymbol{J}_2^{-1}}{\partial \boldsymbol{J}_2} : \frac{\partial \boldsymbol{J}_2}{\partial \boldsymbol{\xi}} = \frac{\partial \boldsymbol{J}_2^{-1}}{\partial \boldsymbol{J}_2} : \frac{\partial^2 \boldsymbol{x}}{\partial \boldsymbol{\xi}\partial \boldsymbol{\xi}}, \tag{2.36}$$

$$\frac{\partial^2 \boldsymbol{J}_2^{-1}}{\partial \boldsymbol{\xi}\partial \boldsymbol{\xi}} = \frac{\partial \boldsymbol{J}_2^{-1}}{\partial \boldsymbol{J}_2} : \frac{\partial^2 \boldsymbol{J}_2}{\partial \boldsymbol{\xi}\partial \boldsymbol{\xi}} = \frac{\partial \boldsymbol{J}_2^{-1}}{\partial \boldsymbol{J}_2} : \frac{\partial^3 \boldsymbol{x}}{\partial \boldsymbol{\xi}\partial \boldsymbol{\xi}\partial \boldsymbol{\xi}}. \tag{2.37}$$

The derivatives

$$\frac{\partial^2 \boldsymbol{x}}{\partial \boldsymbol{\xi}\partial \boldsymbol{\xi}} = \boldsymbol{B}^{\mathrm{t}} \cdot \frac{\partial^2 \boldsymbol{R}}{\partial \boldsymbol{\xi}\partial \boldsymbol{\xi}}, \quad \frac{\partial^3 \boldsymbol{x}}{\partial \boldsymbol{\xi}\partial \boldsymbol{\xi}\partial \boldsymbol{\xi}} = \boldsymbol{B}^{\mathrm{t}} \cdot \frac{\partial^3 \boldsymbol{R}}{\partial \boldsymbol{\xi}\partial \boldsymbol{\xi}\partial \boldsymbol{\xi}} \tag{2.38}$$

are obtained in analogy to (2.16).

3 Fibre-reinforced solids with fibre-bending stiffness

In classic modelling approaches for fibre-reinforced solids, the fibres are solely characterised by a unit vector representing the fibre direction. As a natural consequence, these models only account for the tensile stiffness of the fibres, whereas their resistance with respect to, e.g., twisting or bending is neglected. However, experiments have revealed that the latter may become significant on the micro and nano scale. In this chapter, the modelling approach proposed in [153] for fibre-reinforced solids with fibre bending stiffness is adopted and isogeometric analysis is employed for its numerical treatment. In Sect. 3.1, the framework for a small strain setting is established and in Sect. 3.2 an extension to the more general case including finite deformations is presented in order to enable the simulation of more complex boundary value problems.

The key contributions of this chapter are:

- globally C^1-continuous IGA frameworks for the simulation of fibre-reinforced solids with fibre bending stiffness in a small and finite strain setting
- validation of both frameworks by comparison with analytical solutions
- investigation of size effects and analysis of the impact of the fibre bending stiffness and of the initial fibre direction

3.1 Modelling approach for a small strain setting

The proposed modelling approach for fibre-reinforced composites is presented in this section under the assumption of small strains. It is further assumed that the fibres are convected with the matrix material and that they possess a bending stiffness. The focus lies on composites with reinforcement by one single family of fibres, and these fibres are assumed to be initially straight. The governing equations have been derived in [153] which serves as a basis for the work presented here. Originally, the derivations therein correspond to the general case of finite strains but a consistent linearisation has additionally been performed in order to enable a small strain formulation. The latter is

under investigation in this section while the framework for finite strains will be studied in Sect. 3.2.

3.1.1 Small strain kinematics

For the purpose of studying fibre bending stiffness effects, a generalised continuum approach, particularly gradient elasticity, is considered. In the case of a small strain theory, it takes into account not only the first but also the second gradient of the unknown displacement field $\boldsymbol{u}$. As in standard elasticity theory, the analysis requires the small strain tensor

$$\boldsymbol{\varepsilon} = \frac{1}{2}\left[\boldsymbol{h} + \boldsymbol{h}^{\mathrm{t}}\right] \quad \text{with} \quad \boldsymbol{h} = \nabla_{\boldsymbol{x}}\boldsymbol{u} \tag{3.1}$$

as the symmetric part of the first gradient of the displacement field. For the linearised theory, all terms of order $\mathcal{O}(\varepsilon^n)$ with $\varepsilon = \|\boldsymbol{\varepsilon}\| \ll 1$ and $n \geq 2$ are neglected. Moreover, all partial derivatives of the displacement field are supposed to be of order $\mathcal{O}(\varepsilon)$. Considering these properties, the vector

$$\boldsymbol{\beta} = \boldsymbol{a} + \nabla_{\boldsymbol{x}}\boldsymbol{u} \cdot \boldsymbol{a} \tag{3.2}$$

is introduced [153]. It incorporates the fibre direction which is described by the vector $\boldsymbol{a}$ with $||\boldsymbol{a}|| = \sqrt{\boldsymbol{a} \cdot \boldsymbol{a}} = 1$. The gradient of vector $\boldsymbol{\beta}$ is obtained as

$$\boldsymbol{\gamma} = \nabla_{\boldsymbol{x}}\boldsymbol{\beta} = [\nabla_{\boldsymbol{x}}\nabla_{\boldsymbol{x}}\boldsymbol{u}] \cdot \boldsymbol{a} =: \boldsymbol{\kappa} \cdot \boldsymbol{a} \tag{3.3}$$

under the assumption that the fibres are initially straight and homogeneously distributed. It becomes evident that this second-order tensor $\boldsymbol{\gamma}$ includes, amongst others, the fibre curvature as well as the gradient of the fibre stretch in dependence of second gradients of the displacement field.

3.1.2 Balance equations

The consideration of second-order gradients of the displacement field in the modelling approach, cf. (3.3), motivates the employment of a generalised continuum theory, such as the couple-stress theory. The corresponding balance equations have been derived in [108] and will be summarised in the following sections.

3.1.2.1 Balance of mass

For a body $\Omega \subset \mathbb{R}^3$, as sketched in Fig. 3.1, the total mass is preserved under the assumption that Ω represents a closed system. Consequently, the balance of mass in integral form reads

$$\frac{\mathrm{d}}{\mathrm{d}t}\int_{\Omega}\rho\,\mathrm{d}v = 0 \tag{3.4}$$

with mass density ρ. Application of Reynold's transport theorem leads to the local form which can be denoted as

$$\dot{\rho} + \rho\,\nabla_{\boldsymbol{x}}\cdot\boldsymbol{v} = 0 \tag{3.5}$$

with velocity vector $\boldsymbol{v} = \dot{\boldsymbol{u}}$ and with $\dot{\bullet}$ representing the time derivative of $\bullet$.

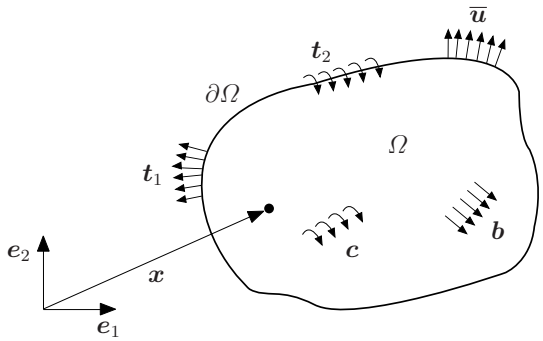

Figure 3.1: Two-dimensional domain Ω in the linear couple-stress theory. Employed vectors: coordinate vector $\boldsymbol{x}$, body force vector $\boldsymbol{b}$, body couple vector $\boldsymbol{c}$, vector of tractions $\boldsymbol{t}_1$ acting on the surface $\partial\Omega$, vector of couples $\boldsymbol{t}_2$ acting on the surface $\partial\Omega$, vector of displacements $\overline{\boldsymbol{u}}$ prescribed on the surface $\partial\Omega$. Reproduced from [170] under the terms of the Creative Commons Attribution 4.0 International License (CC BY 4.0).

3.1.2.2 Balance of linear and angular momentum

The balance of linear momentum takes body forces $\boldsymbol{b}$, that act within the considered domain Ω, as well as tractions $\boldsymbol{t}_1$ on its surface $\partial\Omega$ into account. The sum of these force contributions equals the rate of change of linear momentum, such that the integral form of the balance equation follows as

$$\frac{\mathrm{d}}{\mathrm{d}t}\int_{\Omega}\rho\,\boldsymbol{v}\,\mathrm{d}v = \int_{\partial\Omega}\boldsymbol{t}_1\,\mathrm{d}a + \int_{\Omega}\rho\,\boldsymbol{b}\,\mathrm{d}v. \tag{3.6}$$

The boundary tractions can be rewritten in terms of Cauchy's theorem, accordingly

$$\boldsymbol{t}_1 = \boldsymbol{\sigma}^{\mathrm{t}}\cdot\boldsymbol{n}, \tag{3.7}$$

where $\boldsymbol{n}$ represents the surface outward normal unit vector and where $\boldsymbol{\sigma}$ is the stress tensor. Applying the divergence theorem to the integral form (3.6), the corresponding local form of balance of linear momentum is obtained as

$$\rho\,\dot{\boldsymbol{v}} = \nabla_{\boldsymbol{x}}\cdot\boldsymbol{\sigma}^{\mathrm{t}} + \rho\,\boldsymbol{b}. \tag{3.8}$$

In analogy to the balance of linear momentum, the rate of change of angular momentum equals the sum of all couples that act on Ω. This can be expressed in integral form as

$$\frac{\mathrm{d}}{\mathrm{d}t}\int_{\Omega}\rho\,[\boldsymbol{r}\times\boldsymbol{v}]\,\mathrm{d}v=\int_{\partial\Omega}[\boldsymbol{r}\times\boldsymbol{t}_1+\boldsymbol{t}_2]\,\mathrm{d}a+\int_{\Omega}\rho\,[\boldsymbol{r}\times\boldsymbol{b}+\boldsymbol{c}]\,\mathrm{d}v, \tag{3.9}$$

where $\boldsymbol{r}=\boldsymbol{x}-\boldsymbol{x}_{\mathrm{r}}$ is the distance between the spatial position $\boldsymbol{x}$ and a reference position $\boldsymbol{x}_{\mathrm{r}}$ and where vector $\boldsymbol{c}$ represents the body couples. Similar to the surface tractions $\boldsymbol{t}_1$, the couples that act on the surface of domain Ω are introduced as

$$\boldsymbol{t}_2=\boldsymbol{m}^{\mathrm{t}}\cdot\boldsymbol{n} \tag{3.10}$$

with couple-stress tensor $\boldsymbol{m}$. Application of the divergence theorem yields the local form of the balance equation as

$$\boldsymbol{0}=\nabla_{\boldsymbol{x}}\cdot\boldsymbol{m}^{\mathrm{t}}+\rho\,\boldsymbol{c}+\boldsymbol{\epsilon}:\boldsymbol{\sigma} \tag{3.11}$$

including the permutation tensor $\boldsymbol{\epsilon}$. A general outcome of the balance of angular momentum for higher-gradient continua is that the skew-symmetric part of the stress tensor is non-zero and can be derived by using (3.11). Accordingly, it can be expressed in terms of the divergence of the couple-stress tensor, i.e.

$$\boldsymbol{\sigma}^{\mathrm{skw}}=\frac{1}{2}\boldsymbol{I}\times\left[\nabla_{\boldsymbol{x}}\cdot\boldsymbol{m}^{\mathrm{t}}+\rho\,\boldsymbol{c}\right] \tag{3.12}$$

and the stress tensor follows as

$$\boldsymbol{\sigma}=\boldsymbol{\sigma}^{\mathrm{sym}}+\boldsymbol{\sigma}^{\mathrm{skw}}. \tag{3.13}$$

Inserting this relation into the local form of balance of linear momentum (3.8) leads to a partial differential equation of fourth order which can be denoted as

$$\rho\,\dot{\boldsymbol{v}}=\nabla_{\boldsymbol{x}}\cdot\boldsymbol{\sigma}^{\mathrm{sym}}+\rho\,\boldsymbol{b}+\frac{1}{2}\nabla_{\boldsymbol{x}}\times\left[\nabla_{\boldsymbol{x}}\cdot\boldsymbol{m}^{\mathrm{t}}+\rho\,\boldsymbol{c}\right]. \tag{3.14}$$

This expression represents the governing equation for the couple-stress theory in the format that is also employed in [108]. As this work proceeds, a quasi-static version of (3.14) is considered and all body forces, body couples and couples that may act on the boundary of domain Ω are neglected, i.e. $\boldsymbol{b}=\boldsymbol{0}$, $\boldsymbol{c}=\boldsymbol{0}$, $\boldsymbol{t}_2=\boldsymbol{0}$. The reduced form of the fourth-order PDE accordingly is

$$\boldsymbol{0}=\nabla_{\boldsymbol{x}}\cdot\boldsymbol{\sigma}^{\mathrm{t}} \tag{3.15}$$

$$=\nabla_{\boldsymbol{x}}\cdot\boldsymbol{\sigma}^{\mathrm{sym}}+\frac{1}{2}\nabla_{\boldsymbol{x}}\times\left[\nabla_{\boldsymbol{x}}\cdot\boldsymbol{m}^{\mathrm{t}}\right]. \tag{3.16}$$

Remark 3.1. The *couple-stress tensor* $\boldsymbol{m}$ has been introduced in (3.10) as a second-order tensor. In gradient theories in general, the higher-order stresses are, however, often characterised by a third-order tensor $\boldsymbol{\pi}$ denoted as *hyper-stress* or *double-stress tensor* [109]. The stress tensor in (3.13) can then alternatively be defined as

$$\boldsymbol{\sigma} = \boldsymbol{\sigma}^{\mathrm{sym}} - \nabla_{\boldsymbol{x}} \cdot \boldsymbol{\pi}. \tag{3.17}$$

With this definition at hand, the couple-stress tensor can be interpreted as the skew-symmetric part of such a hyper-stress tensor, so that

$$\boldsymbol{m}^{\mathrm{t}} = \boldsymbol{\epsilon} : \boldsymbol{\pi} \tag{3.18}$$

under consideration of balance equation (3.15).

3.1.2.3 Balance of energy

Finally, the balance of mechanical energy is considered, whereas contributions associated with the thermal energy are neglected. With internal energy U, the corresponding balance equation reads

$$\begin{aligned} \frac{\mathrm{d}}{\mathrm{d}t} \int_{\Omega} \rho \left[\frac{1}{2} \boldsymbol{v} \cdot \boldsymbol{v} + U \right] \mathrm{d}v = \int_{\partial\Omega} \left[\boldsymbol{t}_1 \cdot \boldsymbol{v} + \frac{1}{2} \boldsymbol{t}_2 \cdot \nabla_{\boldsymbol{x}} \times \boldsymbol{v} \right] \mathrm{d}a \\ + \int_{\Omega} \rho \left[\boldsymbol{b} \cdot \boldsymbol{v} + \frac{1}{2} \boldsymbol{c} \cdot \nabla_{\boldsymbol{x}} \times \boldsymbol{v} \right] \mathrm{d}v. \end{aligned} \tag{3.19}$$

The local form is obtained by using the balance equations of momentum in the form of (3.8) and (3.11), so that

$$\rho \dot{U} = \boldsymbol{\sigma}^{\mathrm{sym}} : \nabla_{\boldsymbol{x}} \boldsymbol{v} + \frac{1}{2} \boldsymbol{m}^{\mathrm{t}} : \nabla_{\boldsymbol{x}} \nabla_{\boldsymbol{x}} \times \boldsymbol{v}. \tag{3.20}$$

It becomes evident that the skew-symmetric part of the stress tensor does not occur in the balance equation. Similarly, as further elaborated in [108], the spherical part of the couple-stress tensor does not contribute to the energy balance due to the identity $\boldsymbol{I} : \nabla_{\boldsymbol{x}} \nabla_{\boldsymbol{x}} \times \boldsymbol{v} = 0$. As a consequence, the spherical part of $\boldsymbol{m}$ remains indeterminate. As this work proceeds, the term *couple-stress tensor* will refer to the deviatoric part

$$\overline{\boldsymbol{m}} = \boldsymbol{m} - \frac{1}{3} \operatorname{tr}(\boldsymbol{m}) \boldsymbol{I} \tag{3.21}$$

of the tensor for the sake of simplicity, whereas its spherical part is assumed to be zero.

3.1.3 Isogeometric finite element formulation

Within the finite element analysis, a discretised weak form of the fourth-order partial differential equation (3.15) is derived. In the following sections, the respective weak form is presented, and the discretisation is performed with the use of discretised kinematic quantities including the second derivative of the displacement field. For the discretisation NURBS basis functions are employed in the context of isogeometric analysis. In particular, the IGA formulation proposed in [172] is recapitulated.

3.1.3.1 Weak form of the governing equation

In order to obtain a weak formulation, the balance of linear momentum in the reduced form (3.15) is multiplied by a test function $\boldsymbol{\eta}$ and integrated over the domain Ω. Therein, the stress decomposition (3.13) is accounted for along with the skew-symmetric stresses (3.12) obtained from the balance of angular momentum. After applying the divergence theorem twice, the weak form results in

$$0 = \int_{\Omega} \nabla_{\boldsymbol{x}} \boldsymbol{\eta} : \boldsymbol{\sigma}^{\mathrm{sym}} \, \mathrm{d}v - \int_{\partial\Omega} \boldsymbol{\eta} \cdot \boldsymbol{t}_1 \, \mathrm{d}a - \int_{\Omega} \left[\tfrac{1}{2} \boldsymbol{\epsilon} : \nabla_{\boldsymbol{x}} \nabla_{\boldsymbol{x}} \boldsymbol{\eta} \right] : \boldsymbol{m}^{\mathrm{t}} \, \mathrm{d}v. \tag{3.22}$$

It can be observed that the last term in (3.22) includes the scalar product of two second-gradient quantities. More specifically speaking, the couple-stress tensor contains second-gradient contributions in terms of $\boldsymbol{\gamma}$ in the model proposed in [153] as will be discussed later on. In (3.22) this tensor is multiplied by the second gradient of test function $\boldsymbol{\eta}$ before integration is performed. Accordingly, square-integrability of the second derivatives of the basis functions must be ensured for an appropriate finite element discretisation. NURBS basis functions used in isogeometric analysis fulfil this property as discussed in detail in Sect. 2.1.3 and in [40, 80, 129] and are thus employed in the following.

3.1.3.2 Discretised weak form

The discretisation of the weak form (3.22) is performed by means of NURBS basis functions R. In accordance with the isoparametric concept and with a Bubnov-Galerkin interpolation scheme, all fields and their corresponding test functions as well as the geometry are discretised by the same basis functions. Accordingly, the discretisation of the test function and of the kinematic quantities for an element e follows as

$$\boldsymbol{\eta}^e = \sum_{A=1}^{\mathrm{n_{en}}} \boldsymbol{\eta}^A R^A, \quad \boldsymbol{h}^e = \sum_{A=1}^{\mathrm{n_{en}}} \boldsymbol{u}^A \otimes \nabla_{\boldsymbol{x}} R^A, \quad \boldsymbol{\kappa}^e = \sum_{A=1}^{\mathrm{n_{en}}} \boldsymbol{u}^A \otimes \nabla_{\boldsymbol{x}} \nabla_{\boldsymbol{x}} R^A, \tag{3.23}$$

where $\mathrm{n_{en}}$ is the number of basis functions that have support on the particular element. Inserting the first relation into (3.22) and taking into account an assembly over the

elements related to Ω by the assembly operator $\mathbf{A}$, the discretised weak form of the governing equation results in

$$\mathbf{0} = \mathop{\mathbf{A}}_{e=1}^{\mathrm{n_{el}}} \sum_{A=1}^{\mathrm{n_{en}}} \int_{\Omega^e} \nabla_{\boldsymbol{x}} R^A \cdot \boldsymbol{\sigma}^{\mathrm{sym}} \,\mathrm{d}v + \int_{\Omega^e} \left[\tfrac{1}{2}\, \boldsymbol{\epsilon} \cdot \nabla_{\boldsymbol{x}} \nabla_{\boldsymbol{x}} R^A\right] : \boldsymbol{m}^{\mathrm{t}} \,\mathrm{d}v - \int_{\partial\Omega^e} R^A\, \boldsymbol{t}_1 \,\mathrm{d}a \tag{3.24}$$

where the first two terms resemble the internal force contributions

$$\boldsymbol{f}^{\mathrm{h}}_{\mathrm{int}} = \mathop{\mathbf{A}}_{e=1}^{\mathrm{n_{el}}} \sum_{A=1}^{\mathrm{n_{en}}} \int_{\Omega^e} \nabla_{\boldsymbol{x}} R^A \cdot \boldsymbol{\sigma}^{\mathrm{sym}} \,\mathrm{d}v + \int_{\Omega^e} \left[\tfrac{1}{2}\, \boldsymbol{\epsilon} \cdot \nabla_{\boldsymbol{x}} \nabla_{\boldsymbol{x}} R^A\right] : \boldsymbol{m}^{\mathrm{t}} \,\mathrm{d}v \tag{3.25}$$

and the last term in (3.24) represents the external force vector

$$\boldsymbol{f}^{\mathrm{h}}_{\mathrm{ext}} = \mathop{\mathbf{A}}_{e=1}^{\mathrm{n_{el}}} \sum_{A=1}^{\mathrm{n_{en}}} \int_{\partial\Omega^e} R^A\, \boldsymbol{t}_1 \,\mathrm{d}a. \tag{3.26}$$

Therein, the total number of elements is denoted as $\mathrm{n_{el}}$. The corresponding tangent contributions and all relevant sensitivities are derived in Appendix B.1.1.

3.1.4 Validation by an analytical solution

For validation purposes, a cylindrical tube subject to a pure azimuthal shear deformation is analysed within a linearised, plane strain setting. In [44], the boundary value problem has been presented in detail and a (semi-)analytical as well as a numerical solution has been provided for different properties of the fibre-reinforced material. To be precise, a compressible or incompressible matrix material is considered along with fibres with or without the ability to extend and compress. For the particular application to a cylindrical tube, it is further assumed that the fibres are aligned with the radial direction. For this case it has been found in [44] that azimuthal shear strain and radial stretching become uncoupled. This observation holds regardless of the assumptions made on the extensibility of the fibres and on the compressibility of the matrix.

In this contribution, the problem of pure azimuthal shear on a cylindrical tube is addressed in terms of the proposed isogeometric analysis framework with global C^1-continuity. In the following, the employed constitutive model is presented and the geometry model for the cylinder is discussed. After specification of the boundary conditions, representative simulation results are evaluated and compared to the solution provided in [44].

3.1.4.1 Specification of the constitutive model

In the theory of fibre-reinforced composites with fibre bending stiffness, the stored energy takes into account not only the strain and the fibre direction vector, as in a classic structural tensor approach in transverse isotropy. It additionally considers the tensor $\boldsymbol{\gamma}$, as defined in (3.3) for the linearised setting, that incorporates the fibre curvature. A representation of the stored energy density function in terms of $\mathrm{n_I}$ invariants I_i, that are dependent on $\{\boldsymbol{\varepsilon}, \boldsymbol{a}, \boldsymbol{\gamma}\}$, is possible, i.e.

$$W\left(I_i\left(\boldsymbol{\varepsilon}, \boldsymbol{a}, \boldsymbol{\gamma}\right)\right). \tag{3.27}$$

As proposed in [14], an additive decomposition of the stored energy density function according to

$$W = W^{\mathrm{iso}} + W^{\lambda_{\boldsymbol{a}}} + W^{\boldsymbol{\kappa}} \tag{3.28}$$

is considered in this thesis. For the isotropic part, resembling the matrix material, a quadratic form in the small strain tensor is adopted. More specifically speaking,

$$W^{\mathrm{iso}} = \frac{1}{2}\,\lambda\, I_1^2 + \mu\, I_2 \tag{3.29}$$

is employed with invariants

$$I_1 = \mathrm{tr}(\boldsymbol{\varepsilon}), \quad I_2 = \mathrm{tr}(\boldsymbol{\varepsilon}^2) \tag{3.30}$$

and Lamé parameters λ and μ which are specified as

$$\lambda = 1.037 \times 10^5\,\mathrm{N\,mm^{-2}}, \quad \mu = 4.444 \times 10^4\,\mathrm{N\,mm^{-2}} \tag{3.31}$$

for the examples in this thesis, cf. [14]. The second part $W^{\lambda_{\boldsymbol{a}}}$ describes the transversely isotropic behaviour of the material reinforced by a single family of fibres. However, this part is assumed to be constant unless otherwise stated because focus lies on the examination of the fibre curvature and fibre bending stiffness. These properties are considered in the last part of the stored energy density function given above. In [153], a set of seven invariants associated with the higher-gradient contributions is provided after consistent linearisation from the invariants for the general, non-linear case. Under additional assumptions such as consideration of only those invariants which do not inherit any coupling between the kinematic quantities $\boldsymbol{\varepsilon}$ and $\boldsymbol{\gamma}$, the set of invariants can be further reduced. Within the scope of this work, only one invariant is incorporated as proposed in [14, 172] so that the higher-gradient energy contribution reads

$$W^{\boldsymbol{\kappa}} = c\, I_6 \tag{3.32}$$

with fibre bending stiffness parameter c, and with invariant

$$I_6 = [\boldsymbol{\gamma} \cdot \boldsymbol{a}] \cdot [\boldsymbol{\gamma} \cdot \boldsymbol{a}] \tag{3.33}$$

which includes the fibre curvature and the fibre stretch gradient as the projection of $\boldsymbol{\gamma}$ onto the fibre direction. Fibre splay and fibre twist, on the other hand, are not incorporated in (3.33). In particular, this formulation is also consistent with the model employed in [44] for the analytical solutions which are used for validation in this section. Comparing the different material parameters included in the energy contributions (3.29) and (3.32), it can be observed that the Lamé parameters possess the unit $\mathrm{N\,mm^{-2}}$, whereas the unit of the fibre bending stiffness parameter c is N. This parameter is clearly associated with a length scale and, as a consequence, the model can capture size effects as will be elaborated in the numerical simulations later on. In view of the cylindrical tube under investigation, parameter c has been specifically related to an intrinsic length l in [44] which represents the fibre thickness.

On the basis of the stored energy density function (3.27), it follows from the derivations in [153] that the symmetric part of the stress tensor takes the form

$$\boldsymbol{\sigma}^{\mathrm{sym}} = \sum_{n=1}^{\mathrm{n_I}} \frac{\partial W}{\partial I_n} \frac{\partial I_n}{\partial \boldsymbol{\varepsilon}} \tag{3.34}$$

which yields

$$\boldsymbol{\sigma}^{\mathrm{sym}} = \lambda \,\mathrm{tr}(\boldsymbol{\varepsilon})\, \boldsymbol{I} + 2\,\mu\, \boldsymbol{\varepsilon} \tag{3.35}$$

for the particular energy function (3.28). Together with its skew-symmetric counterpart specified in (3.12), the total stress tensor follows from (3.13). The couple-stress tensor is derived from the stored energy density function in a similar manner. It can be expressed as

$$\overline{\boldsymbol{m}}^{\mathrm{t}} = \frac{2}{3}\, \boldsymbol{\epsilon} : \sum_{n=1}^{\mathrm{n_I}} \frac{\partial W}{\partial I_n} \left[\boldsymbol{\beta} \otimes \frac{\partial I_n}{\partial \boldsymbol{\gamma}} + \left[\frac{\partial I_n}{\partial \boldsymbol{\gamma}} \right]^{\mathrm{t}} \otimes \boldsymbol{\beta} \right] \tag{3.36}$$

which yields

$$\overline{\boldsymbol{m}}^{\mathrm{t}} = \frac{8}{3}\, c\, \boldsymbol{\epsilon} : \left[\boldsymbol{a} \otimes [\nabla_{\boldsymbol{x}} \nabla_{\boldsymbol{x}} \boldsymbol{u}] : [\boldsymbol{a} \otimes \boldsymbol{a}] \right] \otimes \boldsymbol{a} \tag{3.37}$$

for the energy function specified in (3.28) and under consideration of the assumptions made on higher-order terms in Sect. 3.1.1.

In the latter expression, the fibre curvature is included and contributes to the couple-stress tensor. On the contrary, fibre stretch gradients do not exhibit any contribution to the couple-stresses since they are associated with zero coefficients of the permutation symbol. This results from the particular choice of the energy function together with the assumption of small strains and holds despite the fact that fibre stretch gradients are

generally included in the underlying kinematic quantity $\boldsymbol{\gamma}$ introduced in (3.3) and in invariant I_6 in (3.33).

Remark 3.2. Although the vector $\boldsymbol{\beta}$ does not occur explicitly in the parameter list of the stored energy density function (3.27), it is included in the general expression (3.36) for the couple-stress tensor $\overline{\boldsymbol{m}}$. The related derivation is presented in [153, (9.9)], in analogy to the finite strain version, and a linear form is proposed [153, (9.12)].

3.1.4.2 Boundary value problem

For the solution of the fourth-order partial differential equation (3.15) applied to a two-dimensional cylindrical tube, two different sets of boundary conditions are presented in [44]. They are associated with a pure azimuthal shear deformation of the tube. In both cases, the inner radius of the cylinder is kept fixed while the points on the outer radius are subjected to a circumferential displacement resulting in a shear deformation. Besides these Dirichlet boundary conditions, the couple-stress is forced to vanish on the outer boundary. On the inner boundary, either the same assumption is employed or the fibre slope is set to zero. For the results that will be presented in the following section, the first option is considered, so that the complete set of boundary conditions for the tube with inner radius r_i and outer radius r_o can be summarised as

$$u_\varphi(r = r_i) = 0, \qquad u_\varphi(r = r_o) = \overline{u}_\varphi, \tag{3.38}$$

$$m_{rz}(r = r_i) = 0, \quad m_{rz}(r = r_o) = 0, \tag{3.39}$$

using a cylindrical base system $\{\boldsymbol{e}_r, \boldsymbol{e}_\varphi, \boldsymbol{e}_z\}$. The latter two conditions are in accordance with the assumption of vanishing surface couple-stresses from Sect. 3.1.2.2. In the present example, the prescribed azimuthal displacement is specified to $\overline{u}_\varphi = 0.025\,\mathrm{mm}$ and is prescribed by means of Dirichlet boundary conditions following the procedure in Sect. 2.2.3. The boundary conditions as well as the discretisation of the tube are presented in Fig. 3.2. The geometry is discretised by $\mathrm{n_{el}} = 6912$ finite elements, whereas the underlying polynomial degree is $p = q = 4$. The radii of the tube under investigation are $r_i = 1.0\,\mathrm{mm}$ and $r_o = 2.5\,\mathrm{mm}$. Further details on the geometry and discretisation of the tube are provided in Appendix B.2.1 with particular focus on the enforcement of C^1-continuity by knot removal as discussed in Sect. 2.3.1.

3.1.4.3 Results and comparison

The numerical results obtained by the IGA framework proposed in this work are compared to the (semi-)analytical solution provided in [44] in order to evaluate the accuracy of the isogeometric analysis approach. The solution in [44] is obtained by means of a power series method. For the comparison of the resulting stresses and couple-stresses as well as of the fibre slope in response to mechanical shear loading, dimensionless quantities are provided. In particular, scalar c in (3.32), which represents the fibre

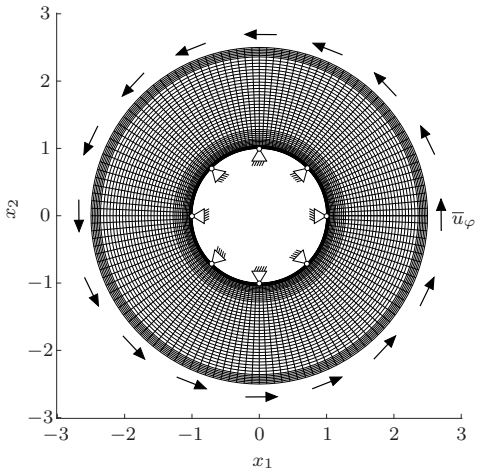

Figure 3.2: Boundary conditions and discretisation of the tube including $n_{el} = 6912$ elements. Reproduced from [170] under the terms of the Creative Commons Attribution 4.0 International License (CC BY 4.0).

bending stiffness, correlates with the material parameter d_f defined in [44] through the relation $d_f = 8\,c/3$. The conversion factors used in the following to derive associated non-dimensional quantities are also employed in [12]. Accordingly, the dimensionless parameter

$$\lambda^* = \frac{d_f}{2\,\mu\,r_i\,[r_o - r_i]} \tag{3.40}$$

is defined for the fibre bending stiffness. It becomes evident once again that a length scale is introduced since the inner and outer radii r_i and r_o of the cylinder occur in the definition of this non-dimensional material parameter which is related to the curvature of the fibres. Using the ratio

$$\zeta = \frac{r_o}{r_i}, \tag{3.41}$$

the dimensionless stress contributions follow as

$$\boldsymbol{\sigma}^* = \frac{r_i}{\overline{u}_\varphi\,\mu}\frac{\zeta^2 - 1}{\zeta}\,\boldsymbol{\sigma}, \quad \boldsymbol{m}^* = \frac{1}{\overline{u}_\varphi\,\mu}\frac{\zeta^2 - 1}{\zeta}\,\boldsymbol{m}. \tag{3.42}$$

From the dimensionless expressions of the radius and azimuthal displacement

$$r^* = \frac{r}{r_i}, \quad u_\varphi^* = \frac{u_\varphi}{\overline{u}_\varphi} \tag{3.43}$$

the respective form of the fibre slope $[u_\varphi]'$ can be derived, so that

$$[u_\varphi^*]' := \frac{\partial u_\varphi^*}{\partial r^*} = \frac{r_i}{\overline{u}_\varphi} \frac{\partial u_\varphi}{\partial r}. \tag{3.44}$$

In the present work, the simulation is performed for different values of the non-dimensional quantity λ^* introduced in (3.40), namely $\lambda^* \in \{0.0, 0.005, 0.03, 0.1, \pi\}$, and the influence of this fibre bending stiffness parameter on the fibre deformation as well as on the stress and couple-stress distributions is examined.

Fibre deformation and slope Focussing first on the fibre deformation pattern, Fig. 3.3 shows how a radial fibre that was initially aligned with the horizontal direction deforms under the influence of the azimuthal shear loading. It becomes evident that an increase in the parameter λ^*, which is associated with the fibre bending stiffness, leads to less bending of the fibres. In fact, for rather large values such as $\lambda^* = \pi$, the fibres almost remain straight. In Table 3.1, the fibre slope at the inner boundary, i.e. $r = r_i = 1.0\,\text{mm}$, is examined. The values corresponding to the analytical solution are taken from [44] for comparison. It is found that the deviation is smaller than 0.4% for all considered values of λ^* so that the isogeometric analysis yields accurate results in this regard.

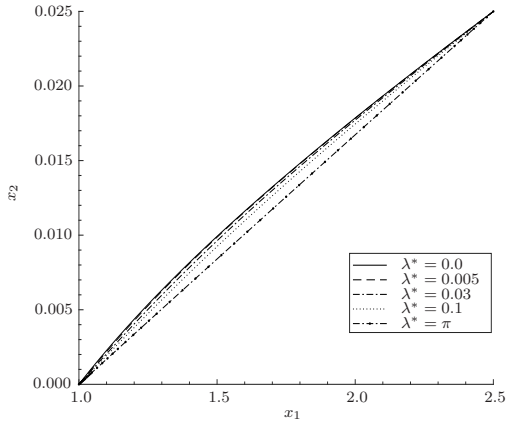

Figure 3.3: Deformation of a radial fibre. Reproduced from [170] under the terms of the Creative Commons Attribution 4.0 International License (CC BY 4.0).

Table 3.1: Fibre slope at the inner tube boundary $r = r_i$. Analytically obtained values are taken from [44] for comparison.

λ^*	0.0	0.005	0.03	0.1	π
$[u_\varphi^*]'_{\text{ana}}\|_{r=r_i}$	0.952	0.887	0.825	0.771	0.674
$[u_\varphi^*]'_{\text{num}}\|_{r=r_i}$	0.954	0.886	0.823	0.768	0.674
% deviation	0.21	0.11	0.24	0.39	0.04

Stress and couple-stress distributions Regarding the stress and couple-stress distributions for the two-dimensional boundary value problem at hand, the relevant (dimensionless) coefficients under investigation are $[\sigma_{r\varphi}]^*$, $[\sigma_{\varphi r}]^*$ and $[m_{rz}]^*$ with respect to a cylindrical coordinate system where $\boldsymbol{e}_z$ points in the out-of-plane direction. In addition to the coefficients of the total stress tensor, the values for its symmetric part, specifically $\left[\sigma^{\mathrm{sym}}_{r\varphi}\right]^* = \left[\sigma^{\mathrm{sym}}_{\varphi r}\right]^*$, are analysed in this section and shown in Fig. 3.4a together with the couple-stress coefficients. Comparing the results of the IGA simulation against the analytical values, taken from [44] and presented in Fig. 3.4b, no significant difference can be observed. Accordingly, a high accuracy of the isogeometric approach can be deduced for the particular boundary value problem studied. A more detailed view on the couple-stress coefficient $[m_{rz}]^*$ is given in Fig. 3.5. For $\lambda^* = 0$, the couple-stress remains zero, because the higher-order terms are not activated. For all other values of λ^*, the couple-stress coefficient increases with increasing values of the non-dimensional material parameter. Due to the particular boundary conditions discussed in Sect. 3.1.4.2, couple-stresses vanish at the boundaries of the tube which is in accordance with the results for $[m_{rz}]^*$.

Focussing on the total stress tensor which includes not only the symmetric but also a skew-symmetric part, Fig. 3.6a shows how the resulting stress coefficients $[\sigma_{r\varphi}]^*$ and $[\sigma_{\varphi r}]^*$ are distributed over the radius of the cylinder. In Fig. 3.6b, the respective results from [44] are employed. When comparing the plots, a similar profile along the radius can be observed. Both figures show that the stress coefficient $[\sigma_{r\varphi}]^*$ is rather similar for all fibre bending stiffness values. For $[\sigma_{\varphi r}]^*$ on the contrary, a monotonous decrease is obtained for perfectly flexible fibres and very small values of λ^*, whereas for higher values, a parabolic shape is observable near the inner boundary. In further comparison of Fig. 3.6a and 3.6b, slightly different values occur especially at the inner radius of the cylinder. Since the deviation is smaller than 5% this might be caused by numerical errors. It is further noted in [45], that one term is missing in the expression of the skew-symmetric stresses in [44]. However, the results presented therein are considered to be very accurate.

3.1.5 Simulation of curvature effects in a fibre-reinforced beam

A beam subject to a bending deformation is studied as second representative numerical example. The beam is made of an isotropic matrix material which is reinforced by fibres possessing bending stiffness. By this example, the influence of the fibre bending stiffness is again studied but the fibre direction is additionally investigated and size effects are analysed in more depth.

3.1.5.1 Boundary value problem

A two-dimensional cantilever beam, as shown in Fig. 3.7, is bent under the action of a constant traction at its free end. As in the previous example, the beam is reinforced by a single family of fibres under the assumption that the fibres are embedded in the

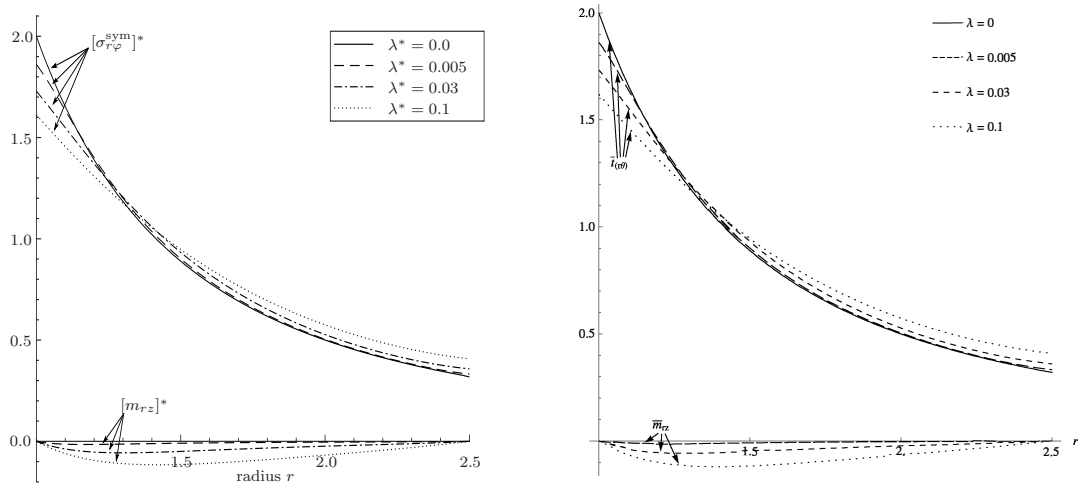

(a) Distribution of $[\sigma^{\mathrm{sym}}_{r\varphi}]^*$ and $[m_{rz}]^*$ resulting from the isogeometric analysis. Reproduced from [170] under the terms of the Creative Commons Attribution 4.0 International License (CC BY 4.0).

(b) Distribution of $\overline{t}_{(r\theta)}$, corresponding to $[\sigma^{\mathrm{sym}}_{r\varphi}]^*$, and $\overline{m}_{rz}$, corresponding to $[m_{rz}]^*$. First published in Journal of Mechanics of Materials and Structures in Vol. 6 (2011), No. 1-4, published by Mathematical Sciences Publishers [44].

Figure 3.4: Comparison of the results for the dimensionless stress coefficient $[\sigma^{\mathrm{sym}}_{r\varphi}]^*$ and couple-stress coefficient $[m_{rz}]^*$.

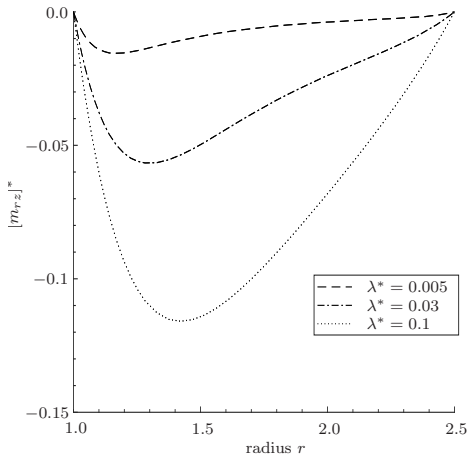

Figure 3.5: Distribution of the dimensionless couple-stress coefficient $[m_{rz}]^*$. Reproduced from [170] under the terms of the Creative Commons Attribution 4.0 International License (CC BY 4.0).

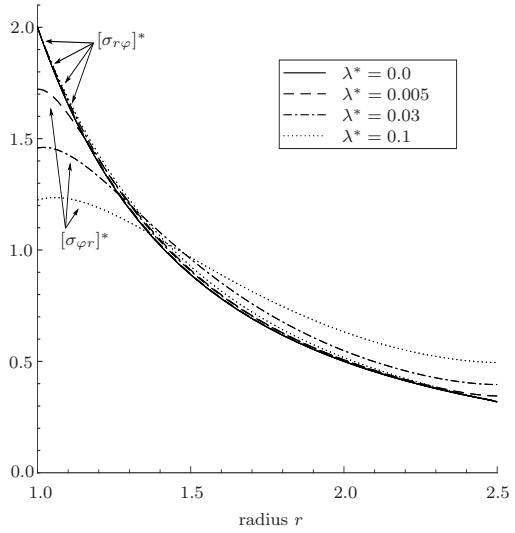

(a) Distribution of $[\sigma_{r\varphi}]^*$ and $[\sigma_{\varphi r}]^*$ resulting from the isogeometric analysis. Reproduced from [170] under the terms of the Creative Commons Attribution 4.0 International License (CC BY 4.0).

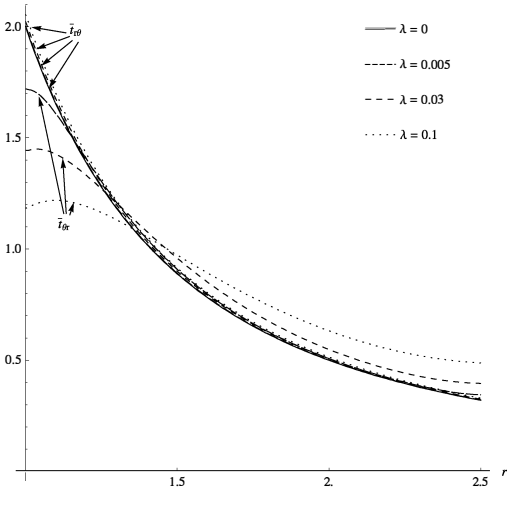

(b) Distribution of $\bar{t}_{r\theta}$ and $\bar{t}_{\theta r}$, corresponding to $[\sigma_{r\varphi}]^*$ and $[\sigma_{\varphi r}]^*$. First published in Journal of Mechanics of Materials and Structures in Vol. 6 (2011), No. 1-4, published by Mathematical Sciences Publishers [44].

Figure 3.6: Comparison of the results for the dimensionless stress coefficients $[\sigma_{r\varphi}]^*$ and $[\sigma_{\varphi r}]^*$.

matrix material and that they resist bending. Overall, a linearised setting and a plane strain state are assumed. The height of the beam is determined to $h = 10\,\text{mm}$ and a length $l = 100\,\text{mm}$ is considered, so that the ratio of its dimensions is 1/10. Details on the geometry in the context of IGA, such as knot vectors, control points and weights are provided in Appendix B.2.2. The chosen polynomial degree is $p = q = 4$. In Fig. 3.7, the discretisation including $\text{n}_{\text{el}} = 1000$ elements is presented which has been obtained by means of knot insertion, cf. Sect. 2.2.2.

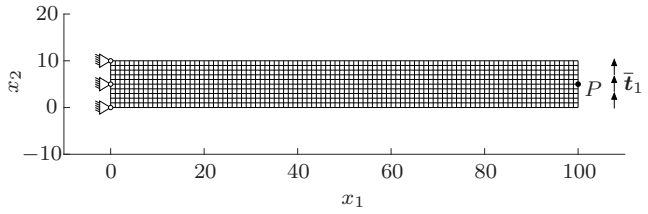

Figure 3.7: Boundary conditions and discretisation of the beam with $\text{n}_{\text{el}} = 1000$ elements. Reproduced from [170] under the terms of the Creative Commons Attribution 4.0 International License (CC BY 4.0).

As shown in Fig. 3.7, the beam under consideration is fixed on its left end. More precisely speaking, the displacements as well as the couple-stresses on this surface are assumed to be zero. Changes in the fibre slope are, however, enabled, i.e. the beam is simply supported. Accordingly, no Dirichlet boundary conditions are prescribed with

respect to the normal displacement gradients. On the opposite side, the beam is loaded by a traction $\|\bar{\boldsymbol{t}}_1\| = 30\,\mathrm{N\,mm^{-2}}$ which is uniformly distributed over the right surface and accounted for in the analysis by means of Neumann boundary conditions.

The constitutive model as well as the values of material parameters are adopted from the previous example, cf. Sect. 3.1.4.1.

3.1.5.2 Results and discussion

The purpose of studying the bending deformation of a fibre-reinforced beam in the proposed IGA framework is to elaborate the influence of the particular fibre properties such as their direction and bending stiffness. In a first step, the fibres are assumed to be aligned with the beam's axis, i.e. the fibre angle $\alpha = \arccos(\boldsymbol{a} \cdot \boldsymbol{e}_1)$ describing the angle between fibre vector $\boldsymbol{a}$ and the horizontal axis, is zero. For this setting, the fibre bending stiffness is varied. In a second step, a constant value of the fibre bending stiffness parameter is chosen while different values for the fibre angle are examined.

Influence of the fibre bending stiffness The fibre bending stiffness is represented by parameter c in the part of the energy function (3.32) that is related with the curvature of the fibres. For the limiting case $c = 0$, the underlying model coincides with the case of perfectly flexible fibres. In Fig. 3.8a, the vertical displacement u_y^P of the tip of the beam, represented by point P in Fig. 3.7, is depicted with a logarithmic scale for parameter c. It is observed that the displacement takes its maximum value for a vanishing fibre bending stiffness. By variation of c in the range of $c \in [0\,\mathrm{N}, 1 \times 10^7\,\mathrm{N}]$, an S-shaped curve is obtained. With an increasing bending stiffness of the fibres, the bending of the beam decreases monotonously. Moreover, it is observed that the slope of the curve decreases for high values of c and that a second limiting value is approached.

Influence of the fibre direction Complementing the previous setting, different fibre directions are analysed while the fibre bending stiffness parameter is kept at $c = 1 \times 10^5\,\mathrm{N}$. In particular, the fibre angle takes values in the range $\alpha \in [0, \pi/2]$. A monotonous increase of the vertical tip displacement can be observed when the fibre angle is increased, cf. Fig. 3.8b. Similar to the results with varying fibre bending stiffness, an S-shaped curve is obtained. The minimum resistance against bending is found for $\alpha = \pi/2$ so that the fibres lie vertically in the beam, i.e. in the direction of the applied force. On the other hand, when the fibres are aligned with the beam's axis, the impact of the fibre bending stiffness is most noticeable. In particular, a reduction of the vertical displacement at point P of approximately 18 % is observed, compared to a beam that is reinforced with fibres in vertical direction.

Size effect The geometry of the beam is now modified with respect to different height-to-length ratios in order to investigate how bending stiffness parameter c is related to size effects. To be precise, $l = 150\,\mathrm{mm}$ is chosen for the beam length and its height is varied

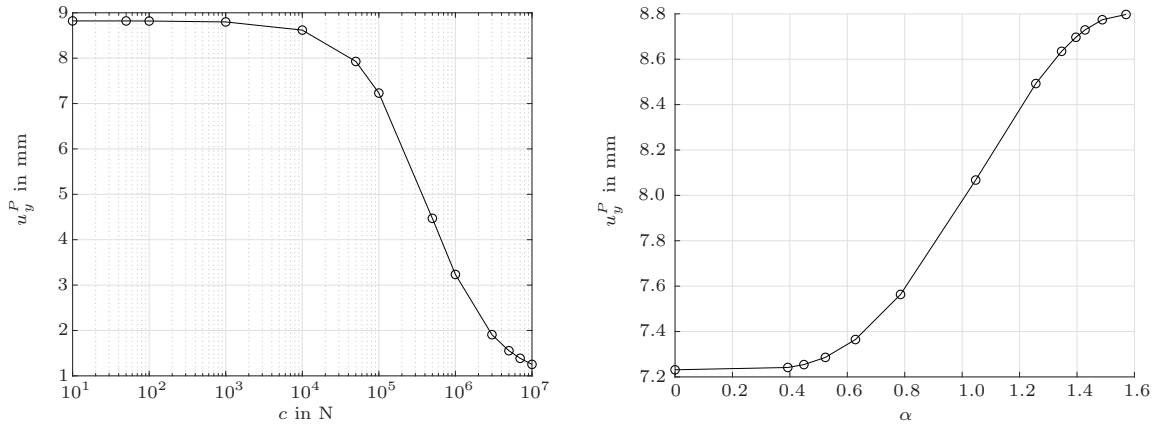

(a) Tip displacement in dependence of the fibre bending stiffness parameter c.

(b) Tip displacement in dependence of the fibre angle α.

Figure 3.8: Results for the tip displacement of the fibre-reinforced beam. Reproduced from [170] under the terms of the Creative Commons Attribution 4.0 International License (CC BY 4.0).

in the range $h \in [5\,\text{mm}, 25\,\text{mm}]$. The fibres are aligned with the beam's axis, i.e. $\alpha = 0$ is kept fixed, whereas for parameter c different values are employed for comparison. More specifically speaking, c is either set to zero, such that perfectly flexible fibres are present, or a value of $c \in \{1 \times 10^4\,\text{N}, 1 \times 10^5\,\text{N}, 1 \times 10^6\,\text{N}\}$ is considered. In order to study the impact of different sample sizes, the beams with different height-to-length-ratios h/l are simulated subject to a prescribed vertical force F at the tip of the beam. In accordance with the Euler-Bernoulli beam theory, cf. [99, 181], the force is scaled by the cube of the beam height such that the analytically calculated maximum displacement

$$u_{\max} = \frac{F\,l^3}{3\,E\,I_y} \tag{3.45}$$

remains constant, independently of the slenderness where $I_y \sim h^3$ holds for the area moment of inertia. Accordingly,

$$F = \|\bar{\boldsymbol{t}}_1\|\,A_0 \left[\frac{h}{h_0}\right]^3 \tag{3.46}$$

is considered for the prescribed force with reference beam height $h_0 = 10\,\text{mm}$ adopted from Sect. 3.1.5.1 and with $A_0 = h_0\,b$ being the corresponding cross-sectional area with unit width $b = 1\,\text{mm}$ for the two-dimensional setting. For the Young's modulus $E^* \approx 1.2 \times 10^5\,\text{Nmm}^{-2}$ of the underlying material, derived from the Lamé parameters in (3.31), the correction

$$E = \frac{E^*}{1-\nu^2} \tag{3.47}$$

with $\nu \approx 0.35$ is used in the analytical calculations in order to account for the plane strain state in the simulations.

In Fig. 3.9, the simulation results for height-to-length ratios $h/l \in \{$(a) 0.04, (b) 0.06, (c) 0.08$\}$ are presented. Fig. 3.9a shows that, for a vanishing fibre bending stiffness, the deflection of the beam is hardly affected by its slenderness. A small deviation from the analytically obtained constant value, however, can be observed in Fig. 3.10. This is due to the increasing discrepancy with the assumption of slim beams when the h/l-ratio increases. If the bending resistance of the fibres is activated by setting $c > 0$, a stiffer response is observed, see Fig. 3.9b and Fig. 3.10. This effect is most prominent for slim beams and vanishes if the beam height increases. For a fibre bending stiffness value of $c = 1 \times 10^4\,\mathrm{N}$, a convergence towards the non-reinforced beam can be observed in particular. For higher bending stiffness a similar convergence behaviour is expected if even larger beams were studied. It can be deduced that the proposed method is capable of reproducing size effects that occur as a consequence of variable fibre bending stiffness values or different geometric dimensions.

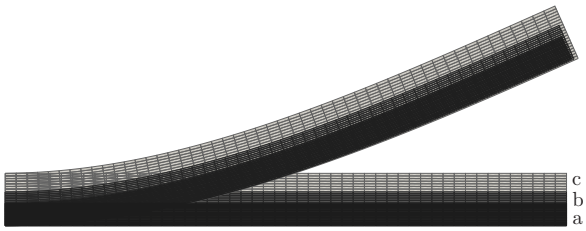

(a) Initial and deformed configuration of a fibre-reinforced beam with $c = 0$ and $h/l \in \{$(a) 0.04, (b) 0.06, (c) 0.08$\}$.

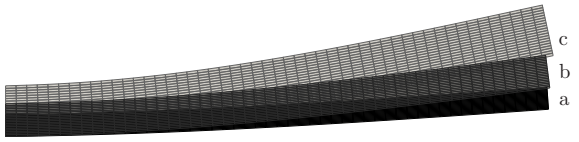

(b) Deformed configuration of a fibre-reinforced beam with $c = 10^6\,\mathrm{N}$ and $h/l \in \{$(a) 0.04, (b) 0.06, (c) 0.08$\}$.

Figure 3.9: Deformed configuration of the fibre-reinforced beam with and without fibre bending stiffness. Reprinted from [173] under the terms of the Creative Commons Attribution-NonCommercial License (CC BY NC).

In addition to these investigations, a comparison with transversely isotropic effects in fibre-reinforced solids is carried out. For this purpose, the transversely isotropic energy contribution $W^{\lambda_{\boldsymbol{a}}}$ introduced in (3.28) is revisited, but instead of assuming it to be constant as in Sect. 3.1.4.1, the function

$$W^{\lambda_{\boldsymbol{a}}} = \alpha\, I_4\, I_1 + 2\left[\mu_{\parallel} - \mu\right] I_5 + \frac{1}{2}\,\beta\, I_4^2 \tag{3.48}$$

with invariants

$$I_4 = \boldsymbol{a} \cdot \boldsymbol{\varepsilon} \cdot \boldsymbol{a}, \quad I_5 = \boldsymbol{a} \cdot \boldsymbol{\varepsilon}^2 \cdot \boldsymbol{a} \tag{3.49}$$

is adopted from [152]. The material constants for the isotropic and transversely isotropic energy contributions are taken from [152] as

$$\lambda = 5.64 \times 10^3\,\mathrm{N\,mm^{-2}}, \quad \mu = 2.46 \times 10^3\,\mathrm{N\,mm^{-2}},$$
$$\mu_\parallel = 5.66 \times 10^3\,\mathrm{N\,mm^{-2}}, \quad \alpha = -1.27 \times 10^3\,\mathrm{N\,mm^{-2}},$$
$$\beta = 2.273 \times 10^5\,\mathrm{N\,mm^{-2}}. \tag{3.50}$$

With these considerations at hand, the bending beam is studied once more with and without accounting for the tensile stiffness of the fibres in addition to their bending stiffness. Moreover, the corresponding size effect is investigated by scaling the sample size as well as the prescribed force along with a constant height-to-length ratio $h/l = 1/15$. The prescribed force is $F = 2\,\mathrm{N}$ for the reference sample with height $h = 10\,\mathrm{mm}$ and length $l = 150\,\mathrm{mm}$. In Fig. 3.11, the corresponding results are presented in terms of the beam deflection which is normalised with respect to the beam height and plotted in dependence of the size of the body. For the results in Fig. 3.11a, transverse isotropy is not activated, i.e. the tensile stiffness of the fibres is not accounted for, whereas Fig. 3.11b includes these contributions. The plots show the characteristic S-shaped curves similar to Fig. 3.8 when the bending stiffness of the fibres is non-zero. This indicates once more that the fibre bending stiffness incorporates a length scale since varying either the sample size or this particular material parameter yields similar characteristics. By comparing Fig. 3.11a and Fig. 3.11b, it can be observed that this behaviour is obtained regardless of the activation of the transversely isotropic material properties. However, the effects of both stiffness contributions clearly add up, see Fig. 3.11b, which is in line with the expectations for the particular boundary value problem at hand. For the material constants chosen in (3.50) together with the maximum employed fibre bending stiffness parameter $c = 1 \times 10^6\,\mathrm{N}$, the tensile stiffness of the fibres dominates over the bending stiffness for all sample sizes studied. For different material parameters and even smaller geometric dimensions, however, the resistance against bending may be

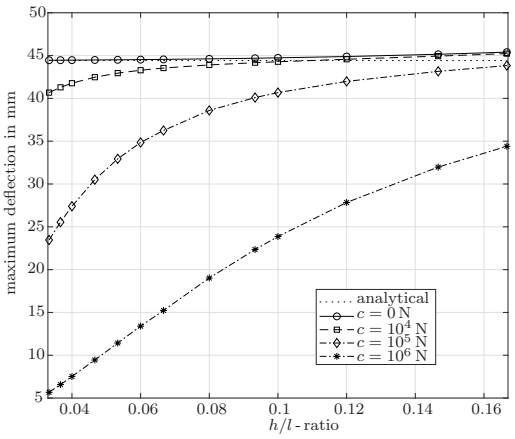

Figure 3.10: Maximum deflection of the fibre-reinforced beam in dependence of its slenderness h/l and fibre bending stiffness c. Reprinted from [173] under the terms of the Creative Commons Attribution-NonCommercial License (CC BY NC).

dominated by the gradient-related contributions since the resulting deflections for $c \neq 0$ and without tensile fibre stiffness are already of similar magnitude as the deflections for $c = 0$ which consider the tensile stiffness of the fibres, see Fig. 3.11a.

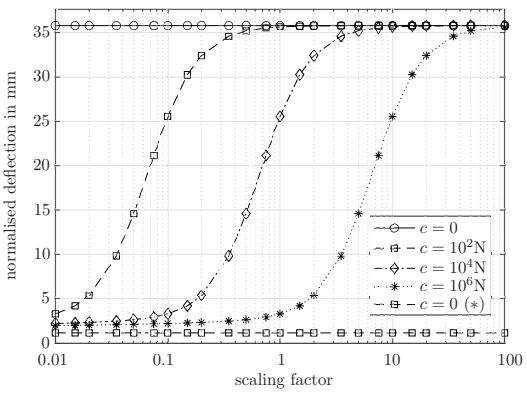

(a) Results without fibre tensile stiffness. For $c = 0$ the results including fibre tensile stiffness are additionally employed for direct comparison and marked by $(*)$.

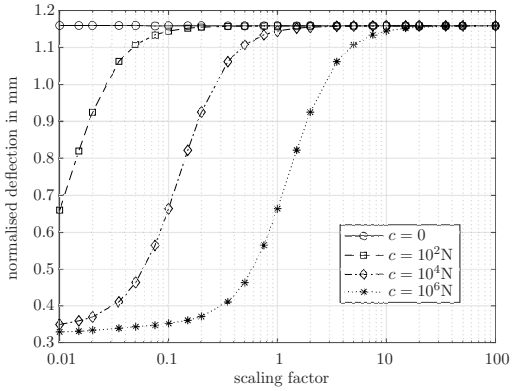

(b) Results including fibre tensile stiffness.

Figure 3.11: Normalised deflection of the fibre-reinforced beam in dependence of its size. Results are plotted for different values of the fibre bending stiffness c and for simulations with and without fibre tensile stiffness, i.e. transversely isotropic energy contributions.

3.2 Modelling approach for a finite strain setting

An isogeometric analysis framework for the numerical simulation of fibre-reinforced composites with fibre bending stiffness has been presented in Sect. 3.1 under the assumption of small strains. Therein, the linearised version of the modelling approach presented in [153] has been employed. In the present section, the model is considered in a more general, finite strain setting. Along with the extension to finite strains, kinematic quantities in terms of the fibre stretch gradient as well as the fibre curvature contribute to the material response.

3.2.1 Finite strain kinematics

For a body $\Omega \subset \mathbb{R}^3$ undergoing finite deformations, two configurations may be considered, namely a reference configuration at time t_0 as well as the current configuration which inherits the deformation of the body at time t. As shown in Fig. 3.12, the nonlinear function $\boldsymbol{\varphi} : \Omega_0 \to \Omega_t$ describes the mapping of the position of a material point $\boldsymbol{X}$ in the reference configuration to its position $\boldsymbol{x}$ in the current configuration. The deformation gradient $\boldsymbol{F} = \nabla_{\boldsymbol{X}} \boldsymbol{\varphi}$ with $J = \det(\boldsymbol{F}) > 0$ is the gradient of this mapping with respect to the reference position $\boldsymbol{X}$. The deformation gradient describes a linear

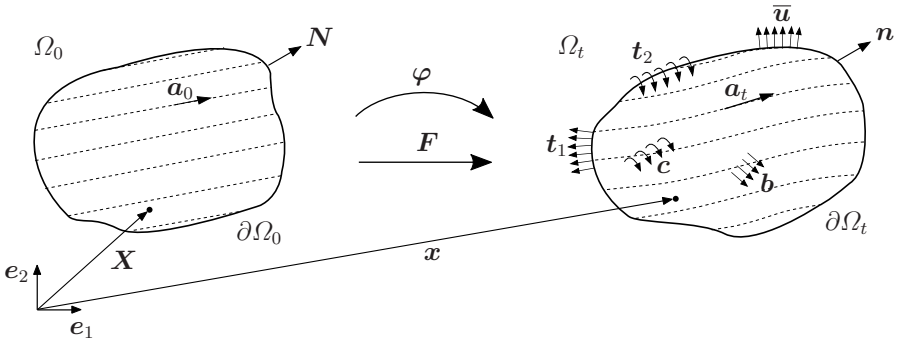

Figure 3.12: Two-dimensional domain Ω in the reference configuration (Ω_0) and current configuration (Ω_t) assuming a couple-stress theory. Employed vectors and tensors: vector of coordinates in the reference configuration $\boldsymbol{x}$ and in the current configuration $\boldsymbol{X}$, placement function $\boldsymbol{\varphi}$, deformation gradient $\boldsymbol{F}$, referential surface outward normal unit vector $\boldsymbol{N}$, current surface outward normal unit vector $\boldsymbol{n}$, referential fibre direction vector $\boldsymbol{a}_0$, current fibre direction vector $\boldsymbol{a}_t$, body force vector $\boldsymbol{b}$, body couple vector $\boldsymbol{c}$, vector of tractions $\boldsymbol{t}_1$ acting on the surface $\partial\Omega_t$, vector of couples $\boldsymbol{t}_2$ acting on the surface $\partial\Omega_t$, vector of displacements $\overline{\boldsymbol{u}}$ prescribed on the surface $\partial\Omega_t$. Reproduced from [171] under the terms of the Creative Commons Attribution 4.0 International License (CC BY 4.0).

relation between line elements $\mathrm{d}\boldsymbol{x}$ in the current configuration and $\mathrm{d}\boldsymbol{X}$ in the reference configuration while its cofactor and determinant relate infinitesimal area as well as infinitesimal volume elements in a similar manner, i.e.

$$\mathrm{d}\boldsymbol{x} = \boldsymbol{F} \cdot \mathrm{d}\boldsymbol{X}, \quad \boldsymbol{n}\,\mathrm{d}a = \mathrm{cof}(\boldsymbol{F}) \cdot \boldsymbol{N}\,\mathrm{d}A, \quad \mathrm{d}V = J\,\mathrm{d}V. \tag{3.51}$$

Vectors $\boldsymbol{N}$ and $\boldsymbol{n}$ denote the surface outward normal unit vectors in the reference and in the current configuration and the cofactor is defined as $\mathrm{cof}(\boldsymbol{F}) = J\,\boldsymbol{F}^{-\mathrm{t}}$. For the specific modelling approach presented in [153] and adopted in this work, the second gradient of the placement function is considered further, so that

$$\boldsymbol{\Upsilon} = \nabla_{\boldsymbol{X}} \boldsymbol{F} = \nabla_{\boldsymbol{X}} \nabla_{\boldsymbol{X}} \boldsymbol{\varphi} \tag{3.52}$$

is introduced.

Within the scope of modelling fibre-reinforced composites, a unit vector field $\boldsymbol{a}_0$ is commonly incorporated into the model as an additional directional quantity. It describes the fibre direction in the reference configuration for a material which is reinforced by a single family of fibres. Under the assumption that the fibres are embedded in the matrix material and convected with the deformation, the fibre direction vector in the deformed configuration is obtained as

$$\boldsymbol{a}_t = \lambda_a\,\overline{\boldsymbol{a}}_t = \boldsymbol{F} \cdot \boldsymbol{a}_0 \quad \text{with} \quad \|\overline{\boldsymbol{a}}_t\| = 1. \tag{3.53}$$

Since not only the direction but also the length of the fibres changes as a consequence of the deformation, the fibre stretch λ_a occurs in (3.53).

Assuming that the embedded fibres are not perfectly flexible but instead exhibit a certain bending stiffness, the gradient of the fibre direction vector is incorporated into the enhanced material model. With respect to the reference configuration, this gradient takes the form

$$\boldsymbol{\Lambda} = \boldsymbol{F}^{\mathrm{t}} \cdot \boldsymbol{G} \quad \text{with} \quad \boldsymbol{G} = \nabla_{\boldsymbol{X}} \boldsymbol{a}_t = \boldsymbol{a}_0 \cdot \nabla_{\boldsymbol{X}} \boldsymbol{F}^{\mathrm{t}} + \boldsymbol{F} \cdot \nabla_{\boldsymbol{X}} \boldsymbol{a}_0, \tag{3.54}$$

cf. [153]. As discussed in detail in [14], the stress and energy contributions related to this gradient term do, in general, not vanish in the initial state. In order to obtain an initially stress-free and energy-free condition, the fibres are assumed to be straight in the reference configuration, i.e. $\nabla_{\boldsymbol{X}} \boldsymbol{a}_0 = \boldsymbol{0}$.

3.2.2 Balance equations

For the consideration of higher gradients of the placement function, an enhanced continuum model is required. In the present contribution, the couple-stress theory presented in [108] is applied. The spatial versions of the local balance equations will be summarised in the following for the quasi-static case and under the assumption of vanishing body forces and body couples, accordingly $\boldsymbol{b} = \boldsymbol{0}$ and $\boldsymbol{c} = \boldsymbol{0}$, cf. [14, 153]. Since the derivations of the spatial balance equations are analogous to the derivations for the small strain case discussed in detail in Sect. 3.1.2, only the final formulations are denoted in the following which already include all assumptions mentioned above.

3.2.2.1 Balance of mass

Considering a closed system, the local form of the balance of mass reads

$$\dot{\rho} + \rho \, \nabla_{\boldsymbol{x}} \cdot \dot{\boldsymbol{\varphi}} = 0 \tag{3.55}$$

with spatial mass density ρ.

3.2.2.2 Balance of linear and angular momentum

The local form of balance of linear momentum in the absence of mechanical body forces can be expressed as

$$\rho \, \ddot{\boldsymbol{\varphi}} = \nabla_{\boldsymbol{x}} \cdot \boldsymbol{\sigma}^{\mathrm{t}} \tag{3.56}$$

and, for the quasi-static case, reduces to

$$\boldsymbol{0} = \nabla_{\boldsymbol{x}} \cdot \boldsymbol{\sigma}^{\mathrm{t}} \tag{3.57}$$

with an, in general, non-symmetric Cauchy-type stress tensor $\boldsymbol{\sigma}$. From the local form of balance of angular momentum

$$\mathbf{0} = \nabla_{\boldsymbol{x}} \cdot \boldsymbol{m}^{\mathrm{t}} + \boldsymbol{\epsilon} : \boldsymbol{\sigma} \tag{3.58}$$

under vanishing body couples, the skew-symmetric part of $\boldsymbol{\sigma}$ can be directly obtained as a function of the divergence of the couple-stress tensor $\boldsymbol{m}$, to be specific

$$\boldsymbol{\sigma}^{\mathrm{skw}} = \frac{1}{2}\boldsymbol{I} \times \left[\nabla_{\boldsymbol{x}} \cdot \boldsymbol{m}^{\mathrm{t}}\right]. \tag{3.59}$$

Within the isogeometric analysis framework proposed in this work, the balance equations of linear and angular momentum are combined into one partial differential equation which is of fourth order since the couple-stress tensor may, in general, contain second-order derivatives of the placement function. Retaining the assumptions mentioned above and considering the additive decomposition of the stress tensor

$$\boldsymbol{\sigma} = \boldsymbol{\sigma}^{\mathrm{sym}} + \boldsymbol{\sigma}^{\mathrm{skw}}, \tag{3.60}$$

expression (3.59) can be inserted into (3.57) which yields

$$\mathbf{0} = \nabla_{\boldsymbol{x}} \cdot \boldsymbol{\sigma}^{\mathrm{sym}} + \frac{1}{2}\nabla_{\boldsymbol{x}} \times \left[\nabla_{\boldsymbol{x}} \cdot \boldsymbol{m}^{\mathrm{t}}\right]. \tag{3.61}$$

3.2.2.3 Balance of energy

By using balance equations (3.56) and (3.58), the balance of energy in local form follows as

$$\rho\,\dot{U} = \boldsymbol{\sigma}^{\mathrm{sym}} : \nabla_{\boldsymbol{x}}\dot{\boldsymbol{\varphi}} + \frac{1}{2}\boldsymbol{m}^{\mathrm{t}} : \nabla_{\boldsymbol{x}}\nabla_{\boldsymbol{x}} \times \dot{\boldsymbol{\varphi}} \tag{3.62}$$

where U denotes the (mass specific) internal energy. As discussed in detail in [108] and typical for the couple-stress theory, only the deviatoric part $\overline{\boldsymbol{m}} = \boldsymbol{m} - \frac{1}{3}\,\mathrm{tr}(\boldsymbol{m})\,\boldsymbol{I}$ of the couple-stress tensor contributes to the energy balance (3.62) because $\boldsymbol{I} : \nabla_{\boldsymbol{x}}\nabla_{\boldsymbol{x}} \times \dot{\boldsymbol{\varphi}} = 0$ holds. The same applies to the partial differential equation (3.61), where the spherical part of the couple-stress tensor similarly vanishes as a result of the curl and divergence operation. Consequently, the spherical part of the couple-stress tensor does not have any impact on the balance equations relevant for the proposed simulation approach and accordingly remains undetermined as this work proceeds. This is in accordance with the derivations for the small strain setting as discussed in Sect. 3.1.2.3.

3.2.3 Isogeometric finite element formulation

For the solution of the fourth-order partial differential equation in the simulation of fibre-reinforced composites with fibre bending stiffness, isogeometric analysis is employed. Since NURBS basis functions used within IGA provide C^{p-1}-continuity everywhere, except for the locations of repeated knots or control points, global continuity higher than C^0 can be realised, cf. Sect. 2.3. Accordingly, NURBS basis functions are used in the discretised weak form of the governing equation (3.61) which will be derived in the following sections. For the solution of this non-linear equation within a finite element scheme, a linearisation is performed afterwards so that the globally assembled system of equations can be solved by means of the Newton-Raphson method.

3.2.3.1 Weak form of the governing equation

With regard to a finite element formulation of the governing equation (3.61), a weak form is derived. To this end, the quasi-static balance of linear momentum (3.57) is multiplied by a test function $\boldsymbol{\eta}$ and integrated over the spatial domain Ω_t, accordingly

$$0 = \int_{\Omega_t} \boldsymbol{\eta} \cdot \left[\nabla_{\boldsymbol{x}} \cdot \boldsymbol{\sigma}^{\mathrm{t}}\right] \,\mathrm{d}v. \tag{3.63}$$

Application of the divergence theorem and of integration by parts yields

$$0 = \int_{\Omega_t} \nabla_{\boldsymbol{x}}\boldsymbol{\eta} : \boldsymbol{\sigma}^{\mathrm{t}} \,\mathrm{d}v - \int_{\partial\Omega_{\mathrm{t}}} \boldsymbol{\eta} \cdot \boldsymbol{\sigma}^{\mathrm{t}} \cdot \boldsymbol{n} \,\mathrm{d}a. \tag{3.64}$$

Considering an additive decomposition of the stress tensor in the form of (3.60) and by using the definition of the skew-symmetric stress part from the balance of angular momentum (3.59) with $\boldsymbol{\sigma}^{\mathrm{skw}} = -\left[\boldsymbol{\sigma}^{\mathrm{skw}}\right]^{\mathrm{t}}$, (3.64) can be rewritten as

$$0 = \int_{\Omega_t} \nabla_{\boldsymbol{x}}\boldsymbol{\eta} : \boldsymbol{\sigma}^{\mathrm{sym}} \,\mathrm{d}v - \int_{\partial\Omega_{\mathrm{t}}} \boldsymbol{\eta} \cdot \boldsymbol{t}_1 \,\mathrm{d}a + \int_{\Omega_{\mathrm{t}}} \nabla_{\boldsymbol{x}}\boldsymbol{\eta} : \left[\tfrac{1}{2}\left[\nabla_{\boldsymbol{x}} \cdot \boldsymbol{m}^{\mathrm{t}}\right] \cdot \boldsymbol{\epsilon}\right] \,\mathrm{d}v. \tag{3.65}$$

Therein, Cauchy's theorem is employed so that the traction vector $\boldsymbol{t}_1 = \boldsymbol{\sigma}^{\mathrm{t}} \cdot \boldsymbol{n}$ is introduced.
For the last term in (3.65), integration by parts as well as the divergence theorem are applied a second time so that

$$\begin{aligned} 0 = &\int_{\Omega_t} \nabla_{\boldsymbol{x}}\boldsymbol{\eta} : \boldsymbol{\sigma}^{\mathrm{sym}} \,\mathrm{d}v - \int_{\partial\Omega_{\mathrm{t}}} \boldsymbol{\eta} \cdot \boldsymbol{t}_1 \,\mathrm{d}a \\ &- \int_{\Omega_t} \tfrac{1}{2}\left[\boldsymbol{\epsilon} : \nabla_{\boldsymbol{x}}\nabla_{\boldsymbol{x}}\boldsymbol{\eta}\right] : \boldsymbol{m}^{\mathrm{t}} \,\mathrm{d}v + \int_{\partial\Omega_{\mathrm{t}}} \tfrac{1}{2}\,\nabla_{\boldsymbol{x}}\boldsymbol{\eta} : \left[\boldsymbol{t}_2 \cdot \boldsymbol{\epsilon}\right] \,\mathrm{d}a \end{aligned} \tag{3.66}$$

is obtained and represents the weak form of (3.61). Vector $\boldsymbol{t}_2 = \boldsymbol{m}^{\mathrm{t}} \cdot \boldsymbol{n}$ constitutes the couples acting on the surface of the domain such as the previously introduced vector $\boldsymbol{t}_1$ accounts for the surface tractions.

The terms which are related to the couple-stress tensor in (3.66) can be rewritten by using the definition of the curl operator, so that an alternative representation of the weak form reads

$$\begin{aligned} 0 = &\int_{\Omega_t} \nabla_{\boldsymbol{x}} \boldsymbol{\eta} : \boldsymbol{\sigma}^{\mathrm{sym}} \, \mathrm{d}v - \int_{\partial\Omega_{\mathrm{t}}} \boldsymbol{\eta} \cdot \boldsymbol{t}_1 \, \mathrm{d}a \\ &+ \int_{\Omega_t} \left[\nabla_{\boldsymbol{x}} \left[\tfrac{1}{2} \nabla_{\boldsymbol{x}} \times \boldsymbol{\eta}\right]\right] : \boldsymbol{m}^{\mathrm{t}} \, \mathrm{d}v - \int_{\partial\Omega_{\mathrm{t}}} \left[\tfrac{1}{2} \nabla_{\boldsymbol{x}} \times \boldsymbol{\eta}\right] \cdot \boldsymbol{t}_2 \, \mathrm{d}a. \end{aligned} \tag{3.67}$$

This format allows an interpretation of the specific occurrences of the test function from the perspective of the principle of virtual power. The test function $\boldsymbol{\eta}$ itself may be regarded as a virtual velocity field which is related to the classic tensorial quantities in (3.67). In analogy, the term $\frac{1}{2} \nabla_{\boldsymbol{x}} \times \boldsymbol{\eta}$, which corresponds to the higher-gradient terms in (3.67), may be interpreted as a virtual spin vector, cf. [14].

From the weak form (3.66) that has been derived for the deformed configuration, the respective formulation in the reference configuration is obtained by making use of the relations specified in (3.51). From the third term on the right-hand side in (3.66), which includes the second-order gradient of the test function, two separate terms follow from the pull-back operation. The weak form in the reference configuration accordingly reads

$$\begin{aligned} 0 = &\int_{\Omega_0} \nabla_{\boldsymbol{X}} \boldsymbol{\eta} : [\boldsymbol{\sigma}^{\mathrm{sym}} \cdot \operatorname{cof}(\boldsymbol{F})] \, \mathrm{d}V - \int_{\partial\Omega_0} \boldsymbol{\eta} \cdot \boldsymbol{\sigma}^{\mathrm{t}} \cdot \operatorname{cof}(\boldsymbol{F}) \cdot \boldsymbol{N} \, \mathrm{d}A \\ &- \int_{\Omega_0} \tfrac{1}{2} \nabla_{\boldsymbol{X}} \nabla_{\boldsymbol{X}} \boldsymbol{\eta} :\cdot \left[\left[\boldsymbol{\epsilon} \cdot \boldsymbol{m}^{\mathrm{t}}\right] : \left[\boldsymbol{F}^{-\mathrm{t}} \mathbin{\overline{\otimes}} \operatorname{cof}(\boldsymbol{F})\right]\right] \, \mathrm{d}V \\ &- \int_{\Omega_0} \tfrac{1}{2} \nabla_{\boldsymbol{X}} \boldsymbol{\eta} : \left[\left[\boldsymbol{\epsilon} \cdot \boldsymbol{m}^{\mathrm{t}} \cdot \operatorname{cof}(\boldsymbol{F})\right] : \left[\left[\left[-\boldsymbol{F}^{-\mathrm{t}} \mathbin{\underline{\otimes}} \boldsymbol{F}^{-1}\right] : \boldsymbol{\Upsilon}\right] : \left[\boldsymbol{I} \mathbin{\underline{\otimes}} \boldsymbol{I}\right]\right]\right] \, \mathrm{d}V \\ &+ \int_{\partial\Omega_0} \tfrac{1}{2} \nabla_{\boldsymbol{X}} \boldsymbol{\eta} : \left[\left[\boldsymbol{\epsilon} \cdot \boldsymbol{m}^{\mathrm{t}}\right] : \left[\operatorname{cof}(\boldsymbol{F}) \mathbin{\overline{\otimes}} \boldsymbol{F}^{-\mathrm{t}}\right]\right] \cdot \boldsymbol{N} \, \mathrm{d}A. \end{aligned} \tag{3.68}$$

It becomes evident that in (3.68), products of second-gradient contributions are present in the integrals similarly as in (3.22). This leads to enhanced continuity requirements in the sense that global C^0-continuity, as provided by classic Lagrangian basis functions, is not sufficient. Accordingly, NURBS basis functions exhibiting enhanced continuity properties are used for the discretisation in the isogeometric analysis scheme.

3.2.3.2 Discretised weak form

In analogy to the discretisation procedure in Sect. 3.1.3.2, the geometry as well as test function $\boldsymbol{\eta}$ and placement function $\boldsymbol{\varphi}$ are approximated by using the same basis

functions. Within the scope of this work, NURBS basis functions R are employed so that the discretised quantities for one element e are

$$\boldsymbol{\eta}^e = \sum_{A=1}^{\mathrm{n_{en}}} \boldsymbol{\eta}^A R^A, \quad \boldsymbol{\varphi}^e = \sum_{A=1}^{\mathrm{n_{en}}} \boldsymbol{\varphi}^A R^A \tag{3.69}$$

with the number of active basis functions on the element denoted as $\mathrm{n_{en}}$. Inserting both relations into the referential weak form (3.68), a representation is obtained which includes derivatives of the basis functions up to second order. Accordingly, the internal force vector takes the discretised form

$$\begin{aligned} \boldsymbol{f}^{\mathrm{h}}_{\mathrm{int}} = \mathop{\mathsf{A}}_{e=1}^{\mathrm{n_{el}}} \sum_{A=1}^{\mathrm{n_{en}}} & \int_{\Omega_0^e} \boldsymbol{\sigma}^{\mathrm{sym}} \cdot \operatorname{cof}(\boldsymbol{F}) \cdot \nabla_{\boldsymbol{X}} R^A \,\mathrm{d}V \\ & - \int_{\Omega_0^e} \left[\tfrac{1}{2}\, \boldsymbol{\epsilon} \cdot \boldsymbol{m}^{\mathrm{t}} \cdot \boldsymbol{F}^{-\mathrm{t}}\right] : \left[\operatorname{cof}(\boldsymbol{F}) \cdot \left[\nabla_{\boldsymbol{X}} \nabla_{\boldsymbol{X}} R^A\right]\right] \mathrm{d}V \\ & - \int_{\Omega_0^e} \left[\tfrac{1}{2}\, \boldsymbol{\epsilon} \cdot \boldsymbol{m}^{\mathrm{t}} \cdot \operatorname{cof}(\boldsymbol{F})\right] : \left[\left[\left[-\boldsymbol{F}^{-\mathrm{t}} \underline{\otimes} \boldsymbol{F}^{-1}\right] : \boldsymbol{\Upsilon}\right] : \left[\boldsymbol{I} \underline{\otimes} \boldsymbol{I}\right]\right] \cdot \nabla_{\boldsymbol{X}} R^A \,\mathrm{d}V \end{aligned} \tag{3.70}$$

where $\mathrm{n_{el}}$ denotes the total number of elements. The external force vector is respectively

$$\begin{aligned} \boldsymbol{f}^{\mathrm{h}}_{\mathrm{ext}} = \mathop{\mathsf{A}}_{e=1}^{\mathrm{n_{el}}} \sum_{A=1}^{\mathrm{n_{en}}} & \int_{\partial\Omega_0^e} \boldsymbol{\sigma}^{\mathrm{t}} \cdot \operatorname{cof}(\boldsymbol{F}) \cdot \boldsymbol{N}\, R^A \,\mathrm{d}A \\ & - \int_{\partial\Omega_0^e} \left[\tfrac{1}{2}\, \boldsymbol{\epsilon} \cdot \boldsymbol{m}^{\mathrm{t}} \cdot \boldsymbol{F}^{-\mathrm{t}}\right] : \left[\operatorname{cof}(\boldsymbol{F}) \cdot \nabla_{\boldsymbol{X}} R^A \otimes \boldsymbol{N}\right] \mathrm{d}A. \end{aligned} \tag{3.71}$$

3.2.3.3 Linearisation

The solution of equation system (3.68) within the isogeometric analysis framework is obtained by using a Newton-Raphson scheme. The residuum is determined by the internal and external force vectors derived in Sect. 3.2.3.2, i.e.

$$\boldsymbol{r}^{\mathrm{h}} = \boldsymbol{f}^{\mathrm{h}}_{\mathrm{int}} - \boldsymbol{f}^{\mathrm{h}}_{\mathrm{ext}}. \tag{3.72}$$

In the kth iteration step, the linearised form of the residuum reads

$$\boldsymbol{r}^{\mathrm{h}}_{k+1} = \boldsymbol{r}^{\mathrm{h}}_{k} + \Delta \boldsymbol{r}^{\mathrm{h}}. \tag{3.73}$$

Due to the particular dependencies of the residual function $\boldsymbol{r}^{\mathrm{h}} = \widetilde{\boldsymbol{r}}^{\mathrm{h}}(\boldsymbol{F}^{\mathrm{h}}(\widehat{\boldsymbol{\varphi}}), \boldsymbol{\Upsilon}^{\mathrm{h}}(\widehat{\boldsymbol{\varphi}}))$, two contributions are considered for the increment $\Delta\boldsymbol{r}^{\mathrm{h}}$, to be specific

$$\Delta\boldsymbol{r}^{\mathrm{h}} = \frac{\mathrm{d}\boldsymbol{r}^{\mathrm{h}}}{\mathrm{d}\widehat{\boldsymbol{\varphi}}} \cdot \Delta\widehat{\boldsymbol{\varphi}} = \left[\frac{\partial \boldsymbol{r}^{\mathrm{h}}}{\partial \boldsymbol{F}^{\mathrm{h}}} : \frac{\partial \boldsymbol{F}^{\mathrm{h}}}{\partial \widehat{\boldsymbol{\varphi}}} + \frac{\partial \boldsymbol{r}^{\mathrm{h}}}{\partial \boldsymbol{\Upsilon}^{\mathrm{h}}} :\cdot \frac{\partial \boldsymbol{\Upsilon}^{\mathrm{h}}}{\partial \widehat{\boldsymbol{\varphi}}}\right] \cdot \Delta\widehat{\boldsymbol{\varphi}} = \boldsymbol{K} \cdot \Delta\widehat{\boldsymbol{\varphi}} \tag{3.74}$$

with the global list of degrees of freedom $\widehat{\boldsymbol{\varphi}}$, tangent stiffness matrix $\boldsymbol{K}$ and with the partial derivatives

$$\frac{\partial \boldsymbol{F}^{\mathrm{h}}}{\partial \widehat{\boldsymbol{\varphi}}} = \mathop{\mathsf{A}}_{e=1}^{\mathrm{n_{el}}} \sum_{A=1}^{\mathrm{n_{en}}} \boldsymbol{I} \mathbin{\overline{\otimes}} \nabla_{\boldsymbol{X}} R^A, \quad \frac{\partial \boldsymbol{\Upsilon}^{\mathrm{h}}}{\partial \widehat{\boldsymbol{\varphi}}} = \mathop{\mathsf{A}}_{e=1}^{\mathrm{n_{el}}} \sum_{A=1}^{\mathrm{n_{en}}} \left[\boldsymbol{I} \mathbin{\overline{\otimes}} \nabla_{\boldsymbol{X}} \nabla_{\boldsymbol{X}} R^A\right] : [\boldsymbol{I} \mathbin{\underline{\otimes}} \boldsymbol{I}] \tag{3.75}$$

in the discretised form. Under the assumption of dead loads, only the sensitivities of the internal force contributions need to be considered. The global system of equations is finally obtained as

$$-\left[\boldsymbol{r}^{\mathrm{h}}\right]_k = [\boldsymbol{K}]_k \cdot [\Delta\widehat{\boldsymbol{\varphi}}]_k \,. \tag{3.76}$$

The general form of the tangent stiffness matrix $\boldsymbol{K}$ is derived in Appendix B.1.2.

3.2.4 Validation by an analytical solution

Similar to the validation of the linearised framework in Sect. 3.1.4, the numerical results obtained by the proposed IGA approach to finite deformations of fibre-reinforced solids are compared in this section with the (semi-)analytical solution provided in [44]. A plane strain condition is considered and the constitutive model is based on an energy function of similar type as (3.28) in order to maintain consistency with the analytical derivations in [44] subject to small strains.

3.2.4.1 Specification of the constitutive model

The constitutive model for fibre-reinforced composites including fibre bending stiffness has been derived in [153] on the basis of an extended list of invariants for the stored energy density function. Within a non-linear setting, it is formulated as an isotropic function of invariants I_i including the three main kinematic quantities introduced in Sect. 3.2.1 as arguments, i.e.

$$W(I_i(\boldsymbol{C}, \boldsymbol{\Lambda}, \boldsymbol{a}_0)). \tag{3.77}$$

This purely referential representation is based on the Cauchy-Green tensor $\boldsymbol{C} = \boldsymbol{F}^{\mathrm{t}} \cdot \boldsymbol{F}$, the referential fibre direction vector $\boldsymbol{a}_0$ and on the gradient $\boldsymbol{\Lambda}$ of the deformed fibre

vector. In order to reduce the number of invariants, additional assumptions are made in [153] and adopted in this work. By employing only the directional projection

$$\boldsymbol{\kappa}_0 = \boldsymbol{\Lambda} \cdot \boldsymbol{a}_0 \tag{3.78}$$

of the fibre gradient, effects from fibre splay are neglected in addition to effects from fibre twist. Apart therefrom, the sense of the fibre orientation is not relevant from a physics point of view so that the fibre vector may appear in the stored energy only in even powers.

For the particular examples presented in this contribution, the energy takes an additive decomposition and, as in [14] as well as in the small strain model presented in Sect. 3.1.4.1, specifically consists of three parts, namely

$$W = W^{\text{iso}} + W^{\lambda_{\boldsymbol{a}}} + W^{\boldsymbol{\kappa}_0}. \tag{3.79}$$

The isotropic part captures the behaviour of the matrix material without taking into account the reinforcement by fibres. It takes the form

$$W^{\text{iso}} = \lambda \frac{I_3 - 1}{4} - \left[\frac{\lambda}{2} + \mu\right] \ln(\sqrt{I_3}) + \frac{\mu}{2}\left[I_1 - 3\right] \tag{3.80}$$

with

$$I_1 = \boldsymbol{C} : \boldsymbol{I}, \quad I_3 = \det(\boldsymbol{C}). \tag{3.81}$$

For the examples in this section, the Lamé-type constants take the same value as in (3.31). The second part $W^{\lambda_{\boldsymbol{a}}}$ corresponds to the classic fibre stretch-related transversely isotropic contributions of the fibre-reinforced material which are not in the focus of the present contribution. As this work proceeds, $W^{\lambda_{\boldsymbol{a}}}$ is thus assumed to be constant and will not be further specified. The last contribution

$$W^{\boldsymbol{\kappa}_0} = c\, I_6 \tag{3.82}$$

with

$$I_6 = [\boldsymbol{\Lambda} \cdot \boldsymbol{a}_0] \cdot [\boldsymbol{\Lambda} \cdot \boldsymbol{a}_0] = \boldsymbol{\kappa}_0 \cdot \boldsymbol{\kappa}_0 \tag{3.83}$$

incorporates the energy related to the higher-gradient terms that are specific for the material model proposed in [153]. This formulation is based on one invariant only, which has been discussed in detail in Sect. 3.1.4.1. From the particular form of the referential gradient of the fibre direction vector (3.54), it follows that invariant I_6 in (3.83) includes the gradient of the fibre stretch as well as the fibre curvature, see the discussion in [13]. In accordance with the latter, parameter c is associated with a bending stiffness of the fibres. In the examples presented in this contribution, this fibre bending stiffness

parameter as well as the fibre direction will take different values in order to examine their influence on the simulation results.

From the general form of the stored energy density function in (3.77), the stress and couple-stress tensor are derived in [153] by taking the particular dependencies of the invariants into account. Accordingly, the symmetric part of the stress tensor follows as

$$\boldsymbol{\sigma}^{\mathrm{sym}} = J^{-1}\left[2\boldsymbol{F}\cdot\frac{\partial W}{\partial \boldsymbol{C}}\cdot\boldsymbol{F}^{\mathrm{t}} + \boldsymbol{G}\cdot\left[\frac{\partial W}{\partial \boldsymbol{\Lambda}}\right]^{\mathrm{t}}\cdot\boldsymbol{F}^{\mathrm{t}} + \boldsymbol{F}\cdot\frac{\partial W}{\partial \boldsymbol{\Lambda}}\cdot\boldsymbol{G}^{\mathrm{t}}\right] \tag{3.84}$$

and the deviatoric part of the couple-stress tensor takes the form

$$\overline{\boldsymbol{m}}^{\mathrm{t}} = -\frac{2}{3}J^{-1}\boldsymbol{\epsilon} : \left[\boldsymbol{F}\cdot\frac{\partial W}{\partial \boldsymbol{\Lambda}}\cdot\left[\boldsymbol{F}^{\mathrm{t}}\,\overline{\otimes}\,\boldsymbol{a}_t + \boldsymbol{F}^{\mathrm{t}}\otimes\boldsymbol{a}_t\right]\right]. \tag{3.85}$$

Considering the stored energy density function specified in (3.79), the derivations yield

$$\begin{aligned}\boldsymbol{\sigma}^{\mathrm{sym}} = {} & J^{-1}\boldsymbol{F}\cdot\left[\frac{\lambda}{2}\left[I_3-1\right]\boldsymbol{C}^{-1} + \mu\left[\boldsymbol{I}-\boldsymbol{C}^{-1}\right]\right]\cdot\boldsymbol{F}^{\mathrm{t}} \\ & + 2\,c\,J^{-1}\left[\boldsymbol{G}\cdot\left[\boldsymbol{a}_0\otimes\boldsymbol{\Lambda}\cdot\boldsymbol{a}_0\right]\cdot\boldsymbol{F}^{\mathrm{t}} + \boldsymbol{F}\cdot\left[\boldsymbol{\Lambda}\cdot\boldsymbol{a}_0\otimes\boldsymbol{a}_0\right]\cdot\boldsymbol{G}^{\mathrm{t}}\right]\end{aligned} \tag{3.86}$$

and

$$\overline{\boldsymbol{m}}^{\mathrm{t}} = -\frac{4}{3}\,c\,J^{-1}\boldsymbol{\epsilon} : \left[\boldsymbol{F}\cdot\left[\boldsymbol{\Lambda}\cdot\boldsymbol{a}_0\otimes\boldsymbol{a}_0\right]\cdot\left[\boldsymbol{F}^{\mathrm{t}}\,\overline{\otimes}\,\boldsymbol{a}_t + \boldsymbol{F}^{\mathrm{t}}\otimes\boldsymbol{a}_t\right]\right]. \tag{3.87}$$

Recapitulating the structure of the stored energy density function (3.79), the first term in the above given form of the symmetric stress tensor resembles the isotropic energy part, whereas the second term and the contributions of the couple-stress tensor correspond to the energy contribution that incorporates the fibre properties. For vanishing fibre bending stiffness, i.e. $c = 0$, the model reduces to a classic neo-Hookean solid.

In the small strain version of the model that has been discussed in detail in Sect. 3.1, contributions from the fibre stretch gradient are neglected in the specific form of the couple-stress tensor (3.37) because they are of higher order. In contrast thereto, fibre stretch gradients are included in addition to fibre curvature contributions in the non-linear forms of the stress and couple stress tensor (3.86)-(3.87).

In order to obtain the specific form of the tangent stiffness matrix for the considered energy function, the sensitivities of the stress and couple-stress tensor are derived and presented in Appendix B.1.2.

3.2.4.2 Boundary value problem

The pure azimuthal shear deformation of a cylindrical tube with radially aligned fibres is considered in order to compare the numerical results with the analytical solution provided in [44]. Moreover, the results are compared to those obtained by the small

strain framework presented in Sect. 3.1.4.3, as well as by the multi-field method in [12]. For an accurate comparison of the results, the dimensionless versions of the stress and couple-stress tensor (3.42) are considered.

The isogeometric model for the cylindrical tube with radii $r_i = 1\,\mathrm{mm}$ and $r_o = 2.5\,\mathrm{mm}$ is adopted from the simulations in Sect. 3.1.4 and details on the geometry and on the discretisation within IGA are provided in Appendix B.2.1. In particular, the use of knot removal as well as linear constraints for the location and displacement of repeated knots and control points leads to global C^1-continuity which is sufficient for the fulfilment of the integrability condition posed by (3.68).

In accordance with the calculations in [44] and in analogy to the boundary value problem in Sect. 3.1.4.2, the tube is analysed under a pure azimuthal shear deformation which is prescribed on the outer radius by means of Dirichlet boundary conditions, whereas the inner radius is fixed. The azimuthal displacement is chosen in such a way that the outer surface undergoes a rotation of $\pi/9$ around the tube's middle axis. The outer radius of the tube is not changed by this deformation so that the applied boundary conditions yield the total volume of the tube to be conserved. Along with this observation, extensible fibres are assumed in order to obtain pure azimuthal shear in the finite deformation setting, cf. [45]. Surface couples are assumed to vanish at the inner and outer cylinder radius such that $\boldsymbol{t}_2 = \boldsymbol{0}$. The discretised model of the tube including the particular boundary conditions is shown in Fig. 3.13. The finite element mesh contains $\mathrm{n_{el}} = 832$ elements and is based on $\mathrm{n_{cp}} = 1260$ control points.

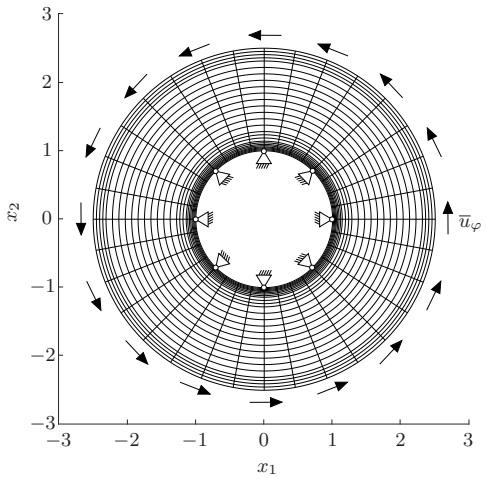

Figure 3.13: Boundary conditions and discretisation of the tube with $\mathrm{n_{el}} = 832$ elements. Reprinted from [171] under the terms of the Creative Commons Attribution 4.0 International License (CC BY 4.0).

3.2.4.3 Results and comparison

In the present example, the fibre bending stiffness is represented by the non-dimensional parameter λ^* defined in (3.40). Within the simulations performed by means of the pro-

posed isogeometric approach, different values for this parameter are considered, namely $\lambda^* \in \{0.0, 0.005, 0.03, 0.1\}$. In all cases, the fibres are initially straight and aligned in radial direction.

Fibre deformation and slope In Fig. 3.14, the deformation pattern of the tube is shown. In the case where $\lambda^* = 0$ the fibres behave perfectly flexible which, together with the neglected tensile stiffness of the fibres, means that the fibres do not have any impact on the deformation. On the other hand, as the energy contributions belonging to the fibres become active by employing non-zero values for the fibre bending stiffness parameter, a resistance against bending can be observed. This resistance becomes more prominent with increasing values of λ^* so that, by choosing λ^* large enough, fibres which remain almost straight during deformation can be obtained.

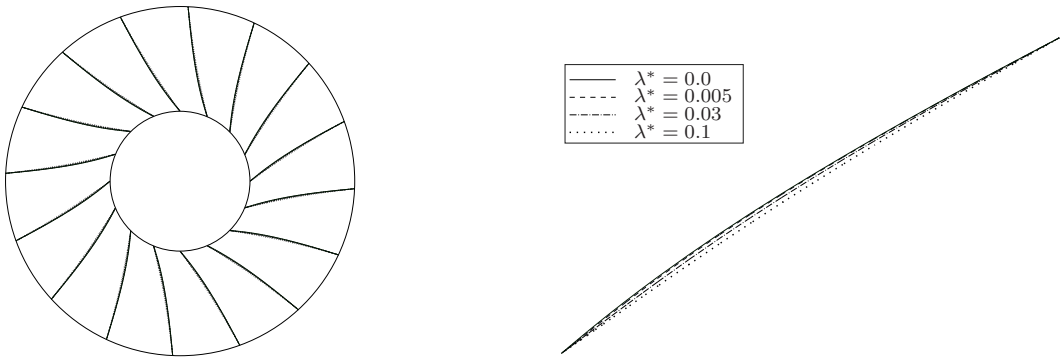

(a) Deformation pattern of the cylindrical tube.

(b) Detail view on the deformation of a fibre with initial alignment in $\boldsymbol{e}_1$-direction.

Figure 3.14: Deformation plots of the cylindrical tube for $\lambda^* \in \{0.0, 0.005, 0.03, 0.1\}$. Reprinted from [171] under the terms of the Creative Commons Attribution 4.0 International License (CC BY 4.0).

Stress and couple-stress distributions In Fig. 3.15a, the results for the dimensionless stress coefficients $[\sigma_{r\varphi}]^*$ and $[\sigma_{\varphi r}]^*$ are presented as a function of the cylinder radius. Fig. 3.15b shows the respective results for the symmetric stress part $[\sigma_{r\varphi}^{\mathrm{sym}}]^*$ as well as for the only non-zero couple-stress coefficient $[m_{rz}]^*$. The presented solutions for the finite strain setting are not only in accordance with the results from [12] produced by a multi-field method by using the same constitutive model, but also with those obtained by the linearised formulation documented in Sect. 3.1.4.3. For a prescribed rotation up to $\pi/9$, as employed in this contribution, both formulations show quantitatively coinciding results. Also the analytical solution, which has been obtained in [44] from the application of a power series method, is in quantitative agreement with the results as shown in Sect. 3.1.4.3. Whereas these observations hold for the prescribed rotation of up to $\pi/9$ of the outer tube radius, a deviation from the small strain results is observable when significantly larger deformations are considered. In Fig. 3.16, simulation results

corresponding to rotations of $\pi/9, \pi/6$ and $2\pi/9$ around the tube's middle axis are presented for $\lambda^* = 0.03$. With an increasingly large deformation, the difference between the linearised and the non-linear modelling approach becomes more pronounced in all stress and couple-stress contributions considered.

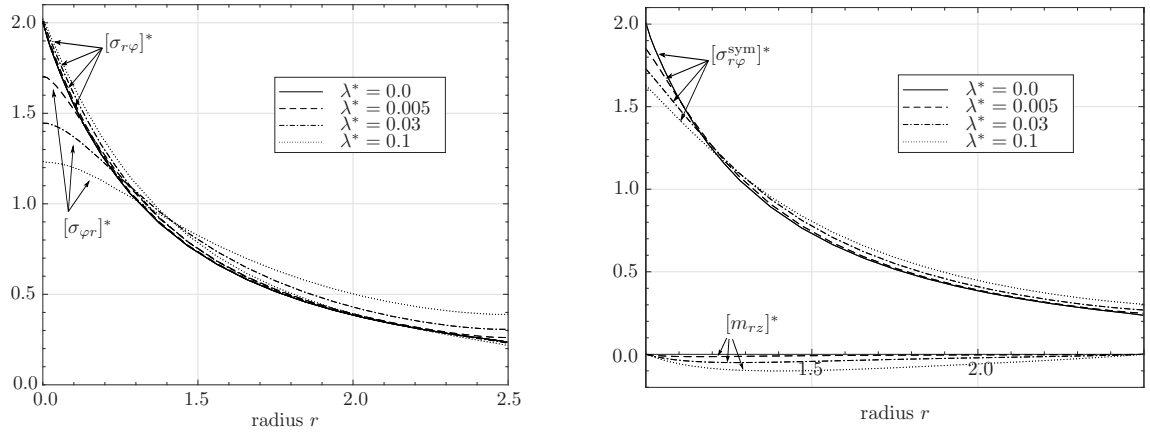

(a) Distribution of $[\sigma_{r\varphi}]^*$ and $[\sigma_{\varphi r}]^*$.

(b) Distribution of $[\sigma^{\mathrm{sym}}_{r\varphi}]^*$ and $[m_{rz}]^*$.

Figure 3.15: Distribution of the dimensionless stress coefficients $[\sigma_{r\varphi}]^*, [\sigma_{\varphi r}]^*, [\sigma^{\mathrm{sym}}_{r\varphi}]^*$ and couple-stress coefficient $[m_{rz}]^*$ for $\lambda^* \in \{0.0, 0.005, 0.03, 0.1\}$. Reproduced from [171] under the terms of the Creative Commons Attribution 4.0 International License (CC BY 4.0).

Remark 3.3. As discussed in this section, the numerical results obtained by the proposed IGA formulation are in accordance with the results obtained in [12] based on a multi-field method. In Table 3.2, a comparison is provided between the governing equations and the degrees of freedom in this reference and in the IGA approach presented in this thesis. The main advantages of IGA in this regard are the lower number of degrees of freedom and the direct solution of the fourth-order PDE along with the strong enforcement of C^1-continuity.

3.2.5 Simulation of curvature effects in a fibre-reinforced notched plate

A more complex example for studying fibre bending stiffness effects is represented by the fibre-reinforced notched plate shown in Fig. 3.17. By employing an offset between the notches, a bending deformation mode is activated as a tensile test is performed. The influence of the fibre bending stiffness parameter c as well as of the initial fibre direction is elaborated for this boundary value problem.

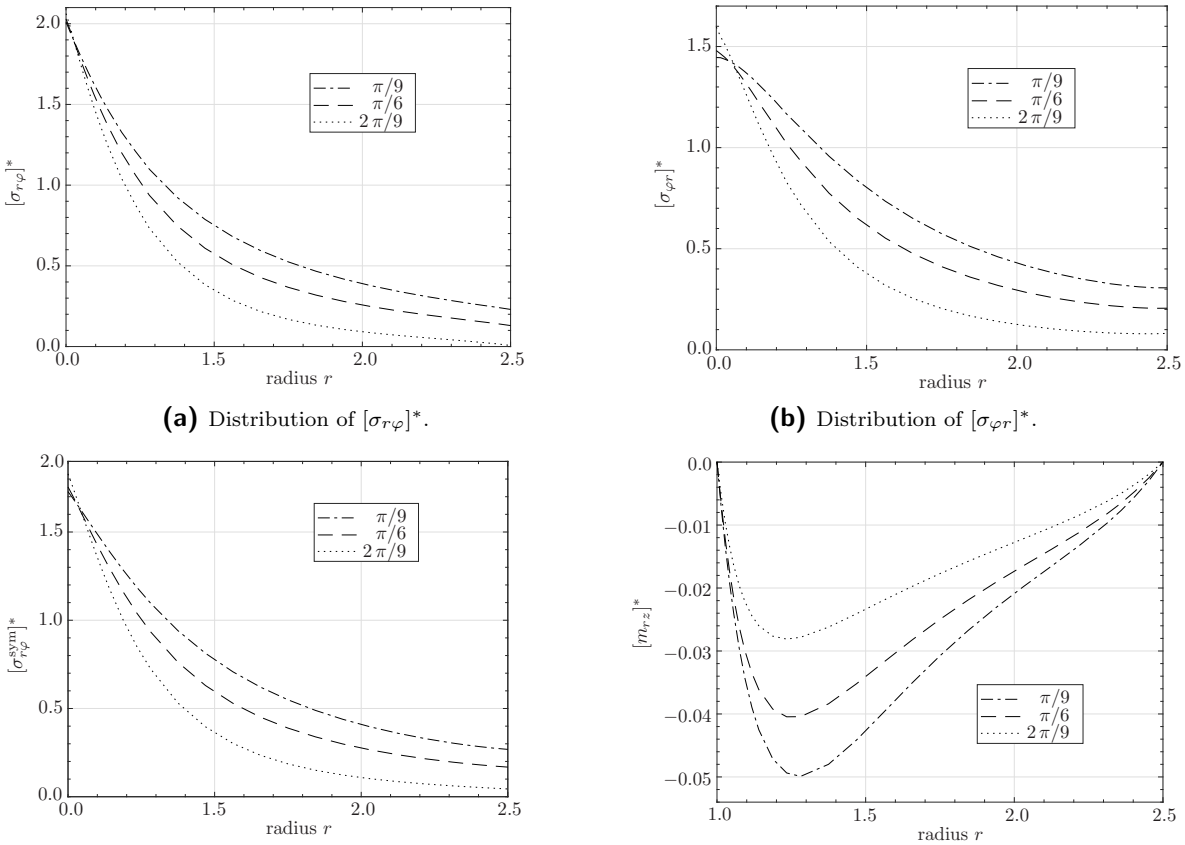

(a) Distribution of $[\sigma_{r\varphi}]^*$.

(b) Distribution of $[\sigma_{\varphi r}]^*$.

(c) Distribution of $[\sigma_{r\varphi}^{\mathrm{sym}}]^*$.

(d) Distribution of $[m_{rz}]^*$.

Figure 3.16: Distribution of the dimensionless stress coefficients $[\sigma_{r\varphi}]^*, [\sigma_{\varphi r}]^*, [\sigma_{r\varphi}^{\mathrm{sym}}]^*$ and couple-stress coefficient $[m_{rz}]^*$ for $\lambda^* = 0.03$ and for a rotation of $\pi/9, \pi/6$ and $2\pi/9$ around the tube's middle axis. Reproduced from [171] under the terms of the Creative Commons Attribution 4.0 International License (CC BY 4.0).

Table 3.2: Comparison of the isogeometric approach with the multi-field method in [12].

	Multi-field method in [12]	IGA approach
Equations	$\mathbf{0} = \nabla_{\boldsymbol{x}} \cdot \boldsymbol{\sigma}^{\mathrm{t}}$ $\mathbf{0} = \nabla_{\boldsymbol{x}} \cdot \boldsymbol{m}^{\mathrm{t}} - \boldsymbol{\epsilon} : \boldsymbol{\sigma}^{\mathrm{skw}}$ $\mathbf{0} = p\,[\boldsymbol{F} - \boldsymbol{\Theta}]$	$\mathbf{0} = \nabla_{\boldsymbol{x}} \cdot \boldsymbol{\sigma}^{\mathrm{sym}} + \frac{1}{2}\nabla_{\boldsymbol{x}} \times \left[\nabla_{\boldsymbol{x}} \cdot \boldsymbol{m}^{\mathrm{t}}\right]$
Fulfilment of continuity requirements	Weak fulfilment	Strong fulfilment
dof	$\{\boldsymbol{\varphi}, \boldsymbol{\sigma}^{\mathrm{skw}}, \boldsymbol{\Theta}\}$	$\{\boldsymbol{\varphi}\}$
#dof in 2D	7	2
#dof in 3D	15	3

3.2.5.1 Specification of the boundary value problem

In Fig. 3.17, the mesh for the notched plate under investigation is shown and the dimensions of the model are presented. The width of the inner part of the plate is $w = 12\,\mathrm{mm}$ and the total length is $l = 120\,\mathrm{mm}$. Between the centre points of the circular notches with radii $r = \frac{3}{8}\,w = 4.5\,\mathrm{mm}$, an offset of $d = \frac{3}{2}\,w = 18\,\mathrm{mm}$ is present. The discretisation of the notched plate is obtained by $\mathrm{n_{el}} = 990$ elements. For the approximation of the placement field and the test function, NURBS basis functions with polynomial degree $p = q = 4$ are employed in accordance with the previous example. The control mesh thus consists of $\mathrm{n_{cp}} = 1410$ control points as discussed in detail in Appendix B.2.3. Within the whole domain, a global continuity of C^{p-1}, accordingly C^3, is ensured due to the characteristic properties of NURBS.

In analogy to a uni-axial tensile test, the plate is clamped at both ends, meaning that displacements in $\boldsymbol{e}_2$-direction of the left and right boundary nodes are prevented. In $\boldsymbol{e}_1$-direction, a uniform displacement is prescribed on both sides. The total elongation of the plate is set to 1/5 of its length so that $\|\overline{\boldsymbol{u}}\| = 12\,\mathrm{mm}$. Similar to the previous example, it is assumed that no surface couples are present, i.e. $\boldsymbol{t}_2 = \boldsymbol{0}$.

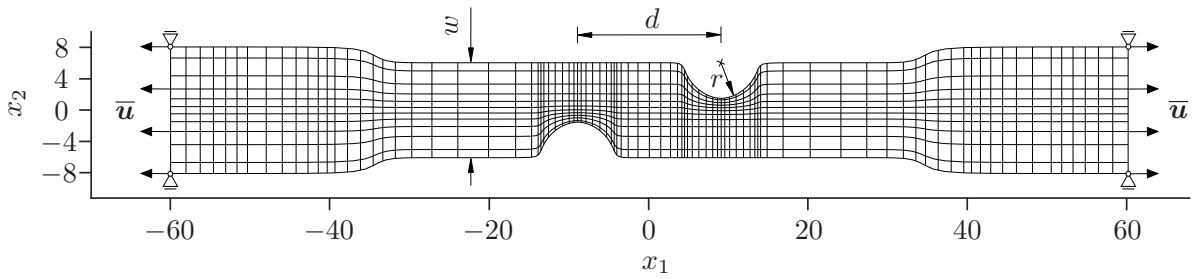

Figure 3.17: Boundary conditions and discretisation of the notched plate including $\mathrm{n_{el}} = 990$ elements. Reprinted from [171] under the terms of the Creative Commons Attribution 4.0 International License (CC BY 4.0).

3.2.5.2 Results and discussion

Within the IGA simulations of the notched plate, two distinct values are employed for the fibre bending stiffness parameter and two different initial fibre directions are considered. Specifically speaking, a reinforcement with fibres that are aligned in $\boldsymbol{e}_1$-direction as well as diagonally aligned fibres are taken into account for fibre bending stiffness parameters $c \in \{2 \times 10^4\,\mathrm{N}, 3 \times 10^4\,\mathrm{N}\}$. In the case of diagonally aligned fibres, the fibre direction vector exhibits an angle of $\alpha = \pi/4$ to the $\boldsymbol{e}_1$-direction.

Deformation In Fig. 3.18, the deformed configuration of the notched plate is shown after the analysis under the above mentioned boundary conditions without the presence of fibres. Due to the particular boundary conditions discussed in Sect. 3.2.5.1, the plate is stretched in $\boldsymbol{e}_1$-direction and the notches change their shape significantly. The middle part of the plate undergoes a bending deformation in consequence of the offset between the two notches. Fig. 3.19 provides a more detailed view on the deformed mesh and compares the deformation pattern for $c = 0$ and $c = 3 \times 10^4\,\mathrm{N}$ for fibres aligned with the $\boldsymbol{e}_1$-direction, i.e. $\alpha = 0$. The largest influence of the fibres on the overall deformation is obtained in the region of the notches. Due to the bending deformation, the fibre curvature part in the energy contribution (3.82) is activated. For the different fibre orientations, Fig. 3.20 presents the deformed mesh in more detail. It is shown that for fibres which are aligned with the $\boldsymbol{e}_1$-direction in the initial configuration, the deformation of the vertical element edges is rather similar to the case of a non-reinforced material. However, if the fibre angle is $\alpha = \pi/4$ in the initial state, a different deformation pattern is obtained in the region of the circular notches. In particular, the vertical element edges are bent into one preferred direction near the lower boundary, cf. Fig. 3.20b.

Stress and couple-stress distributions The distribution of the couple-stresses for the current example is presented in Fig. 3.21-3.24. Due to the two-dimensional setting, the only non-zero couple-stress coefficients are m_{13} and m_{23}. The highest values of these two quantities are concentrated in the region of the notches. In addition, non-zero couple-stresses occur in the transition zones between the middle and end sections of the plate and at the boundary nodes on the left and on the right ends where the displacement in $\boldsymbol{e}_2$-direction is prevented. Regarding the different fibre directions studied in the simulation, a varying distribution of the couple-stresses can be observed. In the case of an initial fibre alignment in $\boldsymbol{e}_1$-direction, couple-stresses especially appear in the region of the notches throughout the whole width of the plate. The absolute values of coefficient m_{13} are significantly larger than those of m_{23}. If, on the other hand, the fibres are initially aligned diagonally in the material, the stresses are more localised at the notches and decrease over the width of plate. Besides, m_{13} and m_{23} show similar distributions.

The distribution of the shear stress coefficient σ_{12} is shown in Fig. 3.25 together with its symmetric and skew-symmetric parts exemplary for the case of fibres initially aligned in $\boldsymbol{e}_1$-direction. Similar to the couple-stresses, the stresses take their maximum values in the inhomogeneously deforming regions close to the notches. In the presented example, the skew-symmetric stresses take values of the same order as their symmetric counterparts so that both contributions possess a significant impact on the total stress values. This relation, however, depends on the prescribed fibre bending stiffness parameter. For rather small values, the symmetric part of the stress tensor becomes more prominent in comparison to the skew-symmetric part, whereas for an increasing fibre bending stiffness, the skew-symmetric stresses exceed the symmetric contributions. Considering $c = 3 \times 10^4\,\mathrm{N}$, as employed for the results shown in Fig. 3.25, the skew-symmetric part $\sigma_{12}^{\mathrm{skw}}$ is dominant.

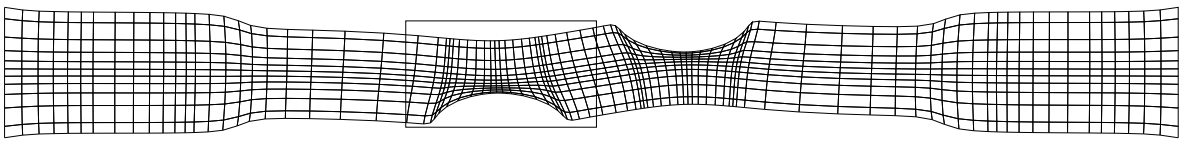

Figure 3.18: Deformed configuration of the notched plate without fibres. Reprinted from [171] under the terms of the Creative Commons Attribution 4.0 International License (CC BY 4.0).

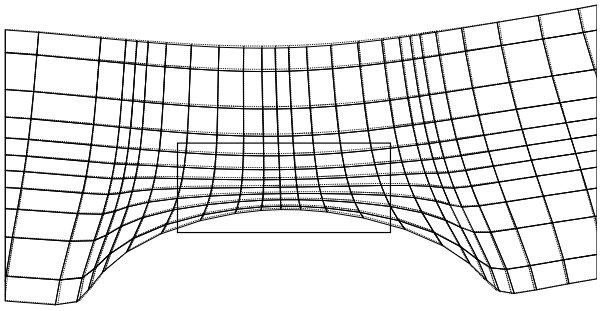

Figure 3.19: Detailed view on the deformed configuration of the notched plate without fibres (solid lines) and with fibres initially aligned in $\boldsymbol{e}_1$-direction (dashed lines) with $c = 3 \times 10^4$ N. Reprinted from [171] under the terms of the Creative Commons Attribution 4.0 International License (CC BY 4.0).

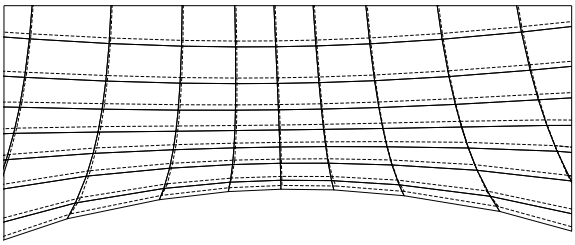

(a) Detailed view on the deformed configuration of the notched plate without fibres (solid lines) and with fibres initially aligned in $\boldsymbol{e}_1$-direction ($\alpha = 0$, dashed lines) with $c = 3 \times 10^4$ N.

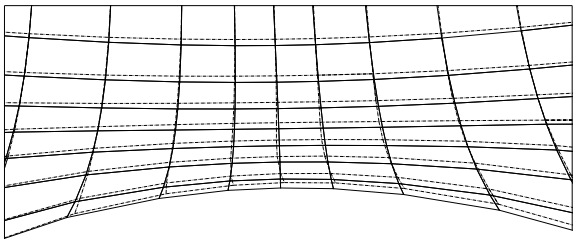

(b) Detailed view on the deformed configuration of the notched plate without fibres (solid lines) and with diagonally aligned fibres ($\alpha = \pi/4$, dashed lines) with $c = 3 \times 10^4$ N.

Figure 3.20: Detailed views on the deformed configurations of the notched plate. Reprinted from [171] under the terms of the Creative Commons Attribution 4.0 International License (CC BY 4.0).

Integrated reaction force Fig. 3.26 presents the integrated reaction force in $\boldsymbol{e}_1$-direction over the prescribed displacement value for the different cases of initial fibre alignment and fibre bending stiffness. It can be observed that the curvature of the graphs, which show an overall non-linear behaviour, is slightly different depending on the initial fibre direction and fibre bending stiffness. Especially in the region of large prescribed deformations an alignment in $\boldsymbol{e}_1$-direction yields the highest reaction force. For higher values of the fibre bending stiffness parameter, the material response becomes stiffer and increasingly distinguishable from the case of a non-reinforced material.

Remark 3.4. In Sect. 3.2.4.1, the energy contribution belonging to a transversely isotropic material behaviour has been assumed to be constant in order to examine the influence of the higher-gradient contributions, respectively of the fibre bending stiffness, exclusively. If the influence of this energy part had additionally been taken into account instead, a more significant difference in the deformations and in the reaction force would have been expected when comparing the non-reinforced with the fibre-reinforced material, in analogy to the results presented in Sect. 3.1.5.2 within the small strain regime.

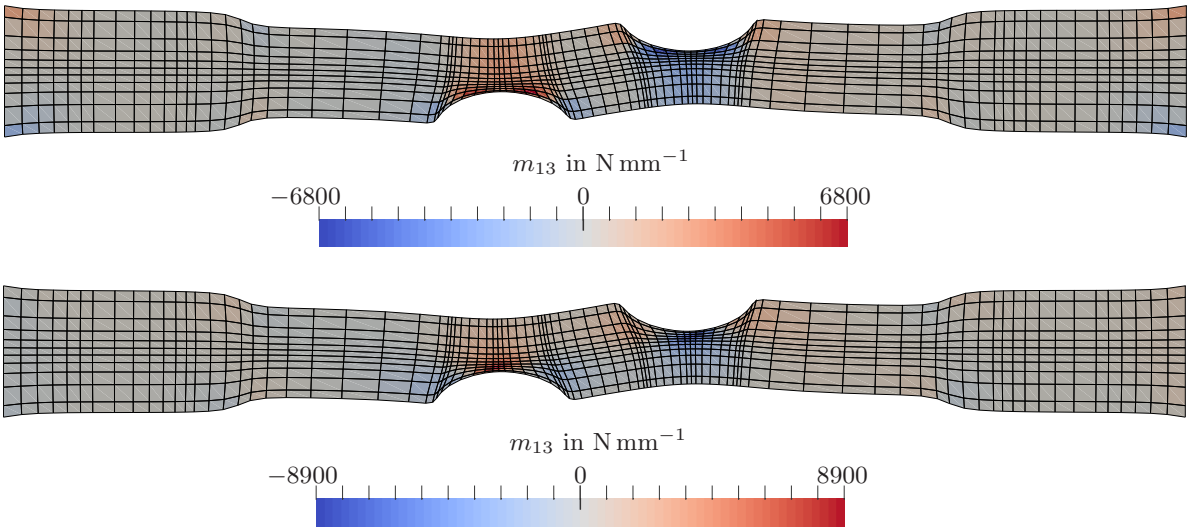

Figure 3.21: Distribution of the couple-stress coefficient m_{13} for the notched plate with fibres aligned in $\boldsymbol{e}_1$-direction (top) and with diagonally aligned fibres (bottom) with $c = 2 \times 10^4\,\mathrm{N}$. Reprinted from [171] under the terms of the Creative Commons Attribution 4.0 International License (CC BY 4.0).

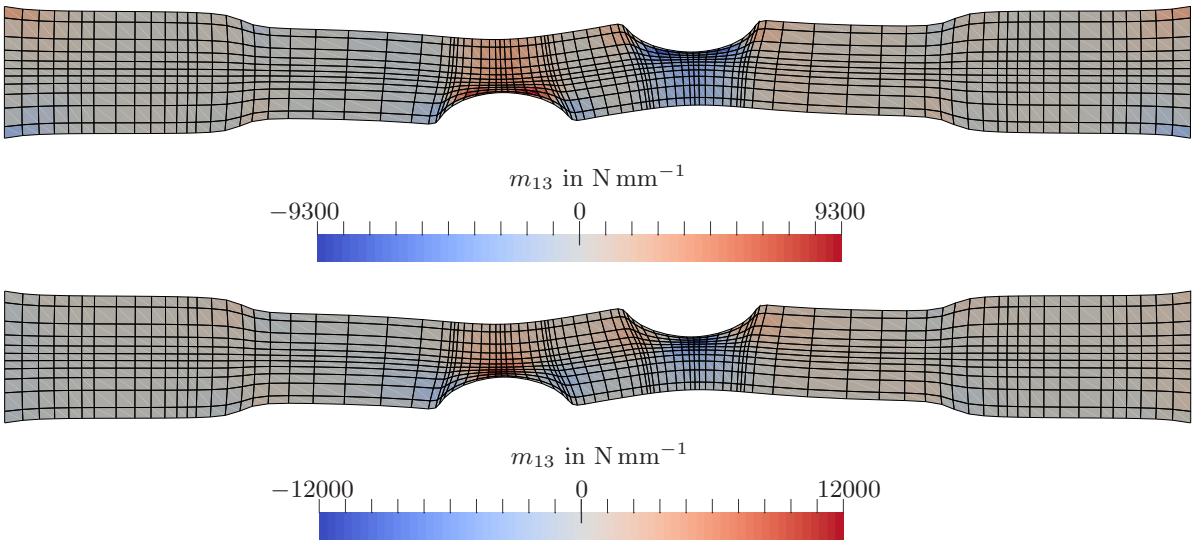

Figure 3.22: Distribution of the couple-stress coefficient m_{13} for the notched plate with fibres aligned in $\boldsymbol{e}_1$-direction (top) and with diagonally aligned fibres (bottom) with $c = 3 \times 10^4\,\mathrm{N}$. Reprinted from [171] under the terms of the Creative Commons Attribution 4.0 International License (CC BY 4.0).

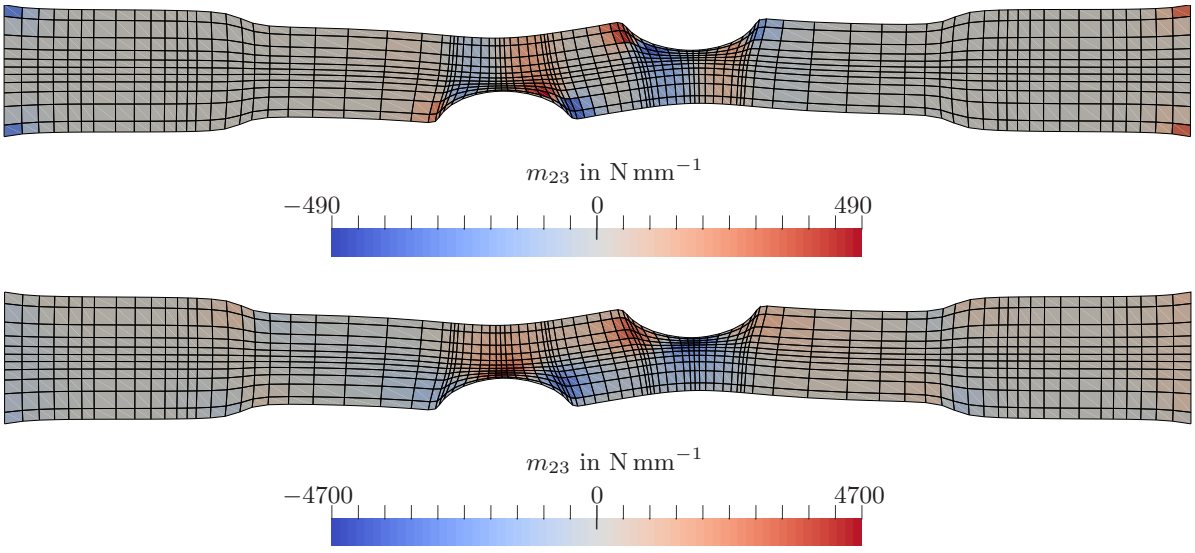

Figure 3.23: Distribution of the couple-stress coefficient m_{23} for the notched plate with fibres aligned in $\boldsymbol{e}_1$-direction (top) and with diagonally aligned fibres (bottom) with $c = 2 \times 10^4\,\mathrm{N}$. Reprinted from [171] under the terms of the Creative Commons Attribution 4.0 International License (CC BY 4.0).

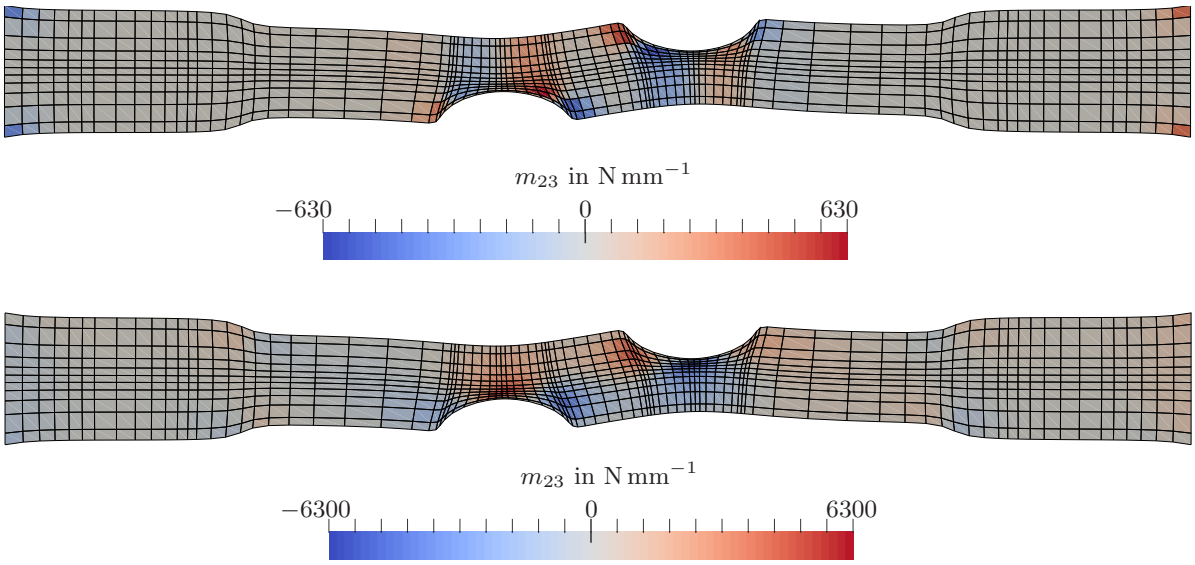

Figure 3.24: Distribution of the couple-stress coefficient m_{23} for the notched plate with fibres aligned in $\boldsymbol{e}_1$-direction (top) and with diagonally aligned fibres (bottom) with $c = 3 \times 10^4$ N. Reprinted from [171] under the terms of the Creative Commons Attribution 4.0 International License (CC BY 4.0).

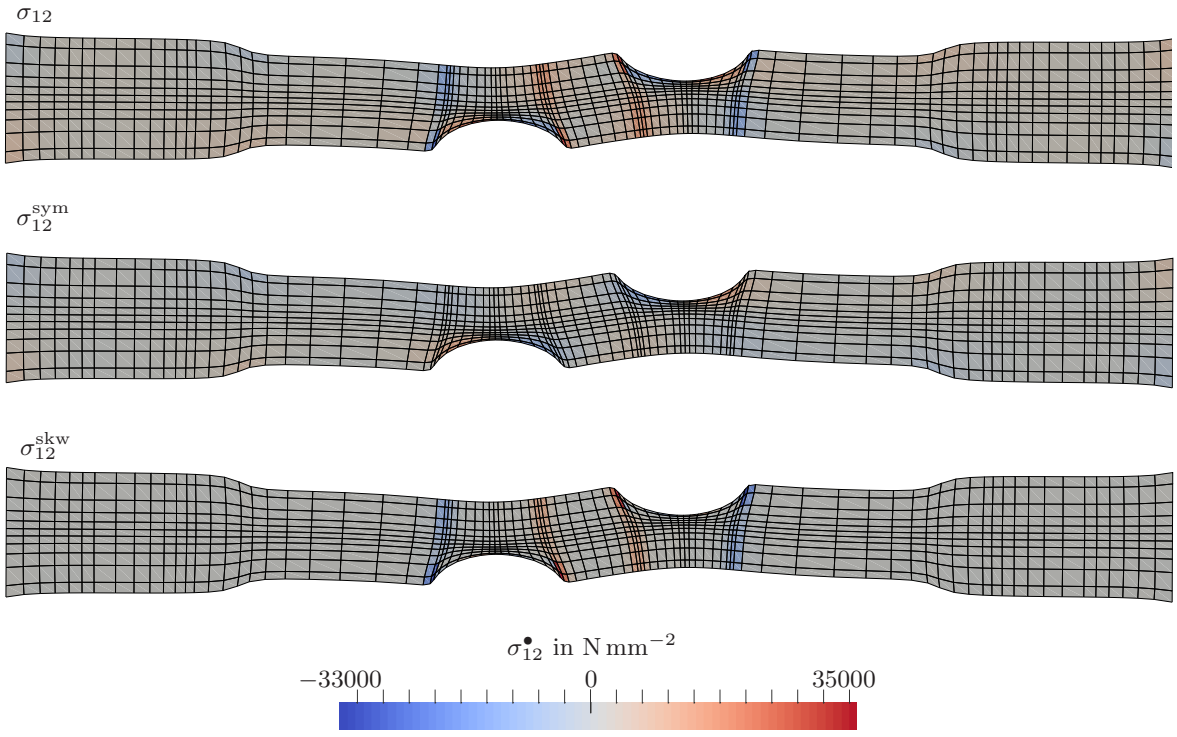

Figure 3.25: Distribution of the stress coefficients σ_{12}, $\sigma_{12}^{\mathrm{sym}}$ and $\sigma_{12}^{\mathrm{skw}}$ for the notched plate with fibres aligned in $\boldsymbol{e}_1$-direction with $c = 3 \times 10^4$ N. Reprinted from [171] under the terms of the Creative Commons Attribution 4.0 International License (CC BY 4.0).

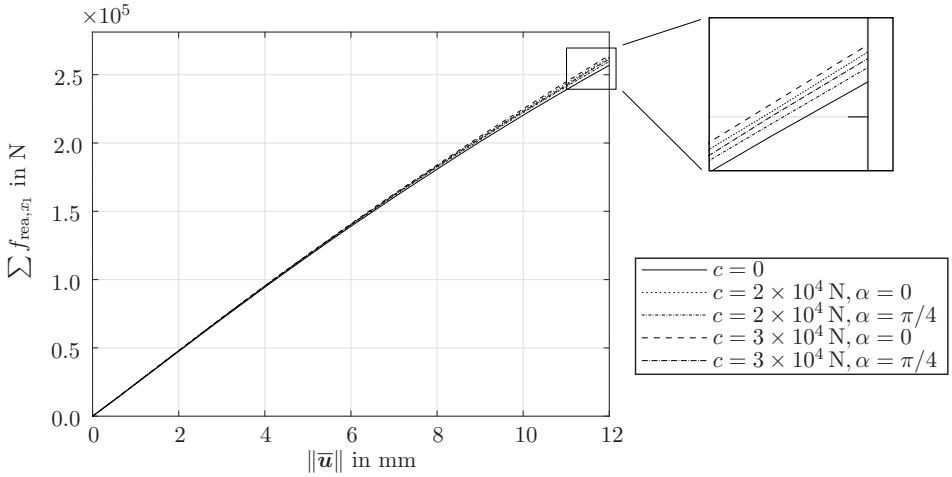

Figure 3.26: Integrated reaction force in $\boldsymbol{e}_1$-direction in dependence of the prescribed displacement on the right boundary of the notched plate. Reproduced from [171] under the terms of the Creative Commons Attribution 4.0 International License (CC BY 4.0).

B Appendix

B.1 Tangent contributions

In the following sections, all tangent contributions are presented which are employed in the proposed small strain as well as finite strain IGA framework for the simulation of fibre-reinforced solids with fibre bending stiffness.

B.1.1 Small strain modelling approach

Based on the material model described in Sect. 3.1.4.1, the tangent operators for the isogeometric finite element analysis can be derived as proposed in [172]. Recapitulating the assumption on higher-order terms made in Sect. 3.1.1, a linear relation between the tensors $\boldsymbol{\sigma}^{\mathrm{sym}}$ and $\boldsymbol{\varepsilon}$ as well as $\overline{\boldsymbol{m}}$ and $\boldsymbol{\kappa}$ is obtained. This results from the derivations in [153, (9.9), (9.12)] where, in particular, the higher-order terms that follow from the dyadic products in (3.36) are neglected. The tangent operators accordingly read

$$\mathsf{E}_1 = \frac{\mathrm{d}\,\boldsymbol{\sigma}^{\mathrm{sym}}}{\mathrm{d}\,\boldsymbol{\varepsilon}}, \quad \mathsf{E}_2 = \frac{\mathrm{d}\,\overline{\boldsymbol{m}}^{\mathrm{t}}}{\mathrm{d}\,\boldsymbol{\kappa}} \tag{3.88}$$

and result in

$$\mathsf{E}_1 = \lambda\, \boldsymbol{I} \otimes \boldsymbol{I} + \mu\, [\boldsymbol{I} \overline{\otimes} \boldsymbol{I} + \boldsymbol{I} \underline{\otimes} \boldsymbol{I}], \quad \mathsf{E}_2 = -\tfrac{8}{3}\, c\, [\boldsymbol{\epsilon} \cdot \boldsymbol{a}] \,\overline{\otimes}\, [\boldsymbol{a} \otimes \boldsymbol{a}] \otimes \boldsymbol{a} \tag{3.89}$$

for the particular form of the stored energy density function (3.28). With these formulations at hand, the symmetric part of the stress tensor as well as the couple-stress tensor can be expressed as

$$\boldsymbol{\sigma}^{\mathrm{sym}} = \mathsf{E}_1 : \boldsymbol{\varepsilon}, \quad \overline{\boldsymbol{m}}^{\mathrm{t}} = \mathsf{E}_2 :\cdot\, \boldsymbol{\kappa} \tag{3.90}$$

which reflects the assumption of linear constitutive relations.
Considering that, for the small strain setting, the internal force vector is a linear function of the displacement field, these relations can be used directly in the discretised weak form (3.24) together with the expressions in (3.23), specifically

$$\begin{aligned} \mathop{\mathsf{A}}_{e=1}^{\mathrm{n_{el}}} \sum_{A=1}^{\mathrm{n_{en}}} \sum_{B=1}^{\mathrm{n_{en}}} \Bigg[& \int_{\Omega^e} \nabla_{\boldsymbol{x}} R^A \cdot \mathsf{E}_1 \cdot \nabla_{\boldsymbol{x}} R^B \,\mathrm{d}v \\ & + \int_{\Omega^e} \left[\tfrac{1}{2}\, \boldsymbol{\epsilon} \cdot \nabla_{\boldsymbol{x}} \nabla_{\boldsymbol{x}} R^A\right] : \mathsf{E}_2 : \nabla_{\boldsymbol{x}} \nabla_{\boldsymbol{x}} R^B \,\mathrm{d}v \Bigg] \cdot \boldsymbol{u}^{eB} = \boldsymbol{f}_{\mathrm{ext}}. \end{aligned} \tag{3.91}$$

B.1.2 Finite strain modelling approach

The tangent stiffness matrix which is used in the iterative solution scheme (3.76) of the finite strain framework is derived as

$$\boldsymbol{K} = \mathop{\mathsf{A}}_{e=1}^{\mathrm{n_{el}}} \sum_{A=1}^{\mathrm{n_{en}}} \sum_{B=1}^{\mathrm{n_{en}}} \boldsymbol{K}^{eAB} \tag{3.92}$$

with

$$\begin{aligned}
\boldsymbol{K}^{eAB} = \int_{\Omega_0^e} & \nabla_{\boldsymbol{X}} R^A \cdot J\, \boldsymbol{F}^{-1} \cdot \frac{\partial \boldsymbol{\sigma}^{\mathrm{sym}}}{\partial \boldsymbol{F}} \cdot \nabla_{\boldsymbol{X}} R^B \\
& + \nabla_{\boldsymbol{X}} R^A \cdot \boldsymbol{F}^{-1} \cdot \boldsymbol{\sigma}^{\mathrm{sym}} \otimes \mathrm{cof}(\boldsymbol{F}) \cdot \nabla_{\boldsymbol{X}} R^B \\
& - \nabla_{\boldsymbol{X}} R^B \cdot \boldsymbol{F}^{-1} \cdot \boldsymbol{\sigma}^{\mathrm{sym}} \otimes \mathrm{cof}(\boldsymbol{F}) \cdot \nabla_{\boldsymbol{X}} R^A \\
& + \nabla_{\boldsymbol{X}} R^A \cdot J\, \boldsymbol{F}^{-1} \cdot \frac{\partial \boldsymbol{\sigma}^{\mathrm{sym}}}{\partial \boldsymbol{\Upsilon}} : \nabla_{\boldsymbol{X}} \nabla_{\boldsymbol{X}} R^B \,\mathrm{d}V \\
+ \tfrac{1}{2} \int_{\Omega_0^e} & - \boldsymbol{\epsilon} \cdot \left[\nabla_{\boldsymbol{X}} R^A \cdot \left[\boldsymbol{F}^{-1} \mathbin{\overline{\otimes}} \mathrm{cof}(\boldsymbol{F})\right] : \boldsymbol{\Upsilon} \cdot \boldsymbol{F}^{-1}\right] : \frac{\partial \boldsymbol{m}^{\mathrm{t}}}{\partial \boldsymbol{F}} \cdot \nabla_{\boldsymbol{X}} R^B \\
& - \boldsymbol{\epsilon} \cdot \left[\nabla_{\boldsymbol{X}} R^A \cdot \left[\boldsymbol{F}^{-1} \mathbin{\overline{\otimes}} \mathrm{cof}(\boldsymbol{F})\right] : \boldsymbol{\Upsilon} \cdot \boldsymbol{F}^{-1}\right] : \boldsymbol{m}^{\mathrm{t}} \otimes \boldsymbol{F}^{-\mathrm{t}} \cdot \nabla_{\boldsymbol{X}} R^B \\
& + \boldsymbol{\epsilon} \cdot \left[\nabla_{\boldsymbol{X}} R^A \cdot \left[\boldsymbol{F}^{-1} \mathbin{\overline{\otimes}} \mathrm{cof}(\boldsymbol{F})\right] : \boldsymbol{\Upsilon}\right] : \left[\boldsymbol{m}^{\mathrm{t}} \cdot \boldsymbol{F}^{-t} \cdot \nabla_{\boldsymbol{X}} R^B \otimes \boldsymbol{F}^{-1}\right] \\
& - \left[\boldsymbol{\epsilon} \cdot \boldsymbol{m}^{\mathrm{t}} \cdot \mathrm{cof}(\boldsymbol{F})\right] : \left[\boldsymbol{F}^{-\mathrm{t}} \cdot \nabla_{\boldsymbol{X}} R^B \otimes \left[\boldsymbol{F}^{-\mathrm{t}} \cdot \left[\nabla_{\boldsymbol{X}} R^A \cdot \boldsymbol{F}^{-1} \cdot \boldsymbol{\Upsilon}\right]\right]^{\mathrm{t}}\right] \\
& - \left[\boldsymbol{\epsilon} \cdot \boldsymbol{m}^{\mathrm{t}} \cdot \mathrm{cof}(\boldsymbol{F})\right] : \left[\boldsymbol{F}^{-\mathrm{t}} \cdot \left[\nabla_{\boldsymbol{X}} R^B \cdot \boldsymbol{F}^{-1} \cdot \boldsymbol{\Upsilon}\right]\right] \otimes \boldsymbol{F}^{-\mathrm{t}} \cdot \nabla_{\boldsymbol{X}} R^A \\
& + \left[\boldsymbol{\epsilon} \cdot \left[\boldsymbol{F}^{-\mathrm{t}} \mathbin{\overline{\otimes}} \mathrm{cof}(\boldsymbol{F})\right] : \nabla_{\boldsymbol{X}} \nabla_{\boldsymbol{X}} R^A\right] : \frac{\partial \boldsymbol{m}^{\mathrm{t}}}{\partial \boldsymbol{F}} \cdot \nabla_{\boldsymbol{X}} R^B \\
& + \left[\left[\boldsymbol{\epsilon} \cdot \boldsymbol{m}^{\mathrm{t}} \cdot \mathrm{cof}(\boldsymbol{F})\right] : \left[\boldsymbol{F}^{-\mathrm{t}} \mathbin{\overline{\otimes}} \nabla_{\boldsymbol{X}} R^B\right]\right] \cdot \nabla_{\boldsymbol{X}} \nabla_{\boldsymbol{X}} R^A \cdot \boldsymbol{F}^{-1} \\
& + \left[\boldsymbol{\epsilon} \cdot \boldsymbol{m}^{\mathrm{t}} \cdot \mathrm{cof}(\boldsymbol{F})\right] : \left[\boldsymbol{F}^{-\mathrm{t}} \cdot \nabla_{\boldsymbol{X}} R^B \otimes \left[\boldsymbol{F}^{-\mathrm{t}} \cdot \nabla_{\boldsymbol{X}} \nabla_{\boldsymbol{X}} R^A\right] : [\boldsymbol{I} \mathbin{\underline{\otimes}} \boldsymbol{I}]\right] \\
& - \left[\boldsymbol{\epsilon} \cdot \boldsymbol{m}^{\mathrm{t}} \cdot \mathrm{cof}(\boldsymbol{F})\right] : \left[\boldsymbol{F}^{-\mathrm{t}} \cdot \nabla_{\boldsymbol{X}} \nabla_{\boldsymbol{X}} R^A\right] \otimes \boldsymbol{F}^{-\mathrm{t}} \cdot \nabla_{\boldsymbol{X}} R^B \\
& - \left[\boldsymbol{\epsilon} \cdot \left[\nabla_{\boldsymbol{X}} R^A \cdot \left[\boldsymbol{F}^{-1} \mathbin{\overline{\otimes}} \mathrm{cof}(\boldsymbol{F})\right] : \boldsymbol{\Upsilon} \cdot \boldsymbol{F}^{-1}\right]\right] : \frac{\partial \boldsymbol{m}^{\mathrm{t}}}{\partial \boldsymbol{\Upsilon}} : \nabla_{\boldsymbol{X}} \nabla_{\boldsymbol{X}} R^B \\
& + \left[\boldsymbol{\epsilon} \cdot \boldsymbol{m}^{\mathrm{t}}\right] : \left[\boldsymbol{F}^{-\mathrm{t}} \mathbin{\overline{\otimes}} \mathrm{cof}(\boldsymbol{F})\right] : \nabla_{\boldsymbol{X}} \nabla_{\boldsymbol{X}} R^B \otimes \boldsymbol{F}^{-\mathrm{t}} \cdot \nabla_{\boldsymbol{X}} R^A \\
& + \left[\boldsymbol{\epsilon} \cdot \left[\boldsymbol{F}^{-\mathrm{t}} \mathbin{\overline{\otimes}} \mathrm{cof}(\boldsymbol{F})\right] : \nabla_{\boldsymbol{X}} \nabla_{\boldsymbol{X}} R^A\right] : \frac{\partial \boldsymbol{m}^{\mathrm{t}}}{\partial \boldsymbol{\Upsilon}} : \nabla_{\boldsymbol{X}} \nabla_{\boldsymbol{X}} R^B \,\mathrm{d}V .
\end{aligned} \tag{3.93}$$

The sensitivities of the symmetric part of the stress tensor as well as of the couple-stress tensor which are included in this representation of the tangent stiffness matrix are based on the stored energy density function (3.79) and read

$$\frac{\partial \boldsymbol{\sigma}^{\mathrm{sym}}}{\partial \boldsymbol{F}} = \left[\tfrac{\lambda}{2}\left[I_3 - 1\right] \boldsymbol{F} \cdot \boldsymbol{C}^{-1} + \mu\, \boldsymbol{F} \cdot \left[\boldsymbol{I} - \boldsymbol{C}^{-1}\right]\right] \cdot \boldsymbol{F}^{\mathrm{t}} \otimes \frac{\partial J^{-1}}{\partial \boldsymbol{F}}$$

$$
\begin{aligned}
&+ J^{-1}\boldsymbol{I}\,\overline{\otimes}\,\boldsymbol{F}\cdot\left[\tfrac{\lambda}{2}\left[I_3-1\right]\boldsymbol{C}^{-1}+\mu\left[\boldsymbol{I}-\boldsymbol{C}^{-1}\right]\right]\\
&+ J^{-1}\boldsymbol{F}\cdot\left[\tfrac{\lambda}{2}\left[I_3-1\right]\boldsymbol{C}^{-1}+\mu\left[\boldsymbol{I}-\boldsymbol{C}^{-1}\right]\right]\,\overline{\otimes}\,\boldsymbol{I}\\
&+ \tfrac{\lambda}{2}J^{-1}\boldsymbol{F}\cdot\left[\boldsymbol{C}^{-1}\cdot\boldsymbol{F}^{\mathrm{t}}\right]\otimes\frac{\partial I_3}{\partial\boldsymbol{F}}+J^{-1}\left[\tfrac{\lambda}{2}\left[I_3-1\right]-\mu\right]\left[\boldsymbol{F}\,\overline{\otimes}\,\boldsymbol{F}\right]:\frac{\partial\boldsymbol{C}^{-1}}{\partial\boldsymbol{F}}\\
&+ 2\,c\Bigg[\left[\boldsymbol{G}\cdot\boldsymbol{a}_0\otimes\boldsymbol{F}\cdot\boldsymbol{\Lambda}\cdot\boldsymbol{a}_0+\boldsymbol{F}\cdot\boldsymbol{\Lambda}\cdot\boldsymbol{a}_0\otimes\boldsymbol{G}\cdot\boldsymbol{a}_0\right]\otimes\frac{\partial J^{-1}}{\partial\boldsymbol{F}}\\
&\qquad+J^{-1}\left[\boldsymbol{G}\cdot\boldsymbol{a}_0\otimes\boldsymbol{I}\otimes\boldsymbol{\Lambda}\cdot\boldsymbol{a}_0+\boldsymbol{I}\,\overline{\otimes}\,\left[\boldsymbol{G}\cdot\boldsymbol{a}_0\otimes\boldsymbol{\Lambda}\cdot\boldsymbol{a}_0\right]\right]\\
&\qquad+J^{-1}\left[\boldsymbol{I}\,\underline{\otimes}\,\boldsymbol{I}\right]:\left[\left[\boldsymbol{F}\cdot\boldsymbol{\Lambda}\cdot\boldsymbol{a}_0\otimes\boldsymbol{a}_0\right]\cdot\left[\left[\boldsymbol{I}\,\underline{\otimes}\,\boldsymbol{I}\right]:\frac{\partial\boldsymbol{G}}{\partial\boldsymbol{F}}\right]\right]\\
&\qquad+J^{-1}\left[\boldsymbol{G}\cdot\boldsymbol{a}_0\otimes\boldsymbol{F}\otimes\boldsymbol{a}_0\right]:\frac{\partial\boldsymbol{\Lambda}}{\partial\boldsymbol{F}}\\
&\qquad+J^{-1}\left[\boldsymbol{I}\,\underline{\otimes}\,\boldsymbol{I}\right]:\left[\left[\boldsymbol{G}\cdot\boldsymbol{a}_0\otimes\boldsymbol{F}\otimes\boldsymbol{a}_0\right]:\frac{\partial\boldsymbol{\Lambda}}{\partial\boldsymbol{F}}\right]\\
&\qquad+J^{-1}\boldsymbol{F}\cdot\boldsymbol{\Lambda}\cdot\boldsymbol{a}_0\otimes\boldsymbol{a}_0\cdot\frac{\partial\boldsymbol{G}^{\mathrm{t}}}{\partial\boldsymbol{F}}\Bigg],
\end{aligned}
\tag{3.94}
$$

$$
\begin{aligned}
\frac{\partial\boldsymbol{\sigma}^{\mathrm{sym}}}{\partial\boldsymbol{\Upsilon}}=\;&2\,c\,J^{-1}\Bigg[\left[\boldsymbol{I}\,\underline{\otimes}\,\boldsymbol{I}\right]:\left[\left[\boldsymbol{a}_0\otimes\left[\boldsymbol{\Lambda}\cdot\boldsymbol{a}_0\right]\cdot\boldsymbol{F}^{\mathrm{t}}\right]^{\mathrm{t}}\cdot\frac{\partial\boldsymbol{G}^{\mathrm{t}}}{\partial\boldsymbol{\Upsilon}}\right]\\
&\qquad+\left[\boldsymbol{G}\cdot\boldsymbol{a}_0\otimes\boldsymbol{F}\otimes\boldsymbol{a}_0\right]:\frac{\partial\boldsymbol{\Lambda}}{\partial\boldsymbol{\Upsilon}}\\
&\qquad+\left[\boldsymbol{F}\,\overline{\otimes}\,\left[\boldsymbol{a}_0\cdot\boldsymbol{G}^{\mathrm{t}}\otimes\boldsymbol{a}_0\right]\right]:\frac{\partial\boldsymbol{\Lambda}}{\partial\boldsymbol{\Upsilon}}+\left[\boldsymbol{F}\cdot\boldsymbol{\Lambda}\cdot\boldsymbol{a}_0\otimes\boldsymbol{a}_0\right]\cdot\frac{\partial\boldsymbol{G}^{\mathrm{t}}}{\partial\boldsymbol{\Upsilon}}\Bigg],
\end{aligned}
\tag{3.95}
$$

$$
\begin{aligned}
\frac{\partial\overline{\boldsymbol{m}}^{\mathrm{t}}}{\partial\boldsymbol{F}}=-\tfrac{4}{3}\,c\Bigg[&\boldsymbol{\epsilon}:\left[\boldsymbol{F}\cdot\boldsymbol{\Lambda}\cdot\boldsymbol{a}_0\otimes\boldsymbol{a}_0\cdot\boldsymbol{F}^{\mathrm{t}}\,\overline{\otimes}\,\boldsymbol{a}_t\right]\otimes\frac{\partial J^{-1}}{\partial\boldsymbol{F}}\\
&+\boldsymbol{\epsilon}:\left[\boldsymbol{F}\cdot\boldsymbol{\Lambda}\cdot\boldsymbol{a}_0\otimes\boldsymbol{a}_0\cdot\boldsymbol{F}^{\mathrm{t}}\otimes\boldsymbol{a}_t\right]\otimes\frac{\partial J^{-1}}{\partial\boldsymbol{F}}\\
&+J^{-1}\left[\boldsymbol{\epsilon}\cdot\boldsymbol{a}_t\right]\,\overline{\otimes}\,\left[\boldsymbol{a}_0\cdot\boldsymbol{F}^{\mathrm{t}}\otimes\boldsymbol{\Lambda}\cdot\boldsymbol{a}_0\right]\\
&+J^{-1}\left[\boldsymbol{\epsilon}\cdot\boldsymbol{F}\cdot\boldsymbol{a}_0\right]\,\overline{\otimes}\,\left[\boldsymbol{a}_t\otimes\boldsymbol{\Lambda}\cdot\boldsymbol{a}_0\right]\\
&+J^{-1}\left[\boldsymbol{I}\,\underline{\otimes}\,\boldsymbol{I}\right]:\left[\left[\boldsymbol{a}_0\cdot\boldsymbol{F}^{\mathrm{t}}\right]\otimes\left[\left[\boldsymbol{\epsilon}\cdot\boldsymbol{a}_t\right]\cdot\boldsymbol{F}\otimes\boldsymbol{a}_0\right]:\frac{\partial\boldsymbol{\Lambda}}{\partial\boldsymbol{F}}\right]\\
&+J^{-1}\left[\boldsymbol{I}\,\underline{\otimes}\,\boldsymbol{I}\right]:\left[\boldsymbol{a}_t\otimes\left[\left[\boldsymbol{\epsilon}\cdot\left[\boldsymbol{a}_0\cdot\boldsymbol{F}^{\mathrm{t}}\right]\right]\cdot\boldsymbol{F}\otimes\boldsymbol{a}_0\right]:\frac{\partial\boldsymbol{\Lambda}}{\partial\boldsymbol{F}}\right]\\
&+J^{-1}\left[\boldsymbol{\epsilon}:\left[\boldsymbol{F}\cdot\boldsymbol{\Lambda}\cdot\boldsymbol{a}_0\otimes\boldsymbol{a}_t\right]\otimes\boldsymbol{a}_0\right]\,\underline{\otimes}\,\boldsymbol{I}\\
&-J^{-1}\left[\boldsymbol{\epsilon}\cdot\boldsymbol{F}\cdot\boldsymbol{\Lambda}\cdot\boldsymbol{a}_0\right]\,\overline{\otimes}\,\left[\boldsymbol{a}_t\otimes\boldsymbol{a}_0\right]\\
&+J^{-1}\boldsymbol{\epsilon}:\left[\left[\boldsymbol{F}\cdot\boldsymbol{\Lambda}\cdot\boldsymbol{a}_0\otimes\boldsymbol{a}_0\cdot\boldsymbol{F}^{\mathrm{t}}\right]\,\overline{\otimes}\,\frac{\partial\boldsymbol{a}_t}{\partial\boldsymbol{F}}\right]\\
&+J^{-1}\boldsymbol{\epsilon}:\left[\boldsymbol{F}\cdot\boldsymbol{\Lambda}\cdot\boldsymbol{a}_0\otimes\boldsymbol{a}_0\cdot\boldsymbol{F}^{\mathrm{t}}\right]\otimes\frac{\partial\boldsymbol{a}_t}{\partial\boldsymbol{F}}\Bigg],
\end{aligned}
\tag{3.96}
$$

$$\frac{\partial \overline{\boldsymbol{m}}^{\mathrm{t}}}{\partial \boldsymbol{\Upsilon}} = -\tfrac{4}{3}\, c\, J^{-1} \boldsymbol{\epsilon} : \Big[[\boldsymbol{F} \otimes \boldsymbol{a}_t] : \Big[\boldsymbol{I} \underline{\otimes} \left[\boldsymbol{I} \overline{\otimes} \left[\boldsymbol{a}_0 \cdot \boldsymbol{F}^{\mathrm{t}} \otimes \boldsymbol{a}_0 \right] \right] \Big] + \left[\boldsymbol{F} \otimes \boldsymbol{a}_0 \cdot \boldsymbol{F}^{\mathrm{t}} \right] : \Big[\boldsymbol{I} \underline{\otimes} \left[\boldsymbol{I} \overline{\otimes} \left[\boldsymbol{a}_t \otimes \boldsymbol{a}_0 \right] \right] \Big] \Big] : \frac{\partial \boldsymbol{\Lambda}}{\partial \boldsymbol{\Upsilon}}. \tag{3.97}$$

Therein, the sensitivities of the kinematic quantities with respect to the deformation gradient as well as to the second gradient of the placement function are

$$\frac{\partial \boldsymbol{C}^{-1}}{\partial \boldsymbol{F}} = \frac{\partial \boldsymbol{C}^{-1}}{\partial \boldsymbol{C}} : \frac{\partial \boldsymbol{C}}{\partial \boldsymbol{F}} \tag{3.98}$$

with

$$\frac{\partial \boldsymbol{C}^{-1}}{\partial \boldsymbol{C}} = -\tfrac{1}{2} \left[\boldsymbol{C}^{-1} \overline{\otimes} \boldsymbol{C}^{-1} + \boldsymbol{C}^{-1} \underline{\otimes} \boldsymbol{C}^{-1} \right], \quad \frac{\partial \boldsymbol{C}}{\partial \boldsymbol{F}} = \boldsymbol{I} \underline{\otimes} \boldsymbol{F}^{\mathrm{t}} + \boldsymbol{F}^{\mathrm{t}} \overline{\otimes} \boldsymbol{I}, \tag{3.99}$$

as well as

$$\begin{aligned} \frac{\partial \boldsymbol{\Lambda}}{\partial \boldsymbol{F}} = {} & \boldsymbol{I} \underline{\otimes} \left[\boldsymbol{a}_0 \cdot \left[\boldsymbol{I} \underline{\otimes} \boldsymbol{I} \right] : \boldsymbol{\Upsilon} \right] : \left[\boldsymbol{I} \underline{\otimes} \boldsymbol{I} \right] \\ & + \boldsymbol{I} \underline{\otimes} \left[\left[\boldsymbol{F} \cdot \nabla_{\boldsymbol{X}} \boldsymbol{a}_0 \right] : \left[\boldsymbol{I} \underline{\otimes} \boldsymbol{I} \right] \right] + \boldsymbol{F}^{\mathrm{t}} \overline{\otimes} \left[\nabla_{\boldsymbol{X}} \boldsymbol{a}_0 \right]^{\mathrm{t}}, \end{aligned} \tag{3.100}$$

$$\frac{\partial \boldsymbol{G}}{\partial \boldsymbol{F}} = \boldsymbol{I} \overline{\otimes} \left[\nabla_{\boldsymbol{X}} \boldsymbol{a}_0 \right]^{\mathrm{t}}, \tag{3.101}$$

$$\frac{\partial J^{-1}}{\partial \boldsymbol{F}} = -J^{-1} \boldsymbol{F}^{-\mathrm{t}}, \quad \frac{\partial I_3}{\partial \boldsymbol{F}} = 2\, I_3\, \boldsymbol{F}^{-\mathrm{t}}, \quad \frac{\partial \boldsymbol{a}_t}{\partial \boldsymbol{F}} = \boldsymbol{I} \otimes \boldsymbol{a}_0, \tag{3.102}$$

$$\frac{\partial \boldsymbol{C}}{\partial \boldsymbol{\Upsilon}} = \boldsymbol{0}, \quad \frac{\partial \boldsymbol{G}}{\partial \boldsymbol{\Upsilon}} = \boldsymbol{I} \overline{\otimes} \boldsymbol{I} \overline{\otimes} \boldsymbol{a}_0, \quad \frac{\partial \boldsymbol{\Lambda}}{\partial \boldsymbol{\Upsilon}} = \boldsymbol{F}^{\mathrm{t}} \overline{\otimes} \boldsymbol{I} \overline{\otimes} \boldsymbol{a}_0. \tag{3.103}$$

B.2 Aspects on geometry and discretisation in IGA

All geometric representations in Sect. 3.1 and Sect. 3.2 are based on NURBS, respectively B-Splines. In the subsequent sections, the underlying knot vectors and control points are denoted and information on the polynomial degrees of the basis functions is provided.

B.2.1 Cylindrical tube

In contrast to the representation with non-rational B-Splines, a circle can be exactly constructed by using NURBS. The main idea is to select a set of control points and to calculate the corresponding weights by ensuring that the requirement

$$x_1^2 + x_2^2 = r^2 \tag{3.104}$$

is fulfilled for every point (x_1, x_2) of the circle with radius r. A full circle can be constructed from a quarter or half circle representation by connecting either four quarter-

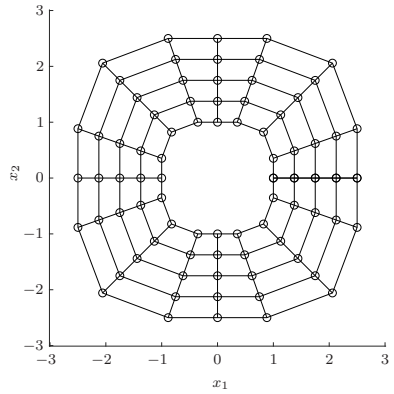

(a) Control mesh with $\mathrm{n_{cp}} = 85$.

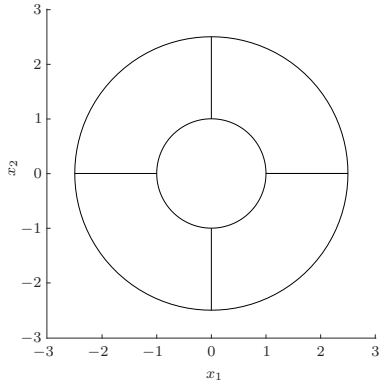

(b) Coarsest physical mesh with $\mathrm{n_{el}} = 4$.

Figure 3.27: Control mesh and coarsest physical mesh of the cylindrical tube.

or two half circle curves by means of multiply occurring knots [128]. For the cylindrical tube model employed in Sect. 3.1.4.2 and Sect. 3.2.4.2, a polynomial degree of $p = 4$ is chosen such that the (open) knot vector for the complete circle follows as

$$\Xi = \{0, 0, 0, 0, 0, \tfrac{1}{4}, \tfrac{1}{4}, \tfrac{1}{4}, \tfrac{1}{4}, \tfrac{1}{2}, \tfrac{1}{2}, \tfrac{1}{2}, \tfrac{1}{2}, \tfrac{3}{4}, \tfrac{3}{4}, \tfrac{3}{4}, \tfrac{3}{4}, 1, 1, 1, 1, 1\}. \tag{3.105}$$

For the two-dimensional isogeometric analysis, the knot vector for the second parametric direction is added on the basis of the same polynomial degree $q = 4$, accordingly

$$\mathcal{H} = \{0, 0, 0, 0, 0, 1, 1, 1, 1, 1\}. \tag{3.106}$$

The number of control points for the coarsest mesh of the cylindrical tube is $\mathrm{n_{cp}} = \mathrm{n} \cdot \mathrm{m} = 85$ since the control mesh consists of $\mathrm{m} = 5$ curves containing $\mathrm{n} = 17$ control points each. The control points $[\boldsymbol{B}_i]_j$ in the j^{th} curve are given by

$$[\boldsymbol{B}]_j = c_j \begin{bmatrix} 1.0 & 1.0 & 0.823 & 0.354 & 0.0 & -0.354 & -0.823 & -1.0 \\ 0.0 & -0.354 & -0.823 & -1.0 & -1.0 & -1.0 & -0.823 & -0.354 \end{bmatrix}$$
$$\begin{bmatrix} -1.0 & -1.0 & -0.823 & -0.354 & 0.0 & 0.354 & 0.823 & 1.0 & 1.0 \\ 0.0 & 0.354 & 0.823 & 1.0 & 1.0 & 1.0 & 0.823 & 0.354 & 0.0 \end{bmatrix}^{\mathrm{t}} \tag{3.107}$$

with $c_j \in \{1.0, 1.375, 1.75, 2.125, 2.5\}$ and $j = 1, \ldots, \mathrm{m}$. The corresponding weights are

$$[w]_j = \begin{bmatrix} 1.0 & 1.0 & 0.943 & 1.0 & 1.0 & 1.0 & 0.943 & 1.0 \\ 1.0 & 1.0 & 0.943 & 1.0 & 1.0 & 1.0 & 0.943 & 1.0 & 1.0 \end{bmatrix}^{\mathrm{t}} \tag{3.108}$$

and are the same for every curve.

With these quantities at hand, the control mesh in Fig. 3.27a is obtained for the two-dimensional tube. The physical mesh results from application of the NURBS basis

functions according to (2.7) and is shown in Fig. 3.27b. While this figure represents the coarsest mesh for the geometry under investigation, strategies for mesh refinement, cf. Sect. 2.2.2, and increase of continuity, cf. Sect. 2.3.1, are applied in order to obtain the models based on which the simulations in this thesis are carried out. In particular, knot removal is performed in order to increase the continuity at locations of repeated knots in the knot vector (3.105). Thereby, the multiplicity of each of the inner knots is reduced by 1. Moreover, knot insertion is applied with the purpose of mesh refinement. In order to obtain accurate results near the inner and outer radii of the cylinder, a small mesh size is chosen particularly for these areas, see Fig. 3.2 and Fig. 3.13.

B.2.2 Cantilever beam

For the isogeometric model of the beam under investigation in Sect. 3.1.5.1, the polynomial degree of the underlying NURBS basis functions is chosen to be $p = q = 4$. The corresponding knot vectors Ξ and $\mathcal{H}$ are the same for both parametric directions and given by

$$\Xi = \mathcal{H} = \{0, 0, 0, 0, 0, 1, 1, 1, 1, 1\}. \tag{3.109}$$

Since only two distinct knot values are considered, the coarsest mesh for the beam simply consists of one finite element. In consistency with these knot vectors, the geometry model for the beam contains $\mathrm{n} = \mathrm{m} = 5$ control points in each direction so that the total number of control points is $\mathrm{n_{cp}} = \mathrm{n} \cdot \mathrm{m} = 25$. The control point coordinates are

$$\boldsymbol{B} = \begin{bmatrix} 0.0 & 25 & 50 & 75 & 100 & 0.0 & 25 & 50 & 75 & 100 & 0.0 & 25 & 50 & 75 \\ 0.0 & 0.0 & 0.0 & 0.0 & 0.0 & 2.5 & 2.5 & 2.5 & 2.5 & 2.5 & 5.0 & 5.0 & 5.0 & 5.0 \\ 100 & 0.0 & 25 & 50 & 75 & 100 & 0.0 & 25 & 50 & 75 & 100 \\ 5.0 & 7.5 & 7.5 & 7.5 & 7.5 & 7.5 & 10.0 & 10.0 & 10.0 & 10.0 & 10.0 \end{bmatrix}^{\mathrm{t}} \tag{3.110}$$

and all weights are equal to 1.0. Accordingly, the underlying NURBS basis functions become B-Splines, i.e. piecewise polynomials [40, 80]. The resulting control mesh and physical mesh are presented in Fig. 3.28. The refined mesh in Fig. 3.7 which is employed

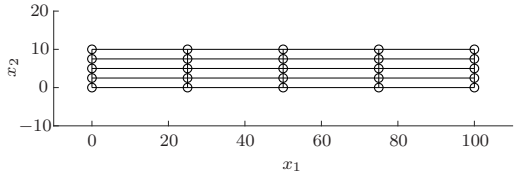

(a) Control mesh with $\mathrm{n_{cp}} = 25$. Reproduced from [170] under the terms of the Creative Commons Attribution 4.0 International License (CC BY 4.0).

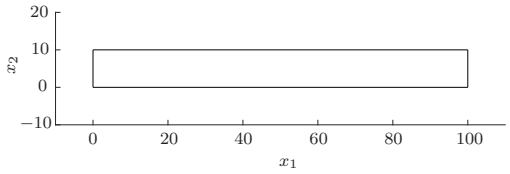

(b) Coarsest physical mesh with $\mathrm{n_{el}} = 1$.

Figure 3.28: Control mesh and coarsest physical mesh of the beam.

for the simulations carried out in this work, is obtained by means of knot insertion in both parametric directions according to the procedure described in Sect. 2.2.2.

B.2.3 Notched plate

The two-dimensional notched plate introduced in Sect. 3.2.5.1 is based on NURBS basis functions with polynomial degree $p = q = 4$. The knot vectors for this model can be written as

$$\begin{aligned}\Xi = \{&0,0,0,0,0,0.0303,0.0606,0.0909,0.1212,0.1515,0.1818,0.2121,0.2424,\\ &0.2727,0.3030,0.3333,0.3636,0.3939,0.4242,0.4545,0.4848,0.5152,\\ &0.5455,0.5758,0.6061,0.6364,0.6667,0.6970,0.7273,0.7576,0.7879,\\ &0.8182,0.8485,0.8788,0.9091,0.9394,0.9697,1,1,1,1,1\}, \qquad (3.111)\\ \mathcal{H} = \{&0,0,0,0,0,1,1,1,1,1\}. \qquad (3.112)\end{aligned}$$

Accordingly, the coarsest mesh of the plate includes $\mathrm{n_{cp}} = \mathrm{n}\cdot\mathrm{m} = 185$ control points where $\mathrm{n} = 37$ and $\mathrm{m} = 5$. The control points $[\boldsymbol{B}]_j$ for the first curve with $j = 1$ read

$$\begin{aligned}[\boldsymbol{B}]_1 = \begin{bmatrix} -60.0 & -50.0 & -40.0 & -35.0 & -34.0 & -30.0 & -25.0 & -15.0 & -13.7 \\ -8.0 & -8.0 & -8.0 & -8.0 & -6.0 & -6.0 & -6.0 & -6.0 & -6.0 \end{bmatrix}\\ \begin{bmatrix} -13.5 & -11.909 & -9.795 & -9.0 & -8.205 & -6.091 & -4.5 & -4.3 \\ -4.409 & -2.295 & -1.5 & -1.5 & -1.5 & -2.295 & -4.409 & -6.0 \end{bmatrix}\\ \begin{bmatrix} -3.0 & 0.0 & 3.0 & 4.3 & 4.5 & 6.091 & 8.205 & 9.0 & 9.795 & 11.909 \\ -6.0 & -6.0 & -6.0 & -6.0 & -6.0 & -6.0 & -6.0 & -6.0 & -6.0 & -6.0 \end{bmatrix}\\ \begin{bmatrix} 13.5 & 13.7 & 15.0 & 25.0 & 30.0 & 34.0 & 35.0 & 40.0 & 50.0 & 60.0 \\ -6.0 & -6.0 & -6.0 & -6.0 & -6.0 & -6.0 & -8.0 & -8.0 & -8.0 & -8.0 \end{bmatrix}^{\mathrm{t}} \qquad (3.113)\end{aligned}$$

whereas the last curve with $j = 5$ is represented by the control points

$$\begin{aligned}[\boldsymbol{B}]_5 = \begin{bmatrix} -60.0 & -50.0 & -40.0 & -35.0 & -34.0 & -30.0 & -25.0 & -15.0 & -13.7 \\ 8.0 & 8.0 & 8.0 & 8.0 & 6.0 & 6.0 & 6.0 & 6.0 & 6.0 \end{bmatrix}\\ \begin{bmatrix} -13.5 & -11.909 & -9.795 & -9.0 & -8.205 & -6.091 & -4.5 & -4.3 \\ 6.0 & 6.0 & 6.0 & 6.0 & 6.0 & 6.0 & 6.0 & 6.0 \end{bmatrix}\\ \begin{bmatrix} -3.0 & 0.0 & 3.0 & 4.3 & 4.5 & 6.091 & 8.205 & 9.0 & 9.795 & 11.909 \\ 6.0 & 6.0 & 6.0 & 6.0 & 4.409 & 2.295 & 1.5 & 1.5 & 1.5 & 2.295 \end{bmatrix}\\ \begin{bmatrix} 13.5 & 13.7 & 15.0 & 25.0 & 30.0 & 34.0 & 35.0 & 40.0 & 50.0 & 60.0 \\ 4.409 & 6.0 & 6.0 & 6.0 & 6.0 & 6.0 & 8.0 & 8.0 & 8.0 & 8.0 \end{bmatrix}^{\mathrm{t}}. \qquad (3.114)\end{aligned}$$

For $j = 2, \ldots, 4$ the remaining controls points are obtained using

$$[\boldsymbol{B}]_j = \begin{bmatrix} -60.0 & -50.0 & -40.0 & -35.0 & -34.0 & -30.0 & -25.0 & -15.0 & -13.7 \\ \alpha_j & \alpha_j & \alpha_j & \alpha_j & \alpha_j & \alpha_j & \alpha_j & \alpha_j & \alpha_j \\ -13.5 & -11.909 & -9.795 & -9.0 & -8.205 & -6.091 & -4.5 & -4.3 & \\ \alpha_j & \alpha_j & \alpha_j & \alpha_j & \alpha_j & \alpha_j & \alpha_j & \alpha_j & \\ -3.0 & 0.0 & 3.0 & 4.3 & 4.5 & 6.091 & 8.205 & 9.0 & 9.795 & 11.909 \\ \alpha_j & \alpha_j & \alpha_j & \alpha_j & \alpha_j & \alpha_j & \alpha_j & \alpha_j & \alpha_j & \alpha_j \\ 13.5 & 13.7 & 15.0 & 25.0 & 30.0 & 34.0 & 35.0 & 40.0 & 50.0 & 60.0 \\ \alpha_j & \alpha_j & \alpha_j & \alpha_j & \alpha_j & \alpha_j & \alpha_j & \alpha_j & \alpha_j & \alpha_j \end{bmatrix}^{\mathrm{t}} \tag{3.115}$$

with constants $\alpha_2 = -0.5, \alpha_3 = 0.0$ and $\alpha_4 = 0.5$. The corresponding control point weights are all 1.0 except for $[w_{11}]_1 = [w_{15}]_1 = [w_{23}]_5 = [w_{27}]_5 = 0.9428$ where the first index correlates with the i^{th} curve in ξ-direction and the second index represents the j^{th} curve in η-direction in consistency with the definitions in (2.6) and (2.8). In Fig. 3.29, the resulting control mesh for the notched plate is shown together with the coarsest physical mesh. By application of knot insertion, cf. Sect. 2.2.2, the refined mesh in Fig. 3.17 is obtained.

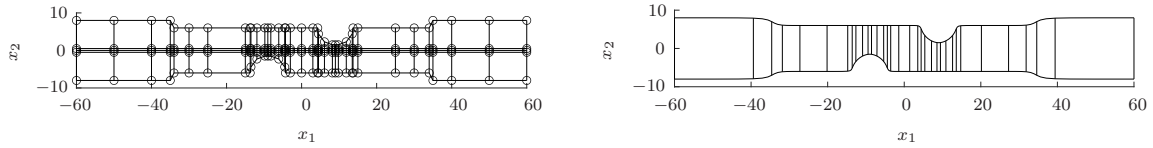

(a) Control mesh with $\mathrm{n_{cp}} = 185$.

(b) Coarsest physical mesh with $\mathrm{n_{el}} = 33$.

Figure 3.29: Control mesh and coarsest physical mesh of the notched plate.

B.3 Convergence study

The results for the cylindrical tube, presented in Sect. 3.1.4.3 for the proposed small strain IGA framework, are obtained with a discretisation based on $\mathrm{n_{el}} = 6912$ elements. The corresponding physical mesh is shown in Fig. 3.2. In order to investigate the convergence behaviour of the isogeometric finite element method with regard to the particular boundary value problem under consideration, two additional discretisations are taken into account. In Fig. 3.30a, the mesh consists of $\mathrm{n_{el}} = 1856$ elements with an element size that is approximately twice as large in both parametric directions compared to the original mesh in Fig. 3.2. In Fig. 3.30b, an even coarser mesh with $\mathrm{n_{el}} = 272$ elements is considered. Similar to the results from Fig. 3.4a and 3.6a, the respective stress and couple-stress coefficients obtained from simulations with the discretisation containing $\mathrm{n_{el}} = 1856$ elements are shown in Fig. 3.31. Analogously, Fig. 3.32 presents the results for the mesh including $\mathrm{n_{el}} = 272$ elements. For a direct comparison, the results for the dimensionless stress coefficient $[\sigma_{\varphi r}]^*$ are additionally provided in Fig. 3.33 for all three discretisations in one plot. The dimensionless material parameter which is related to the length scale is chosen to be $\lambda^* = 0.1$ in this case. By comparing the different graphs, it

can be concluded that the solution converges for a sufficiently fine discretisation. From Fig. 3.33 it can be observed that the graphs for the two finer meshes almost coincide while the results for the mesh with $n_{el} = 272$ elements differ slightly in the boundary regions of the domain. For this discretisation, a non-smooth behaviour can be noted especially at the inner radius, which vanishes as the mesh size decreases. In the interior of the cylindrical tube, the analysis yields an accurate solution already for a coarse mesh.

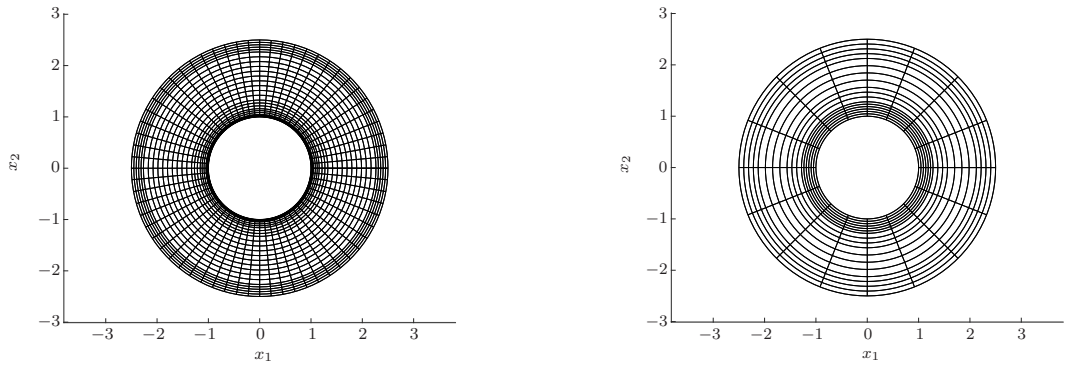

(a) Refined mesh with $n_{cp} = 2442$ and $n_{el} = 1856$.

(b) Refined mesh with $n_{cp} = 572$ and $n_{el} = 272$.

Figure 3.30: IGA discretisation of the cylindrical tube with 272 respectively 1856 elements. Reproduced from [170] under the terms of the Creative Commons Attribution 4.0 International License (CC BY 4.0).

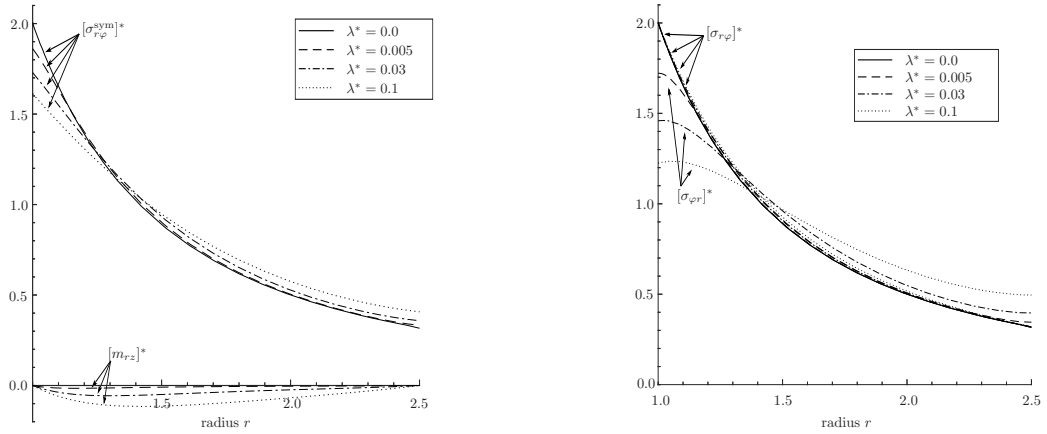

(a) Distribution of the dimensionless stress coefficient $[\sigma_{r\varphi}^{\mathrm{sym}}]^*$ and couple-stress coefficient $[m_{rz}]^*$, $n_{el} = 1856$.

(b) Distribution of the dimensionless stress coefficients $[\sigma_{r\varphi}]^*$ and $[\sigma_{\varphi r}]^*$, $n_{el} = 1856$.

Figure 3.31: Distribution of the dimensionless stress and couple-stress coefficients for the discretisation containing 1856 elements. Reproduced from [170] under the terms of the Creative Commons Attribution 4.0 International License (CC BY 4.0).

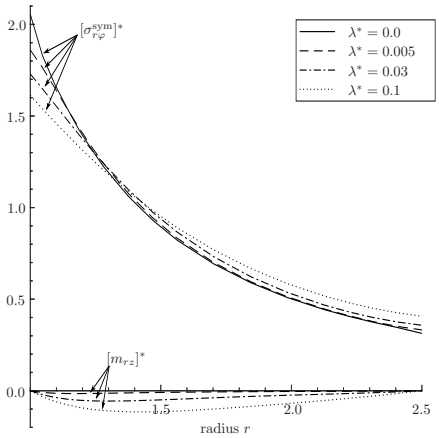

(a) Distribution of the dimensionless stress coefficient $[\sigma^{\mathrm{sym}}_{r\varphi}]^*$ and couple-stress coefficient $[m_{rz}]^*$, $\mathrm{n_{el}} = 272$.

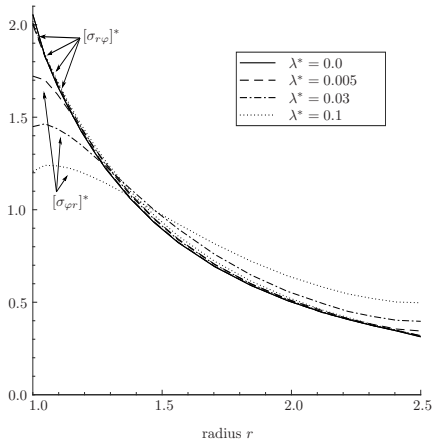

(b) Distribution of the dimensionless stress coefficients $[\sigma_{r\varphi}]^*$ and $[\sigma_{\varphi r}]^*$, $\mathrm{n_{el}} = 272$.

Figure 3.32: Distribution of the dimensionless stress and couple-stress coefficients for the discretisation containing 272 elements. Reproduced from [170] under the terms of the Creative Commons Attribution 4.0 International License (CC BY 4.0).

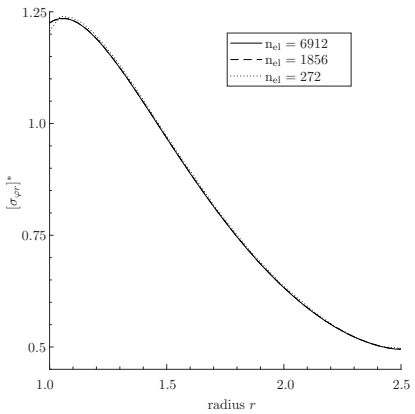

Figure 3.33: Distribution of the dimensionless stress coefficient $[\sigma_{\varphi r}]^*$ for different discretisations and for $\lambda^* = 0.1$. Reproduced from [170] under the terms of the Creative Commons Attribution 4.0 International License (CC BY 4.0).

4 Flexoelectricity-induced bone remodelling and microcrack healing

In experimental studies on cortical bone, evidence has been provided that flexoelectricity acts as an initiator for bone remodelling processes and thereby promotes crack healing [120, 164]. Due to its size dependency, the flexoelectric effect is most relevant on the micro and nano scale and accordingly, a significant impact of this electromechanical phenomenon is expected on the healing of microcracks in bones. In this chapter, a numerical framework for the investigation of flexoelectricity is presented in Sect. 4.1 and applied to a representative numerical example in order to compare the results with an analytical solution for validation purposes. In Sect. 4.2, the process of bone remodelling is discussed in detail with particular focus on its flexoelectric initiation. A modelling approach for the initiation of bone remodelling is presented in Sect. 4.3. To be precise, the model accounts for the flexoelectric and piezoelectric properties of the cortical bone material and for the diffusion of bone cells in a numerical framework with chemo-electro-mechanical coupling. In Sect. 4.4, this framework is extended towards the complete flexoelectricity-induced bone remodelling process including crack healing.

The main features of this chapter are summarised in the following:

- a globally C^1-continuous IGA framework for the simulation of (piezoelectric and) flexoelectric effects in solids in a small strain setting
- validation by comparison with an analytical solution
- a chemo-electro-mechanically coupled modelling approach for the initiation of bone remodelling by flexoelectricity-induced osteocyte apoptosis
- incorporation of non-linear diffusion equations to account for the anisotropic diffusion of bone cells towards crack surfaces
- a cell flux-driven surface growth mechanism to simulate crack healing
- successive regeneration of the osteocyte field during the healing process

4.1 Flexoelectricity

From a physics point of view, flexoelectricity describes the electric polarisation of dielectric materials due to strain gradients. The flexoelectric contribution to the polarisation vector $\boldsymbol{p}$ can thus be expressed as

$$\boldsymbol{p}_{\text{flexo}} = \boldsymbol{\mu} :\cdot \nabla_{\boldsymbol{x}} \boldsymbol{\varepsilon} \tag{4.1}$$

when linear relations are considered, see [1]. Therein, $\boldsymbol{\varepsilon}$ denotes the small strain tensor and $\boldsymbol{\mu}$ is the so-called *flexoelectricity tensor* which is of fourth order. In accordance with the symmetries of the strain gradients $\nabla_{\boldsymbol{x}} \boldsymbol{\varepsilon}$, the flexoelectricity tensor possesses symmetry on the second and third index. Accordingly, 54 non-zero, independent coefficients remain present for this fourth-order tensor, in general. Depending on the particular symmetries of the underlying material, the number of relevant flexoelectric coefficients can be further reduced. A detailed discussion on the symmetries of the flexoelectricity tensor in crystalline solids is provided in [146].

As a direct consequence of the gradient contributions, particularly the strain gradients in relation (4.1), it becomes apparent that flexoelectricity is a size-dependent phenomenon. To be precise, its relevance increases on small scales. Since piezoelectricity, on the other hand, is not size-dependent, the influence of flexoelectricity in devices which are also piezoelectric becomes dominant on the micro and nano scale, whereas at larger scales the piezoelectric effect generally exceeds the flexoelectric one.

Besides the direct flexoelectric effect, which causes strain gradients to evoke electric polarisation and accordingly induce an electric field, inverse and converse effects also exist. They describe the generation of strain gradients due to a prescribed polarisation, and of stresses due to an external electric field gradient, respectively [37]. It is noted that the distinction between the direct and converse effect is not trivial as discussed in detail in, e.g., [36, 143]. More specifically speaking, the converse effect may be included in the formulation for direct flexoelectricity by considering different flexoelectric coefficients and additional higher-order boundary conditions.

Whereas relation (4.1) has been introduced for a small-strain theory, an extension to finite strains has been studied intensively in the literature as well, see, e.g., [35, 48, 115, 159, 177]. These investigations are particularly important for the analysis of soft dielectrics. In the present contribution, however, small strains are considered.

4.1.1 Balance equations

In order to simulate flexoelectric effects in solid materials, a modelling approach including electromechanical coupling is taken into account. In this section, the thermodynamic framework is established including the relevant balance equations as well as the dissipation inequality. Particular focus lies on different choices of thermodynamic potentials.

4.1.1.1 Electromechanical coupling

The balance equations for the electromechanical coupling under consideration are the (static form of) balance of linear momentum and Gauss's law for dielectrics, i.e. in the absence of free charges. Accordingly,

$$\mathbf{0} = \nabla_{\boldsymbol{x}} \cdot \boldsymbol{\sigma}_{\mathrm{tot}} + \rho\, \boldsymbol{b} \qquad \text{in} \quad \Omega \tag{4.2}$$

$$0 = \nabla_{\boldsymbol{x}} \cdot \boldsymbol{d} \qquad \text{in} \quad \Omega \tag{4.3}$$

hold in the domain Ω with mass density ρ. With the polarisation vector (4.1) at hand, the dielectric displacement vector in (4.3) takes the form

$$\boldsymbol{d} = \boldsymbol{p} + \epsilon_0\, \boldsymbol{e} \tag{4.4}$$

where the second term includes the electric field vector $\boldsymbol{e}$ and the permittivity of free space specified as $\epsilon_0 \approx 8.854 \times 10^{-12}\,\mathrm{Fm}^{-1}$. In the balance of linear momentum (4.2), mechanical body forces $\boldsymbol{b}$ are neglected as this works proceeds. Moreover, the total stress tensor $\boldsymbol{\sigma}_{\mathrm{tot}}$ contains contributions from the standard Cauchy-type stress tensor $\boldsymbol{\sigma}$ which is the dual quantity to strain tensor $\boldsymbol{\varepsilon}$ and from the so-called *hyper-stress tensor* $\boldsymbol{\pi}$ which is dual to the strain gradient tensor $\nabla_{\boldsymbol{x}}\boldsymbol{\varepsilon}$. The latter originates from the strain gradient theory and is also referred to as *double stress tensor* [106, 109]. The total stress tensor accordingly follows as

$$\boldsymbol{\sigma}_{\mathrm{tot}} = \boldsymbol{\sigma} - \nabla_{\boldsymbol{x}} \cdot \boldsymbol{\pi}. \tag{4.5}$$

As a consequence, (4.2) is a partial differential equation of up to fourth order, in general, depending on the particular constitutive model at hand. The underlying kinematic relations concern the strains

$$\boldsymbol{\varepsilon} = \frac{1}{2}\left[\nabla_{\boldsymbol{x}}\boldsymbol{u} + [\nabla_{\boldsymbol{x}}\boldsymbol{u}]^{\mathrm{t}}\right] \tag{4.6}$$

derived from the displacement field $\boldsymbol{u}$, and the electric field

$$\boldsymbol{e} = -\nabla_{\boldsymbol{x}}\phi \tag{4.7}$$

as a function of the electric potential ϕ.

4.1.1.2 Balance of energy

The integral form of the balance of energy states that the total rate of internal and kinetic energy equals the sum of all external power contributions. For the electromechanical coupling considered in this work, a formulation including the electric enthalpy instead of

the internal energy as thermodynamic potential is adopted, so that the balance equation reads

$$\dot{\mathcal{H}} + \dot{\mathcal{K}} = \mathcal{P}_{\text{mech}} + \mathcal{P}_{\text{elec}} + \mathcal{Q}_{\text{therm}}. \tag{4.8}$$

Therein, the rate of electric enthalpy

$$\dot{\mathcal{H}} = \frac{\mathrm{d}}{\mathrm{d}t} \int_{\Omega} \rho\, H \,\mathrm{d}v \tag{4.9}$$

is employed with the (mass-specific) electric enthalpy density H.

The rate of kinetic energy in balance equation (4.8) can be expressed as

$$\dot{\mathcal{K}} = \frac{1}{2} \frac{\mathrm{d}}{\mathrm{d}t} \int_{\Omega} \rho\, \dot{\boldsymbol{u}} \cdot \dot{\boldsymbol{u}} \,\mathrm{d}v \tag{4.10}$$

with velocity $\dot{\boldsymbol{u}}$.

For the external mechanical power, different contributions are considered which are in line with strain-gradient theories as derived in [106, 109], i.e.

$$\mathcal{P}_{\text{mech}} = \int_{\Omega} \dot{\boldsymbol{u}} \cdot \rho\, \boldsymbol{b} \,\mathrm{d}v + \int_{\partial\Omega} \dot{\boldsymbol{u}} \cdot \boldsymbol{t} \,\mathrm{d}a + \int_{\partial\Omega} [\nabla_{\boldsymbol{x}} \dot{\boldsymbol{u}} \cdot \boldsymbol{n}] \cdot \boldsymbol{r} \,\mathrm{d}a + \oint_{\mathcal{C}} \dot{\boldsymbol{u}} \cdot [\![\boldsymbol{\tau}]\!] \,\mathrm{d}s \tag{4.11}$$

with the jump operator $[\![\bullet]\!]$ and with three different surface- and line-distributed forces, namely

$$\boldsymbol{t} = \boldsymbol{\sigma} \cdot \boldsymbol{n} - [\nabla_{\boldsymbol{x}} \cdot \boldsymbol{\pi}] \cdot \boldsymbol{n} + [\nabla^s_{\boldsymbol{x}} \cdot \boldsymbol{n}] \, [\boldsymbol{\pi} : [\boldsymbol{n} \otimes \boldsymbol{n}]] - \nabla^s_{\boldsymbol{x}} \cdot [\boldsymbol{\pi} \cdot \boldsymbol{n}] \,, \tag{4.12}$$

$$\boldsymbol{r} = \boldsymbol{\pi} : [\boldsymbol{n} \otimes \boldsymbol{n}] \,, \tag{4.13}$$

$$\boldsymbol{\tau} = \boldsymbol{\pi} : [\boldsymbol{m} \otimes \boldsymbol{n}] \,. \tag{4.14}$$

These include the surface outward normal unit vector $\boldsymbol{n}$ and the corresponding co-normal vector $\boldsymbol{m} = \boldsymbol{n} \cdot [\boldsymbol{s} \cdot \boldsymbol{\epsilon}]$. Vector $\boldsymbol{s}$ is the tangent vector to the boundary curve $\mathcal{C}$ and $\boldsymbol{\epsilon}$ is the third-order permutation tensor. The surface divergence in (4.12) is defined as

$$\nabla^s_{\boldsymbol{x}} \cdot (\bullet) = \nabla^s_{\boldsymbol{x}} (\bullet) : \boldsymbol{I} = [\nabla_{\boldsymbol{x}} \bullet - \boldsymbol{n} \otimes [\boldsymbol{n} \cdot \nabla_{\boldsymbol{x}} \bullet]] : \boldsymbol{I}. \tag{4.15}$$

By using the divergence theorem on the surface integrals as well as Stoke's theorem on the line integral in (4.11), the external mechanical power can be expressed in the form

$$\begin{aligned} \mathcal{P}_{\text{mech}} = &\int_{\Omega} \dot{\boldsymbol{u}} \cdot [\rho\, \boldsymbol{b} + \nabla_{\boldsymbol{x}} \cdot [\boldsymbol{\sigma} - \nabla_{\boldsymbol{x}} \cdot \boldsymbol{\pi}]] \,\mathrm{d}v \\ &+ \int_{\Omega} \nabla_{\boldsymbol{x}} \dot{\boldsymbol{u}} : \boldsymbol{\sigma} \,\mathrm{d}v + \int_{\Omega} \nabla_{\boldsymbol{x}} \nabla_{\boldsymbol{x}} \dot{\boldsymbol{u}} :\cdot \boldsymbol{\pi} \,\mathrm{d}v. \end{aligned} \tag{4.16}$$

More details on these derivations are provided in [106, (9.16)-(9.21)].

The external electrical power in (4.8) can be written as

$$\mathcal{P}_{\text{elec}} = -\int_{\partial\Omega} \dot{\phi}\, \omega \,\mathrm{d}a \tag{4.17}$$

with $\omega = -\boldsymbol{d}\cdot\boldsymbol{n}$ representing the electric charge density at the boundary. Application of the divergence theorem yields

$$\mathcal{P}_{\text{elec}} = \int_{\partial\Omega} \dot{\phi}\,[\boldsymbol{d}\cdot\boldsymbol{n}]\,\mathrm{d}a = \int_{\Omega} \dot{\phi}\,[\nabla_{\boldsymbol{x}}\cdot\boldsymbol{d}]\,\mathrm{d}v + \int_{\Omega} \nabla_{\boldsymbol{x}}\dot{\phi}\cdot\boldsymbol{d}\,\mathrm{d}v. \tag{4.18}$$

For the external thermal power, the heat flux vector $\boldsymbol{q}_{\text{th}} = -k_{\text{th}}\,\nabla_{\boldsymbol{x}}\theta$ with absolute temperature θ, thermal conductivity k_{th} and with $q_{\text{th}} = -\boldsymbol{q}_{\text{th}}\cdot\boldsymbol{n}$ is considered at the surface of the domain together with volume-specific heat sources r_{th}, i.e.

$$\mathcal{Q}_{\text{therm}} = \int_{\Omega} r_{\text{th}}\,\mathrm{d}v + \int_{\partial\Omega} q_{\text{th}}\,\mathrm{d}a = \int_{\Omega} r_{\text{th}} - \nabla_{\boldsymbol{x}}\cdot\boldsymbol{q}_{\text{th}}\,\mathrm{d}v =: \int_{\Omega} Q_{\text{th}}\,\mathrm{d}v. \tag{4.19}$$

Recapitulating (4.8) together with the above derived expressions, and using the (dynamic version of the) balance of linear momentum (4.2) as well as Gauss's law (4.3), the global form of the balance of energy takes the representation

$$\begin{aligned}\int_{\Omega} \rho\,\dot{H}\,\mathrm{d}v = &\int_{\Omega} [\nabla_{\boldsymbol{x}}\dot{\boldsymbol{u}}] : \boldsymbol{\sigma}\,\mathrm{d}v + \int_{\Omega} [\nabla_{\boldsymbol{x}}\nabla_{\boldsymbol{x}}\dot{\boldsymbol{u}}] :\cdot \boldsymbol{\pi}\,\mathrm{d}v \\ &+ \int_{\Omega} \nabla_{\boldsymbol{x}}\dot{\phi}\cdot\boldsymbol{d}\,\mathrm{d}v + \int_{\Omega} Q_{\text{th}}\,\mathrm{d}v.\end{aligned} \tag{4.20}$$

Taking into account that the stress tensor $\boldsymbol{\sigma}$ is symmetric and that the hyper-stress tensor $\boldsymbol{\pi}$ exhibits symmetry on the first two indices, use of the kinematic relation (4.6) and the irrotationality of $\boldsymbol{e}$ (4.7) stipulates the corresponding local form

$$\rho\,\dot{H} = \dot{\boldsymbol{\varepsilon}} : \boldsymbol{\sigma} + \nabla_{\boldsymbol{x}}\dot{\boldsymbol{\varepsilon}} :\cdot \boldsymbol{\pi} - \dot{\boldsymbol{e}}\cdot\boldsymbol{d} + Q_{\text{th}}. \tag{4.21}$$

4.1.1.3 Thermodynamic potentials

In Sect. 4.1.1.2, the electric enthalpy density $H(\boldsymbol{\varepsilon}, \nabla_{\boldsymbol{x}}\boldsymbol{\varepsilon}, \boldsymbol{e}, s)$ has been employed in the balance of energy (4.8). However, other choices regarding the thermodynamic potential are possible for the (thermo-)electro-mechanical coupling under consideration. All different potentials are reasonable to work with and can be transformed to each other by appropriate Legendre(-Fenchel) transformations. Specifically speaking, the free electric enthalpy density H^* is obtained from the relation

$$H^*(\boldsymbol{\varepsilon},\nabla_{\boldsymbol{x}}\boldsymbol{\varepsilon}, \boldsymbol{e}, \theta) = \min_{s}\{H(\boldsymbol{\varepsilon}, \nabla_{\boldsymbol{x}}\boldsymbol{\varepsilon}, \boldsymbol{e}, s) - \theta\, s\} \tag{4.22}$$

including temperature θ as primary variable instead of its dual quantity, i.e. the mass-specific entropy density s.

Furthermore, the free energy densities ψ and $\widetilde{\psi}$ are related to the free electric enthalpy density according to

$$\rho\, H^*(\boldsymbol{\varepsilon},\nabla_{\boldsymbol{x}}\boldsymbol{\varepsilon},\boldsymbol{e},\theta) = \min_{\boldsymbol{d}}\{\rho\,\psi(\boldsymbol{\varepsilon},\nabla_{\boldsymbol{x}}\boldsymbol{\varepsilon},\boldsymbol{d},\theta) - \boldsymbol{e}\cdot\boldsymbol{d}\} \tag{4.23}$$

$$= \min_{\boldsymbol{p}}\{\rho\,\widetilde{\psi}(\boldsymbol{\varepsilon},\nabla_{\boldsymbol{x}}\boldsymbol{\varepsilon},\boldsymbol{p},\theta) - \boldsymbol{e}\cdot\boldsymbol{p}\} - \tfrac{1}{2}\,\epsilon_0\,\boldsymbol{e}\cdot\boldsymbol{e} \tag{4.24}$$

and take the dielectric displacements or the polarisation as arguments, respectively. The equality of the two formulations on the right-hand side of (4.23)-(4.24) can be verified using relation (4.4). In most literature on flexoelectricity, either the polarisation is employed as primary variable, see [95, 98, 143], or the electric field is considered such as in [1, 69, 115] and in the present contribution. Further details on the different thermodynamic potentials in the context of electromechanical coupling can be found in, e.g., [149].

4.1.1.4 Dissipation inequality

With the different thermodynamic potentials in mind, the dissipation inequality is derived in the following considering the full coupling of mechanical, thermal and electrical contributions. Starting with the classic inequality in form of

$$\dot{\mathcal{S}} - \mathcal{R}_{\text{ext}} \geq 0 \tag{4.25}$$

with

$$\dot{\mathcal{S}} = \int_\Omega \rho\,\dot{s}\,\mathrm{d}v, \tag{4.26}$$

$$\mathcal{R}_{\text{ext}} = \int_\Omega \frac{r_{\text{th}}}{\theta}\,\mathrm{d}v + \int_{\partial\Omega} \frac{\overline{q}_{\text{th}}}{\theta}\,\mathrm{d}a = \int_\Omega R_{\text{ext}}\,\mathrm{d}v, \tag{4.27}$$

$$R_{\text{ext}} = \frac{1}{\theta}\left[r_{\text{th}} - \nabla_{\boldsymbol{x}}\cdot\boldsymbol{q}_{\text{th}} + \boldsymbol{q}_{\text{th}}\cdot\nabla_{\boldsymbol{x}}\ln(\theta)\right] = \frac{Q_{\text{th}} + \boldsymbol{q}_{\text{th}}\cdot\nabla_{\boldsymbol{x}}\ln(\theta)}{\theta}, \tag{4.28}$$

it is provided that the total rate of entropy $\dot{\mathcal{S}}$ is larger than or equal to the external entropy supply $\mathcal{R}_{\text{ext}}$ induced by heat sources and fluxes. Localising (4.25) gives rise to the Clausius-Duhem inequality

$$\underbrace{\rho\,\theta\,\dot{s} - Q_{\text{th}} - \boldsymbol{q}_{\text{th}}\cdot\nabla_{\boldsymbol{x}}\ln(\theta)}_{=:\mathcal{D}} \geq 0. \tag{4.29}$$

Under the use of the local form of balance of energy (4.21), it is observed that Q_{th} can be expressed as

$$Q_{\text{th}} = \rho\,\dot{H} - \dot{\boldsymbol{\varepsilon}} : \boldsymbol{\sigma} - \nabla_{\boldsymbol{x}}\dot{\boldsymbol{\varepsilon}} :\cdot \boldsymbol{\pi} + \dot{\boldsymbol{e}} \cdot \boldsymbol{d}. \tag{4.30}$$

By applying a Legendre(-Fenchel) transformation with respect to temperature θ and entropy density s according to (4.22), the time derivative of the electric enthalpy density in (4.30) can be expressed as

$$\dot{H} = \frac{\partial H^*}{\partial \boldsymbol{\varepsilon}} : \dot{\boldsymbol{\varepsilon}} + \frac{\partial H^*}{\partial \nabla_{\boldsymbol{x}}\boldsymbol{\varepsilon}} :\cdot \nabla_{\boldsymbol{x}}\dot{\boldsymbol{\varepsilon}} + \frac{\partial H^*}{\partial \boldsymbol{e}} \cdot \dot{\boldsymbol{e}} + \frac{\partial H^*}{\partial \theta}\,\dot{\theta} + \theta\,\dot{s} + s\,\dot{\theta}. \tag{4.31}$$

The Clausius-Duhem inequality (4.29) accordingly takes the form

$$\begin{aligned}\mathcal{D} = &-\rho\left[\frac{\partial H^*}{\partial \boldsymbol{\varepsilon}} : \dot{\boldsymbol{\varepsilon}} + \frac{\partial H^*}{\partial \nabla_{\boldsymbol{x}}\boldsymbol{\varepsilon}} :\cdot \nabla_{\boldsymbol{x}}\dot{\boldsymbol{\varepsilon}} + \frac{\partial H^*}{\partial \boldsymbol{e}} \cdot \dot{\boldsymbol{e}} + \frac{\partial H^*}{\partial \theta}\,\dot{\theta}\right] - \rho\,s\,\dot{\theta} \\ &+ \dot{\boldsymbol{\varepsilon}} : \boldsymbol{\sigma} + \nabla_{\boldsymbol{x}}\dot{\boldsymbol{\varepsilon}} :\cdot \boldsymbol{\pi} - \dot{\boldsymbol{e}} \cdot \boldsymbol{d} - \boldsymbol{q}_{\text{th}} \cdot \nabla_{\boldsymbol{x}} \ln(\theta) \geq 0.\end{aligned} \tag{4.32}$$

Rearranging terms yields

$$\begin{aligned}\mathcal{D} = &\left[\boldsymbol{\sigma} - \rho\,\frac{\partial H^*}{\partial \boldsymbol{\varepsilon}}\right] : \dot{\boldsymbol{\varepsilon}} + \left[\boldsymbol{\pi} - \rho\,\frac{\partial H^*}{\partial \nabla_{\boldsymbol{x}}\boldsymbol{\varepsilon}}\right] :\cdot \nabla_{\boldsymbol{x}}\dot{\boldsymbol{\varepsilon}} + \left[-\boldsymbol{d} - \rho\,\frac{\partial H^*}{\partial \boldsymbol{e}}\right] \cdot \dot{\boldsymbol{e}} \\ &+ \left[-\rho\,s - \rho\,\frac{\partial H^*}{\partial \theta}\right]\dot{\theta} - \boldsymbol{q}_{\text{th}} \cdot \nabla_{\boldsymbol{x}} \ln(\theta) \geq 0.\end{aligned} \tag{4.33}$$

Following the procedure of Coleman and Noll, the constitutive relations are obtained as

$$\boldsymbol{\sigma} = \rho\,\frac{\partial H^*}{\partial \boldsymbol{\varepsilon}}, \quad \boldsymbol{\pi} = \rho\,\frac{\partial H^*}{\partial \nabla_{\boldsymbol{x}}\boldsymbol{\varepsilon}}, \quad \boldsymbol{d} = -\rho\,\frac{\partial H^*}{\partial \boldsymbol{e}}, \quad s = -\frac{\partial H^*}{\partial \theta}. \tag{4.34}$$

4.1.2 Isogeometric finite element formulation

For the numerical solution of the governing equations (4.2) and (4.3), a globally C^1-continuous isogeometric analysis framework is employed in order to deal with the continuity requirements that flexoelectricity sets on the underlying finite element scheme. In the following, the corresponding weak forms are derived and discretised by using NURBS as basis functions.

4.1.2.1 Weak form of the governing equations

In order to obtain a weak form of the balance of linear momentum (4.2), this equation is multiplied by virtual displacements, respectively test functions, $\delta\boldsymbol{u}$ and integrated over the domain Ω. Neglecting mechanical body forces, the corresponding weak form reads

$$0 = \int_{\Omega} \delta\boldsymbol{u} \cdot [\nabla_{\boldsymbol{x}} \cdot \boldsymbol{\sigma}]\,\mathrm{d}v - \int_{\Omega} \delta\boldsymbol{u} \cdot [\nabla_{\boldsymbol{x}} \cdot [\nabla_{\boldsymbol{x}} \cdot \boldsymbol{\pi}]]\,\mathrm{d}v. \tag{4.35}$$

Integration by parts and twice application of the divergence theorem, together with the surface- and line-distributed forces introduced in (4.12)-(4.14), yields

$$0 = \int_{\Omega} \nabla_{\boldsymbol{x}} \delta \boldsymbol{u} : \boldsymbol{\sigma} \, \mathrm{d}v + \int_{\Omega} \nabla_{\boldsymbol{x}} \nabla_{\boldsymbol{x}} \delta \boldsymbol{u} :\cdot \boldsymbol{\pi} \, \mathrm{d}v \\ - \int_{\partial\Omega} \delta \boldsymbol{u} \cdot \boldsymbol{t} \, \mathrm{d}a - \int_{\partial\Omega} [\nabla_{\boldsymbol{x}} \delta \boldsymbol{u} \cdot \boldsymbol{n}] \cdot \boldsymbol{r} \, \mathrm{d}a - \oint_{\mathcal{C}} \delta \boldsymbol{u} \cdot [\![\boldsymbol{\tau}]\!] \, \mathrm{d}s. \tag{4.36}$$

In the following, the last two terms are neglected in the sense that homogeneous Neumann boundary conditions are incorporated. Accordingly, only the surface integral including the "standard" mechanical tractions $\boldsymbol{t}$ is considered in the derivations as this work proceeds. The scalar product in the second integral term on the right-hand side of (4.36) clearly includes second-order derivatives. Accordingly, a globally C^0-continuous approximation, as performed in classic finite element approaches with Lagrangian basis functions, is not sufficient for this product with regard to the integrability condition. However, isogeometric analysis overcomes the restriction to C^0 inter-element continuity as discussed in detail in Sect. 2.3.

The weak form of Gauss's law (4.3) is obtained by employing the virtual electric potential, respectively test function, $\delta\phi$. Similar to the derivation in (4.36), integration by parts and use of the divergence theorem result in

$$0 = \int_{\Omega} \delta\phi \, [\nabla_{\boldsymbol{x}} \cdot \boldsymbol{d}] \, \mathrm{d}v = - \int_{\Omega} \nabla_{\boldsymbol{x}} \delta\phi \cdot \boldsymbol{d} \, \mathrm{d}v - \int_{\partial\Omega} \delta\phi \, \omega \, \mathrm{d}a. \tag{4.37}$$

4.1.2.2 Discretised weak forms

For the spatial discretisation of the weak forms (4.36)-(4.37), NURBS basis functions R are employed. Following an isoparametric Bubnov-Galerkin approach, the same basis functions are used for the approximation of the geometry as well as for all field variables and test functions. Accordingly, the discretised test functions read

$$\delta \boldsymbol{u}^e = \sum_{A=1}^{\mathrm{n_{en}}} \delta \boldsymbol{u}^A R^A, \quad \delta \phi^e = \sum_{A=1}^{\mathrm{n_{en}}} \delta \phi^A R^A \tag{4.38}$$

with $\mathrm{n_{en}}$ denoting the number of local NURBS basis functions with support on element e. The discrete residual vectors follow as

$$\boldsymbol{r}_{\boldsymbol{u}} = \mathop{\mathbf{A}}_{e=1}^{\mathrm{n_{el}}} \sum_{A=1}^{\mathrm{n_{en}}} \int_{\Omega^e} \boldsymbol{\sigma} \cdot \nabla_{\boldsymbol{x}} R^A \, \mathrm{d}v + \int_{\Omega^e} \boldsymbol{\pi} : \nabla_{\boldsymbol{x}} \nabla_{\boldsymbol{x}} R^A \, \mathrm{d}v - \int_{\partial\Omega^e} \boldsymbol{t} \, R^A \, \mathrm{d}a \tag{4.39}$$

$$\boldsymbol{r}_{\phi} = \mathop{\mathbf{A}}_{e=1}^{\mathrm{n_{el}}} \sum_{A=1}^{\mathrm{n_{en}}} \int_{\Omega^e} \boldsymbol{d} \cdot \nabla_{\boldsymbol{x}} R^A \, \mathrm{d}v + \int_{\partial\Omega^e} \omega \, R^A \, \mathrm{d}a \tag{4.40}$$

with the total number of elements in the finite element scheme referred to as $\mathrm{n_{el}}$ and with operator $\mathbf{A}$ indicating the assembly of local contributions on element level to the global system. The symbol Ω^e denotes the part of the domain Ω associated with element e.

4.1.3 Validation by an analytical solution

A validation of the proposed isogeometric analysis framework for flexoelectric effects in solids is performed by comparison with an analytical solution for a representative boundary value problem. In particular, a two-dimensional cylindrical tube is studied subject to mechanical and electrical loading. The constitutive model includes flexoelectricity and is presented in the following section before the boundary value problem is discussed.

4.1.3.1 Specification of the constitutive model

The simulations performed in this section are based on a free electric enthalpy density formulated in the set of arguments $\{\boldsymbol{\varepsilon}, \nabla_{\boldsymbol{x}}\boldsymbol{\varepsilon}, \boldsymbol{e}\}$ as introduced in (4.22). The chosen form of the free electric enthalpy density is based on the electromechanical contributions proposed in [1]. Under the assumption of isothermal conditions, the function reads

$$\rho\, H^*(\boldsymbol{\varepsilon}, \nabla_{\boldsymbol{x}}\boldsymbol{\varepsilon}, \boldsymbol{e}) = \frac{1}{2}\,\boldsymbol{\varepsilon} : \mathbf{E} : \boldsymbol{\varepsilon} - \frac{1}{2}\,\boldsymbol{e}\cdot\boldsymbol{\chi}\cdot\boldsymbol{e} - \boldsymbol{e}\cdot\boldsymbol{\mu} :\cdot \nabla_{\boldsymbol{x}}\boldsymbol{\varepsilon}. \tag{4.41}$$

From the last term in (4.41) it is clear that the direct flexoelectric effect is explicitly accounted for. However, it can be shown that this formulation implicitly includes contributions from converse flexoelectricity as well. A detailed derivation can be found in, e.g., [36] as well as in [1, 69] based on a free electric enthalpy density as in (4.41).

For the validation purpose in this section, isotropic, linear elasticity is assumed for simplicity so that only two material parameters, specifically Lamé parameters λ and μ, are considered in the elasticity tensor $\mathbf{E}$. Similarly, a simple structure is assumed for permittivity tensor $\boldsymbol{\chi}$ and flexoelectricity tensor $\boldsymbol{\mu}$ by considering only one non-zero material parameter for each of these material tensors, namely scalars χ and $\widehat{\mu}$. For the flexoelectricity tensor a cubic symmetry structure is adopted in particular, whereas shear coefficients are neglected. This is in accordance with the derivations in [1] where this assumption is based on a lack of experimental data for the flexoelectric shear coefficients. With these considerations at hand, the free electric enthalpy density reduces to

$$\rho\, H^*(\boldsymbol{\varepsilon}, \nabla_{\boldsymbol{x}}\boldsymbol{\varepsilon}, \boldsymbol{e}) = \frac{1}{2}\,\lambda\,\mathrm{tr}(\boldsymbol{\varepsilon})^2 + \mu\,\mathrm{tr}(\boldsymbol{\varepsilon}^2) - \frac{1}{2}\,\chi\,\boldsymbol{e}\cdot\boldsymbol{e} - \widehat{\mu}\,\boldsymbol{e}\cdot\nabla_{\boldsymbol{x}}\,\mathrm{tr}(\boldsymbol{\varepsilon}). \tag{4.42}$$

From this expression, the constitutive relations can be derived by using (4.34), i.e.

$$\boldsymbol{\sigma} = \lambda\,\mathrm{tr}(\boldsymbol{\varepsilon})\,\boldsymbol{I} + 2\,\mu\,\boldsymbol{\varepsilon}, \tag{4.43}$$

$$\boldsymbol{\pi} = -\widehat{\mu}\,\boldsymbol{I}\otimes\boldsymbol{e}, \tag{4.44}$$

$$\boldsymbol{d} = \chi\, \boldsymbol{e} + \widehat{\mu}\, \nabla_{\boldsymbol{x}}\, \mathrm{tr}(\boldsymbol{\varepsilon}). \tag{4.45}$$

Accordingly, the total stress tensor defined in (4.5) takes the form

$$\boldsymbol{\sigma}_{\mathrm{tot}} = \lambda\, \mathrm{tr}(\boldsymbol{\varepsilon})\, \boldsymbol{I} + 2\, \mu\, \boldsymbol{\varepsilon} + \widehat{\mu}\, [\nabla_{\boldsymbol{x}} \cdot \boldsymbol{e}]\, \boldsymbol{I} \tag{4.46}$$

and contains contributions from the strain tensor as well as from the divergence of the electric field. The dielectric displacement vector (4.45), on the other hand, is a function of the electric field and of a strain gradient contribution. Accordingly, direct and converse effects are generally included in the formulation as discussed in Sect. 4.1. Moreover, these particular constitutive relations result in the balance of linear momentum (4.2) as well as Gauss's law (4.3) being third-order PDEs. However, if classic strain gradient elasticity (SGE) contributions were accounted for in the free electric enthalpy density function (4.42), balance equation (4.2) would result in a PDE of fourth order. In this work, SGE is not incorporated in order to exclusively investigate flexoelectric effects similar to the approach in [1].

4.1.3.2 Boundary value problem

A flexoelectric, cylindrical tube with inner radius $r_i = 0.1\,\mathrm{mm}$ and outer radius $r_o = 0.2\,\mathrm{mm}$ is studied subject to pure radial compression in a two-dimensional setting. The boundary value problem is visualised in Fig. 4.1. A movement of the inner boundary of the tube is prevented whereas a radial displacement $\overline{u}_r = -0.01\,\mathrm{mm}$ is prescribed on the outer boundary of the tube which leads to a compressive deformation. In addition, a voltage is prescribed in terms of a potential difference $\Delta\phi$ between the outer boundary, where $\overline{\phi} = \pm 1.5\,\mathrm{V}$ is prescribed, and the inner boundary, where the potential is set to zero, i.e. $\Delta\phi = \overline{\phi} = \pm 1.5\,\mathrm{V}$. Accordingly, a closed-circuit setting is adopted. The geometry model for the tube is constructed as described in Appendix B.2.1 under consideration of the different radii in comparison to the model discussed therein. Knot refinement is employed in order to obtain a fine discretisation with $\mathrm{n_{el}} = 25\,000$ elements and equally spaced knots in both parametric directions.

4.1.3.3 Derivation of an analytical solution

For the boundary value problem described in Sect. 4.1.3.2, an analytical solution is provided in [97]. However, the underlying constitutive model differs from the one used in this thesis and introduced in Sect. 4.1.3.1 since the energy function is formulated in a different set of arguments and contains additional strain gradient terms as well as piezoelectric contributions. Moreover, the employed flexoelectricity tensor possesses different symmetry properties. To this end, the analytical solution is derived in the following for the model particularly used in this thesis, whereby it is shown that the results are in accordance with the derivations in [97].

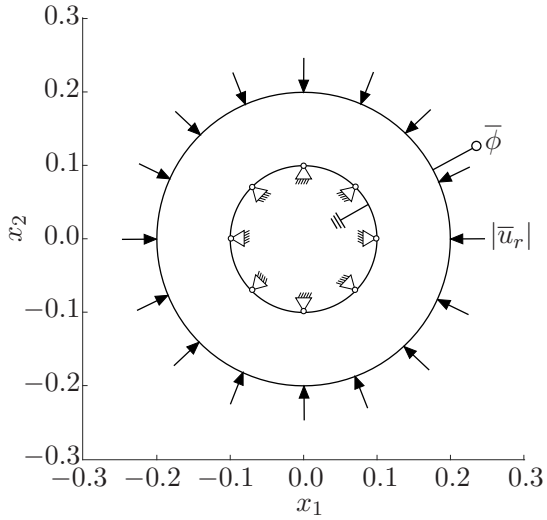

Figure 4.1: Boundary value problem for the flexoelectric cylindrical tube.

Starting with balance equation (4.3), respectively Gauss's law, the insertion of constitutive relation (4.45) yields

$$\chi \, \nabla_{\boldsymbol{x}} \cdot \boldsymbol{e} + \widehat{\mu} \, \nabla_{\boldsymbol{x}} \cdot [\nabla_{\boldsymbol{x}} \, [\mathrm{tr}(\boldsymbol{\varepsilon})]] = 0. \tag{4.47}$$

Together with the kinematic relations (4.6)-(4.7) and the definition of the Laplace operator, the balance equation can be rewritten as

$$\Delta_{\boldsymbol{x}} \, [\chi \, \phi - \widehat{\mu} \, \nabla_{\boldsymbol{x}} \cdot \boldsymbol{u}] = 0. \tag{4.48}$$

Similarly, inserting constitutive relations (4.43)-(4.44) into the balance of linear momentum (4.2) under vanishing body forces and reformulating the divergence and gradient operators yields

$$\nabla_{\boldsymbol{x}} \, [\lambda \, \mathrm{tr}(\boldsymbol{\varepsilon})] + \nabla_{\boldsymbol{x}} \cdot [2 \, \mu \, \boldsymbol{\varepsilon}] + \nabla_{\boldsymbol{x}} \, [\nabla_{\boldsymbol{x}} \cdot \widehat{\mu} \, \boldsymbol{e}] = \boldsymbol{0}. \tag{4.49}$$

By taking the kinematic relations (4.6)-(4.7) for the strain tensor as well as the electric field vector into account, it follows that

$$\nabla_{\boldsymbol{x}} \, [\lambda \nabla_{\boldsymbol{x}} \cdot \boldsymbol{u}] + \nabla_{\boldsymbol{x}} \cdot \left[\mu \left[\nabla_{\boldsymbol{x}} \boldsymbol{u} + [\nabla_{\boldsymbol{x}} \boldsymbol{u}]^{\mathrm{t}}\right]\right] - \nabla_{\boldsymbol{x}} \, [\nabla_{\boldsymbol{x}} \cdot \widehat{\mu} \, \nabla_{\boldsymbol{x}} \phi] = \boldsymbol{0} \tag{4.50}$$

which can be rewritten under the use of $\nabla_{\boldsymbol{x}} \cdot [\nabla_{\boldsymbol{x}} \boldsymbol{u}]^{\mathrm{t}} = \nabla_{\boldsymbol{x}} \, [\nabla_{\boldsymbol{x}} \cdot \boldsymbol{u}]$, accordingly

$$[\lambda + \mu] \, \nabla_{\boldsymbol{x}} \, [\nabla_{\boldsymbol{x}} \cdot \boldsymbol{u}] + \mu \, \nabla_{\boldsymbol{x}} \cdot [\nabla_{\boldsymbol{x}} \boldsymbol{u}] - \widehat{\mu} \, \nabla_{\boldsymbol{x}} \, [\nabla_{\boldsymbol{x}} \cdot \nabla_{\boldsymbol{x}} \phi] = \boldsymbol{0}. \tag{4.51}$$

By inserting balance equation (4.48) into (4.51), the latter can be further reformulated in sole dependence of the displacement field $\boldsymbol{u}$, i.e.

$$[\lambda+\mu]\,\nabla_{\boldsymbol{x}}\,[\nabla_{\boldsymbol{x}}\cdot\boldsymbol{u}]+\mu\,\Delta_{\boldsymbol{x}}\boldsymbol{u}-\widehat{\mu}\,\nabla_{\boldsymbol{x}}\left[\frac{\widehat{\mu}}{\chi}\Delta_{\boldsymbol{x}}\,[\nabla_{\boldsymbol{x}}\cdot\boldsymbol{u}]\right]=\boldsymbol{0}. \tag{4.52}$$

Considering the interchangeability of the gradient operations in the last term on the left-hand side, the balance equation finally results in

$$\nabla_{\boldsymbol{x}}\,[\nabla_{\boldsymbol{x}}\cdot\boldsymbol{u}]\,[\lambda+\mu]+\Delta_{\boldsymbol{x}}\left[\mu\,\boldsymbol{u}-\frac{\widehat{\mu}^2}{\chi}\nabla_{\boldsymbol{x}}\,[\nabla_{\boldsymbol{x}}\cdot\boldsymbol{u}]\right]=\boldsymbol{0}. \tag{4.53}$$

The two derived equations (4.48) and (4.53) are to be solved for the specific boundary value problem introduced in Sect. 4.1.3.2, i.e. for a cylindrical tube subject to pure radial compression. Due to the axisymmetric characteristic of the two-dimensional boundary value problem, a polar base system $\{\boldsymbol{e}_r,\boldsymbol{e}_\varphi\}$ is employed and all partial derivatives with respect to φ vanish, i.e. $\partial\bullet/\partial\varphi=0$. Moreover, $u_\varphi=0$ holds for the azimuthal displacement as a consequence of the boundary conditions. Based on these considerations, the gradient operations in (4.53) can be derived for the polar base system as

$$\nabla_{\boldsymbol{x}}\,[\nabla_{\boldsymbol{x}}\cdot\boldsymbol{u}]=\left[\frac{\partial^2 u_r}{\partial r^2}+\frac{1}{r}\frac{\partial u_r}{\partial r}-\frac{1}{r^2}u_r\right]\boldsymbol{e}_r, \tag{4.54}$$

$$\Delta_{\boldsymbol{x}}\boldsymbol{u}=\left[\frac{\partial^2 u_r}{\partial r^2}+\frac{1}{r}\frac{\partial u_r}{\partial r}-\frac{u_r}{r^2}\right]\boldsymbol{e}_r, \tag{4.55}$$

$$\Delta_{\boldsymbol{x}}\,[\nabla_{\boldsymbol{x}}\,[\nabla_{\boldsymbol{x}}\cdot\boldsymbol{u}]]=\left[\frac{\partial^4 u_r}{\partial r^4}+\frac{2}{r}\frac{\partial^3 u_r}{\partial r^3}-\frac{3}{r^2}\frac{\partial^2 u_r}{\partial r^2}+\frac{3}{r^3}\frac{\partial u_r}{\partial r}-\frac{3}{r^4}u_r\right]\boldsymbol{e}_r. \tag{4.56}$$

Since all terms in (4.54)-(4.56) refer to the same basis vector, a scalar-valued version of (4.53) is obtained, i.e.

$$\begin{aligned}&l_0^2\,\frac{\partial^4 u_r}{\partial r^4}+2\,l_0^2\,\frac{1}{r}\frac{\partial^3 u_r}{\partial r^3}-\left[1+3\,l_0^2\,\frac{1}{r^2}\right]\frac{\partial^2 u_r}{\partial r^2}\\&-\left[\frac{1}{r}-3\,l_0^2\,\frac{1}{r^3}\right]\frac{\partial u_r}{\partial r}+\left[\frac{1}{r^2}-3\,l_0^2\,\frac{1}{r^4}\right]u_r=0.\end{aligned} \tag{4.57}$$

Therein, the definition $l_0^2:=\widehat{\mu}^2/[\chi\,[\lambda+2\,\mu]]$ is considered such that this ordinary differential equation (ODE) is equivalent to the equation derived in [97, (49)] where a different constitutive model is used. Accordingly, the solution

$$u_r(r)=a\,r+\frac{b}{r}+c\,I_1(\lambda_0\,r)+d\,K_1(\lambda_0\,r)\;,\quad a,b,c,d\in\mathbb{R}, \tag{4.58}$$

proposed in [97, (50)] can be adopted. Therein, I_1 and K_1 are the modified first-order Bessel functions of the first and second kind and $\lambda_0:=l_0^{-1}$.

Regarding Gauss's law in the form (4.48), use of the divergence operator in the polar base system as well as of the definition $f_0:=\widehat{\mu}/\chi$ directly yields

$$\Delta_{\boldsymbol{x}}\phi = f_0\,\Delta_{\boldsymbol{x}}\left[\frac{\partial u_r}{\partial r} + \frac{1}{r}u_r\right], \tag{4.59}$$

which is in accordance with [97, (51)] on the basis of different material parameters. The solution to (4.59) as proposed in [97, (52)] reads

$$\phi(r) = f_0\left[2\,a + c\,\lambda_0 I_0(\lambda_0\,r) - d\,\lambda_0 K_0(\lambda_0\,r)\right] + g + h\,\ln(r), \quad a,b,d,g,h \in \mathbb{R} \tag{4.60}$$

with the modified zeroth-order Bessel functions I_0, K_0 of the first and second kind. The derivative of the electric potential follows as

$$\frac{\partial\phi}{\partial r} = f_0\left[c\,\lambda_0^2\,I_1(\lambda_0\,r) + d\,\lambda_0^2\,K_1(\lambda_0\,r)\right] + \frac{h}{r}, \tag{4.61}$$

since $I_0^{'} = I_1$ and $K_0^{'} = -K_1$ hold for the derivatives of the Bessel functions, see [3, (9.6.27)]. The radial electric field can directly be obtained from (4.61) as

$$e_r = -\frac{\partial\phi}{\partial r}. \tag{4.62}$$

For the unknown constants a, b, c, d, g, h in (4.58) and (4.60), six boundary conditions are formulated for the boundary value problem at hand, accordingly

$$u_r(r = r_i) = 0, \qquad u_r(r = r_o) = \overline{u}_r, \tag{4.63}$$

$$\pi_{rrr}(r = r_i) = 0, \quad \pi_{rrr}(r = r_o) = 0, \tag{4.64}$$

$$\phi(r = r_i) = 0, \qquad \phi(r = r_o) = \overline{\phi}. \tag{4.65}$$

These yield a set of six coupled equations, i.e.

$$a\,r_i + \frac{b}{r_i} + c\,I_1(\lambda_0\,r_i) + d\,K_1(\lambda_0\,r_i) = 0 \tag{4.66}$$

$$a\,r_o + \frac{b}{r_o} + c\,I_1(\lambda_0\,r_o) + d\,K_1(\lambda_0\,r_o) = \overline{u}_r \tag{4.67}$$

$$f_0\left[c\,\lambda_0^2\,I_1(\lambda_0\,r_i) + d\,\lambda_0^2\,K_1(\lambda_0\,r_i)\right] + \frac{h}{r_i} = 0 \tag{4.68}$$

$$f_0\left[c\,\lambda_0^2\,I_1(\lambda_0\,r_o) + d\,\lambda_0^2\,K_1(\lambda_0\,r_o)\right] + \frac{h}{r_o} = 0 \tag{4.69}$$

$$f_0\left[2\,a + c\,\lambda_0\,I_0(\lambda_0\,r_i) - d\,\lambda_0\,K_0(\lambda_0\,r_i)\right] + g + h\,\ln(r_i) = 0 \tag{4.70}$$

$$f_0\left[2\,a + c\,\lambda_0\,I_0(\lambda_0\,r_o) - d\,\lambda_0\,K_0(\lambda_0\,r_o)\right] + g + h\,\ln(r_o) = \overline{\phi} \tag{4.71}$$

which can be solved as

$$a = -\frac{b}{r_i^2} - \frac{c}{r_i}I_1(\lambda_0\,r_i) - \frac{d}{r_i}K_1(\lambda_0\,r_i) \tag{4.72}$$

$$b = \frac{r_o\, r_i^2}{r_i^2 - r_o^2}\left[\overline{u}_r + c\left[\frac{r_o}{r_i} I_1(\lambda_0\, r_i) - I_1(\lambda_0\, r_0)\right] + d\left[\frac{r_o}{r_i} K_1(\lambda_0\, r_i) - K_1(\lambda_0\, r_0)\right]\right] \tag{4.73}$$

$$c = d\,\frac{r_0\, K_1(\lambda_0\, r_o) - r_i\, K_1(\lambda_0\, r_i)}{r_i\, I_1(\lambda_0\, r_i) - r_0\, I_1(\lambda_0\, r_o)} \tag{4.74}$$

$$d = \frac{\overline{\phi}}{f_0\, \lambda_0\, \kappa} \tag{4.75}$$

$$g = -f_0\,[2\, a + c\, \lambda_0\, I_0(\lambda_0\, r_i) - d\, \lambda_0\, K_0(\lambda_0\, r_i)] - h\, \ln(r_i) \tag{4.76}$$

$$h = -f_0\, r_i\left[c\, \lambda_0^2\, I_1(\lambda_0\, r_i) + d\, \lambda_0^2\, K_1(\lambda_0\, r_i)\right] \tag{4.77}$$

with scalar

$$\begin{aligned}\kappa = {} & \frac{r_0\, K_1(\lambda_0\, r_o) - r_i\, K_1(\lambda_0\, r_i)}{r_i\, I_1(\lambda_0\, r_i) - r_0\, I_1(\lambda_0\, r_o)}\,[I_0(\lambda_0\, r_o) - I_0(\lambda_0\, r_i)] + K_0(\lambda_0\, r_i) - K_0(\lambda_0\, r_o) \\ & - r_i\, \lambda_0\, \ln(r_o/r_i)\left[\frac{r_0\, K_1(\lambda_0\, r_o) - r_i\, K_1(\lambda_0\, r_i)}{r_i\, I_1(\lambda_0\, r_i) - r_0\, I_1(\lambda_0\, r_o)} I_1(\lambda_0\, r_i) + K_1(\lambda_0\, r_i)\right].\end{aligned} \tag{4.78}$$

For comparison, the case without flexoelectricity, i.e. $\widehat{\mu} = 0$, is additionally considered. The analytical solutions for the radial displacement and electric potential can be directly derived from (4.58) and (4.60) by neglecting flexoelectric contributions, which yields

$$u_r(r) = a\, r + \frac{b}{r}, \quad a, b \in \mathbb{R}, \tag{4.79}$$

$$\phi(r) = c + d\ln(r), \quad c, d \in \mathbb{R}. \tag{4.80}$$

By adopting the boundary conditions (4.63) and (4.65) for the mechanical displacement and electric potential at the inner and outer tube radius, respectively, the four constants in (4.79)-(4.80) follow as

$$a = -\overline{u}_r\,\frac{r_o}{r_i^2 - r_o^2}, \quad b = \overline{u}_r\,\frac{r_o\, r_i^2}{r_i^2 - r_o^2}, \quad c = -\overline{\phi}\,\frac{\ln(r_i)}{\ln(r_o/r_i)}, \quad d = \frac{\overline{\phi}}{\ln(r_o/r_i)}. \tag{4.81}$$

4.1.3.4 Results and comparison

As a result of the applied compressive loading, Fig. 4.2 shows the radial displacement over the tube radius resulting from the analytical calculations derived in the previous section as well as from the numerical simulations by means of isogeometric analysis. In order to investigate the flexoelectric influence on the material behaviour, the results are presented for the case with and without activation of flexoelectric effects and for prescribed voltages of different sign. By comparison it can be observed that a positive prescribed voltage, respectively potential difference $\Delta\phi > 0$ induces tensile strains in the interior of the tube superimposed to the mechanically-induced compressive strains,

cf. Fig. 4.2a. For $\Delta\phi < 0$, on the other hand, an electrically-induced compression is observed in addition to the compressive load prescribed by means of $\overline{u}_r$, see Fig. 4.2b.

Focussing on the electric potential as presented in Fig. 4.3, a change in curvature is observable in the resulting graphs when flexoelectric energy contributions are activated. In the non-flexoelectric case, on the contrary, the calculations yield almost linearly increasing, respectively decreasing graphs. In accordance with this behaviour, the distribution of the electric field over the radius of the cylindrical tube is revealed in Fig. 4.4. The resulting graphs are monotonously increasing, respectively decreasing in r for $\widehat{\mu} = 0$ whereas a convex, respectively concave parabolic shape is obtained for non-zero values of the flexoelectric coefficient. This can be attributed to the particular choice of higher-order boundary conditions in (4.64). To be precise, the radial electric field e_r vanishes at the boundaries along with the radial hyper-stresses π_{rrr} upon activation of flexoelectricity.

In all results shown in Fig. 4.2-4.4 analytically and numerically obtained values are indistinguishable for the case without flexoelectricity and a good agreement is also observed when flexoelectric effects are present. Differences in the results with $\widehat{\mu} \neq 0$ could be due to numerical errors in the isogeometric analysis or related to the employment of Bessel functions in the analytical derivations.

4.2 Bone remodelling

The process of bone remodelling is highly important for maintaining the structural integrity of bones by, e.g., the healing of microcracks within the bone material. Before going into detail on the remodelling processes occurring in damaged bone, three important distinctions shall be made. Firstly, this refers to the terms *bone modelling* and *bone remodelling*. Bone modelling is associated with skeletal development and growth i.e. changes of bone in shape and size, whereas bone remodelling leads to a change in the material properties of bone rather than in its geometry and is the process under investigation in this work, cf. [57, 64]. Secondly, it is important to distinguish whether the respective bone remodelling processes take place in *cancellous* ("spongy") or in *cortical* (compact) bone since these processes are not equal, see [53, 96]. Finally, *targeted* and *non-targeted* remodelling shall be distinguished. Targeted remodelling occurs in response to microdamage, e.g. microcracks, and the associated death of osteocytes. This process aims for the repair of the damaged bone region, whereas non-targeted remodelling is not directed towards a particular location and is regulated by changes in hormones, cf. [53, 83]. In Fig. 4.5 the cortical and cancellous parts of a bone, particularly of a human femur, are shown and the distinct remodelling processes are illustrated.

In the present contribution, the focus lies on targeted bone remodelling in cortical bone. Within this process, three main cell types are involved, namely osteocytes (OY), osteoclasts (OC) and osteoblasts (OB). They work together in temporary units which have been first introduced in [64] as *Basic Multicellular Units* (BMUs). The most im-

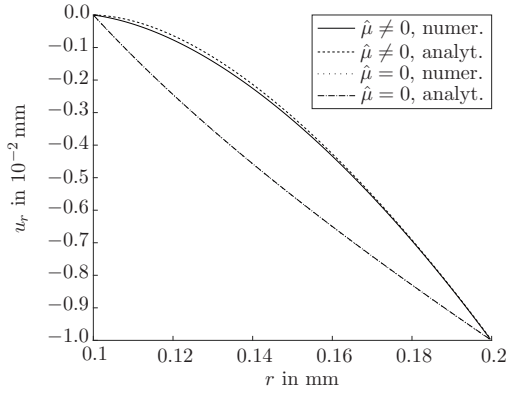

(a) Results for positive prescribed voltage $\Delta\phi = 1.5\,\mathrm{V}$.

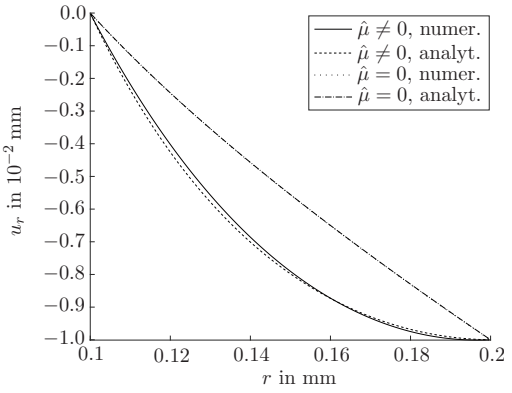

(b) Results for negative prescribed voltage $\Delta\phi = -1.5\,\mathrm{V}$.

Figure 4.2: Radial displacement along the radius of the cylindrical tube. Results with and without flexoelectric effects are shown. Comparison between analytical and numerical (IGA) results.

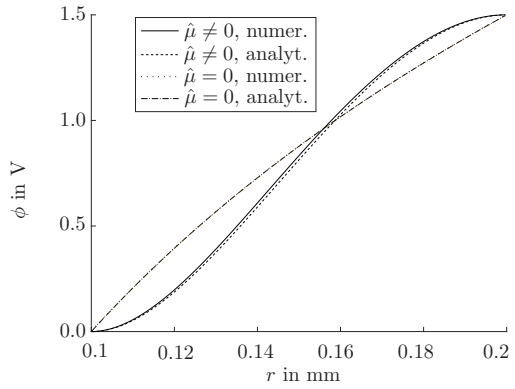

(a) Results for positive prescribed voltage $\Delta\phi = 1.5\,\mathrm{V}$.

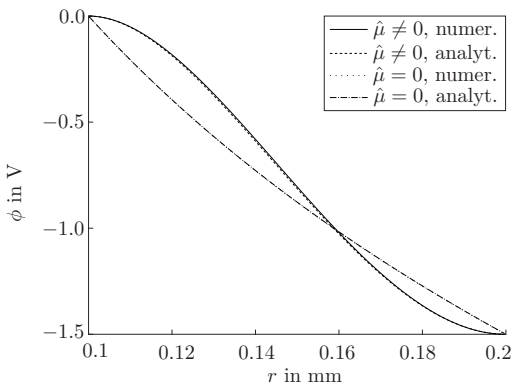

(b) Results for negative prescribed voltage $\Delta\phi = -1.5\,\mathrm{V}$.

Figure 4.3: Electric potential along the radius of the cylindrical tube. Results with and without flexoelectric effects are shown. Comparison between analytical and numerical (IGA) results.

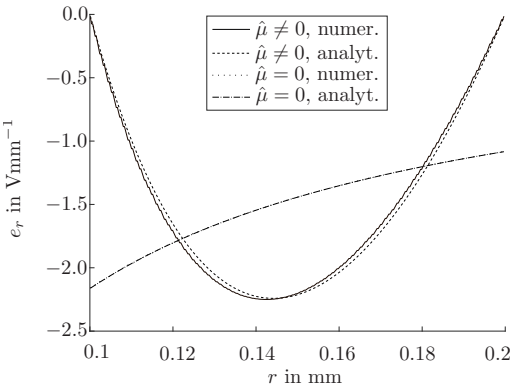

(a) Results for positive prescribed voltage $\Delta\phi = 1.5\,\mathrm{V}$.

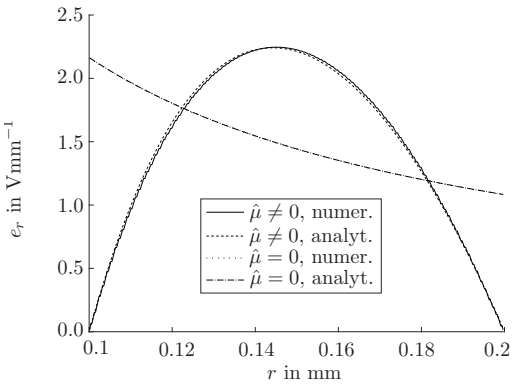

(b) Results for negative prescribed voltage $\Delta\phi = -1.5\,\mathrm{V}$.

Figure 4.4: Radial electric field along the radius of the cylindrical tube. Results with and without flexoelectric effects are shown. Comparison between analytical and numerical (IGA) results.

portant characteristics of these cells are discussed in detail in [41, 96, 110]. *Osteocytes* are mature bone cells embedded in the mineralised bone matrix and make up more than 90 % of cellular bone content. In the context of bone remodelling, osteocytes are of major importance due to their function as mechanosensory cells and their ability to communicate not only with each other but also with cells of a different kind. *Osteoclasts* are multinucleated cells which originate from haematopoietic stem cells in the bone marrow and migrate to remodelling sites in order to resorb old bone. The lifespan of osteoclasts is approx. two weeks in human bone. *Osteoblasts* have their origin in mesenchymal stem cells in the bone marrow. Throughout their lifespan of approx. three months in human bone, they are responsible for the formation of new bone material.

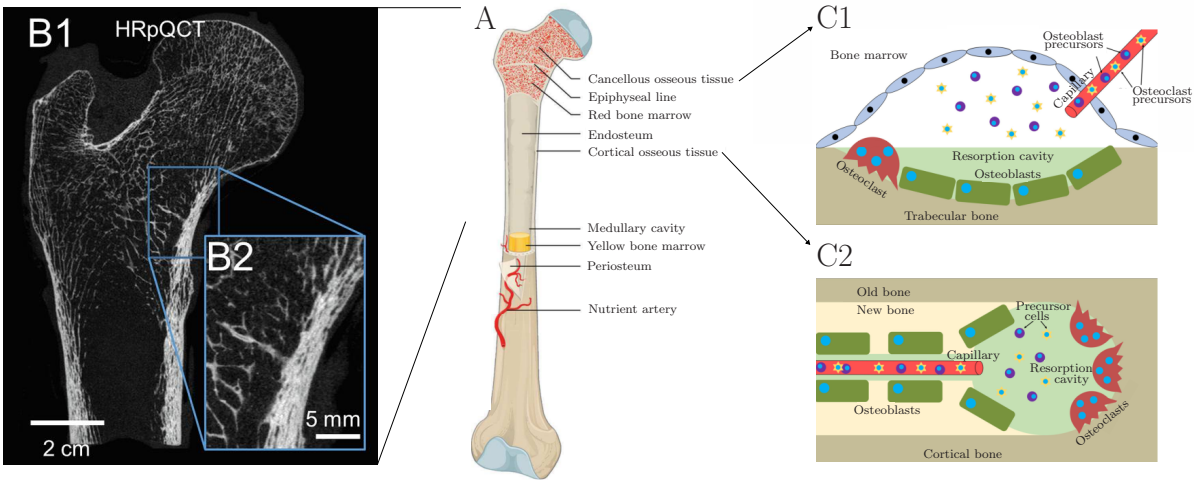

Figure 4.5: Anatomy and physiology of a human femur. (A) Illustration of the internal structure of a femur reproduced from [88]. (B1)-(B2) Microscopy image of the cross section of a femur reproduced from [176] which reveals the cortical and cancellous bone microstructure. (C1)-(C2) Sketch of the remodelling process in cancellous (C1) and cortical (C2) bone reproduced from [121]. All images are reproduced under the terms of the Creative Commons Attribution License (CC BY).

Targeted remodelling processes in cortical bone The process of remodelling in cortical bone is described in detail in, e.g., [53, 64, 83, 96]. One significant question which is not fully answered, is how the remodelling process in bones is initiated. In the literature, the initiation is attributed to different phenomena such as streaming potentials [130], matrix piezoelectricity [65] and, most recently, flexoelectricity [120, 164] which is the main focus of this work.

In the case of a flexoelectricity-induced initiation, the bone remodelling process starts in response to signals, or rather substances, that are secreted by osteocytes undergoing apoptosis due to the induced electric field [53, 120]. In fact, it has been argued in [137] that it might as well be the neighbouring osteocytes and not (only) the dying cells themselves which release substances such as M-CSF and RANKL, that promote osteoclast differentiation and migration. In addition, the decreased number of living osteocytes

decreases the production level of the protein sclerostin which inhibits bone formation [33, 53]. The dense osteocyte network plays an important role in the context of these signalling activities because it enables the communication between individual osteocytes as well as between osteocytes and bone lining cells. These can be found at the bone surfaces, e.g. the endosteal and periosteal surfaces, and are able to communicate with the network of osteocytes in the bone matrix. By transmission of the osteocytic signals to these surfaces, the bone cells for remodelling, namely osteoclasts and osteoblasts are recruited from the vascular system or, to be more precise, from the central capillary of a Haversian or Volkmann's canal near the remodelling site [31, 124, 125]. In the literature, these cells are often summarised in terms of BMUs, as proposed in [64]. Within the scope of this work, however, both cell types are considered individually in order to account for their distinct roles in the remodelling process. Accordingly, the osteocyte signalling leads to the recruitment of osteoclasts which move towards the remodelling site in the form of a so-called *cutting cone* by excavating a tunnel through the bone matrix and thereby removing old and damaged bone [83]. During this activity of matrix dissolution, growth factors which serve as attractants for osteoblasts are released from the bone matrix. Together with factors secreted by the osteoclasts themselves, they recruit osteoblasts to the remodelling site. However, this coupling between osteoclastic resorption and osteoblastic formation is complex and different explanations are proposed in the literature [53, 83, 148]. The recruited osteoblasts start migrating towards the remodelling site by using the tunnel previously built by the osteoclasts as a pathway through the bone. During the *formation phase*, they form new bone material in order to repair all damaged regions, including the initial crack as well as the tunnel itself [53, 96]. More specifically speaking, they accumulate at the damaged surfaces and thereby form new bone material such that, in particular, the crack gradually closes. After their remodelling activity, osteoblasts can transform into lining cells, undergo apoptosis or are embedded (approx. 10 - 20 %) in the new bone matrix and steadily differentiate into osteocytes while the material mineralises [63, 96]. Due to the respective re-increase of the osteocyte concentration, the remodelling process terminates as the level of sclerostin also re-increases [33, 83].

The timeline of the entire remodelling process depends on multiple factors such as location, width and length of the crack as well as age, gender and health of the organism, to name only a few. However, some reference values can be found in the literature. For the *resorption phase*, the values vary between 14 and 30 days and for the *formation phase* between 3 and 4 months [83, 148].

4.3 IGA modelling approach for flexoelectricity-induced initiation of bone remodelling

An isogeometric finite element model is proposed for the simulation of the flexoelectric initiation of cortical bone remodelling in the presence of microcracks. Starting with

flexoelectricity as a trigger mechanism for bone remodelling, signalling mechanisms are incorporated and the subsequent migration of osteoclasts and osteoblasts towards the remodelling site is accounted for. Accordingly, a chemo-electro-mechanically coupled model is established. Due to the complexity of biochemical activities that take place in bones during remodelling, several simplifications are made such that the process is modelled according to the following steps which are illustrated and further described in Fig. 4.6:

1. Flexoelectricity results in an electric field in response to mechanical loading in the fractured bone.
2. The electric field exceeds a critical value in the vicinity of the crack tip so that osteocyte apoptosis occurs.
3. In consequence of osteocyte apoptosis biochemical signals, respectively messenger substances are sent out which initiate the work of BMUs.
4. Osteoclasts migrate through the cortical bone matrix and towards the crack tip to start the remodelling process.
5. Osteoblasts follow in the same direction as osteoclasts towards the remodelling site.

Especially the complex signalling mechanisms are summarised in the proposed modelling approach for the sake of simplicity. Specifically speaking, so-called messenger substances (ME) carry out the signalling tasks entirely, whereas in real bones various signalling mechanisms occur such as secretion of particular proteins such as RANKL and M-CSF [53]. Moreover, the tunnels which are excavated by osteoclasts are not resolved in detail in this work. Instead, the migration of the cells through the bone matrix is modelled without the removal of bone material by taking into account effective field quantities, i.e. the osteoclast and osteoblast concentrations. Overall, a continuum approach is employed for all considered cell types, accounting for the respective cell concentrations instead of individual particles. This is a common assumption for diffusion models at the macroscopic scale, see, e.g., [113]. It is noted, however, that also discrete models exist for the modelling of cell populations [113]. Moreover, it has been stated in [43] that cortical bone fails at strains of approximately 2 %. With this background in mind, a small-strain theory is considered suitable for the modelling of cortical bone, even though it is mentioned that, under certain conditions, bone may exhibit larger strains.

Remark 4.1. In the proposed modelling approach, osteoclasts and osteoblasts are accounted for by independent field variables. Another reasonable choice would be the combination of both cell types in form of BMUs such that one field variable for the BMU concentration would be incorporated into the model. In this work, the separate consideration of the cell types allows a detailed simulation of the behaviour of the main participants during remodelling processes. This makes the model expandable with regard to the spatial and temporal separation of osteoclasts and osteoblasts.

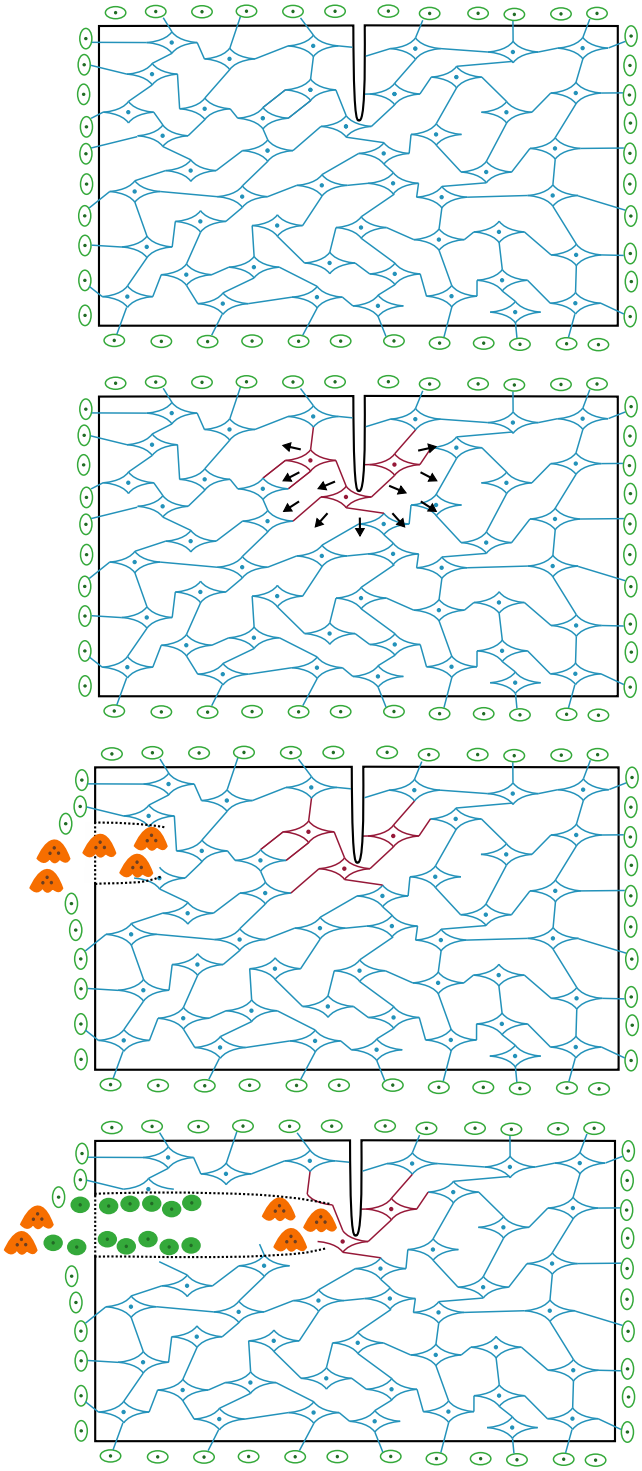

(a) Initial state: *Osteocytes* (OY) are homogeneously distributed throughout the bone, whereas the surfaces are covered by bone lining cells. A dense communication network is provided.

(b) Osteocyte apoptosis and signalling: In consequence of mechanical loading together with the flexoelectric effect, osteocytes undergo apoptosis in the vicinity of the crack tip. *Messenger substances* (ME) are sent out by the apoptotic osteocytes (marked in red), respectively by their neighbours, and transmitted towards the cells at the surfaces. Arrows indicate the origin and direction of this signalling mechanism.

(c) Osteoclast recruitment and diffusion: In response to the biochemical signalling, *osteoclasts* (OC) are recruited to the remodelling site. The cells migrate through the bone matrix towards the crack while preferably moving in direction of osteon alignment.

(d) Osteoblast recruitment and diffusion: *Osteoblasts* (OB) follow in the same direction as the osteoclasts through the cortical bone matrix in order to form new bone material. Throughout the remodelling process, a continuous supply of new osteoclasts and osteoblasts from the vasculature is provided.

Figure 4.6: Simplified, schematic illustration of a bone remodelling process in the presence of a crack. The involved cell types are *osteocytes* (OY, blue), bone lining cells (green), *osteoclasts* (OC, orange) and *osteoblasts* (OB, green, filled). The process takes place in a cracked sample of cortical bone with the horizontal axis being aligned with the osteons. Reproduced from [174] under the terms of the Creative Commons Attribution License (CC BY).

4.3.1 Balance equations

The modelling approach for the flexoelectricity-induced initiation of bone remodelling stipulates chemo-electro-mechanical coupling in terms of a coupled set of partial differential equations. In the subsequent sections, these PDEs are presented and the thermodynamic framework of the model is discussed in detail. Concerning the electromechanical parts of the model, the derivations provided in Sect. 4.1 serve as a basis for the following considerations.

4.3.1.1 Chemo-electro-mechanical coupling

For the simulation of flexoelectricity-induced bone remodelling processes in a two-dimensional setting, the set of degrees of freedom $dof = \{\boldsymbol{u}, \phi, c_{\mathrm{OY}}, c_{\mathrm{ME}}, c_{\mathrm{OC}}, c_{\mathrm{OB}}\}$ is taken into account, containing the displacement vector, the electric potential and the concentrations of osteocytes, messenger substances and (active) osteoclasts and osteoblasts, respectively. With these field variables at hand and with $\dot{\bullet}$ denoting the time derivative of a quantity $\bullet$, the set of balance equations in local form for the chemo-electro-mechanical coupling is given as

$$\mathbf{0} = \nabla_{\boldsymbol{x}} \cdot \boldsymbol{\sigma}_{\mathrm{tot}} \quad \text{in } \Omega \tag{4.82a}$$

$$0 = \nabla_{\boldsymbol{x}} \cdot \boldsymbol{d} \quad \text{in } \Omega \tag{4.82b}$$

$$\dot{c}_{\mathrm{OY}} = s_{\mathrm{OY}}(\|\boldsymbol{e}\|, c_{\mathrm{OY}}) \quad \text{in } \Omega \tag{4.82c}$$

$$\dot{c}_{\mathrm{ME}} = -\nabla_{\boldsymbol{x}} \cdot \boldsymbol{q}_{\mathrm{ME}} + s_{\mathrm{ME}}(c_{\mathrm{OY}}) \quad \text{in } \Omega \tag{4.82d}$$

$$\dot{c}_{\mathrm{OC}} = -\nabla_{\boldsymbol{x}} \cdot \boldsymbol{q}_{\mathrm{OC}} \quad \text{in } \Omega \tag{4.82e}$$

$$\dot{c}_{\mathrm{OB}} = -\nabla_{\boldsymbol{x}} \cdot \boldsymbol{q}_{\mathrm{OB}} \quad \text{in } \Omega \tag{4.82f}$$

for the domain Ω under consideration. To be precise, equation (4.82a) represents the balance of linear momentum for the quasi-static case without the presence of body forces. Therein, the total stress tensor $\boldsymbol{\sigma}_{\mathrm{tot}}$ can be decomposed into the classic stress tensor $\boldsymbol{\sigma}$ and a contribution of the hyper-stress tensor $\boldsymbol{\pi}$ according to (4.5).

Balance equation (4.82b) is a reduced form of the first Maxwell equation, also termed Gauss's law, without the presence of free charges. Accordingly, the divergence of dielectric displacements $\boldsymbol{d}$ vanishes.

The remaining equations (4.82c)-(4.82f) determine the time derivatives of the concentrations of bone cells and messenger substances in the domain Ω by source terms and by diffusion. The source term s_{OY} for the osteocytes in (4.82c) is assumed to be a function of the norm of the electric field as well as of the osteocyte concentration itself. It captures that in consequence of mechanical loading, the flexoelectricity-induced electric field eventually exceeds a predefined critical value for osteocyte apoptosis. In [120] and references cited therein, this threshold value is determined to $10\,\mathrm{Vmm}^{-1}$, whereas a lower electric field magnitude such as $1\,\mathrm{Vmm}^{-1}$ can already lead to osteocyte damage and to the death of individual cells. Accordingly, the source, or rather sink term for

the osteocytes is incorporated into the model which considers a critical value e_{crit} as argument of an exponential function, together with the local electric field magnitude and the current osteocyte concentration, i.e.

$$s_{\text{OY}} = -k_{\text{OY},1}\left[1 - \exp\left(-\frac{\|\boldsymbol{e}\|}{e_{\text{crit}}}\frac{c_{\text{OY}}}{k_{\text{OY},2}}\right)\right]. \tag{4.83}$$

By this saturation-type format it is ensured that, if the critical electric field value is reached and the osteocyte concentration is rather high – e.g. in the initial state – a high number of osteocytes undergoes apoptosis as it has been observed in the experiments performed in [120]. If, on the other hand, an electric field below the threshold value is present or if the osteocyte concentration is low – e.g. when a huge number of osteocytes had already died – the sink term decreases, see Fig. 4.7. More specifically speaking, it can be shown analytically that by using formulation (4.83) negative cell concentrations, which would be unphysical, are avoided, see Appendix C.3.1. The constant parameters $k_{\text{OY},1}$ and $k_{\text{OY},2}$ help to further adjust the apoptosis behaviour of the osteocytes according to the experimental findings. With $e_{\text{crit}} = 5\,\text{Vmm}^{-1}$ and the remaining parameters provided in Table 4.3 in Sect. 4.3.3.2, it becomes apparent from Fig. 4.7 that, by approaching $\|\boldsymbol{e}\| = 10\,\text{Vmm}^{-1}$, an immediate death of a large number of osteocytes takes place in the state where the bone cells have not previously been damaged, i.e. $c_{\text{OY}} = c_{\text{OY}}^{\text{init}}$.

As a consequence of osteocyte apoptosis, chemical signals are released which cause bone remodelling processes to begin. The complex signalling mechanisms are accounted for in this work by messenger substances. Consequently, the source term

$$s_{\text{ME}} = k_{\text{ME}}\left[1 - \frac{c_{\text{OY}}}{c_{\text{OY}}^{\text{init}}}\right] \tag{4.84}$$

is employed in (4.82d) which leads to the production of messenger substances at locations where the current osteocyte concentration has decreased in comparison to its initial value. The magnitude of messenger substance production can be adjusted by the constant parameter k_{ME}.

The movement or, specifically speaking, diffusion of the bone cells and messenger substances in (4.82d)-(4.82f) is accounted for by the flux vectors

$$\boldsymbol{q}_{\text{ME}} = -D_{\text{ME}}\,\nabla_{\boldsymbol{x}} c_{\text{ME}}, \tag{4.85}$$
$$\boldsymbol{q}_{\text{OC}} = -\boldsymbol{D}_{\text{OC}} \cdot \nabla_{\boldsymbol{x}} c_{\text{OC}}, \tag{4.86}$$
$$\boldsymbol{q}_{\text{OB}} = -\boldsymbol{D}_{\text{OB}} \cdot \nabla_{\boldsymbol{x}} c_{\text{OB}}, \tag{4.87}$$

i.e. by the negative concentration gradients of the considered species together with diffusion coefficients or tensors, respectively. A constant diffusion coefficient D_{ME} is used to describe the movement of messenger substances, whereas for the osteoclast and osteoblast cells evolving diffusion tensors are employed which account for anisotropic or, in

other words, directionally dependent diffusion. Accordingly, the directional dependency is accounted for in the diffusion tensors

$$\boldsymbol{D}_{\mathrm{OC}} = D_{\mathrm{OC}}\, \boldsymbol{A} \tag{4.88}$$

$$\boldsymbol{D}_{\mathrm{OB}} = \Lambda(c_{\mathrm{OC}})\, D_{\mathrm{OB}}\, \boldsymbol{A} \tag{4.89}$$

with structural tensor

$$\boldsymbol{A} = \eta_{\uparrow} \left[\boldsymbol{a}_{\mathrm{g}} \otimes \boldsymbol{a}_{\mathrm{g}}\right] + \eta_{\parallel} \left[\boldsymbol{a}_{\mathrm{b}} \otimes \boldsymbol{a}_{\mathrm{b}}\right] + \eta_{\perp} \left[\boldsymbol{I} - \boldsymbol{a}_{\mathrm{b}} \otimes \boldsymbol{a}_{\mathrm{b}}\right]. \tag{4.90}$$

Therein, the first term describes a targeted cell movement in the direction of the gradient of the messenger substance concentration by considering the normalised vector

$$\boldsymbol{a}_{\mathrm{g}} = \frac{\nabla_{\boldsymbol{x}} c_{\mathrm{ME}}}{\|\nabla_{\boldsymbol{x}} c_{\mathrm{ME}}\|} \tag{4.91}$$

and the constant parameter $\eta_{\uparrow}$. Since messenger substances are produced at the locations where osteocyte apoptosis takes place, i.e. in the vicinity of the crack tip, the migration of osteoclasts and osteoblasts is accordingly directed by the microdamage as is the case in real bones as discussed in detail in [100]. However, the bone structure itself also influences the path of the bone cells. In particular, new osteons result from bone remodelling processes so that, as a consequence, BMUs mostly move parallel to existing osteons [31]. In Fig. 4.8, this coincides with the longitudinal bone axis ($\boldsymbol{e}_1$-axis) which is typically the principal loading direction in the bone. Thus, the second and third term in (4.90) include the diffusion in bone axis direction on the one hand, and in the plane perpendicular to that axis on the other hand, with different constant scaling factors $\eta_{\parallel}$ and $\eta_{\perp}$. Vector $\boldsymbol{a}_{\mathrm{b}}$ accordingly represents the unit normal vector in x_1-direction which is aligned with the longitudinal bone axis, i.e. $\boldsymbol{a}_{\mathrm{b}} = \boldsymbol{e}_1$. By a proper choice of the three parameters $\eta_{\uparrow}$, $\eta_{\parallel}$ and $\eta_{\perp}$, the model can capture the preferred movement of BMUs in direction of osteon alignment in addition to the targeted BMU steering by the crack event, accordingly. Furthermore, the diffusion tensors in (4.88)-(4.89) ensure that osteoclasts and osteoblasts move in the same direction, or, in other words, that the latter move through the tunnels that would in reality have been excavated by osteoclasts beforehand. However, the coefficients D_{OC} and D_{OB} are, in general, not equal so that the two cell types can have different diffusion velocities. In addition, the diffusion tensor for osteoblasts includes the function

$$\Lambda(c_{\mathrm{OC}}) = \begin{cases} 1 & \text{if } c_{\mathrm{OC}} > 0, \\ 0 & \text{otherwise} \end{cases} \tag{4.92}$$

in order to ensure that osteoblasts can only travel through bone when osteoclasts are already present to clear the path. In the physical process considered, this behaviour incorporates a time delay, i.e. the migration of osteoblasts does not follow immediately

after the start of osteoclast movement. A time delay has not yet been captured in the proposed model. However, introduction of the function $\Lambda(c_{\mathrm{OC}})$ allows extensions in this regard, e.g. by including cell concentrations of previous time steps. An alternative is the introduction of separate signalling mechanisms for the osteoclast and osteoblast cells. This will be discussed in detail in Sect. 4.4.1.1.

A summary of the governing equations in the proposed modelling approach as well as of all source and flux terms is provided in Table 4.1.

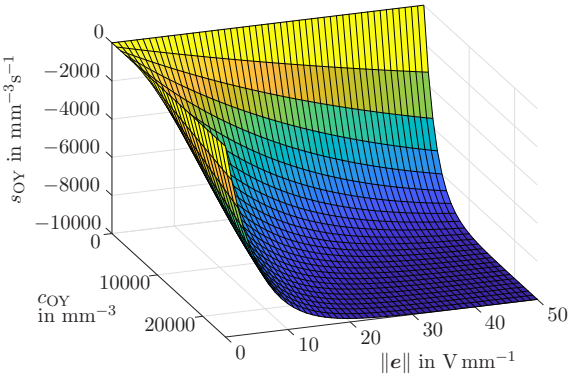

Figure 4.7: Sink term for the osteocyte concentration as a function of the electric field magnitude and of the cell concentration itself. In the initial state in which $c_{\mathrm{OY}} = 2.5 \times 10^4\,\mathrm{mm}^{-3}$ holds, the magnitude of the sink term increases rapidly when the electric field approaches a magnitude of $10\,\mathrm{V mm}^{-1}$. Reproduced from [174] under the terms of the Creative Commons Attribution License (CC BY).

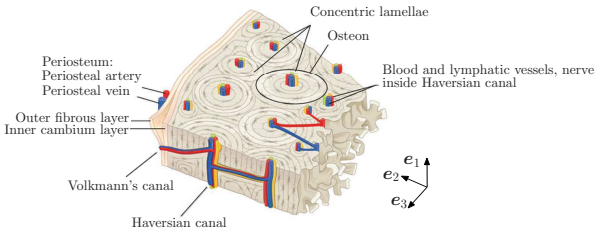

Figure 4.8: Structure of the cortical bone layer of a human femur. The $\boldsymbol{e}_1$-axis of the chosen coordinate system is aligned with the longitudinal axis of the bone which coincides with the main direction of osteon progression. Reproduced from [88] under the terms of the Creative Commons Attribution License (CC BY).

Remark 4.2. An alternative approach for the structural tensor $\boldsymbol{A}$ is

$$\boldsymbol{A} = \widetilde{\eta}_{\parallel} \left[\boldsymbol{a}_{\mathrm{b}} \otimes \boldsymbol{a}_{\mathrm{b}}\right] + \widetilde{\eta}_{\perp} \left[\boldsymbol{I} - \boldsymbol{a}_{\mathrm{b}} \otimes \boldsymbol{a}_{\mathrm{b}}\right] \tag{4.93}$$

in which $\widetilde{\eta}_{\parallel}$ and $\widetilde{\eta}_{\perp}$ are not constant parameters but rather functions of the gradient of messenger substances, i.e.

$$\widetilde{\eta}_{\parallel} = \eta_{\parallel} \left[\left[\boldsymbol{a}_{\mathrm{g}} \otimes \boldsymbol{a}_{\mathrm{g}}\right] : \left[\boldsymbol{a}_{\mathrm{b}} \otimes \boldsymbol{a}_{\mathrm{b}}\right]\right], \quad \widetilde{\eta}_{\perp} = \eta_{\perp} \left[\left[\boldsymbol{a}_{\mathrm{g}} \otimes \boldsymbol{a}_{\mathrm{g}}\right] : \left[\boldsymbol{I} - \boldsymbol{a}_{\mathrm{b}} \otimes \boldsymbol{a}_{\mathrm{b}}\right]\right]. \tag{4.94}$$

Thereby, a projection of this gradient onto the directions predefined by the bone structure is incorporated. However, this approach is not considered in the following since it leads to a physically less reasonable behaviour for the particular boundary value problem studied in Sect. 4.3.3.2 – steep concentration profiles are encountered in the vicinity of the crack tip and, moreover, diffusion of bone cells into the right part of the considered domain is suppressed.

Table 4.1: Governing balance equations, source terms and flux terms.

Balance equations	
$\mathbf{0} = \nabla_{\boldsymbol{x}} \cdot \boldsymbol{\sigma}_{\text{tot}}$	in Ω
$0 = \nabla_{\boldsymbol{x}} \cdot \boldsymbol{d}$	in Ω
$\dot{c}_{\text{OY}} = s_{\text{OY}}(\|\boldsymbol{e}\|, c_{\text{OY}})$	in Ω
$\dot{c}_{\text{ME}} = -\nabla_{\boldsymbol{x}} \cdot \boldsymbol{q}_{\text{ME}} + s_{\text{ME}}(c_{\text{OY}})$	in Ω
$\dot{c}_{\text{OC}} = -\nabla_{\boldsymbol{x}} \cdot \boldsymbol{q}_{\text{OC}}$	in Ω
$\dot{c}_{\text{OB}} = -\nabla_{\boldsymbol{x}} \cdot \boldsymbol{q}_{\text{OB}}$	in Ω

Source terms	Flux terms
$s_{\text{OY}} = -k_{\text{OY},1}\left[1 - \exp\left(-\frac{\|\boldsymbol{e}\|}{e_{\text{crit}}}\frac{c_{\text{OY}}}{k_{\text{OY},2}}\right)\right]$	$\boldsymbol{q}_{\text{ME}} = -D_{\text{ME}}\,\nabla_{\boldsymbol{x}} c_{\text{ME}}$
$s_{\text{ME}} = k_{\text{ME}}\left[1 - \frac{c_{\text{OY}}}{c_{\text{OY}}^{\text{init}}}\right]$	$\boldsymbol{q}_{\text{OC}} = -\boldsymbol{D}_{\text{OC}} \cdot \nabla_{\boldsymbol{x}} c_{\text{OC}}$
	$\boldsymbol{q}_{\text{OB}} = -\boldsymbol{D}_{\text{OB}} \cdot \nabla_{\boldsymbol{x}} c_{\text{OB}}$
	$\boldsymbol{D}_{\text{OC}} = D_{\text{OC}}\,\boldsymbol{A}$
	$\boldsymbol{D}_{\text{OB}} = \Lambda(c_{\text{OC}})\,D_{\text{OB}}\,\boldsymbol{A}$

4.3.1.2 Balance of energy

In Sect. 4.1.1.2, the balance of energy has been derived for an electromechanically coupled framework including flexoelectricity. In this section, these derivations are extended with respect to the chemical contributions from the bone cell concentrations while the electrical and mechanical contributions are equal. Accordingly, the integral form of the balance of energy reads

$$\dot{\mathcal{H}} + \dot{\mathcal{K}} = \mathcal{P}_{\text{mech}} + \mathcal{P}_{\text{elec}} + \mathcal{Q}_{\text{chem}} + \mathcal{Q}_{\text{therm}} \tag{4.95}$$

with the (mass-specific) electric enthalpy density H as thermodynamic potential. A detailed discussion on alternative choices for the thermodynamic potential can be found in Sect. 4.1.1.3. In Sect. 4.1.1.2, the rates of electric enthalpy and kinetic energy, $\dot{\mathcal{H}}$ and $\dot{\mathcal{K}}$, as well as the mechanical and electrical powers $\mathcal{P}_{\text{mech}}$ and $\mathcal{P}_{\text{elec}}$ have been specified. In order to incorporate the activity of bone cells into the model proposed in this work, external chemical contributions are additionally considered including the source terms (4.83)-(4.84) per unit volume as well as the chemical fluxes introduced in (4.85)-(4.87), i.e.

$$\mathcal{Q}_{\text{chem,OY}} = \int_{\Omega} \mu_{\text{OY}}^{c}\, s_{\text{OY}}\, \mathrm{d}v =: \int_{\Omega} Q_{\text{OY}}\, \mathrm{d}v \tag{4.96}$$

$$\begin{aligned}\mathcal{Q}_{\text{chem,ME}} &= \int_{\partial\Omega} \mu^c_{\text{ME}}\, q_{\text{ME}}\, \mathrm{d}a \,+\, \int_{\Omega} \mu^c_{\text{ME}}\, s_{\text{ME}}\, \mathrm{d}v \\ &= -\int_{\Omega} \nabla_{\boldsymbol{x}} \cdot [\mu^c_{\text{ME}}\, \boldsymbol{q}_{\text{ME}}]\, \mathrm{d}v + \int_{\Omega} \mu^c_{\text{ME}}\, s_{\text{ME}}\, \mathrm{d}v =: \int_{\Omega} Q_{\text{ME}}\, \mathrm{d}v \end{aligned} \tag{4.97}$$

$$\mathcal{Q}_{\text{chem,OC}} = \int_{\partial\Omega} \mu^c_{\text{OC}}\, q_{\text{OC}}\, \mathrm{d}a = -\int_{\Omega} \nabla_{\boldsymbol{x}} \cdot [\mu^c_{\text{OC}}\, \boldsymbol{q}_{\text{OC}}]\, \mathrm{d}v =: \int_{\Omega} Q_{\text{OC}}\, \mathrm{d}v \tag{4.98}$$

$$\mathcal{Q}_{\text{chem,OB}} = \int_{\partial\Omega} \mu^c_{\text{OB}}\, q_{\text{OB}}\, \mathrm{d}a = -\int_{\Omega} \nabla_{\boldsymbol{x}} \cdot [\mu^c_{\text{OB}}\, \boldsymbol{q}_{\text{OB}}]\, \mathrm{d}v =: \int_{\Omega} Q_{\text{OB}}\, \mathrm{d}v \tag{4.99}$$

with the chemical potentials μ^c_{OY}, μ^c_{ME}, μ^c_{OC} and μ^c_{OB}, respectively, cf. [8, 133]. In addition, the relations

$$q_{\text{ME}} = -\,\boldsymbol{q}_{\text{ME}} \cdot \boldsymbol{n}, \quad q_{\text{OC}} = -\,\boldsymbol{q}_{\text{OC}} \cdot \boldsymbol{n}, \quad q_{\text{OB}} = -\,\boldsymbol{q}_{\text{OB}} \cdot \boldsymbol{n} \tag{4.100}$$

are used therein with $\boldsymbol{n}$ the surface outward normal unit vector.

Taking these derivations into account together with the (dynamic version of the) balance of linear momentum (4.82a) and Gauss's law (4.82b), the balance of energy (4.95) can be rewritten as

$$\begin{aligned}\int_{\Omega} \rho\, \dot{H}\, \mathrm{d}v = &\int_{\Omega} [\nabla_{\boldsymbol{x}} \dot{\boldsymbol{u}}] : \boldsymbol{\sigma}\, \mathrm{d}v + \int_{\Omega} [\nabla_{\boldsymbol{x}} \nabla_{\boldsymbol{x}} \dot{\boldsymbol{u}}] :\cdot\, \boldsymbol{\pi}\, \mathrm{d}v + \int_{\Omega} \nabla_{\boldsymbol{x}} \dot{\phi} \cdot \boldsymbol{d}\, \mathrm{d}v \\ &+ \int_{\Omega} Q_{\text{OY}}\, \mathrm{d}v + \int_{\Omega} Q_{\text{ME}}\, \mathrm{d}v + \int_{\Omega} Q_{\text{OC}}\, \mathrm{d}v + \int_{\Omega} Q_{\text{OB}}\, \mathrm{d}v \\ &+ \int_{\Omega} Q_{\text{th}}\, \mathrm{d}v \end{aligned} \tag{4.101}$$

and the local form results in

$$\rho\, \dot{H} = \dot{\boldsymbol{\varepsilon}} : \boldsymbol{\sigma} + \nabla_{\boldsymbol{x}} \dot{\boldsymbol{\varepsilon}} :\cdot\, \boldsymbol{\pi} - \dot{\boldsymbol{e}} \cdot \boldsymbol{d} + Q_{\text{OY}} + Q_{\text{ME}} + Q_{\text{OC}} + Q_{\text{OB}} + Q_{\text{th}}. \tag{4.102}$$

4.3.1.3 Dissipation inequality

In Sect. 4.1.1.4, the Clausius-Duhem inequality (4.29) has been derived for the electromechanical coupling under consideration. In the context of bone remodelling, chemical contributions are additionally taken into account so that the thermal power can be expressed as

$$Q_{\text{th}} = \rho\, \dot{H} - \dot{\boldsymbol{\varepsilon}} : \boldsymbol{\sigma} - \nabla_{\boldsymbol{x}} \dot{\boldsymbol{\varepsilon}} :\cdot\, \boldsymbol{\pi} + \dot{\boldsymbol{e}} \cdot \boldsymbol{d} - Q_{\text{OY}} - Q_{\text{ME}} - Q_{\text{OC}} - Q_{\text{OB}} \tag{4.103}$$

by rearranging the local form of balance of energy (4.102). Therein, the chemical powers $Q_\bullet$ with $\bullet \in \{\text{OY}, \text{ME}, \text{OC}, \text{OB}\}$ can be specified by using the diffusion equations (4.82c)-(4.82f) together with the definitions (4.96)-(4.99) such that

$$Q_\bullet = \mu_\bullet^c\, s_\bullet - \nabla_{\boldsymbol{x}} \cdot [\mu_\bullet^c\, \boldsymbol{q}_\bullet] = \underbrace{\mu_\bullet^c\, s_\bullet - \mu_\bullet^c\, \nabla_{\boldsymbol{x}} \cdot \boldsymbol{q}_\bullet}_{=\,\mu_\bullet^c\, \dot{c}_\bullet} - \boldsymbol{q}_\bullet \cdot \nabla_{\boldsymbol{x}} \mu_\bullet^c$$
$$= \mu_\bullet^c\, \dot{c}_\bullet - \boldsymbol{q}_\bullet \cdot \nabla_{\boldsymbol{x}} \mu_\bullet^c \tag{4.104}$$

with the chemical potential $\mu_\bullet^c$ describing the change of energy in response to a change of concentration $c_\bullet$ of the respective species.

The time derivative of the electric enthalpy density in (4.103) is obtained by using a Legendre(-Fenchel) transformation in form of (4.22) with respect to temperature θ and mass-specific entropy density s, accordingly

$$\dot{H} = \frac{\partial H^*}{\partial \boldsymbol{\varepsilon}} : \dot{\boldsymbol{\varepsilon}} + \frac{\partial H^*}{\partial \nabla_{\boldsymbol{x}} \boldsymbol{\varepsilon}} :\cdot \nabla_{\boldsymbol{x}} \dot{\boldsymbol{\varepsilon}} + \frac{\partial H^*}{\partial \boldsymbol{e}} \cdot \dot{\boldsymbol{e}} + \frac{\partial H^*}{\partial \theta}\, \dot{\theta} + \sum_\bullet \frac{\partial H^*}{\partial c_\bullet}\, \dot{c}_\bullet + \theta\, \dot{s} + s\, \dot{\theta}. \tag{4.105}$$

Inserting (4.103) and (4.105) into the Clausius-Duhem inequality (4.29) and rearranging terms, the inequality takes the form

$$\mathcal{D} = \left[\boldsymbol{\sigma} - \rho \frac{\partial H^*}{\partial \boldsymbol{\varepsilon}}\right] : \dot{\boldsymbol{\varepsilon}} + \left[\boldsymbol{\pi} - \rho \frac{\partial H^*}{\partial \nabla_{\boldsymbol{x}} \boldsymbol{\varepsilon}}\right] :\cdot \nabla_{\boldsymbol{x}} \dot{\boldsymbol{\varepsilon}} + \left[-\boldsymbol{d} - \rho \frac{\partial H^*}{\partial \boldsymbol{e}}\right] \cdot \dot{\boldsymbol{e}}$$
$$+ \left[-\rho\, s - \rho \frac{\partial H^*}{\partial \theta}\right] \dot{\theta} + \sum_\bullet \left[\left[\mu_\bullet^c - \rho \frac{\partial H^*}{\partial c_\bullet}\right] \dot{c}_\bullet - \boldsymbol{q}_\bullet \cdot \nabla_{\boldsymbol{x}} \mu_\bullet^c\right]$$
$$- \boldsymbol{q}_{\mathrm{th}} \cdot \nabla_{\boldsymbol{x}} \ln(\theta) \geq 0 \tag{4.106}$$

and the constitutive relations result in

$$\boldsymbol{\sigma} = \rho \frac{\partial H^*}{\partial \boldsymbol{\varepsilon}}, \quad \boldsymbol{\pi} = \rho \frac{\partial H^*}{\partial \nabla_{\boldsymbol{x}} \boldsymbol{\varepsilon}}, \quad \boldsymbol{d} = -\rho \frac{\partial H^*}{\partial \boldsymbol{e}}, \quad s = -\frac{\partial H^*}{\partial \theta}, \quad \mu_\bullet^c = \rho \frac{\partial H^*}{\partial c_\bullet}. \tag{4.107}$$

The remaining expression in (4.106) is referred to as "reduced dissipation inequality" and reads

$$\sum_\bullet [-\boldsymbol{q}_\bullet \cdot \nabla_{\boldsymbol{x}} \mu_\bullet^c] - \boldsymbol{q}_{\mathrm{th}} \cdot \nabla_{\boldsymbol{x}} \ln(\theta) \geq 0, \tag{4.108}$$

which includes thermal and chemical contributions only, cf. [8, 133]. In [6, 133], further details are provided on chemical thermodynamics in particular.

4.3.2 Isogeometric finite element formulation

Isogeometric analysis is used in this work in order to solve the governing system of partial differential equations (4.82). Since flexoelectricity couples electric polarisation with strain gradients, cf. (4.1), and (in general) leads to a partial differential equation of fourth order, global C^1-continuity is at least required within the underlying finite element scheme, see the discussion in Sect. 4.1.2.1. The weak form of the governing

equations is derived in the following and the discretisation is performed by means of C^1-continuous NURBS basis functions.

4.3.2.1 Weak form of the governing equations

The weak form of the balance of linear momentum and Gauss's law including flexoelectricity has been derived in Sect. 4.1.2.1. Analogously, the weak formulation of the rate equations (4.82c)-(4.82f) is obtained by introducing test functions for the chemical concentrations. Accordingly, multiplying (4.82c) with a virtual osteocyte concentration, respectively test function, δc_{OY} and integrating over the domain Ω yields the weak form

$$0 = \int_{\Omega} \delta c_{\mathrm{OY}}\, \dot{c}_{\mathrm{OY}}\, \mathrm{d}v - \int_{\Omega} \delta c_{\mathrm{OY}}\, s_{\mathrm{OY}}\, \mathrm{d}v. \tag{4.109}$$

For the rate equation of messenger substances (4.82d), the virtual concentration, respectively test function, δc_{ME} is employed and leads to

$$\begin{aligned} 0 &= \int_{\Omega} \delta c_{\mathrm{ME}}\, \dot{c}_{\mathrm{ME}}\, \mathrm{d}v + \int_{\Omega} \delta c_{\mathrm{ME}}\, \nabla_{\boldsymbol{x}} \cdot \boldsymbol{q}_{\mathrm{ME}}\, \mathrm{d}v - \int_{\Omega} \delta c_{\mathrm{ME}}\, s_{\mathrm{ME}}\, \mathrm{d}v \\ &= \int_{\Omega} \delta c_{\mathrm{ME}}\, \dot{c}_{\mathrm{ME}}\, \mathrm{d}v - \int_{\Omega} \nabla_{\boldsymbol{x}} \delta c_{\mathrm{ME}} \cdot \boldsymbol{q}_{ME}\, \mathrm{d}v \\ &\quad - \int_{\partial\Omega} \delta c_{\mathrm{ME}}\, q_{\mathrm{ME}}\, \mathrm{d}a - \int_{\Omega} \delta c_{\mathrm{ME}}\, s_{\mathrm{ME}}\, \mathrm{d}v \end{aligned} \tag{4.110}$$

where integration by parts as well as the divergence theorem have been used. Similarly, (4.82e) and (4.82f) which refer to the osteoclast and osteoblast concentrations are transferred into their corresponding weak formulations by using the virtual concentrations, respectively test functions, δc_{OC} and δc_{OB} which yields

$$0 = \int_{\Omega} \delta c_{\mathrm{OC}}\, \dot{c}_{\mathrm{OC}}\, \mathrm{d}v - \int_{\Omega} \nabla_{\boldsymbol{x}} \delta c_{\mathrm{OC}} \cdot \boldsymbol{q}_{OC}\, \mathrm{d}v - \int_{\partial\Omega} \delta c_{\mathrm{OC}}\, q_{\mathrm{OC}}\, \mathrm{d}a \tag{4.111}$$

and

$$0 = \int_{\Omega} \delta c_{\mathrm{OB}}\, \dot{c}_{\mathrm{OB}}\, \mathrm{d}v - \int_{\Omega} \nabla_{\boldsymbol{x}} \delta c_{\mathrm{OB}} \cdot \boldsymbol{q}_{OB}\, \mathrm{d}v - \int_{\partial\Omega} \delta c_{\mathrm{OB}}\, q_{\mathrm{OB}}\, \mathrm{d}a. \tag{4.112}$$

4.3.2.2 Discretised weak forms

The spatial discretisation of the weak forms derived in Sect. 4.3.2.1 is performed under the use of NURBS basis functions R and by employing an isoparametric Bubnov-

Galerkin approach. The discretised test functions for the unknown mechanical, electrical and chemical fields follow as

$$\delta \boldsymbol{u}^e = \sum_{A=1}^{\mathrm{n_{en}}} \delta \boldsymbol{u}^A R^A, \quad \delta \phi^e = \sum_{A=1}^{\mathrm{n_{en}}} \delta \phi^A R^A, \quad \delta c_\bullet^e = \sum_{A=1}^{\mathrm{n_{en}}} \delta c_\bullet^A R^A \tag{4.113}$$

with $\bullet \in \{\mathrm{OY}, \mathrm{ME}, \mathrm{OC}, \mathrm{OB}\}$.

For the time discretisation, a Backward-Euler scheme is applied so that the time derivative of the concentration $c_\bullet$ is approximated by

$$\dot{c}_\bullet \approx \frac{c_{\bullet,n+1} - c_{\bullet,n}}{\Delta t} \tag{4.114}$$

with time increment Δt and with index n denoting the respective time step. In the following, all quantities corresponding to this time step are marked with subscript n while all other (non-marked) quantities correspond to the time step $n+1$.

Considering the discretisation in both space and time, the discretised weak forms lead to the discrete residual vectors

$$\boldsymbol{r}_{\boldsymbol{u}} = \mathop{\mathsf{A}}_{e=1}^{\mathrm{n_{el}}} \sum_{A=1}^{\mathrm{n_{en}}} \int_{\Omega^e} \boldsymbol{\sigma} \cdot \nabla_{\boldsymbol{x}} R^A \,\mathrm{d}v + \int_{\Omega^e} \boldsymbol{\pi} : \nabla_{\boldsymbol{x}} \nabla_{\boldsymbol{x}} R^A \,\mathrm{d}v - \int_{\partial\Omega^e} \boldsymbol{t}\, R^A \,\mathrm{d}a \tag{4.115}$$

$$\boldsymbol{r}_{\phi} = \mathop{\mathsf{A}}_{e=1}^{\mathrm{n_{el}}} \sum_{A=1}^{\mathrm{n_{en}}} \int_{\Omega^e} \boldsymbol{d} \cdot \nabla_{\boldsymbol{x}} R^A \,\mathrm{d}v + \int_{\partial\Omega^e} \omega\, R^A \,\mathrm{d}a \tag{4.116}$$

$$\boldsymbol{r}_{\mathrm{OY}} = \mathop{\mathsf{A}}_{e=1}^{\mathrm{n_{el}}} \sum_{A=1}^{\mathrm{n_{en}}} \int_{\Omega^e} R^A \,\frac{c_{\mathrm{OY}} - c_{\mathrm{OY},n}}{\Delta t} \,\mathrm{d}v - \int_{\Omega^e} R^A \, s_{\mathrm{OY}} \,\mathrm{d}v \tag{4.117}$$

$$\begin{aligned} \boldsymbol{r}_{\mathrm{ME}} = \mathop{\mathsf{A}}_{e=1}^{\mathrm{n_{el}}} \sum_{A=1}^{\mathrm{n_{en}}} & \int_{\Omega^e} R^A \,\frac{c_{\mathrm{ME}} - c_{\mathrm{ME},n}}{\Delta t} \,\mathrm{d}v - \int_{\Omega^e} \nabla_{\boldsymbol{x}} R^A \cdot \boldsymbol{q}_{\mathrm{ME}} \,\mathrm{d}v \\ & - \int_{\partial\Omega^e} R^A \, q_{\mathrm{ME}} \,\mathrm{d}a - \int_{\Omega^e} R^A \, s_{\mathrm{ME}} \,\mathrm{d}v \end{aligned} \tag{4.118}$$

$$\begin{aligned} \boldsymbol{r}_{\mathrm{OC}} = \mathop{\mathsf{A}}_{e=1}^{\mathrm{n_{el}}} \sum_{A=1}^{\mathrm{n_{en}}} & \int_{\Omega^e} R^A \,\frac{c_{\mathrm{OC}} - c_{\mathrm{OC},n}}{\Delta t} \,\mathrm{d}v - \int_{\Omega^e} \nabla_{\boldsymbol{x}} R^A \cdot \boldsymbol{q}_{\mathrm{OC}} \,\mathrm{d}v \\ & - \int_{\partial\Omega^e} R^A \, q_{\mathrm{OC}} \,\mathrm{d}a \end{aligned} \tag{4.119}$$

$$\begin{aligned} \boldsymbol{r}_{\mathrm{OB}} = \mathop{\mathsf{A}}_{e=1}^{\mathrm{n_{el}}} \sum_{A=1}^{\mathrm{n_{en}}} & \int_{\Omega^e} R^A \,\frac{c_{\mathrm{OB}} - c_{\mathrm{OB},n}}{\Delta t} \,\mathrm{d}v - \int_{\Omega^e} \nabla_{\boldsymbol{x}} R^A \cdot \boldsymbol{q}_{\mathrm{OB}} \,\mathrm{d}v \\ & - \int_{\partial\Omega^e} R^A \, q_{\mathrm{OB}} \,\mathrm{d}a. \end{aligned} \tag{4.120}$$

The corresponding tangent contributions are provided in Appendix C.1.1.

4.3.3 Simulation of flexoelectricity-induced initiation of bone remodelling

The proposed modelling approach is applied to bone remodelling processes within cortical bone. The specific constitutive model including the particular structure of the piezoelectricity as well as flexoelectricity tensors used therein is discussed in the following. Afterwards, the initial boundary value problem addressed within the scope of this work is described in detail and the finite element discretisation of the cortical bone specimen under investigation is presented.

4.3.3.1 Specification of the constitutive model

The chosen form of the free electric enthalpy density is based on the electromechanical contributions proposed in Sect. 4.1.3.1 together with additional chemical terms. Under isothermal conditions, this stipulates the formulation

$$\rho\, H^* = \frac{1}{2}\,\boldsymbol{\varepsilon} : \mathbf{E} : \boldsymbol{\varepsilon} - \frac{1}{2}\,\boldsymbol{e}\cdot\boldsymbol{\chi}\cdot\boldsymbol{e} - \boldsymbol{e}\cdot\mathbf{e} : \boldsymbol{\varepsilon} - \boldsymbol{e}\cdot\boldsymbol{\mu} :\cdot \nabla_{\boldsymbol{x}}\boldsymbol{\varepsilon} + \sum_{\bullet}\frac{1}{2}\,\gamma_{\bullet}\, c_{\bullet}^{2}. \tag{4.121}$$

Therein, $\mathbf{E}$ denotes the fourth-order elasticity tensor, $\boldsymbol{\chi}$ is the second-order permittivity tensor and $\mathbf{e}$ represents the third-order piezoelectricity tensor which couples mechanical strains with the electric field. The flexoelectricity tensor $\boldsymbol{\mu}$ is of fourth order as introduced in (4.1). The constants $\gamma_{\bullet}$ relate the respective chemical potentials to the concentrations of the corresponding species $\bullet \in \{\mathrm{OY,ME,OC,OB}\}$. In virtue of (4.107)-(4.108) and (4.85)-(4.87), choosing $\gamma_{\bullet} > 0$ results in thermodynamically consistent relations for the diffusion processes considered. As this work proceeds, the parameters $\gamma_{\bullet}$ will, however, remain unspecified since they do not appear in the governing equations (4.82) or in the corresponding weak forms and stiffness contributions, see Sect. 4.3.2.

The constitutive relations can be derived from the free electric enthalpy density function (4.121) by following (4.107) and result in

$$\boldsymbol{\sigma} = \mathbf{E} : \boldsymbol{\varepsilon} - \boldsymbol{e}\cdot\mathbf{e}, \tag{4.122}$$

$$\boldsymbol{\pi} = -\,\boldsymbol{e}\cdot\boldsymbol{\mu}, \tag{4.123}$$

$$\boldsymbol{d} = \boldsymbol{\chi}\cdot\boldsymbol{e} + \mathbf{e} : \boldsymbol{\varepsilon} + \boldsymbol{\mu} :\cdot \nabla_{\boldsymbol{x}}\boldsymbol{\varepsilon}, \tag{4.124}$$

$$\mu_{\bullet}^{c} = \gamma_{\bullet}\, c_{\bullet}. \tag{4.125}$$

As a direct consequence of (4.123) together with (4.5), the electric field gradient contributes to the total stress tensor $\boldsymbol{\sigma}_{\mathrm{tot}}$ through the divergence of the hyper-stress tensor, i.e.

$$\boldsymbol{\sigma}_{\mathrm{tot}} = \mathbf{E} : \boldsymbol{\varepsilon} - \boldsymbol{e}\cdot\mathbf{e} + \nabla_{\boldsymbol{x}}\cdot\left[\boldsymbol{e}\cdot\boldsymbol{\mu}\right]. \tag{4.126}$$

As discussed in Sect. 4.1.3.1, the constitutive model includes contributions from both direct and converse flexoelectric effects, accordingly.

The material tensors incorporated in the free electric enthalpy density function (4.121) are specified in the following with regard to the characteristics of cortical bone material. In this context, a Voigt-type notation is employed so that the stress and hyper-stress tensor, as well as the strain tensor and its gradient are written as

$$
\begin{aligned}
{}^{\text{Voi}}[\boldsymbol{\sigma}] &= [\sigma_{11}, \sigma_{22}, \sigma_{33}, \sigma_{23}, \sigma_{13}, \sigma_{12}]^{\text{t}}\,, && (4.127)\\
{}^{\text{Voi}}[\boldsymbol{\pi}] &= \big[\pi_{111}, \pi_{112}, \pi_{113}, \pi_{221}, \pi_{222}, \pi_{223}, \pi_{331}, \pi_{332}, \pi_{333},\\
&\qquad \pi_{231}, \pi_{232}, \pi_{233}, \pi_{131}, \pi_{132}, \pi_{133}, \pi_{121}, \pi_{122}, \pi_{123}\big]^{\text{t}}, && (4.128)\\
[\boldsymbol{\varepsilon}]^{\text{Voi}} &= [\varepsilon_{11}, \varepsilon_{22}, \varepsilon_{33}, 2\,\varepsilon_{23}, 2\,\varepsilon_{13}, 2\,\varepsilon_{12}]^{\text{t}}\,, && (4.129)\\
[\nabla_{\boldsymbol{x}}\boldsymbol{\varepsilon}]^{\text{Voi}} &= \big[\varepsilon_{11,1}, \varepsilon_{11,2}, \varepsilon_{11,3}, \varepsilon_{22,1}, \varepsilon_{22,2}, \varepsilon_{22,3}, \varepsilon_{33,1}, \varepsilon_{33,2}, \varepsilon_{33,3}, 2\,\varepsilon_{23,1},\\
&\qquad 2\,\varepsilon_{23,2}, 2\,\varepsilon_{23,3}, 2\,\varepsilon_{13,1}, 2\,\varepsilon_{13,2}, 2\,\varepsilon_{13,3}, 2\,\varepsilon_{12,1}, 2\,\varepsilon_{12,2}, 2\,\varepsilon_{12,3}\big]^{\text{t}}. && (4.130)
\end{aligned}
$$

Cortical bone is mainly composed of an inorganic phase, more precisely the mineral hydroxyapatite [$Ca_{10}(PO_4)_6(OH)_2$], and an organic matrix primarily formed by type I collagen, see [83, 110]. Transversely isotropic properties have been found in terms of the elastic behaviour of this material with the longitudinal bone axis, i.e. the direction of osteon alignment, as the preferred direction, cf. Fig. 4.8. In [52], different elastic moduli have been observed in experiments with femur bone samples depending on the loading direction, namely longitudinal or transverse. Accordingly, a transversely isotropic material behaviour is considered for the cortical bone material investigated in the present contribution. The elasticity tensor can thus be written as

$$
{}^{\text{Voi}}[\mathbf{E}] = \begin{bmatrix}
E_{1111} & E_{1122} & E_{1122} & 0 & 0 & 0\\
E_{1122} & E_{2222} & E_{2233} & 0 & 0 & 0\\
E_{1122} & E_{2233} & E_{2222} & 0 & 0 & 0\\
0 & 0 & 0 & E_{2323} & 0 & 0\\
0 & 0 & 0 & 0 & E_{1313} & 0\\
0 & 0 & 0 & 0 & 0 & E_{1313}
\end{bmatrix} \qquad (4.131)
$$

with

$$
\begin{aligned}
E_{1111} &= D\left[\frac{1-\nu_{\perp}^2}{Y_{\perp}^2}\right], & E_{2222} &= D\left[\frac{1}{Y_{\perp}\,Y_{\parallel}} - \frac{\nu_{\parallel}^2}{Y_{\parallel}^2}\right],\\
E_{1122} &= D\left[\frac{[1+\nu_{\perp}]\,\nu_{\parallel}}{Y_{\perp}\,Y_{\parallel}}\right], & E_{2233} &= D\left[\frac{\nu_{\perp}}{Y_{\perp}\,Y_{\parallel}} + \frac{\nu_{\parallel}^2}{Y_{\parallel}^2}\right],\\
E_{2323} &= G_{\perp}, & E_{1313} &= G_{\parallel},
\end{aligned}
$$

$$\nu_\perp = \frac{Y_\perp}{2\,G_\perp} - 1, \qquad D = \frac{Y_\perp^2\, Y_\parallel^2}{[1+\nu_\perp]\left[[1-\nu_\perp]\, Y_\parallel - 2\,\nu_\parallel^2 Y_\perp\right]}, \tag{4.132}$$

and with the x_1-axis being the longitudinal bone axis, cf. Fig. 4.8 and [114]. The five independent material parameters therein are, in general, dependent on the porosity of the bone material which has been investigated in detail in [52]. Within the scope of this work, mean values are employed, see Table 4.2.

In accordance with [15, 57, 58, 62], the permittivity tensor as well as the piezoelectricity tensor take the form

$$[\boldsymbol{\chi}] = \begin{bmatrix} \chi_{11} & 0 & 0 \\ 0 & \chi_{22} & 0 \\ 0 & 0 & \chi_{22} \end{bmatrix} \tag{4.133}$$

and

$$^{\text{Voi}}[\mathbf{e}] = \begin{bmatrix} \mathsf{e}_{111} & \mathsf{e}_{122} & \mathsf{e}_{122} & 0 & 0 & 0 \\ 0 & 0 & 0 & 0 & \mathsf{e}_{213} & \mathsf{e}_{212} \\ 0 & 0 & 0 & 0 & \mathsf{e}_{212} & -\mathsf{e}_{213} \end{bmatrix} \tag{4.134}$$

considering a hexagonal symmetry structure. The piezoelectric behaviour of bone is attributed to the collagen fibres which are arranged in spiral structures along the bone axis, cf. [15, 57, 65]. It is noted that the matrices (4.133) and (4.134) correspond to a setting where this axis coincides with the first coordinate axis, which differs from the forms given in the mentioned references. As a consequence of the entries in the third row of the piezoelectricity tensor, out-of-plane polarisation can, in general, occur.

For the flexoelectricity tensor, cubic symmetry is assumed in accordance with the underlying experimental studies in [120, 164]. The tensor can be written in Voigt-type notation as

$$^{\text{Voi}}[\boldsymbol{\mu}] = \begin{bmatrix} \mu_{1111} & 0 & 0 & \mu_{1221} & 0 & 0 & \mu_{1221} & 0 & 0 \\ 0 & \mu_{1221} & 0 & 0 & \mu_{1111} & 0 & 0 & \mu_{1221} & 0 \\ 0 & 0 & \mu_{1221} & 0 & 0 & \mu_{1221} & 0 & 0 & \mu_{1111} \\ 0 & 0 & 0 & 0 & 0 & \mu_{1133} & 0 & \mu_{1133} & 0 \\ 0 & 0 & \mu_{1133} & 0 & 0 & 0 & \mu_{1133} & 0 & 0 \\ 0 & \mu_{1133} & 0 & \mu_{1133} & 0 & 0 & 0 & 0 & 0 \end{bmatrix}, \tag{4.135}$$

see [146]. In this reference as well as in [89, 90], detailed investigations on the symmetry of the flexoelectricity tensor have been carried out. Since the flexoelectricity tensor relates a third-order tensor to a tensor of first order, the symmetry properties are not as intuitive as for other well-known fourth-order tensors such as the elasticity tensor. In the experimental works in [120, 164], only the coefficients $\mu_{1111} = \mu_{1221}$ are considered non-

zero, whereas $\mu_{1133} = 0$ is assumed in consistency with the assumptions made in Sect. 4.1.3.1. Since the simulations in the present contribution are based on the experimental evidence from [120], the same assumption is employed for the flexoelectric coefficients in (4.135). However, it shall be noted that further research on the flexoelectric coefficients for bone material might eventually lead to more information on the shear components and could straightforwardly be incorporated into the proposed model. Together with the two-dimensional setting considered, the assumption of vanishing shear coefficients yields that only the top left block of the flexoelectricity tensor in form of (4.135), including the first two rows and the first five columns, contributes to the electromechanical coupling in the simulations in this work. For the calculation of the respective value $\mu_{1111} = \mu_{1221} = \mu_{\text{eff}}$, the relation

$$\mu_{\text{eff}} = f_{\text{eff}}\,\epsilon = f_{\text{eff}}\,\epsilon_0\,\epsilon_r \tag{4.136}$$

is used with $f_{\text{eff}} = 11\,\text{V}$, cf. [120], and with the relative dielectric constant chosen as $\epsilon_r = 10$ in accordance with [164]. The complete set of material parameters is summarised in Table 4.2.

Table 4.2: Material parameters for cortical bone.

	$Y_\parallel$	$Y_\perp$	$G_\parallel$	$G_\perp$	$\nu_\parallel$
value	1.661×10^4	9.55×10^3	4.74×10^3	3.28×10^3	0.37
unit	N mm^{-2}	N mm^{-2}	N mm^{-2}	N mm^{-2}	-

	χ_{11}	χ_{22}	$\mu_{1111} = \mu_{1221}$	μ_{1133}
value	106.248×10^{-3}	8.854×10^{-2}	9.739×10^{-4}	0.0
unit	$\text{nCV}^{-1}\text{mm}^{-1}$	$\text{nCV}^{-1}\text{mm}^{-1}$	nCmm^{-1}	nCmm^{-1}

	e_{111}	e_{122}	e_{213}	e_{212}
value	1.872	1.507	0.0	3.576
unit	nCmm^{-2}	nCmm^{-2}	nCmm^{-2}	nCmm^{-2}

4.3.3.2 Initial boundary value problem

The process of bone remodelling is addressed in this work on the basis of flexoelectricity-induced electric fields which lead to osteocyte apoptosis. Since flexoelectricity converts mechanical energy into electrical energy by coupling strain gradients to electric polarisation, the effect is particularly relevant in the vicinity of cracks where large strain gradients occur. For this reason, a small excerpt of cortical bone including a narrow radial crack is investigated in this section. The bone excerpt is assumed to be located in a femur with the x_1-axis being the longitudinal bone axis, see Fig. 4.8. Specifically

speaking, the sample is taken from the cortical bone layer in the diaphysis of the bone, i.e. the bone shaft as illustrated in Fig. 4.9. The crack is extended in radial direction, respectively x_2-direction with respect to the underlying coordinate system.

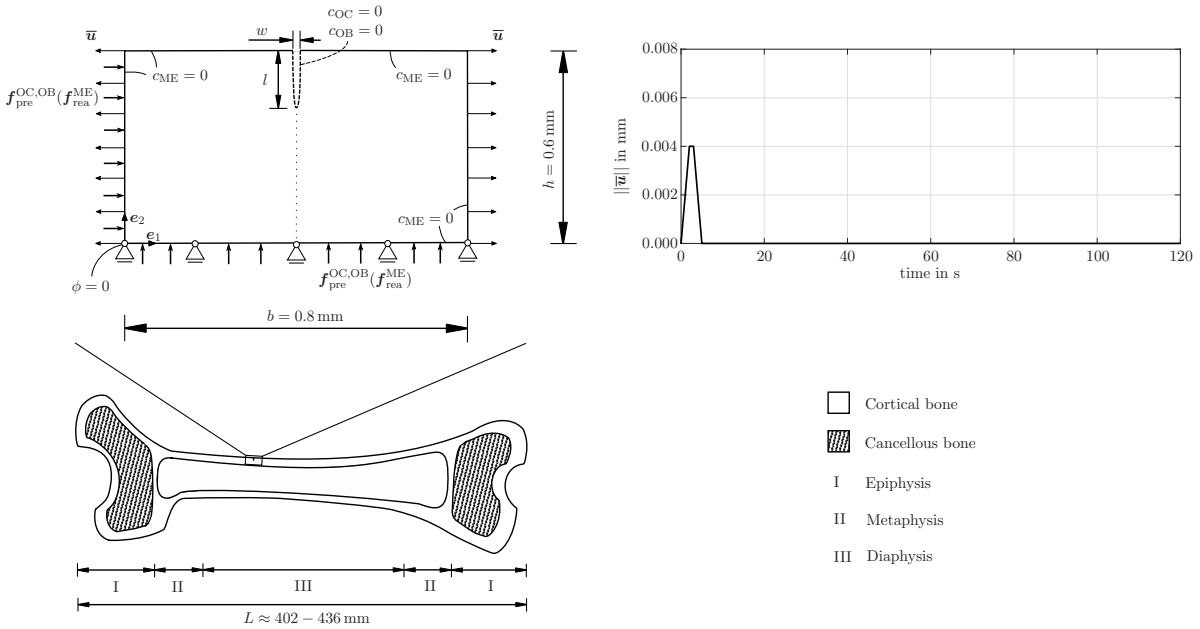

Figure 4.9: Sketch of a human femur including its average length measured by [112]. The cortical bone sample under investigation in this work is located in the diaphysis of the bone. The initial boundary value problem in the IGA simulations is shown and the load curve which characterises the tensile load prescribed on the left and right boundaries of a cracked domain is presented. Reproduced from [174] under the terms of the Creative Commons Attribution License (CC BY).

Fig. 4.9 also presents the geometry of the specimen under investigation as well as the prescribed boundary conditions. In particular, a two-dimensional setting and plane strain conditions are employed. The specimen is subjected to a mechanical load in terms of Dirichlet boundary conditions. To be precise, a displacement is prescribed in direction of the longitudinal bone axis and leads to tensile loading. This setting can be associated with the end of the crack event. The corresponding load curve is shown in Fig. 4.9. The load is prescribed in terms of one pulse over a time period of 5 s. Thereafter, the bone is left at rest while the diffusion processes associated with the bone remodelling take place. For the higher-order mechanical tractions (4.12)-(4.14) stemming from flexoelectricity, homogeneous Neumann boundary conditions are chosen at all boundaries of the domain. The same applies to higher-order electromechanical boundary conditions that may be included in the context with combined direct and converse flexoelectric contributions as discussed in Sect. 4.1. The electric potential is fixed to zero at the lower left-hand corner of the sample. Under the presented loading conditions it is expected to take its maximum value at the crack tip. At all boundaries, except for the crack flanks, the concentration c_{ME} is fixed to zero throughout the whole simulation assuming that the

messenger substances leave the domain in order to communicate with the cells at the bone surfaces. As a consequence of these homogeneous Dirichlet boundary conditions, a flux of messenger substances through the boundaries occurs. In dependence of this outflux of messenger substances over the domain boundaries, or, in the finite element approach rather of the corresponding "generalised reaction forces" $\boldsymbol{f}_{\text{rea}}^{\text{ME}}$ resulting from the solution of the global system of equations at the corresponding Dirichlet nodes, a flow of osteoclasts and osteoblasts in opposing direction is prescribed, cf. Fig. 4.9. Accordingly, the prescribed generalised forces read

$$\boldsymbol{f}_{\text{pre}}^{\text{OC}} = -\, k_{\text{OC}}\, \boldsymbol{f}_{\text{rea}}^{\text{ME}} \qquad \text{if} \quad \|\boldsymbol{f}_{\text{rea}}^{\text{ME}}\| \geq f_{\text{rea,min}}^{\text{ME}} \tag{4.137}$$

$$\boldsymbol{f}_{\text{pre}}^{\text{OB}} = -\, k_{\text{OB}}\, \boldsymbol{f}_{\text{rea}}^{\text{ME}} \qquad \text{if} \quad \|\boldsymbol{f}_{\text{rea}}^{\text{ME}}\| \geq f_{\text{rea,min}}^{\text{ME}} \tag{4.138}$$

with constant parameters k_{OC} and k_{OB}. More details on the numerical implementation are provided in Appendix C.2.1. These boundary conditions are employed for the left and bottom surface of the domain under consideration. From a physics point of view, it is accordingly assumed that for this particular boundary value problem BMUs originate either in a Volkmann's canal parallel to the crack and next to the left-hand boundary of the specimen or in a Haversian canal perpendicular to the crack and next to the bottom boundary of the specimen. More specifically speaking, the cells will migrate from the surface nearest to the crack, where the magnitude of the messenger substance flux exceeds the predefined threshold value. This is in line with the information provided in [31, 124, 125], stating that a new BMU originates from the nearest Haversian or Volkmann's canal depending on the crack location. According to [96], new osteoclasts and osteoblasts steadily differentiate from their precursor cells in the bone marrow and migrate through the vasculature towards the remodelling site since their life span is lower than the duration of a remodelling cycle, cf. Sect. 4.2. Consequently, a continuous cell flux over the boundary is provided in the proposed model after the initiation by osteocyte apoptosis. In analogy to the homogeneous Dirichlet boundary conditions applied to the messenger substances, the cell concentrations of osteoclasts and osteoblasts are forced to vanish at the crack flanks indicated by a dashed line in Fig. 4.9. Thereby, an outflux of these bone cells is enabled with the underlying assumption being that the cells leave the domain over the crack flanks for the purpose of remodelling. This boundary condition is a starting point for the modelling of osteoblast accumulation at the crack surface and, eventually, crack healing as will be discussed in Sect. 4.4.

The model parameters and initial values are summarised in Table 4.3 and Table 4.4, respectively. For the bone cell concentrations, data from [110] is used in which the concentration of osteocytes in bones is given as 2.5×10^4 cells per mm^3. Regarding the number of osteoblasts and osteoclasts, it is estimated that the osteoblast concentration is smaller approximately by a factor of 10 than the osteocyte concentration and that there are significantly more osteoblasts than osteoclasts, see [63, 96] and references cited therein. The model parameters and initial conditions are chosen on the basis of this information.

Table 4.3: Model parameters.

	b	h	l_c	w_c	e_{crit}	$f^{\text{ME}}_{\text{rea,min}}$	$k_{\text{OY},1}$	$k_{\text{OY},2}$
value	0.8	0.6	0.175	0.008	5.0	0.05	1.0×10^4	2.5×10^4
unit	mm	mm	mm	mm	Vmm^{-1}	s^{-1}	$\text{mm}^{-3}\text{s}^{-1}$	mm^{-3}

	k_{ME}	k_{OC}	k_{OB}	D_{ME}	D_{OC}	D_{OB}	$\eta_{\parallel}$	$\eta_{\perp}$	$\eta_{\uparrow}$
value	2.0×10^5	0.5	1.0	2.0	0.02	0.01	0.2	0.02	0.78
unit	$\text{mm}^{-3}\text{s}^{-1}$	-	-	mm^2s^{-1}	mm^2s^{-1}	mm^2s^{-1}	-	-	-

Table 4.4: Initial conditions.

	$c^{\text{init}}_{\text{OY}}$	$c^{\text{init}}_{\text{ME}}$	$c^{\text{init}}_{\text{OC}}$	$c^{\text{init}}_{\text{OB}}$
value	2.5×10^4	0	0	0
unit	mm^{-3}	mm^{-3}	mm^{-3}	mm^{-3}

The geometry and finite element discretisation of the bone sample under investigation are presented in Fig. 4.10. After mesh refinement in both parametric directions by knot insertion, cf. Sect. 2.2.2, the physical mesh contains 16 008 elements. The number of control points is 16 732 which leads to 117 124 degrees of freedom in total. A convergence study with respect to the discretisation is provided in Appendix C.6. The geometry is obtained in the framework of isogeometric analysis by employing two patches which are connected along the vertical symmetry line of the domain, indicated by the dotted line in Fig. 4.9. Since a globally C^1-continuous IGA framework is used, prescribing C^1-continuity across this patch boundary is of particular importance and is discussed in detail in Sect. 2.3.2. In Appendix C.4.1, more details on the construction of the IGA geometry as well as on the employment of C^1-continuity are provided.

4.3.3.3 Purely flexoelectric initiation

The initial boundary value problem presented in Sect. 4.3.3.2 is solved within the proposed IGA framework in order to investigate the flexoelectric initiation of cellular diffusion processes during remodelling in cortical bone. In this section, the focus lies exclusively on the flexoelectric effect as a trigger mechanism for bone remodelling whereas in Sect. 4.3.3.4 piezoelectricity is additionally taken into account in order to compare the impact of both effects on osteocyte apoptosis near microcracks. Overall, the simulations are performed within a time span of 120 s so that the initiation of bone remodelling as well as the beginning of the cell diffusion processes, which can take several months in total, are captured. For the time increment $\Delta t = 1/8\,\text{s}$ is employed whereas different choices are investigated in the convergence study in Appendix C.6.

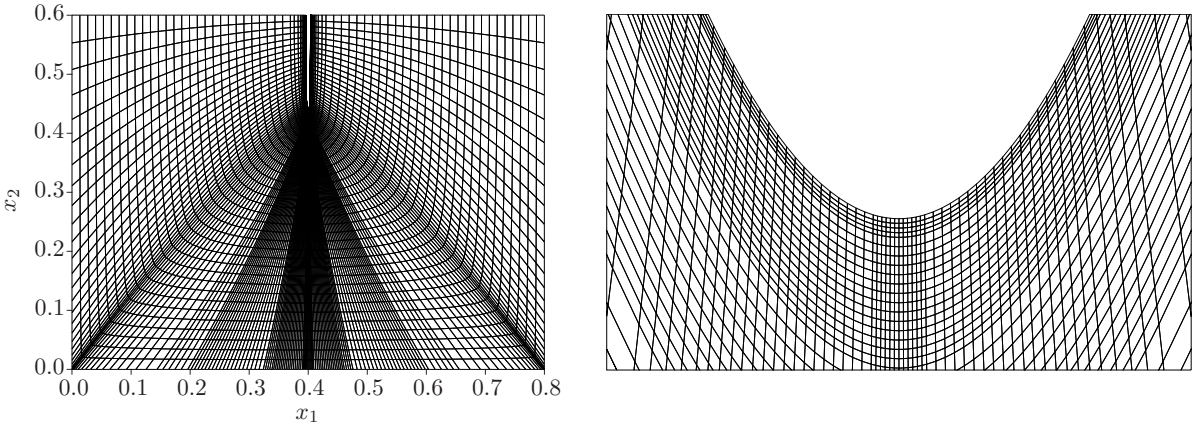

(a) Discretisation of the cracked domain including 16 008 elements.

(b) Detail view on the mesh near the crack tip.

Figure 4.10: IGA discretisation of the cracked domain. Reproduced from [174] under the terms of the Creative Commons Attribution License (CC BY).

Considering the model parameters, initial values as well as material parameters from Sect. 4.3.3.1 and Sect. 4.3.3.2 and disregarding piezoelectricity at first, the simulation results are presented in Fig. 4.11-4.16. From Fig. 4.11 it is apparent that the applied mechanical load leads to a non-uniform strain field in the vicinity of the crack tip. The relevant strain gradient coefficients which contribute to the flexoelectric response are $\varepsilon_{11,1}, \varepsilon_{11,2}, \varepsilon_{22,1}$ and $\varepsilon_{22,2}$ for the two-dimensional boundary value problem under consideration. The figure reveals their distributions near the crack tip at maximum load which is prescribed between $t = 2\,\mathrm{s}$ and $t = 3\,\mathrm{s}$, cf. Fig. 4.9. For the coefficients $\varepsilon_{11,1}$ and $\varepsilon_{22,1}$, a change in sign is observable at the crack tip, whereas the coefficients $\varepsilon_{11,2}$ and $\varepsilon_{22,2}$, i.e. the gradient contributions with respect to the x_2-axis, take extremal values at this location.

As a consequence of the strain gradients together with the flexoelectric effect, an electric field of maximum magnitude $\|\boldsymbol{e}\| = 11.6\,\mathrm{V mm^{-1}}$ can be observed near the crack tip, see Fig. 4.12. Interestingly, this maximum value is not observed exactly at the crack tip but slightly next to it at the crack flanks. At the crack tip itself, the magnitude of the electric field vector is zero since the x_1- and x_2-component both vanish at this location. As discussed in detail in Sect. 4.3.1.1, an electric field of the magnitude observed in Fig. 4.12 causes osteocyte apoptosis in cortical bone. This behaviour is reflected by Fig. 4.13. In this particular case, the osteocyte concentration has locally decreased by up to 85 % due to the induced electric field over a pulse of 5 s, cf. Fig. 4.9. At a distance from the crack, however, the electric field does not reach the critical value for osteocyte apoptosis so that the bone cell concentration remains unchanged in comparison to the initial state.

At the locations where osteocytes have died, messenger substances are produced as shown in Fig. 4.14. The figure presents the concentration as well as the flux of messenger substances in the cortical bone specimen. According to their uniform diffusive behaviour,

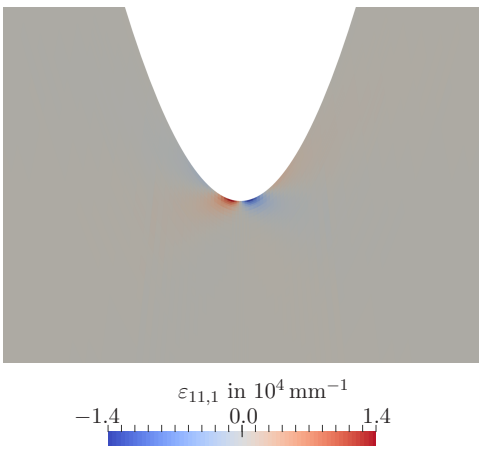

(a) Strain gradient coefficient $\varepsilon_{11,1}$.

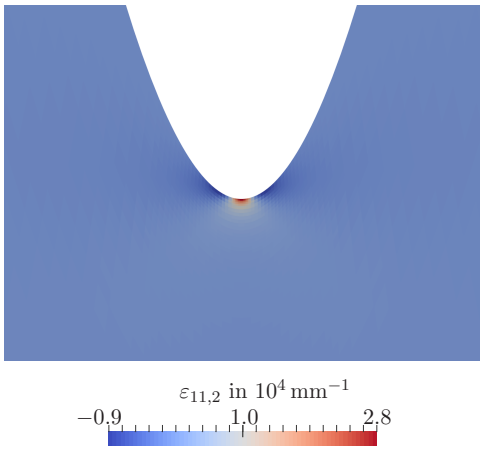

(b) Strain gradient coefficient $\varepsilon_{11,2}$.

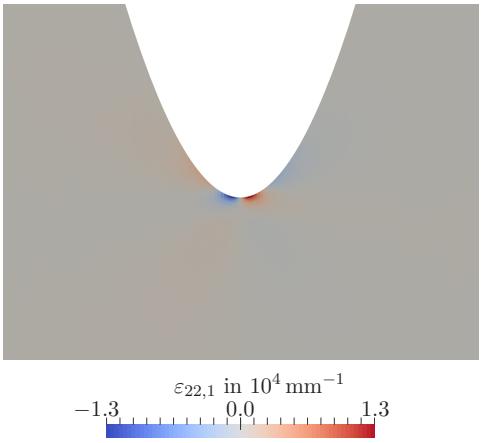

(c) Strain gradient coefficient $\varepsilon_{22,1}$.

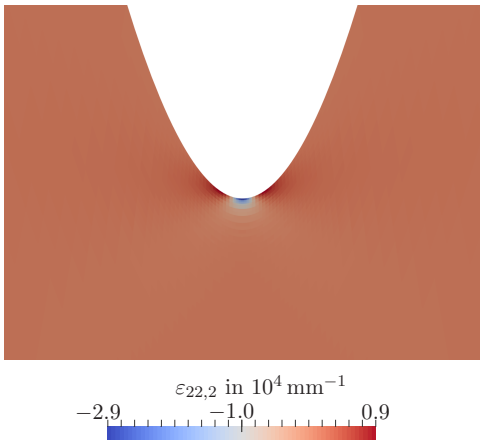

(d) Strain gradient coefficient $\varepsilon_{22,2}$.

Figure 4.11: Distribution of the strain gradient coefficients $\varepsilon_{11,1}, \varepsilon_{11,2}, \varepsilon_{22,1}$ and $\varepsilon_{22,2}$ at maximum load $\|\boldsymbol{u}_{\mathrm{pre}}\| = 0.004\,\mathrm{mm}$ at time $t = 3\,\mathrm{s}$. The distribution near the crack tip is shown. Reprinted from [174] under the terms of the Creative Commons Attribution License (CC BY).

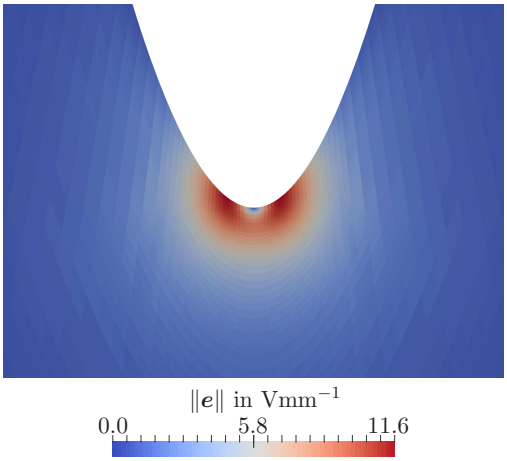

Figure 4.12: Electric field magnitude $\|\boldsymbol{e}\|$ at maximum load $\|\boldsymbol{u}_{\text{pre}}\|$ at time $t = 3\,\text{s}$ near the crack tip. Reprinted from [174] under the terms of the Creative Commons Attribution License (CC BY).

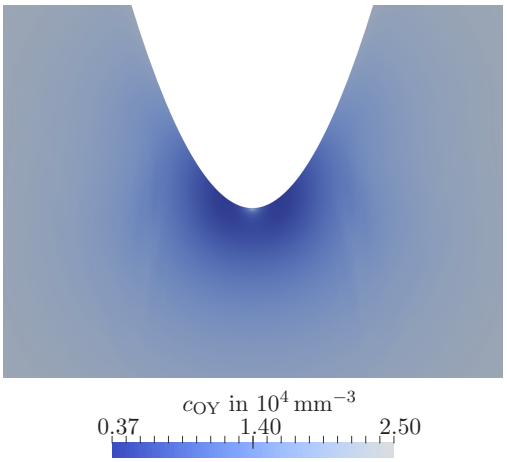

Figure 4.13: Osteocyte concentration c_{OY} after mechanical loading at time $t = 5\,\text{s}$ near the crack tip. Reprinted from [174] under the terms of the Creative Commons Attribution License (CC BY).

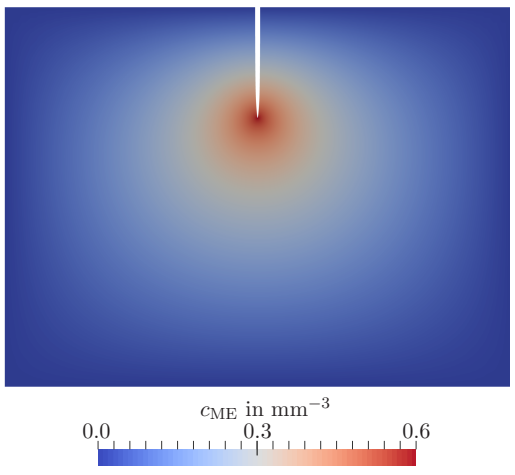

(a) Messenger substance concentration c_{ME}.

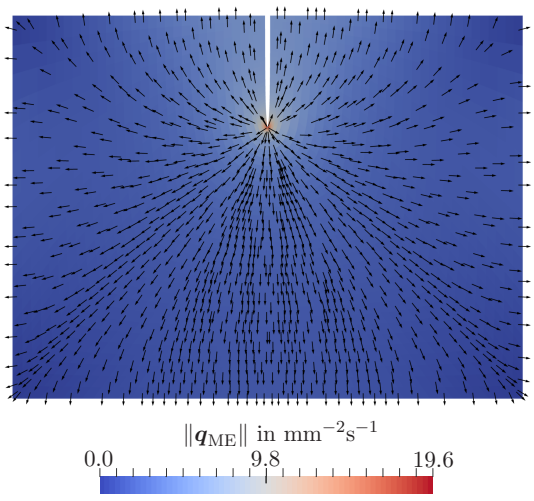

(b) Messenger substance flux $\boldsymbol{q}_{\text{ME}}$.

Figure 4.14: Messenger substance concentration c_{ME} and flux $\boldsymbol{q}_{\text{ME}}$ at time $t = 5\,\text{s}$. In (b), the contour plot indicates the magnitude of the flux, whereas the glyphs show the flux directions. Reprinted from [174] under the terms of the Creative Commons Attribution License (CC BY).

they start migrating through the bone matrix and towards the domain surfaces. Due to the Dirichlet boundary conditions prescribed as indicated in Fig. 4.9, an outflux of messenger substances over the boundaries occurs.

In response to this outflux, osteoclastic and osteoblastic cells enter the domain through the boundaries. In particular, these cells enter the domain over the left surface which means that the respective threshold value of the messenger substance outflux has been reached there. The concentration as well as the flux of the bone cells is presented in Fig. 4.15-4.16 for two different points of time, namely directly after mechanical loading at time $t = 5\,\mathrm{s}$ as well as at the end of the simulation, i.e. $t = 120\,\mathrm{s}$. The contour plots and glyph representations show that the diffusion of osteoclasts and osteoblasts within the bone excerpt is mainly directed towards the crack tip. In addition, it becomes apparent that a migration in the direction of osteon alignment, i.e. in the direction of the longitudinal bone axis, is preferred in comparison to the diffusion process in the plane perpendicular to that axis. This results from the particular choice of parameters $\eta_{\parallel}$, $\eta_{\perp}$ and $\eta_{\uparrow}$ for the diffusion tensors, see Table 4.3. Moreover, the outflux of the bone cells through the crack flanks is observable from the simulation results. A comparison between Fig. 4.15c and 4.16c additionally yields that the cell concentration of osteoblasts is generally larger than the concentration of osteoclasts, whereas the concentration of both of the two BMU-forming cell types is significantly smaller than the initial number of osteocytes. This is in accordance with the literature on bone remodelling as discussed in detail in Sect. 4.3.3.2.

Size effect Since flexoelectricity is a size-dependent phenomenon, specimens of various sizes are investigated in the following and the results are studied with regard to the electric field magnitude as well as to the apoptosis behaviour of osteocytes. In particular, the size of the specimen under investigation has been reduced by a factor of 2.0 and increased by the same factor, respectively. The results are presented in Fig. 4.17. As expected from the general property of flexoelectricity, the electric field in response to the (scaled) mechanical load decreases on larger scales, whereas it takes higher values when the size of the domain is reduced. With regard to osteocyte apoptosis, which is primarily dependent on the magnitude of the electric field, the highest impact can be found on the smallest bone excerpt as well. To be precise, the concentration of osteocytes in this sample has locally decreased by up to 92 % in the vicinity of the crack tip where cell apoptosis is most prominent, as shown in Fig. 4.17b. In comparison, the decrease in the largest sample takes a maximum value of approx. 74 %, cf. Fig. 4.17f. Interestingly, not only the magnitude but also the distribution of the electric field differs slightly at the different scales. More specifically speaking, the electric field is rather focussed on the crack tip in the large specimen in Fig. 4.17e, whereas it spreads more towards the crack flanks as well as towards the region below the crack tip in the small specimen in Fig. 4.17a. This directly affects the apoptosis behaviour of osteocytes as well, see Fig. 4.17b and 4.17f.

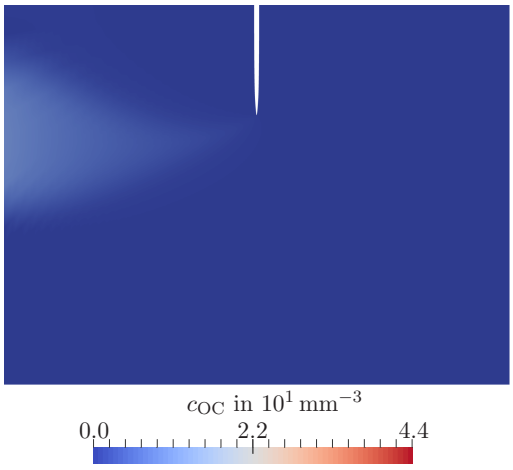

(a) Osteoclast concentration c_{OC}, $t = 5\,s$.

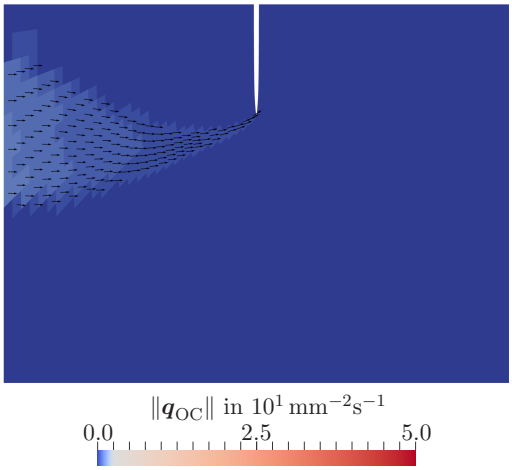

(b) Osteoclast flux $\boldsymbol{q}_{OC}$, $t = 5\,s$.

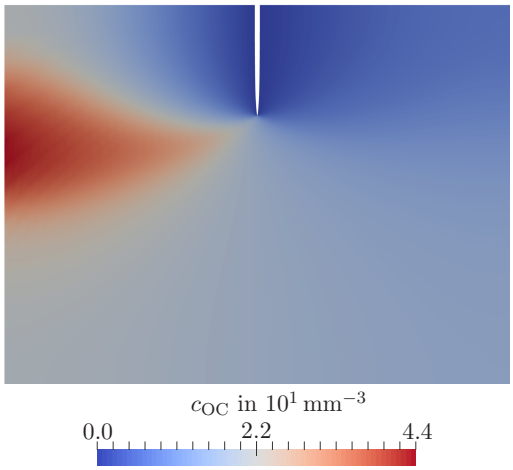

(c) Osteoclast concentration c_{OC}, $t = 120\,s$.

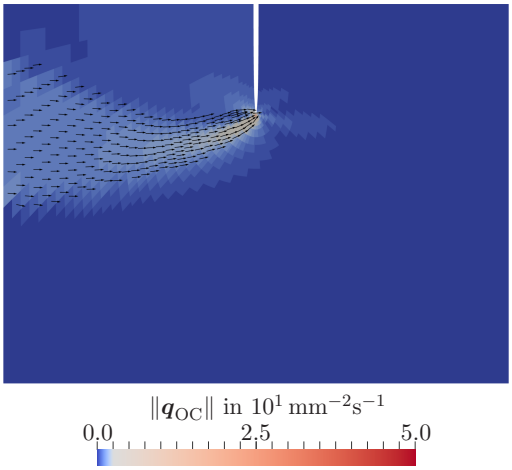

(d) Osteoclast flux $\boldsymbol{q}_{OC}$, $t = 120\,s$.

Figure 4.15: Osteoclast cell concentration c_{OC} and flux $\boldsymbol{q}_{OC}$ after mechanical loading at time $t = 5\,s$ and at the end of the simulation, i.e. $t = 120\,s$. In (b) and (d), the contour plot indicates the magnitude of the flux, whereas the glyphs show the flux directions in the most relevant region. Reprinted from [174] under the terms of the Creative Commons Attribution License (CC BY).

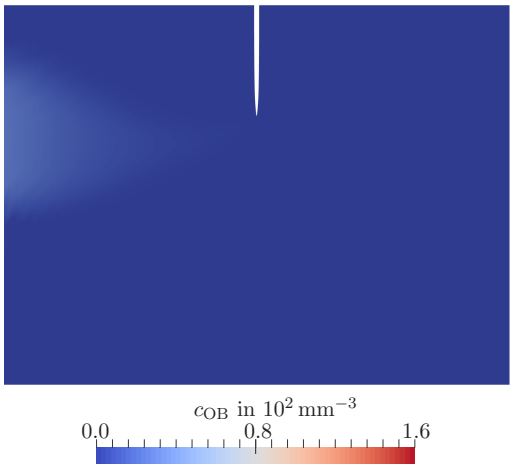

(a) Osteoblast concentration c_{OB}, $t = 5$ s.

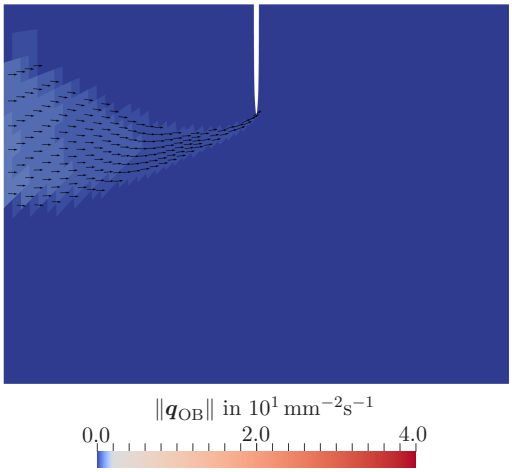

(b) Osteoblast flux $\boldsymbol{q}_{OB}$, $t = 5$ s.

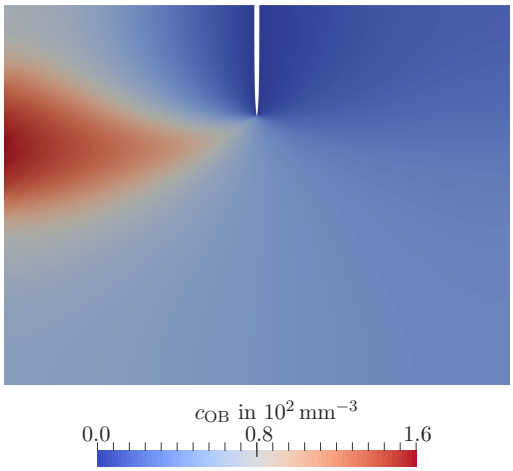

(c) Osteoblast concentration c_{OB}, $t = 120$ s.

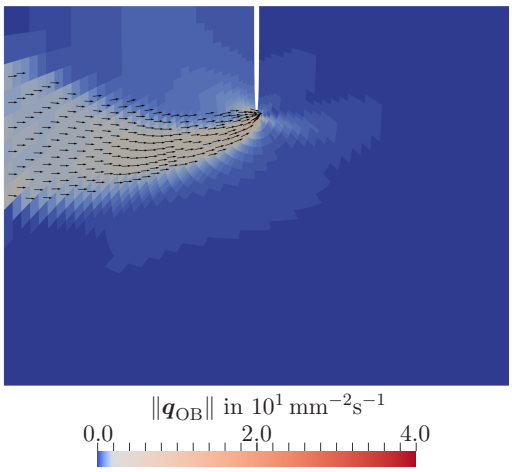

(d) Osteoblast flux $\boldsymbol{q}_{OB}$, $t = 120$ s.

Figure 4.16: Osteoblast cell concentration c_{OB} and flux $\boldsymbol{q}_{OB}$ after mechanical loading at time $t = 5$ s and at the end of the simulation, i.e. $t = 120$ s. In (b) and (d), the contour plot indicates the magnitude of the flux, whereas the glyphs show the flux directions in the most relevant region. Reprinted from [174] under the terms of the Creative Commons Attribution License (CC BY).

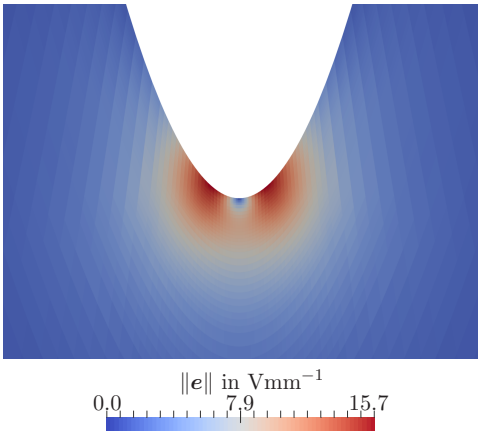

(a) Electric field magnitude $\|\boldsymbol{e}\|$ at time $t = 3\,\mathrm{s}$ near the crack tip. Scale factor: 0.5

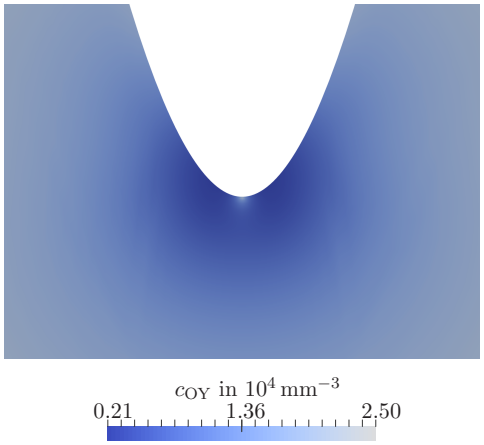

(b) Osteocyte concentration c_{OY} at time $t = 5\,\mathrm{s}$ near the crack tip. Scale factor: 0.5

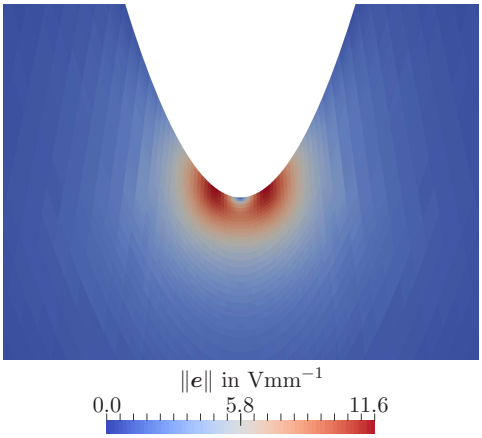

(c) Electric field magnitude $\|\boldsymbol{e}\|$ at time $t = 3\,\mathrm{s}$ near the crack tip. Scale factor: 1.0

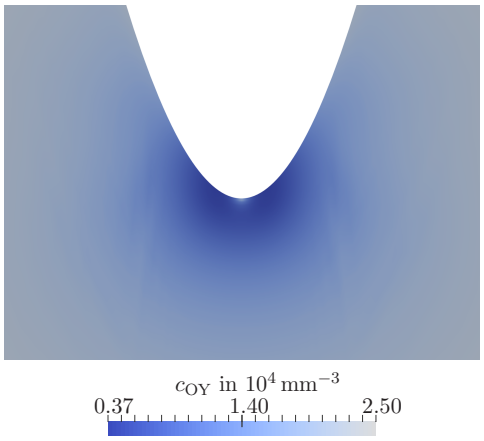

(d) Osteocyte concentration c_{OY} at time $t = 5\,\mathrm{s}$ near the crack tip. Scale factor: 1.0

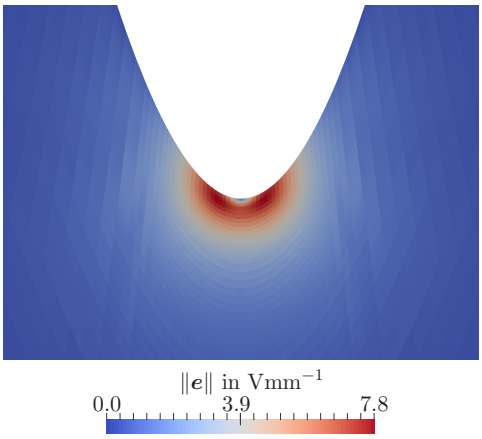

(e) Electric field magnitude $\|\boldsymbol{e}\|$ at time $t = 3\,\mathrm{s}$ near the crack tip. Scale factor: 2.0

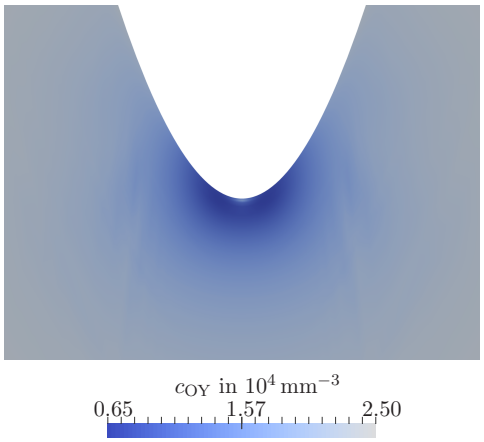

(f) Osteocyte concentration c_{OY} at time $t = 5\,\mathrm{s}$ near the crack tip. Scale factor: 2.0

Figure 4.17: Electric field magnitude and osteocyte concentration for simulations with varying specimen size. The geometric dimensions as well as the applied mechanical load are scaled by a factor of 0.5, 1.0 and 2.0 with respect to the original values specified in Sect. 4.3.3.2. Reprinted from [174] under the terms of the Creative Commons Attribution License (CC BY).

Influence of the diffusion directions The results presented in Fig. 4.18 have been obtained by simulations in which different parameters for the diffusivity of osteoclasts and osteoblasts have been chosen in order to investigate their influence on the cellular behaviour within the proposed model. Specifically speaking, the constants $\eta_{\parallel}$, $\eta_{\perp}$ and $\eta_{\uparrow}$ have been varied including settings where some of them were set to zero so that the respective contribution to the diffusion tensor vanished. The combinations investigated in this context are summarised in Table 4.5 and the corresponding results regarding the behaviour of osteoclasts are presented in Fig. 4.18. Since the same directional dependencies are employed for the diffusion of osteoclasts and osteoblasts, the simulation results for the latter are not explicitly shown.

The straightforward approach in which it is assumed that BMUs migrate directly to the remodelling site, is accounted for in the first simulation (I). The diffusion direction of osteoclasts and osteoblasts is accordingly determined by the gradient of messenger substances only. As a consequence, the cell flux is targeted towards the crack tip as revealed in Fig. 4.18b and leads to the distribution of osteoclastic cells presented in Fig. 4.18a. A strong localisation at the crack tip can be observed, since a diffusion in directions other than the one determined by vector $\boldsymbol{a}_{\mathrm{g}}$ is strictly excluded. If, on the contrary, the gradient-controlled diffusion term is neglected such that the direction of bone cell diffusion is solely dependent on the transversely isotropic bone structure (II), a significant increase in cell density is observable in the right half of the domain, see Fig. 4.18c-4.18d. From a physics point of view, this means that the BMUs do not necessarily reach the remodelling site where they are required for crack healing. Both approaches, (I) and (II), can thus not model the movement of osteoclasts and osteoblasts sufficiently accurate. Taking both contributions into account instead (III), as it has been done for the simulation results that have been presented in Fig. 4.15 and which are shown again for reasons of comparison in Fig. 4.18e-4.18f, a more reasonable behaviour of the bone cells is obtained. Specifically speaking, their migration is directed towards the crack while a preferred movement in direction of osteon alignment is observable.

Table 4.5: Variations of the parameters $\eta_{\parallel}, \eta_{\perp}$ and $\eta_{\uparrow}$ for the diffusion tensors (4.88)-(4.89).

No.	$\eta_{\parallel}$	$\eta_{\perp}$	$\eta_{\uparrow}$
I	0.0	0.0	1.0
II	0.98	0.02	0.0
III	0.2	0.02	0.78

4.3.3.4 Combined flexoelectric and piezoelectric initiation

As discussed in Sect. 4.2, cortical bone also exhibits piezoelectric properties besides flexoelectricity. Accordingly, non-zero values for the piezoelectric coefficients, as denoted in Table 4.2, are taken into account in the following. In particular, the purely flexoelectric

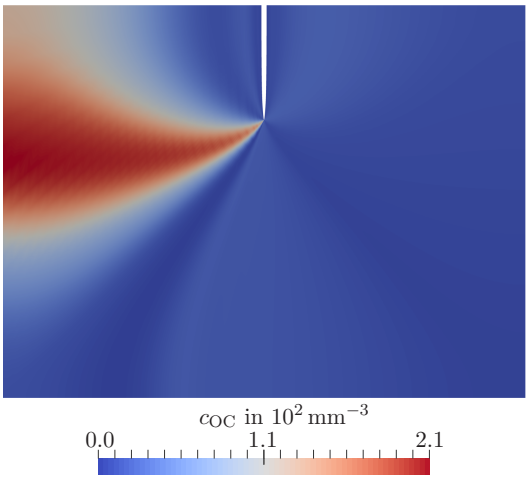

(a) I: Osteoclast concentration c_{OC}, $t = 120$ s.

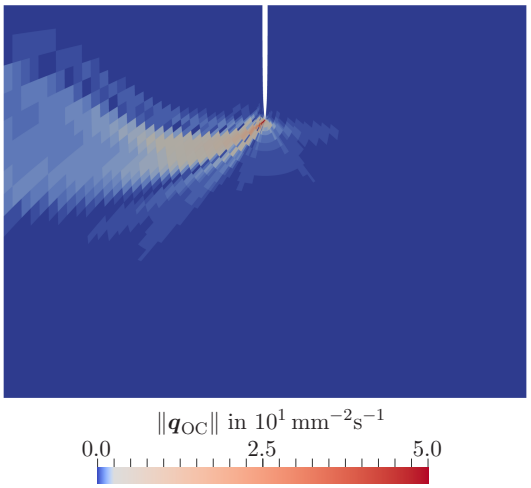

(b) I: Magnitude of osteoclast flux $\|\boldsymbol{q}_{OC}\|$, $t = 120$ s.

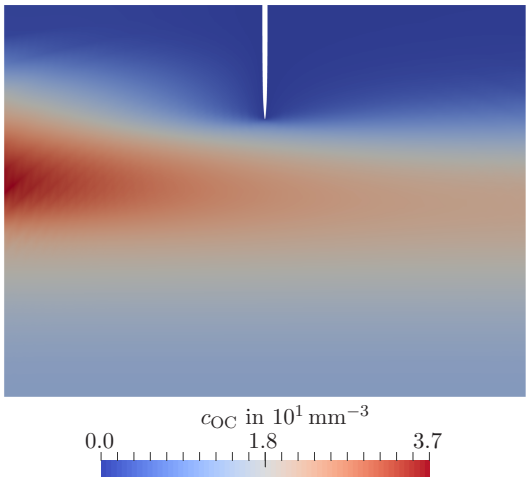

(c) II: Osteoclast concentration c_{OC}, $t = 120$ s.

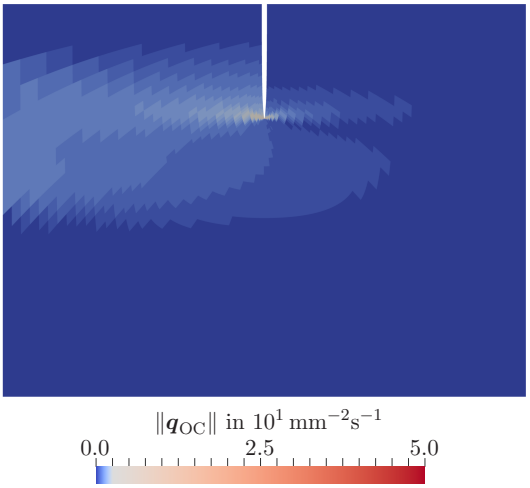

(d) II: Osteoclast flux $\|\boldsymbol{q}_{OC}\|$, $t = 120$ s.

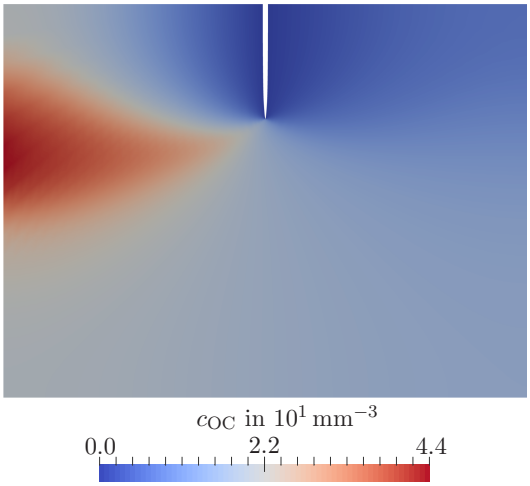

(e) III: Osteoclast concentration c_{OC}, $t = 120$ s.

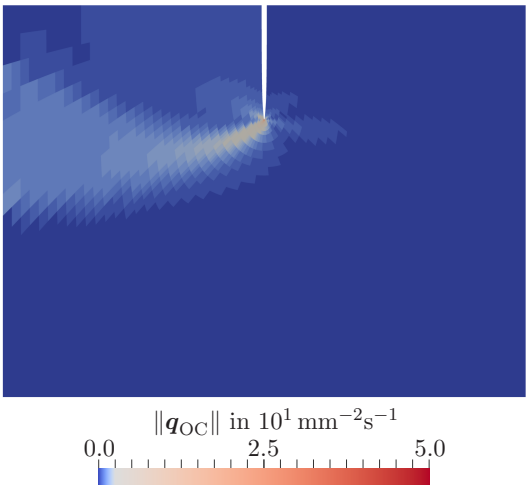

(f) III: Magnitude of osteoclast flux $\|\boldsymbol{q}_{OC}\|$, $t = 120$ s.

Figure 4.18: Osteoclast cell concentration c_{OC} and magnitude of the flux $\|\boldsymbol{q}_{OC}\|$ at the end of the simulation, i.e. $t = 120$ s, for the different parameter sets defined in Table 4.5. Reprinted from [174] under the terms of the Creative Commons Attribution License (CC BY).

or piezoelectric response as well as the combination of both is investigated. By comparing Fig. 4.19a and 4.19c, it is apparent that the electric field induced by piezoelectricity is not only higher in terms of its magnitude but also less focussed on the crack tip in comparison to the flexoelectric response for the boundary value problem under consideration. This is due to the coupling between electric polarisation and mechanical strains activated by the piezoelectric effect. Thereby, an electric field is induced in a larger part of the domain, including regions further away from the crack where an increasingly homogeneous strain field can be found. With regard to the apoptosis behaviour of osteocytes, Fig. 4.19d indicates that, in the case of pure piezoelectricity, the regions to the left and right of the lower crack flanks are most critical for cell death.

If both, piezoelectricity and flexoelectricity, are activated, an unsymmetrical pattern arises with regard to the electric field distribution, see Fig. 4.19e. In addition, it is observable that its maximum magnitude is lower in comparison with the purely piezoelectric result. This behaviour, which seems unintuitive at first, can be attributed to the different underlying physical mechanisms that manifest themselves in the specific form of the flexoelectricity and piezoelectricity tensors. In order to obtain a deeper understanding of this behaviour, the individual coefficients e_1 and e_2 of the electric field are presented in Fig. 4.20 and supplementary plots combining both the information on the magnitude and on the direction of the electric field are provided in Appendix C.5.1. Fig. 4.21 additionally presents the strain coefficients $\varepsilon_{11}, \varepsilon_{22}$ and ε_{12} which are responsible for the electromechanical coupling in the purely piezoelectric model. According to the form of the piezoelectricity tensor defined in (4.134), the normal strain components contribute to the electric field in x_1-direction, whereas the shear components contribute to the component in x_2-direction. Consequently, the change in sign in Fig. 4.21c is reflected by the e_2 coefficient in Fig. 4.20d whereas the distribution of ε_{11} and ε_{22} in Fig. 4.21a-4.21b is reflected by the coefficient e_1, see Fig. 4.20b. In a similar manner, the strain gradient contributions presented in Fig. 4.11 can be evaluated together with the particular form of the flexoelectricity tensor from (4.135). Thereby, the distributions e_1 and e_2 presented in Fig. 4.20a and 4.20c are obtained which show the opposite behaviour compared to their counterparts derived for pure piezoelectricity. These characteristics finally lead to the unsymmetrical pattern observed in the magnitude of the electric field. Regarding the apoptosis of osteocytes, see Fig. 4.19f, this effect is also observable since the decrease of the osteocyte concentration is directly related to the electric field magnitude, as discussed in Sect. 4.3.1.1.

Finally, the size effect shall be studied together with combined flexoelectric and piezoelectric mechanisms. In contrast to flexoelectricity, piezoelectricity is not a size dependent phenomenon. This means that the latter is expected to play a less significant role on small scales but to dominate on larger scales. In order to investigate this behaviour by the simulations, the size and the loading of the cracked domain are scaled by factors of 0.5 and 2.0, analogously to the studies in Sect. 4.3.3.3 and the results are presented in Fig. 4.22. The unsymmetrical distribution of the electric field is found to be more noticeable with decreasing specimen size. For the larger sample in Fig. 4.22c, the piezoelectric

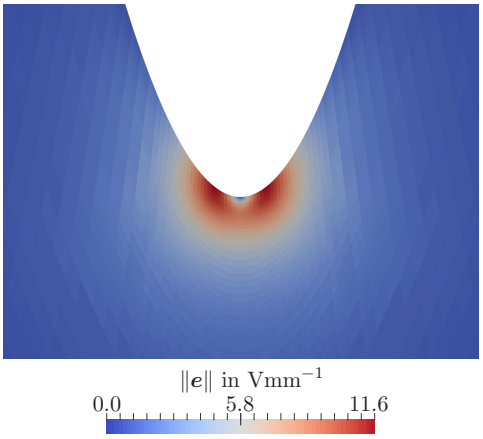

(a) Electric field magnitude $\|\boldsymbol{e}\|$ at time $t = 3\,\mathrm{s}$ near the crack tip. Pure flexoelectricity.

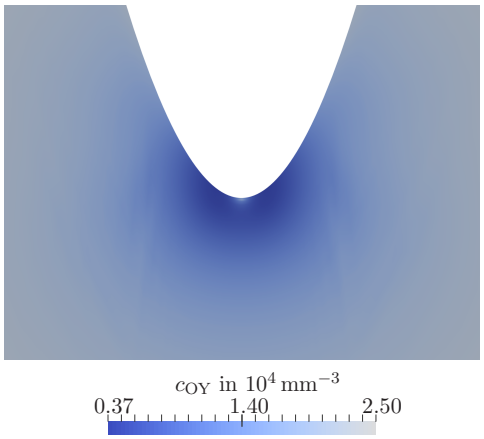

(b) Osteocyte concentration c_{OY} at time $t = 5\,\mathrm{s}$ near the crack tip. Pure flexoelectricity.

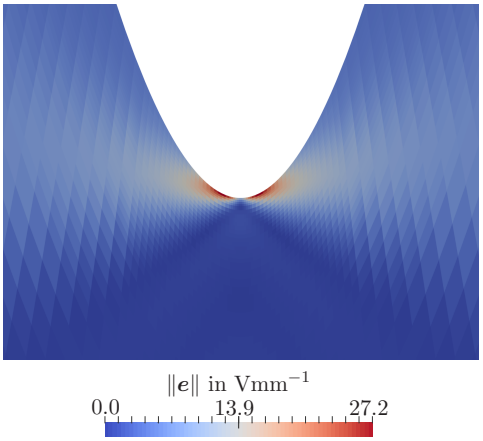

(c) Electric field magnitude $\|\boldsymbol{e}\|$ at time $t = 3\,\mathrm{s}$ near the crack tip. Pure piezoelectricity.

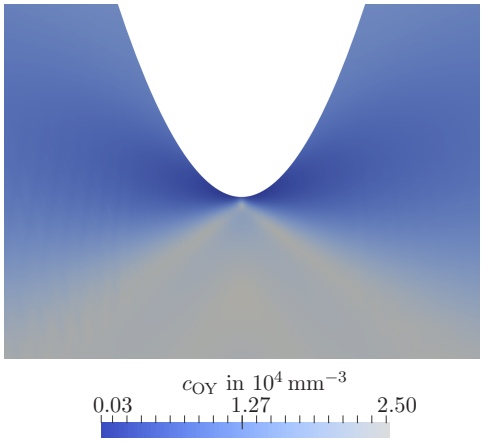

(d) Osteocyte concentration c_{OY} at time $t = 5\,\mathrm{s}$ near the crack tip. Pure piezoelectricity.

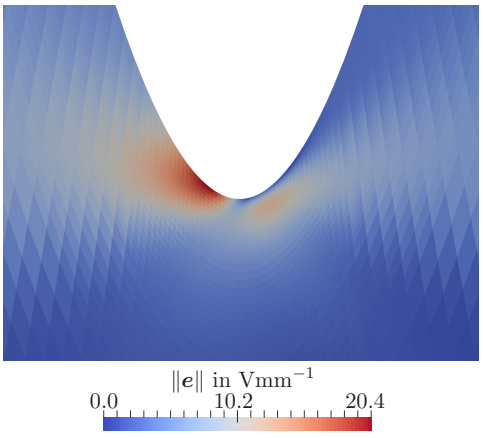

(e) Electric field magnitude $\|\boldsymbol{e}\|$ at time $t = 3\,\mathrm{s}$ near the crack tip. Combined flexoelectricity and piezoelectricity.

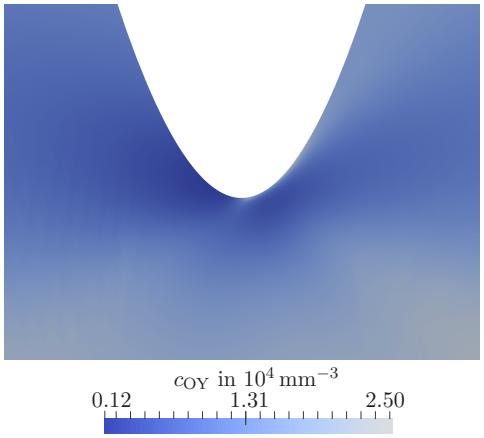

(f) Osteocyte concentration c_{OY} at time $t = 5\,\mathrm{s}$ near the crack tip. Combined flexoelectricity and piezoelectricity.

Figure 4.19: Electric field magnitude $\|\boldsymbol{e}\|$ and osteocyte concentration c_{OY} for simulations considering pure flexoelectricity, pure piezoelectricity and both effects combined. Reprinted from [174] under the terms of the Creative Commons Attribution License (CC BY).

effect clearly exceeds the flexoelectric one such that the results regarding the electric field distribution are rather similar to those obtained previously by setting all flexoelectric coefficients to zero, see Fig. 4.19c. However, at increasingly small scales, the flexoelectric effect gains importance. Since the piezoelectricity-induced electric field does not change with the sample size, flexoelectricity will generally exceed piezoelectricity when small enough scales are considered.

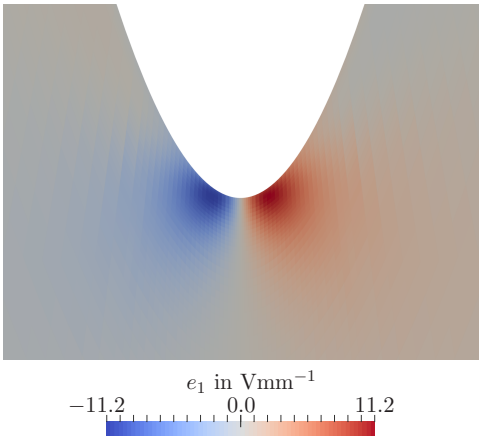

(a) Electric field coefficient e_1 near the crack tip. Pure flexoelectricity.

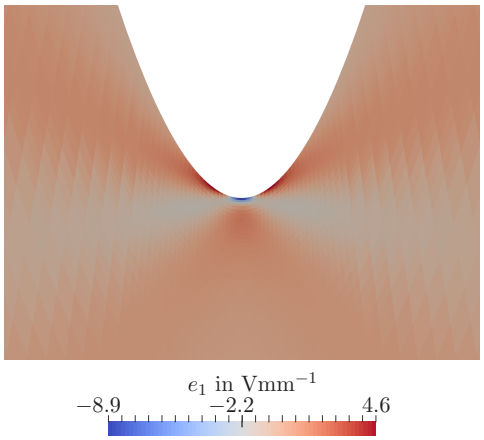

(b) Electric field coefficient e_1 near the crack tip. Pure piezoelectricity.

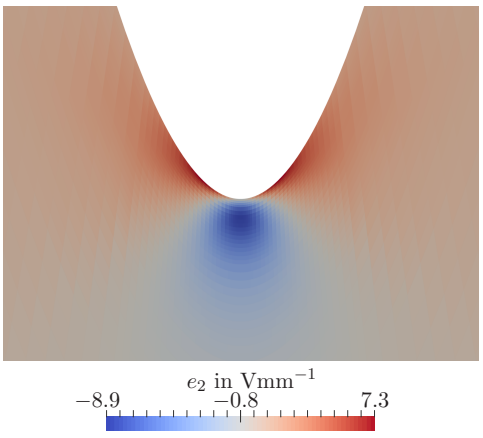

(c) Electric field coefficient e_2 near the crack tip. Pure flexoelectricity.

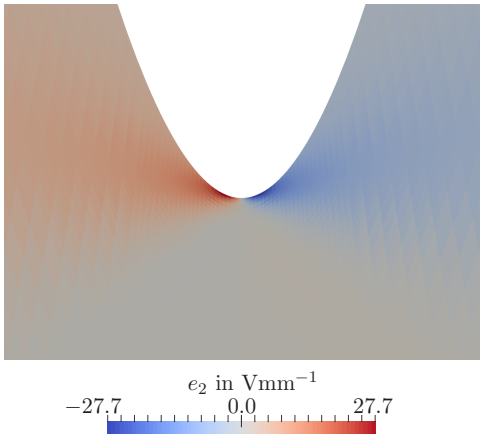

(d) Electric field coefficient e_2 near the crack tip. Pure piezoelectricity.

Figure 4.20: Electric field coefficients e_1 and e_2 at time $t = 5\,\mathrm{s}$ for simulations considering either pure flexoelectricity or pure piezoelectricity. Reprinted from [174] under the terms of the Creative Commons Attribution License (CC BY).

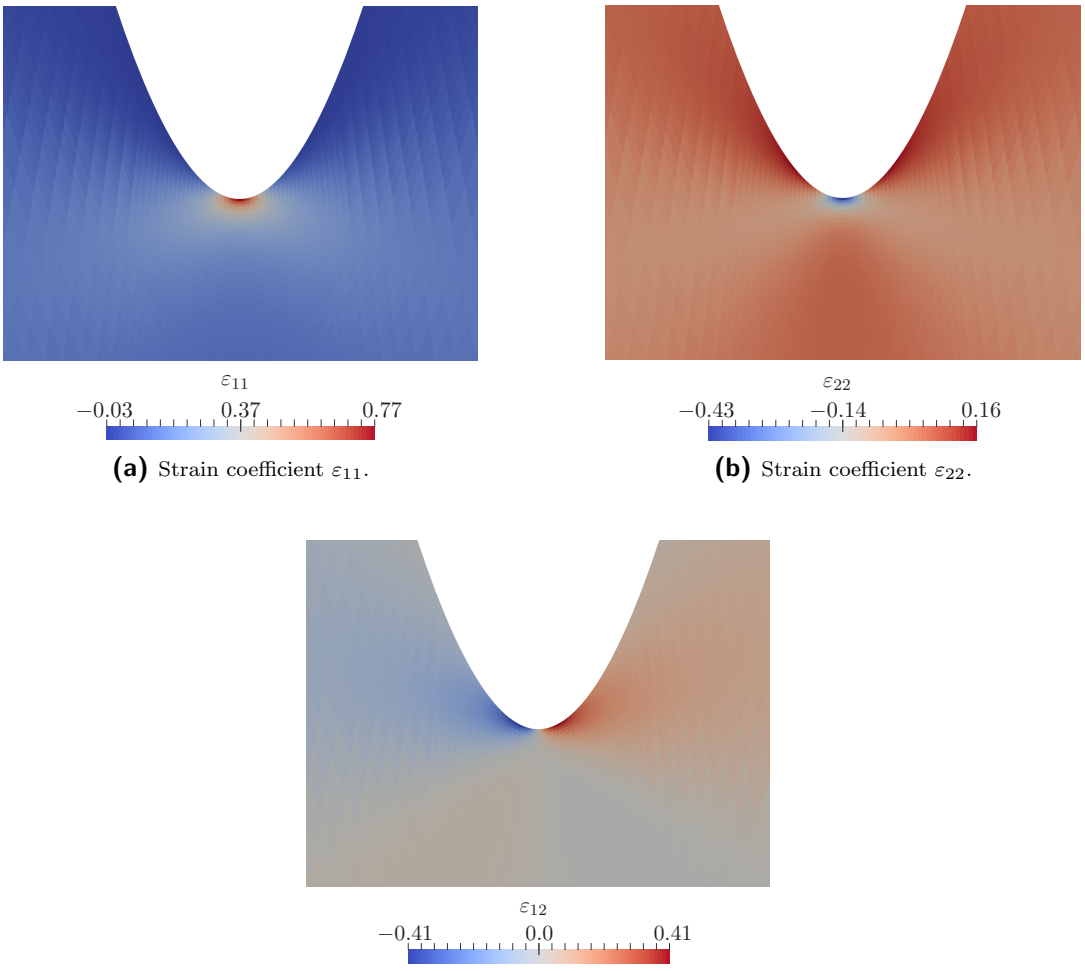

(a) Strain coefficient ε_{11}.

(b) Strain coefficient ε_{22}.

(c) Strain coefficient ε_{12}.

Figure 4.21: Strain coefficients $\varepsilon_{11}, \varepsilon_{22}$ and ε_{12} at maximum load $\|\boldsymbol{u}_{\text{pre}}\|$ at time $t = 3\,\text{s}$. Pure piezoelectricity is considered in the simulations. The distribution near the crack tip is shown. Reprinted from [174] under the terms of the Creative Commons Attribution License (CC BY).

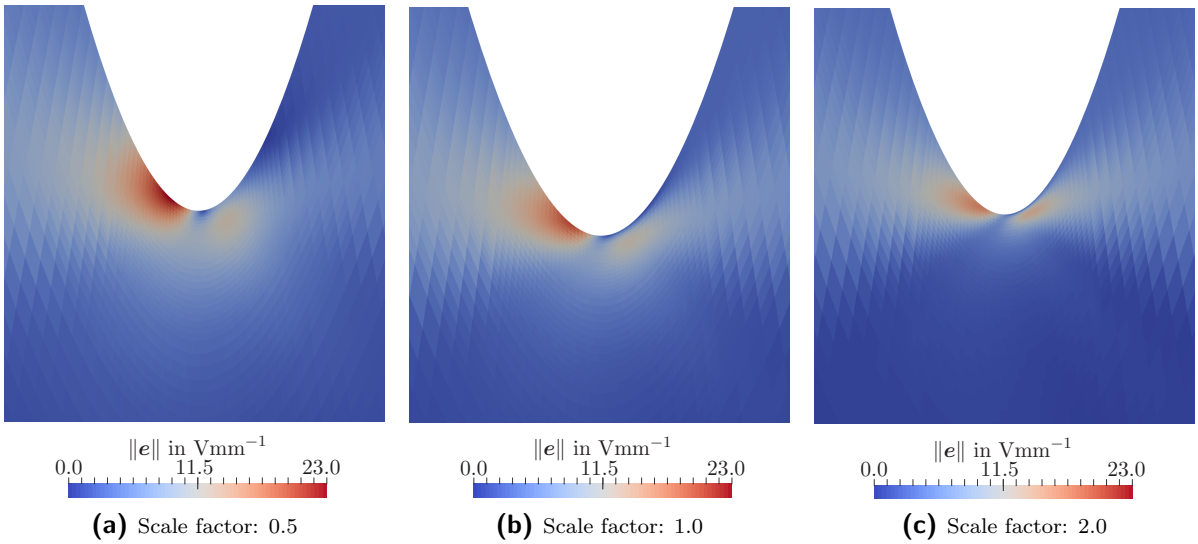

(a) Scale factor: 0.5 **(b)** Scale factor: 1.0 **(c)** Scale factor: 2.0

Figure 4.22: Electric field magnitude $\|\boldsymbol{e}\|$ for simulations with varying specimen size and with combined flexoelectricity and piezoelectricity. The geometry parameters as well as the applied mechanical load are scaled by a factor of 0.5, 1.0 and 2.0 with respect to the original values specified in Sect. 4.3.3.2. The results are shown at time $t = 3\,\mathrm{s}$ near the crack tip. Reprinted from [174] under the terms of the Creative Commons Attribution License (CC BY).

4.4 IGA-FEA modelling approach for flexoelectricity-induced bone remodelling and microcrack healing

The modelling approach proposed in Sect. 4.3 captures the initiation of bone remodelling by flexoelectricity, i.e. osteocyte apoptosis and subsequent signalling mechanisms which lead to the recruitment of osteoclasts and osteoblasts towards the remodelling site. The bone-forming activity of the bone cells in the subsequent remodelling process, however, is not included in that model and will be the focus of this section. The governing equations as well as the numerical aspects are thus similar to a certain extent whereas an extension with respect to surface growth is made and more detailed signalling mechanisms as well as the regeneration of the global osteocyte field during crack healing are incorporated. Moreover, crack evolution is captured in a discretised manner so that osteocyte apoptosis is accounted for along the entire crack length and not only near the crack tip at the final state of cracking. From a numerics point of view, the computational framework is not fully embedded in isogeometric analysis as in Sect. 4.3 but in a combined IGA-FEA scheme and a separation of time scales between the fast crack event and the comparably slow cell diffusion processes together with the crack healing is employed.

The modelled process is illustrated in Fig. 4.23 with detailed captions summarising the main information on the modelling approach which will be presented in the subsequent sections. In particular, the following steps are included:

1. Flexoelectricity-induced electric fields occur during crack evolution in the mechanically loaded, cortical bone structure.
2. Osteocytes undergo apoptosis in locations where the induced electric field exceeds a critical value.
3. Messenger substances are produced in consequence of osteocytes apoptosis which initiates the remodelling process.
4. Osteoclasts are recruited from the vasculature by the messenger substances and migrate through the bone matrix towards the crack tip while producing, respectively releasing new messenger substances.
5. These messenger substances recruit osteoblasts which subsequently migrate towards the remodelling site similar to the osteoclasts.
6. Osteoblasts which reach the open crack surfaces form new bone material by means of surface growth.
7. During bone formation, osteoblasts differentiate into osteocytes so that the osteocyte concentration successively regenerates.

Due to the complexity of the biochemical processes taking place during bone remodelling, several simplifications are considered which are consistent with the assumptions made in Sect. 4.3. To be precise, cells are not accounted for individually but in form of "smeared" concentration fields as is a common assumption for diffusion models, see, e.g., [113, Chapter 11]. Moreover, the complex biochemical signalling mechanisms which regulate the remodelling process are represented by the activity of different messenger substances. The (lower-scale) tunnels excavated by osteoclasts are not explicitly resolved. Besides, new bone material which is produced by the remodelling activity of osteoblasts is considered intact and mineralised, such that the mineralisation process itself is not modelled and osteoblasts transform into osteocytes instantaneously.

4.4.1 Balance equations

In the following sections, the multiphysics modelling approach proposed for the investigation of the bone remodelling process including crack healing is presented in extension of the model established in Sect. 4.3.1. For the sake of completeness, the entire set of partial differential equations as well as all source and flux terms are provided in Sect. 4.4.1.1 whereas in the subsequent sections only new contributions are discussed.

4.4.1.1 Chemo-electro-mechanical coupling

Being an extension of the model presented in Sect. 4.3.1, the bone remodelling process illustrated in Fig. 4.23 gives rise to a chemo-electro-mechanically coupled modelling approach in order to account for flexoelectric effects and their impact on bone cell migration and crack healing. The diffusion equations for the bone cells and messenger substances,

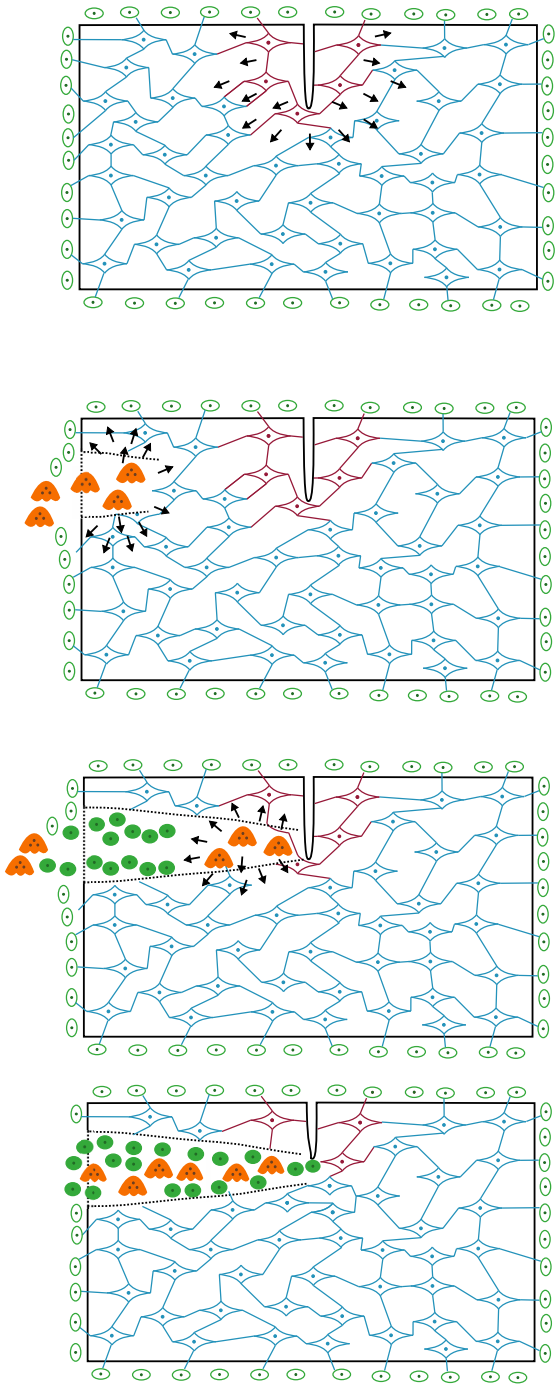

(a) Initiation of bone remodelling by osteocyte apoptosis: During crack evolution, high strain gradients can be found in the vicinity of the crack tip. As a result of the flexoelectric effect, local electric fields occur accordingly, which lead to *osteocyte* (OY) apoptosis. In the schematic, the crack at the end of the fracture event is shown and dead osteocytes, indicated by the red colour, are found in the vicinity of the crack. Signals, respectively substances, that are sent out by dying osteocytes and their neighbouring cells are transmitted through the dense osteocyte network and towards the lining cells on the surfaces. They are accounted for in terms of *messenger substances* (MC) in the model and indicated by black arrows.

(b) Osteoclast recruitment and activity: *Osteoclasts* (OC) are recruited for the remodelling process as a consequence of the osteocyte signalling. Under a steady supply from the vasculature, they enter the domain and migrate through the bone matrix. Their movement is directed towards the crack or, in other words, steered by the microdamage [100]. In addition, the main direction of osteon alignment influences the diffusion direction of these bone cells. During the activity of osteoclasts, growth factors are produced as well as released from the matrix and serve as attractants for osteoblasts as they diffuse through the bone. They are accounted for as a second type of *messenger substances* (MB), as indicated by black arrows.

(c) Osteoblast recruitment and activity: The produced *messenger substances* (MB) steadily recruit *osteoblasts* (OB) in a similar manner as osteoclasts have priorly been recruited. Osteoblasts subsequently enter the domain and follow the osteoclasts through the bone matrix, i.e. they move with the same anisotropic diffusion direction towards the crack. Throughout the remodelling process, osteoblasts are steadily supplied from the vasculature.

(d) Crack healing and regeneration of the osteocyte field: When osteoblasts reach the crack surfaces, they form new bone material by surface growth, and thereby gradually heal the crack. During this process, osteoblasts transform to osteocytes while they become embedded in the new bone matrix. For the sake of simplicity, the mineralisation process is neglected in this context or, in other words, it is assumed that the newly produced bone material is fully mineralised instantaneously at the time of apposition.

Figure 4.23: Sketch of a targeted remodelling process in cortical bone in the presence of an initial crack. The illustration shows the simplified process which is considered in the proposed modelling approach. The main cell types involved are *osteocytes* (OY, blue), *osteoclasts* (OC, orange) and *osteoblasts* (OB, green, filled). Bone lining cells (green, not filled) are also included in the sketch although they do not act as an independent field in the modelling approach but are implicitly accounted for through appropriate boundary conditions. All *messenger substances* (MC, MB) are indicated by black arrows. In the presented setting, the horizontal axis is the longitudinal bone axis. Reprinted from [175] under the terms of the Creative Commons Attribution License (CC BY).

in combination with the balance equations for the electromechanical continuum under investigation, form a set of coupled balance equations which can be written as

$$\mathbf{0} = \nabla_{\boldsymbol{x}} \cdot \boldsymbol{\sigma}_{\mathrm{tot}} \quad \text{in } \Omega \tag{4.139a}$$
$$0 = \nabla_{\boldsymbol{x}} \cdot \boldsymbol{d} \quad \text{in } \Omega \tag{4.139b}$$
$$\dot{c}_{\mathrm{OY}} = -s_{\mathrm{OY}/e}(\|\boldsymbol{e}\|, c_{\mathrm{OY}}) + s_{\mathrm{OY/OB}}(c_{\mathrm{OY}}, c_{\mathrm{OB}}) \quad \text{in } \Omega \tag{4.139c}$$
$$\dot{c}_{\mathrm{MC}} = -\nabla_{\boldsymbol{x}} \cdot \boldsymbol{q}_{\mathrm{MC}} + s_{\mathrm{MC}}(c_{\mathrm{OY}}) \quad \text{in } \Omega \tag{4.139d}$$
$$\dot{c}_{\mathrm{OC}} = -\nabla_{\boldsymbol{x}} \cdot \boldsymbol{q}_{\mathrm{OC}} \quad \text{in } \Omega \tag{4.139e}$$
$$\dot{c}_{\mathrm{MB}} = -\nabla_{\boldsymbol{x}} \cdot \boldsymbol{q}_{\mathrm{MB}} + s_{\mathrm{MB}}(c_{\mathrm{OC}}) \quad \text{in } \Omega \tag{4.139f}$$
$$\dot{c}_{\mathrm{OB}} = -\nabla_{\boldsymbol{x}} \cdot \boldsymbol{q}_{\mathrm{OB}} - s_{\mathrm{OY/OB}}(c_{\mathrm{OY}}, c_{\mathrm{OB}}) \quad \text{in } \Omega \tag{4.139g}$$

and is to be solved for the mechanical displacements $\boldsymbol{u}$, the electric potential ϕ as well as all involved chemical concentrations as degrees of freedom, i.e. $dof = \{\boldsymbol{u}, \phi, c_{\mathrm{OY}}, c_{\mathrm{MC}}, c_{\mathrm{OC}}, c_{\mathrm{MB}}, c_{\mathrm{OB}}\}$, in the domain Ω. In comparison to the model proposed in Sect. 4.3.1, additional messenger substances (MB) are introduced, which contribute to the reversal from the osteoclastic resorption phase to the osteoblastic formation phase, and a new source term ($s_{\mathrm{OY/OB}}$) is added to account for the differentiation of osteoblasts into osteocytes.

In the quasi-static balance of linear momentum (4.139a), mechanical body forces are neglected in this work which yields a divergence-free total stress tensor $\boldsymbol{\sigma}_{\mathrm{tot}}$. As shown in (4.5), this tensor contains higher-gradient contributions through the hyperstress tensor $\boldsymbol{\pi}$ (energetically conjugate to $\nabla_{\boldsymbol{x}}\boldsymbol{\varepsilon}$) in addition to the Cauchy-type stress tensor $\boldsymbol{\sigma}$ (energetically conjugate to $\boldsymbol{\varepsilon}$).

The second balance equation (4.139b) states Gauss's law of electricity with the assumption of no free charges since a dielectric material is considered. Accordingly, the dielectric displacement vector $\boldsymbol{d}$ is also divergence-free.

The evolution of the osteocyte concentration c_{OY} in time (4.139c) is modelled in terms of a source term as well as a sink term with different coupling properties. More specifically speaking, the sink term

$$s_{\mathrm{OY}/e} = k_{\mathrm{OY},1}\left[1 - \exp\left(-\frac{\|\boldsymbol{e}\|}{e_{\mathrm{crit}}}\frac{c_{\mathrm{OY}}}{c_{\mathrm{OY}}^{\mathrm{init}}}\right)\right] \tag{4.140}$$

models the apoptotic behaviour of the bone cells as revealed by the experiments performed in [120]. As shown in Fig. 4.24, the sink term increases rapidly when the norm of the electric field reaches a value of $10\,\mathrm{Vmm}^{-1}$ which has been found to be a critical value for immediate cell death. However, cell damage and apoptosis already start at values of $1\,\mathrm{Vmm}^{-1}$, cf. [120]. Further details on this sink term can be found in Sect. 4.3.1.1. The second term on the right-hand side of (4.139c) governs the differentiation

of osteoblasts into osteocytes during the formation of new bone material as discussed in detail in Sect. 4.2. Accordingly, the source term is defined as

$$s_{\mathrm{OY/OB}} = k_{\mathrm{OY},2}\left[1 - \exp\left(-\frac{c_{\mathrm{OB}}}{c_{\mathrm{OB}}^{\mathrm{crit}}}\frac{\left[c_{\mathrm{OY}}^{\mathrm{init}} - c_{\mathrm{OY}}\right]}{c_{\mathrm{OY}}^{\mathrm{init}}}\right)\right]. \tag{4.141}$$

It possesses a similar saturation-type structure as the sink term (4.140) in order to ensure that the concentration of osteocytes increases due to the presence of osteoblasts but does not exceed the reference value of $c_{\mathrm{OY}}^{\mathrm{init}} = 2.5 \times 10^4\,\mathrm{mm}^{-3}$, cf. Fig. 4.25. In Appendix C.3.2 this issue is addressed in terms of a numerical study.

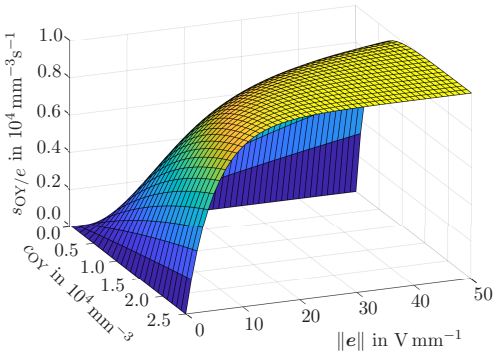

Figure 4.24: Sink term $s_{\mathrm{OY}/e}$ for the osteocyte concentration as a function of the electric field magnitude and of the osteocyte concentration itself. In the initial state in which $c_{\mathrm{OY}}^{\mathrm{init}} = 2.5 \times 10^4\,\mathrm{mm}^{-3}$ holds, the magnitude of the sink term increases rapidly when the electric field approaches a magnitude of $10\,\mathrm{V\,mm}^{-1}$. Reproduced from [175] under the terms of the Creative Commons Attribution License (CC BY).

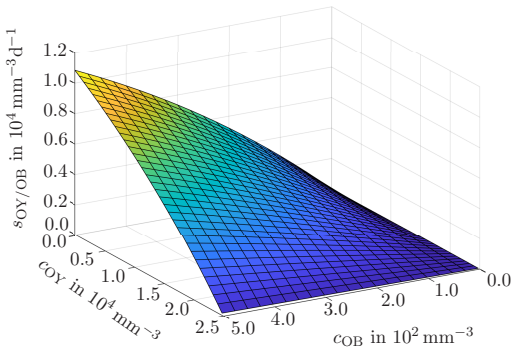

Figure 4.25: Sink term $s_{\mathrm{OY/OB}}$ for the osteocyte concentration as a function of the osteoblast concentration and of the osteocyte concentration. Within the bone remodelling process, osteoblasts differentiate into osteocytes while becoming embedded in the bone matrix. Consequently, the osteocyte concentration increases with the number of active osteoblasts until the initial osteocyte concentration $c_{\mathrm{OY}}^{\mathrm{init}} = 2.5 \times 10^4\,\mathrm{mm}^{-3}$ in healthy bone is regained. Reprinted from [175] under the terms of the Creative Commons Attribution License (CC BY).

Diffusion equation (4.139d) describes the migration of messenger substances which are produced in consequence to osteocyte apoptosis and subsequently transmitted through the bone matrix in order to recruit osteoclasts to the remodelling site. These represent "active" signalling mechanisms in terms of osteoclastic secretion of, e.g., M-CSF and RANKL on the one hand, and "passive" signalling mechanisms by the decreased level of sclerostin on the other hand, cf. Sect. 4.2. Accordingly, the corresponding source term reads

$$s_{\mathrm{MC}} = k_{\mathrm{MC}}\left[1 - \frac{c_{\mathrm{OY}}}{c_{\mathrm{OY}}^{\mathrm{init}}}\right] \tag{4.142}$$

equally as in (4.84) and takes positive values as soon as the local osteocyte concentration has decreased with respect to the initial value $c_{\mathrm{OY}}^{\mathrm{init}}$. The diffusive behaviour of the messenger substances is isotropic such that the flux term in (4.139d) reads

$$\boldsymbol{q}_{\mathrm{MC}} = -D_{\mathrm{MC}}\,\nabla_{\boldsymbol{x}} c_{\mathrm{MC}} \tag{4.143}$$

with the constant diffusion coefficient D_{MC}, cf. (4.85).

The recruitment of osteoclasts by the messenger substances is incorporated into the model through boundary conditions under the assumption that the bone excerpt under investigation is connected to the surrounding vascular system. Specifically speaking, it is assumed that Haversian and Volkmann's canals are located at the boundaries of the considered domain. As soon as the flux of messenger substances exceeds a predefined threshold at these boundaries or, more physically speaking as soon as enough signals have been detected, osteoclasts enter the domain. For the finite element model, this means that the osteoclast flux at each surface node S is prescribed by coupling the corresponding entry $f^S_{\mathrm{OC,pre}}$ in the global generalised surface force vector to the respective generalised reaction force value $f^S_{\mathrm{MC,rea}}$, i.e.

$$\begin{aligned} \overline{q}_{\mathrm{OC}} &= \begin{cases} -\,k_{\mathrm{OC}}\,q_{\mathrm{MC}} & \text{if} \quad q_{\mathrm{MC}} \geq q_{\mathrm{MC,min}} \\ 0 & \text{else} \end{cases} \\ \text{such that} \quad f^S_{\mathrm{OC,pre}} &= \begin{cases} -\,k_{\mathrm{OC}}\,f^S_{\mathrm{MC,rea}} & \text{if} \quad f^S_{\mathrm{MC,rea}} \geq f^S_{\mathrm{MC,min}} \\ 0 & \text{else} \end{cases} \end{aligned} \tag{4.144}$$

with

$$\boldsymbol{f}_{\bullet,*} = \mathop{\mathbf{A}}_{e=1}^{\mathrm{n_{sel}}} \sum_{A=1}^{\mathrm{n_{en}}} \int_{\partial\Omega_f^e} N^A\, q_{\bullet,*}\,\mathrm{d}a, \qquad \bullet \in \{\mathrm{OC},\,\mathrm{MC}\}, \quad * \in \{\mathrm{pre},\mathrm{rea},\mathrm{min}\}. \tag{4.145}$$

Therein, constant k_{OC} specifies the linear relation between the coefficients of the generalised force contributions and $q_{\mathrm{MC,min}} \geq 0$ is the prescribed threshold value for the outflux of messenger substances at the boundary $\partial\Omega_f^e$. The respective threshold value $f^S_{\mathrm{MC,min}}$ at node S is calculated from $q_{\mathrm{MC,min}}$ by using the $\mathrm{n_{en}}$ basis functions N^A on each of the $\mathrm{n_{sel}}$ surface elements, assembling the local contributions on element level to their global counterparts by operator $\mathbf{A}$, and extracting the nodal value corresponding to node S. After osteoclasts have entered the domain, the diffusive term in (4.139e) describes their migration through the bone. As discussed in [100], osteoclasts are steered by the microdamage in order to perform targeted bone remodelling at the damaged site. Moreover, these bone cells move preferably in the direction of osteon alignment, see Sect. 4.3.1.1. Based on these two characteristics, the modelling approach for the osteoclast cell flux is assumed to take the form

$$\boldsymbol{q}_{\mathrm{OC}} = -\boldsymbol{D}_{\mathrm{OC}} \cdot \nabla_{\boldsymbol{x}} c_{\mathrm{OC}} \tag{4.146}$$

with the anisotropic diffusion tensor

$$\boldsymbol{D}_{\mathrm{OC}} = D_{\mathrm{OC}}\, \boldsymbol{A} \tag{4.147}$$

based on structural tensor $\boldsymbol{A}$ which has been introduced in (4.90).

The coupling between osteoclastic and osteoblastic activity is accounted for by a second type of messenger substances in the present modelling approach. These include, e.g., matrix-derived growth factors such as TGF-β and IGPs as well as osteoclast-derived coupling factors like BMP-6 and Wnt10b, see [148] and the discussion in Sect. 4.2. The production and diffusion of these messenger substances is described by diffusion equation (4.139f). Therein, the source term

$$s_{\mathrm{MB}} = k_{\mathrm{MB}}\, c_{\mathrm{OC}} \tag{4.148}$$

describes the increase of the messenger substance concentration c_{MB} in response to the presence of osteoclasts in terms of a linear relation with scalar factor k_{MB}. In analogy to the diffusive behaviour of the messenger substances for the osteoclast recruitment, the flux term

$$\boldsymbol{q}_{\mathrm{MB}} = -D_{\mathrm{MB}}\, \nabla_{\boldsymbol{x}} c_{\mathrm{MB}} \tag{4.149}$$

is determined by the constant diffusion coefficient D_{MB}.

Finally, the diffusion of the osteoblasts is considered in (4.139g). The recruitment of osteoblasts by their messenger substances is incorporated by the prescription of influx boundary conditions by analogy with (4.144)-(4.145). Accordingly, the influx of osteoblasts is prescribed by using a constant factor k_{OB} which yields

$$\begin{aligned} \overline{q}_{\mathrm{OB}} &= \begin{cases} -\,k_{\mathrm{OB}}\, q_{\mathrm{MB}} & \text{if} \quad q_{\mathrm{MB}} \geq q_{\mathrm{MB,min}} \\ 0 & \text{else} \end{cases} \\ \text{such that} \quad f^{S}_{\mathrm{OB,pre}} &= \begin{cases} -\,k_{\mathrm{OB}}\, f^{S}_{\mathrm{MB,rea}} & \text{if} \quad f^{S}_{\mathrm{MB,rea}} \geq f^{S}_{\mathrm{MB,min}} \\ 0 & \text{else} \end{cases} \end{aligned} \tag{4.150}$$

i.e. an influx is activated as soon as the threshold for the outflux of messenger substances is reached at the surface node S under consideration. The diffusion of osteoblasts is modelled similarly to the osteoclast diffusion such that the flux

$$\boldsymbol{q}_{\mathrm{OB}} = -\boldsymbol{D}_{\mathrm{OB}} \cdot \nabla_{\boldsymbol{x}} c_{\mathrm{OB}} \tag{4.151}$$

is governed by the anisotropic diffusion tensor

$$\boldsymbol{D}_{\mathrm{OB}} = D_{\mathrm{OB}}\, \boldsymbol{A}\,. \tag{4.152}$$

Since in the cortical bone remodelling process, osteoclasts excavate tunnels through which osteoblasts migrate, the diffusion direction of the osteoblast field in the proposed modelling approach is the same as the direction for the osteoclast diffusion, see (4.147). The remaining term in (4.139g) is the sink term stemming from the differentiation of osteoblasts to osteocytes during the formation of new bone and subsequent mineralisation. It is the direct counterpart to source term (4.141) for the osteocyte concentration in (4.139c), such that the transformation between the two cell types is modelled consistently. The governing set of equations including the definition of all source terms and flux terms is summarised in Table 4.6.

Table 4.6: Governing balance equations, source terms and flux terms.

Balance equations	
$\mathbf{0} = \nabla_{\boldsymbol{x}} \cdot \boldsymbol{\sigma}_{\mathrm{tot}}$	in Ω
$0 = \nabla_{\boldsymbol{x}} \cdot \boldsymbol{d}$	in Ω
$\dot{c}_{\mathrm{OY}} = -s_{\mathrm{OY}/e}(\Vert\boldsymbol{e}\Vert, c_{\mathrm{OY}}) + s_{\mathrm{OY/OB}}(c_{\mathrm{OY}}, c_{\mathrm{OB}})$	in Ω
$\dot{c}_{\mathrm{MC}} = -\nabla_{\boldsymbol{x}} \cdot \boldsymbol{q}_{\mathrm{MC}} + s_{\mathrm{MC}}(c_{\mathrm{OY}})$	in Ω
$\dot{c}_{\mathrm{OC}} = -\nabla_{\boldsymbol{x}} \cdot \boldsymbol{q}_{\mathrm{OC}}$	in Ω
$\dot{c}_{\mathrm{MB}} = -\nabla_{\boldsymbol{x}} \cdot \boldsymbol{q}_{\mathrm{MB}} + s_{\mathrm{MB}}(c_{\mathrm{OC}})$	in Ω
$\dot{c}_{\mathrm{OB}} = -\nabla_{\boldsymbol{x}} \cdot \boldsymbol{q}_{\mathrm{OB}} - s_{\mathrm{OY/OB}}(c_{\mathrm{OY}}, c_{\mathrm{OB}})$	in Ω

Source terms	Flux terms
$s_{\mathrm{OY}/e} = k_{\mathrm{OY},1}\left[1 - \exp\left(-\frac{\Vert\boldsymbol{e}\Vert}{e_{\mathrm{crit}}}\frac{c_{\mathrm{OY}}}{c_{\mathrm{OY}}^{\mathrm{init}}}\right)\right]$	$\boldsymbol{q}_{\mathrm{MC}} = -D_{\mathrm{MC}}\,\nabla_{\boldsymbol{x}} c_{\mathrm{MC}}$
$s_{\mathrm{OY/OB}} = k_{\mathrm{OY},2}\left[1 - \exp\left(-\frac{c_{\mathrm{OB}}}{c_{\mathrm{OB}}^{\mathrm{crit}}}\frac{[c_{\mathrm{OY}}^{\mathrm{init}} - c_{\mathrm{OY}}]}{c_{\mathrm{OY}}^{\mathrm{init}}}\right)\right]$	$\boldsymbol{q}_{\mathrm{OC}} = -\boldsymbol{D}_{\mathrm{OC}} \cdot \nabla_{\boldsymbol{x}} c_{\mathrm{OC}}$
$s_{\mathrm{MC}} = k_{\mathrm{MC}}\left[1 - \frac{c_{\mathrm{OY}}}{c_{\mathrm{OY}}^{\mathrm{init}}}\right]$	$\boldsymbol{q}_{\mathrm{MB}} = -D_{\mathrm{MB}}\,\nabla_{\boldsymbol{x}} c_{\mathrm{MB}}$
$s_{\mathrm{MB}} = k_{\mathrm{MB}}\,c_{\mathrm{OC}}$	$\boldsymbol{q}_{\mathrm{OB}} = -\boldsymbol{D}_{\mathrm{OB}} \cdot \nabla_{\boldsymbol{x}} c_{\mathrm{OB}}$
	$\boldsymbol{D}_{\mathrm{OC}} = D_{\mathrm{OC}}\,\boldsymbol{A}$
	$\boldsymbol{D}_{\mathrm{OB}} = D_{\mathrm{OB}}\,\boldsymbol{A}$

4.4.1.2 Balance of energy

The balance of energy for the chemo-electro-mechanical coupling in this work has been derived in Sect. 4.3.1.2. The chemical contributions in the global form (4.95) are reformulated in the following for the particular modelling approach proposed in Sect. 4.4.1.1.

Taking into account contributions from the osteocytes, osteoclasts and osteoblasts as well as from the different types of messenger substances, the chemical powers are

$$\mathcal{Q}_{\text{chem,OY}} = -\int_\Omega \mu^c_{\text{OY}}\, s_{\text{OY}/e}\,\mathrm{d}v + \int_\Omega \mu^c_{\text{OY}}\, s_{\text{OY/OB}}\,\mathrm{d}v =: \int_\Omega Q_{\text{OY}}\,\mathrm{d}v, \tag{4.153}$$

$$\begin{aligned}\mathcal{Q}_{\text{chem,MC}} &= \int_{\partial\Omega} \mu^c_{\text{MC}}\, q_{\text{MC}}\,\mathrm{d}a + \int_\Omega \mu^c_{\text{MC}}\, s_{\text{MC}}\,\mathrm{d}v \\ &= -\int_\Omega \nabla_{\boldsymbol{x}} \cdot [\mu^c_{\text{MC}}\, \boldsymbol{q}_{\text{MC}}]\,\mathrm{d}v + \int_\Omega \mu^c_{\text{MC}}\, s_{\text{MC}}\,\mathrm{d}v =: \int_\Omega Q_{\text{MC}}\,\mathrm{d}v,\end{aligned} \tag{4.154}$$

$$\mathcal{Q}_{\text{chem,OC}} = \int_{\partial\Omega} \mu^c_{\text{OC}}\, q_{\text{OC}}\,\mathrm{d}a = -\int_\Omega \nabla_{\boldsymbol{x}} \cdot [\mu^c_{\text{OC}}\, \boldsymbol{q}_{\text{OC}}]\,\mathrm{d}v =: \int_\Omega Q_{\text{OC}}\,\mathrm{d}v, \tag{4.155}$$

$$\begin{aligned}\mathcal{Q}_{\text{chem,MB}} &= \int_{\partial\Omega} \mu^c_{\text{MB}}\, q_{\text{MB}}\,\mathrm{d}a + \int_\Omega \mu^c_{\text{MB}}\, s_{\text{MB}}\,\mathrm{d}v \\ &= -\int_\Omega \nabla_{\boldsymbol{x}} \cdot [\mu^c_{\text{MB}}\, \boldsymbol{q}_{\text{MB}}]\,\mathrm{d}v + \int_\Omega \mu^c_{\text{MB}}\, s_{\text{MB}}\,\mathrm{d}v =: \int_\Omega Q_{\text{MB}}\,\mathrm{d}v,\end{aligned} \tag{4.156}$$

$$\begin{aligned}\mathcal{Q}_{\text{chem,OB}} &= \int_{\partial\Omega} \mu^c_{\text{OB}}\, q_{\text{OB}}\,\mathrm{d}a - \int_\Omega \mu^c_{\text{OB}}\, s_{\text{OY/OB}}\,\mathrm{d}v \\ &= -\int_\Omega \nabla_{\boldsymbol{x}} \cdot [\mu^c_{\text{OB}}\, \boldsymbol{q}_{\text{OB}}]\,\mathrm{d}v - \int_\Omega \mu^c_{\text{OB}}\, s_{\text{OY/OB}}\,\mathrm{d}v =: \int_\Omega Q_{\text{OB}}\,\mathrm{d}v,\end{aligned} \tag{4.157}$$

with the chemical potentials μ^c_{OY}, μ^c_{MC}, μ^c_{OC}, μ^c_{MB}, μ^c_{OB} and with the surface fluxes

$$\begin{aligned} q_{\text{MC}} &= -\,\boldsymbol{q}_{\text{MC}} \cdot \boldsymbol{n}, \quad q_{\text{OC}} = -\,\boldsymbol{q}_{\text{OC}} \cdot \boldsymbol{n}, \\ q_{\text{MB}} &= -\,\boldsymbol{q}_{\text{MB}} \cdot \boldsymbol{n}, \quad q_{\text{OB}} = -\,\boldsymbol{q}_{\text{OB}} \cdot \boldsymbol{n}. \end{aligned} \tag{4.158}$$

Under the use of the (dynamic version of the) balance of linear momentum (4.139a) and Gauss's law (4.139b), the global form of the balance of energy thus results in

$$\begin{aligned}\int_\Omega \rho\,\dot{H}\,\mathrm{d}v = &\int_\Omega [\nabla_{\boldsymbol{x}}\dot{\boldsymbol{u}}] : \boldsymbol{\sigma}\,\mathrm{d}v + \int_\Omega [\nabla_{\boldsymbol{x}}\nabla_{\boldsymbol{x}}\dot{\boldsymbol{u}}] :\cdot\, \boldsymbol{\pi}\,\mathrm{d}v + \int_\Omega \nabla_{\boldsymbol{x}}\dot{\phi} \cdot \boldsymbol{d}\,\mathrm{d}v \\ &+ \int_\Omega Q_{\text{OY}}\,\mathrm{d}v + \int_\Omega Q_{\text{MC}}\,\mathrm{d}v + \int_\Omega Q_{\text{OC}}\,\mathrm{d}v \\ &+ \int_\Omega Q_{\text{MB}}\,\mathrm{d}v + \int_\Omega Q_{\text{OB}}\,\mathrm{d}v + \int_\Omega Q_{\text{th}}\,\mathrm{d}v\end{aligned} \tag{4.159}$$

and the corresponding local form is

$$\begin{aligned}\rho\,\dot{H} = &\,\dot{\boldsymbol{\varepsilon}} : \boldsymbol{\sigma} + \nabla_{\boldsymbol{x}}\dot{\boldsymbol{\varepsilon}} :\cdot\, \boldsymbol{\pi} - \dot{\boldsymbol{e}} \cdot \boldsymbol{d} \\ &+ Q_{\text{OY}} + Q_{\text{MC}} + Q_{\text{OC}} + Q_{\text{MB}} + Q_{\text{OB}} + Q_{\text{th}}.\end{aligned} \tag{4.160}$$

4.4.1.3 Dissipation inequality

In Sect. 4.3.1.3, the dissipation inequality, respectively Clausius-Duhem inequality has been derived for the chemo-electro-mechanical coupling proposed in this work. The results therein can be adopted for the present section. Accordingly, the dissipation inequality (4.106) holds whereas the considered chemical contributions therein must be specified as $\bullet \in \{\mathrm{OY}, \mathrm{MC}, \mathrm{OC}, \mathrm{MB}, \mathrm{OB}\}$. The same applies to the constitutive relations (4.107) derived by following the procedure of Coleman and Noll.

4.4.2 Modelling of bone cell-driven surface growth

The targeted diffusion of osteoblasts towards the crack surface, as described in Sect. 4.4.1.1, is the starting point for crack healing since these cells form new bone material on the open surfaces. From a modelling point of view, this means that the outflux of osteoblasts $-q_{\mathrm{OB}} = \boldsymbol{q}_{\mathrm{OB}} \cdot \boldsymbol{n}$ over these surfaces can be regarded as the driving force for surface growth. Within the scope of the present contribution, growth is modelled in discrete time steps, denoted as *spurts*, as will be discussed in more detail in Sect. 4.4.5.3. Accordingly, the outflux of cells is integrated over the time interval between two distinct growth spurts and determines the prescribed growth in normal direction of the considered growing surface. The expansion of the outer surface (in one growth spurt) can then be described by a displacement

$$\overline{u}_n^{\mathrm{G}} = \boldsymbol{u}^{\mathrm{G}} \cdot \boldsymbol{n} = k_{\mathrm{flt}} \sum_i \left[-q_{\mathrm{OB}}\right]_i \, \Delta t_i \tag{4.161}$$

for each individual surface node. Therein, Δt_i are the time increments used in the simulation whereas $\Delta t^{\mathrm{G}} = \sum_i \Delta t_i$ is the time between two adjacent growth spurts. The constant factor k_{flt} (flt: form, lifetime) represents an estimate for the volume of osteoid produced by one osteoblast cell over its entire lifetime. Since this factor is dependent on several characteristic values such as the radius of the resorption cavity and the surface curvature, the value employed in this work is based on average values from the literature. More specifically speaking, the average lifetime of active osteoblasts is taken from [96] as 3 months $\approx$ 90 days (d) and the produced bone volume by one osteoblast per day is estimated on the basis of [27, 28] as $k_{\mathrm{form}} = 150\,\mu\mathrm{m}^3\,\mathrm{d}^{-1}$ per cell. Consequently, $k_{\mathrm{flt}} \approx 1.35 \times 10^{-5}\,\mathrm{mm}^3$ per cell is used. For the simulations performed within the scope of this work, a smoothing of the pointwise prescribed normal displacement (4.161) is incorporated by averaging over a set of five neighbouring surface nodes.

4.4.3 Computational framework

Due to the different time scales of the fast crack event (seconds) with the resulting osteocyte apoptosis on the one hand, and the slow diffusion processes of bone cells as well as the successive healing process (days up to months) on the other hand, a separation

of time scales is employed in the proposed computational framework. Moreover, the higher-order PDEs resulting from the incorporation of flexoelectric effects, cf. (4.139a)-(4.139b), require an at least C^1-continuous discretisation, whereas the subsequent diffusion processes can be solved via a classic finite element method with C^0-continuous basis functions. For the flexoelectric calculations, isogeometric analysis is thus a reasonable choice since higher-order PDEs can be solved directly without resorting to mixed-type multi-field formulations. On the other hand, the prescription of growth as discussed in Sect. 4.4.5.3 is more intuitive in a finite element framework since typical FEA basis functions are interpolatory in contrast to NURBS-based IGA discretisations. These different aspects motivate a framework in which the crack event and resulting flexoelectricity-induced osteocyte apoptosis are implemented by using isogeometric analysis with global C^1-continuity and a time scale of seconds, whereas the diffusion equations as well as the surface growth mechanisms are incorporated in a classic finite element scheme with a time scale of days. The coupling between the two parts of the simulation is performed by projection of nodal values as indicated in the flowchart presented in Fig. 4.26. In order to simplify the transfer of nodal values from the IGA simulation to the FEA simulation, the same physical mesh is used in both frameworks. However, the nodal points in the mesh are, unlike in the classic finite element scheme, not the degrees of freedom in IGA. Consequently, a projection of the field variables to the nodal points in the mesh via the basis functions is required before the transfer can be carried out. Both frameworks are treated in more detail in the following sections.

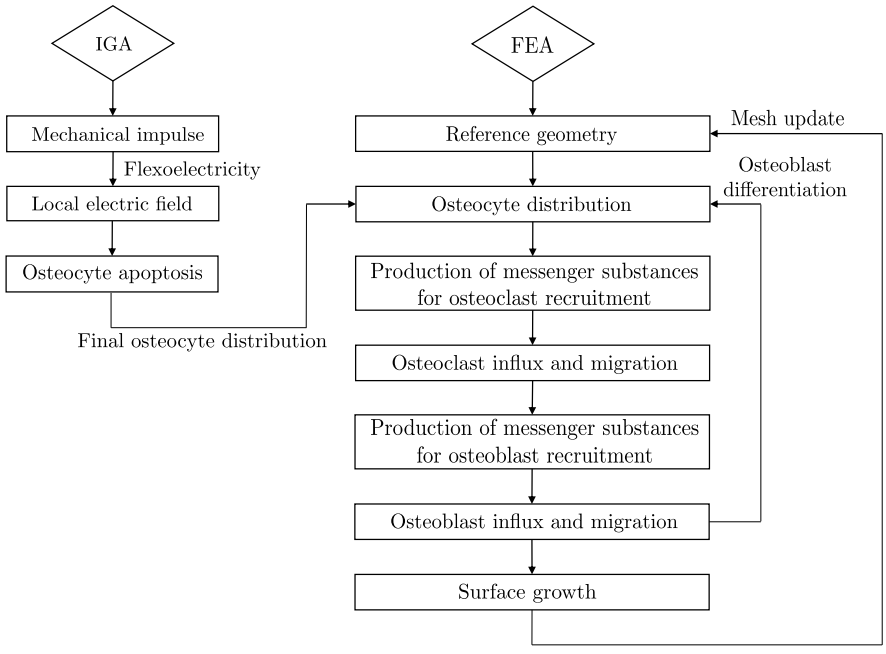

Figure 4.26: Combined IGA-FEA scheme for bone remodelling simulations including flexoelectricity and surface growth. Reproduced from [175] under the terms of the Creative Commons Attribution License (CC BY).

4.4.4 IGA framework

Within the IGA framework, the electromechanical response to mechanical loading as well as the apoptosis of osteocytes as a consequence of induced electric fields is captured. The set of degrees of freedom for this part of the simulation is $\{\boldsymbol{u}, \phi, c_{\mathrm{OY}}\}$. For the approximation of these fields, quadratic NURBS basis functions are employed which possess advantageous continuity properties as discussed in detail in Sect. 2.1.3. Within the scope of this work, a multipatch IGA framework is established such that the required C^1-continuity of the basis functions needs to be retained at the patch interfaces in particular. This is accomplished by the use of appropriate linear constraints as discussed in detail in Sect. 4.3.3.2 and corresponding Appendix C.4.1.

As indicated in Fig. 4.26, the overall aim of the IGA simulation is the calculation of the osteocyte distribution after apoptosis has been induced by a crack event. In the present contribution, the crack evolution is simulated in discrete time steps and the final osteocyte concentration along the entire crack is obtained by interpolation. More details on this procedure will be given in Sect. 4.4.6.3 together with the corresponding simulation results for a representative numerical example.

4.4.4.1 Weak form of the governing equations

In the IGA framework, the governing equations are the balance of linear momentum (4.139a), Gauss's law (4.139b) and the rate equation of the osteocyte concentration (4.139c). In the latter, however, only the sink term with respect to the electric field (4.140) is active whereas the source term (4.141), which incorporates the differentiation of osteoblasts into osteocytes, is neglected since osteoblasts are not accounted for in the IGA framework. The weak form of the governing equations is obtained as

$$0 = \int_{\Omega} \nabla_{\boldsymbol{x}} \delta\boldsymbol{u} : \boldsymbol{\sigma} \, \mathrm{d}v + \int_{\Omega} \nabla_{\boldsymbol{x}} \nabla_{\boldsymbol{x}} \delta\boldsymbol{u} :\cdot \boldsymbol{\pi} \, \mathrm{d}v - \int_{\partial\Omega} \delta\boldsymbol{u} \cdot \boldsymbol{t} \, \mathrm{d}a \tag{4.162}$$

$$0 = -\int_{\Omega} \nabla_{\boldsymbol{x}} \delta\phi \cdot \boldsymbol{d} \, \mathrm{d}v - \int_{\partial\Omega} \delta\phi \, \omega \, \mathrm{d}a \tag{4.163}$$

$$0 = \int_{\Omega} \delta c_{\mathrm{OY}} \, \dot{c}_{\mathrm{OY}} \, \mathrm{d}v + \int_{\Omega} \delta c_{\mathrm{OY}} \, s_{\mathrm{OY}/e} \, \mathrm{d}v \tag{4.164}$$

by following the procedure discussed in Sect. 4.1.2.1 and Sect. 4.3.2.1.

4.4.4.2 Discretised weak forms

With the discretised test functions specified in (4.113) and under the use of a Backward-Euler integration scheme, cf. (4.114), the discretised forms of (4.162)-(4.164) result in

$$\boldsymbol{r}_{\boldsymbol{u}} = \mathop{\mathbf{A}}_{e=1}^{\mathrm{n_{el}}} \sum_{A=1}^{\mathrm{n_{en}}} \int_{\Omega^e} \boldsymbol{\sigma} \cdot \nabla_{\boldsymbol{x}} R^A \, \mathrm{d}v + \int_{\Omega^e} \boldsymbol{\pi} : \nabla_{\boldsymbol{x}} \nabla_{\boldsymbol{x}} R^A \, \mathrm{d}v - \int_{\partial\Omega^e} \boldsymbol{t} \, R^A \, \mathrm{d}a \tag{4.165}$$

$$\boldsymbol{r}_{\phi} = \mathop{\mathbf{A}}_{e=1}^{\mathrm{n_{el}}} \sum_{A=1}^{\mathrm{n_{en}}} \int_{\Omega^e} \boldsymbol{d} \cdot \nabla_{\boldsymbol{x}} R^A \,\mathrm{d}v + \int_{\partial\Omega^e} \omega \, R^A \,\mathrm{d}a \tag{4.166}$$

$$\boldsymbol{r}_{\mathrm{OY}} = \mathop{\mathbf{A}}_{e=1}^{\mathrm{n_{el}}} \sum_{A=1}^{\mathrm{n_{en}}} \int_{\Omega^e} R^A \, \frac{c_{\mathrm{OY}} - c_{\mathrm{OY},n}}{\Delta t} \,\mathrm{d}v + \int_{\Omega^e} R^A \, s_{\mathrm{OY}/e} \,\mathrm{d}v. \tag{4.167}$$

These contribute to the residual vector $\boldsymbol{r} = [\boldsymbol{r}_{\boldsymbol{u}}, \boldsymbol{r}_{\phi}, \boldsymbol{r}_{\mathrm{OY}}]^{\mathrm{t}}$ with respect to the vector of degrees of freedom $\boldsymbol{\varphi} = [\boldsymbol{u}, \phi, c_{\mathrm{OY}}]^{\mathrm{t}}$ in the IGA simulations. The tangent contributions corresponding to the residual vectors in the underlying Newton-Raphson scheme are derived in Appendix C.1.2.

4.4.5 FEA framework

The second part of the simulation takes place within a finite element framework with Lagrangian basis functions. In particular, 4-noded quadrilateral elements are employed for the discretisation of the geometry and unknown fields which, for this second part, read $\{\boldsymbol{x}, c_{\mathrm{OY}}, c_{\mathrm{MC}}, c_{\mathrm{OC}}, c_{\mathrm{MB}}, c_{\mathrm{OB}}\}$. In this list of degrees of freedom, vector $\boldsymbol{x}$ representing the geometry in terms of nodal coordinates has been added, since these coordinates may change due to the mesh update procedure which is incorporated for the handling of surface growth as will be discussed in detail in Sect. 4.4.5.3. The initial mesh, however, originates from the IGA framework such that the nodal coordinates coincide in both simulations before growth occurs.

4.4.5.1 Weak form of the governing equations

Complementing (4.162)-(4.164), the weak form of the governing equations (4.139c)-(4.139g) in the FEA scheme is derived in the following. Regarding the rate equation for the osteocyte concentration, the coupling between osteocytes and electric contributions is not part of the FEA framework but has been incorporated into the IGA framework. The source term which models the differentiation of osteoblasts into osteocytes during remodelling is, however, considered in the weak form for the finite element analysis which results in

$$0 = \int_{\Omega} \delta c_{\mathrm{OY}} \, \dot{c}_{\mathrm{OY}} \,\mathrm{d}v - \int_{\Omega} \delta c_{\mathrm{OY}} \, s_{\mathrm{OY/OB}} \,\mathrm{d}v. \tag{4.168}$$

The weak form of the rate equation of messenger substances (4.139d) which are responsible for osteoclast recruitment, is obtained by employing the virtual concentration, respectively test function, δc_{MC}, accordingly

$$
\begin{aligned}
0 &= \int_{\Omega} \delta c_{\mathrm{MC}}\, \dot{c}_{\mathrm{MC}}\, \mathrm{d}v + \int_{\Omega} \delta c_{\mathrm{MC}}\, \nabla_{\boldsymbol{x}} \cdot \boldsymbol{q}_{\mathrm{MC}}\, \mathrm{d}v - \int_{\Omega} \delta c_{\mathrm{MC}}\, s_{\mathrm{MC}}\, \mathrm{d}v \\
&= \int_{\Omega} \delta c_{\mathrm{MC}}\, \dot{c}_{\mathrm{MC}}\, \mathrm{d}v - \int_{\Omega} \nabla_{\boldsymbol{x}} \delta c_{\mathrm{MC}} \cdot \boldsymbol{q}_{MC}\, \mathrm{d}v \\
&\quad - \int_{\partial\Omega} \delta c_{\mathrm{MC}}\, q_{\mathrm{MC}}\, \mathrm{d}a - \int_{\Omega} \delta c_{\mathrm{MC}}\, s_{\mathrm{MC}}\, \mathrm{d}v. \qquad (4.169)
\end{aligned}
$$

Analogously, the weak form of the rate equations (4.139e)-(4.139g) is derived by using the virtual concentrations, respectively test functions, $\delta c_{\mathrm{OC}}, \delta c_{\mathrm{MB}}$ and δc_{OB} so that

$$
0 = \int_{\Omega} \delta c_{\mathrm{OC}}\, \dot{c}_{\mathrm{OC}}\, \mathrm{d}v - \int_{\Omega} \nabla_{\boldsymbol{x}} \delta c_{\mathrm{OC}} \cdot \boldsymbol{q}_{OC}\, \mathrm{d}v - \int_{\partial\Omega} \delta c_{\mathrm{OC}}\, q_{\mathrm{OC}}\, \mathrm{d}a \qquad (4.170)
$$

$$
\begin{aligned}
0 &= \int_{\Omega} \delta c_{\mathrm{MB}}\, \dot{c}_{\mathrm{MB}}\, \mathrm{d}v - \int_{\Omega} \nabla_{\boldsymbol{x}} \delta c_{\mathrm{MB}} \cdot \boldsymbol{q}_{MB}\, \mathrm{d}v \\
&\quad - \int_{\partial\Omega} \delta c_{\mathrm{MB}}\, q_{\mathrm{MB}}\, \mathrm{d}a - \int_{\Omega} \delta c_{\mathrm{MB}}\, s_{\mathrm{MB}}\, \mathrm{d}v \qquad (4.171)
\end{aligned}
$$

$$
\begin{aligned}
0 &= \int_{\Omega} \delta c_{\mathrm{OB}}\, \dot{c}_{\mathrm{OB}}\, \mathrm{d}v - \int_{\Omega} \nabla_{\boldsymbol{x}} \delta c_{\mathrm{OB}} \cdot \boldsymbol{q}_{OB}\, \mathrm{d}v \\
&\quad - \int_{\partial\Omega} \delta c_{\mathrm{OB}}\, q_{\mathrm{OB}}\, \mathrm{d}a + \int_{\Omega} \delta c_{\mathrm{OB}}\, s_{\mathrm{OY/OB}}\, \mathrm{d}v. \qquad (4.172)
\end{aligned}
$$

4.4.5.2 Discretised weak forms

Within the FEA framework, the weak forms (4.168)-(4.172) are discretised by using Lagrangian basis functions L. Similar to the IGA discretisation in this work, an isoparametric Bubnov-Galerkin approach is employed so that the discretisation of the test functions for the concentration fields $c_\bullet$ with $\bullet \in \{\mathrm{OY}, \mathrm{MC}, \mathrm{OC}, \mathrm{MB}, \mathrm{OB}\}$ follows as

$$
\delta c_{\bullet}^{e} = \sum_{A=1}^{\mathrm{n_{en}}} \delta c_{\bullet}^{A} L^{A} \qquad (4.173)
$$

where $\mathrm{n_{en}}$ is the number of Lagrangian basis functions per element. For derivatives in time, the Backward-Euler method is used as in (4.114).

In the FEA framework, the global residual vector for the global vector of unknowns $\boldsymbol{\varphi} = [c_{\mathrm{OY}}, c_{\mathrm{MC}}, c_{\mathrm{OC}}, c_{\mathrm{MB}}, c_{\mathrm{OB}}]^{\mathrm{t}}$ is $\boldsymbol{r} = [\boldsymbol{r}_{\mathrm{OY}}, \boldsymbol{r}_{\mathrm{MC}}, \boldsymbol{r}_{\mathrm{OC}}, \boldsymbol{r}_{\mathrm{MB}}, \boldsymbol{r}_{\mathrm{OB}}]^{\mathrm{t}}$. The individual contributions to the global residual vector can be written as

$$
\boldsymbol{r}_{\mathrm{OY}} = \mathop{\mathbf{A}}_{e=1}^{\mathrm{n_{el}}} \sum_{A=1}^{\mathrm{n_{en}}} \int_{\Omega^e} L^{A}\, \frac{c_{\mathrm{OY}} - c_{\mathrm{OY},n}}{\Delta t}\, \mathrm{d}v - \int_{\Omega^e} L^{A}\, s_{\mathrm{OY/OB}}\, \mathrm{d}v \qquad (4.174)
$$

$$\boldsymbol{r}_{\mathrm{MC}} = \mathop{\mathsf{A}}_{e=1}^{\mathrm{n_{el}}} \sum_{A=1}^{\mathrm{n_{en}}} \int_{\Omega^e} L^A \, \frac{c_{\mathrm{MC}} - c_{\mathrm{MC},n}}{\Delta t} \, \mathrm{d}v - \int_{\Omega^e} \nabla_{\boldsymbol{x}} L^A \cdot \boldsymbol{q}_{\mathrm{MC}} \, \mathrm{d}v - \int_{\partial\Omega^e} L^A \, q_{\mathrm{MC}} \, \mathrm{d}a - \int_{\Omega^e} L^A \, s_{\mathrm{MC}} \, \mathrm{d}v \tag{4.175}$$

$$\boldsymbol{r}_{\mathrm{OC}} = \mathop{\mathsf{A}}_{e=1}^{\mathrm{n_{el}}} \sum_{A=1}^{\mathrm{n_{en}}} \int_{\Omega^e} L^A \, \frac{c_{\mathrm{OC}} - c_{\mathrm{OC},n}}{\Delta t} \, \mathrm{d}v - \int_{\Omega^e} \nabla_{\boldsymbol{x}} L^A \cdot \boldsymbol{q}_{\mathrm{OC}} \, \mathrm{d}v - \int_{\partial\Omega^e} L^A \, q_{\mathrm{OC}} \, \mathrm{d}a \tag{4.176}$$

$$\boldsymbol{r}_{\mathrm{MB}} = \mathop{\mathsf{A}}_{e=1}^{\mathrm{n_{el}}} \sum_{A=1}^{\mathrm{n_{en}}} \int_{\Omega^e} L^A \, \frac{c_{\mathrm{MB}} - c_{\mathrm{MB},n}}{\Delta t} \, \mathrm{d}v - \int_{\Omega^e} \nabla_{\boldsymbol{x}} L^A \cdot \boldsymbol{q}_{\mathrm{MB}} \, \mathrm{d}v - \int_{\partial\Omega^e} L^A \, q_{\mathrm{MB}} \, \mathrm{d}a - \int_{\Omega^e} L^A \, s_{\mathrm{MB}} \, \mathrm{d}v \tag{4.177}$$

$$\boldsymbol{r}_{\mathrm{OB}} = \mathop{\mathsf{A}}_{e=1}^{\mathrm{n_{el}}} \sum_{A=1}^{\mathrm{n_{en}}} \int_{\Omega^e} L^A \, \frac{c_{\mathrm{OB}} - c_{\mathrm{OB},n}}{\Delta t} \, \mathrm{d}v - \int_{\Omega^e} \nabla_{\boldsymbol{x}} L^A \cdot \boldsymbol{q}_{\mathrm{OB}} \, \mathrm{d}v - \int_{\partial\Omega^e} L^A \, q_{\mathrm{OB}} \, \mathrm{d}a + \int_{\Omega^e} L^A \, s_{\mathrm{OY/OB}} \, \mathrm{d}v. \tag{4.178}$$

In C.1.2, the corresponding tangent contributions are derived.

4.4.5.3 Moving mesh approach

A main feature of the finite element framework established in this contribution is the surface growth algorithm. The numerical implementation of surface growth follows the approach proposed in [21] based on an evolving reference configuration. However, the algorithm has been developed for a finite deformation setting but is employed for small deformations within the scope of this work.

The general idea of the algorithm is a mesh update in prescribed growth intervals Δt^{G} in which a movement of the outer domain boundaries is applied instantaneously. For the sake of consistency, $\Delta t \leq \Delta t^{\mathrm{G}}$ has to hold for the time increment in the simulation. In each of these growth spurts the updated domain Ω results from the union of the previously existing domain $\widetilde{\Omega}$ and the newly grown domain $\mathcal{G}$, i.e. $\Omega = \widetilde{\Omega} \cup \mathcal{G}$, as indicated in Fig. 4.27. On the growing boundary $\partial\widetilde{\Omega}^{\mathrm{G}}$, the nodal points of the finite element mesh are displaced according to the prescribed growth $\overline{u}_n^{\mathrm{G}}$. In order to avoid large mesh distortions, the locations of all interior nodes as well as the tangential placements of the boundary nodes are also updated. For this purpose, a linear elastic boundary value problem is solved with respect to the unknown nodal displacements $\boldsymbol{u}^{\mathrm{G}}$ of the finite element mesh. Therein, isotropic Hooke elasticity is employed with Young's modulus $Y_{\mathrm{mesh}} = 210\,000\,\mathrm{N\,mm^{-2}}$ and Poisson's ratio $\mu_{\mathrm{mesh}} = 0.3$. It shall be emphasised that

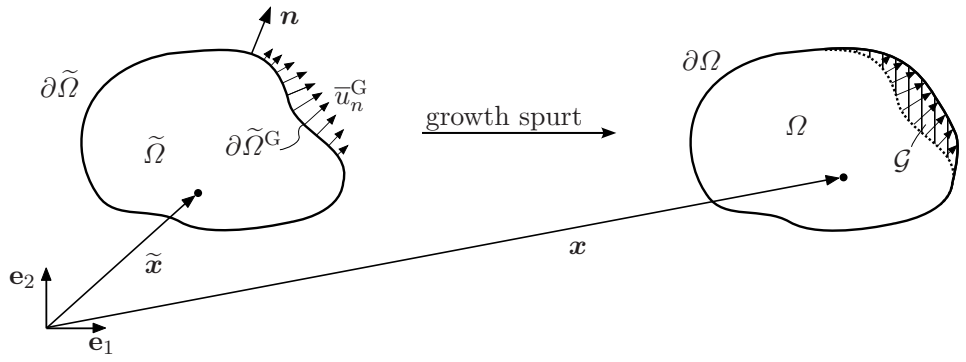

Figure 4.27: Domain before ($\widetilde{\Omega}$) and after (Ω) one growth spurt. Growth is applied on the growth surface $\partial\widetilde{\Omega}^{G}$ by a prescribed growth displacement $\overline{u}_n^{\mathrm{G}}$ in surface outward normal direction determined by unit vector $\boldsymbol{n}$. The coordinate vector of a point in domain $\widetilde{\Omega}$ is denoted as $\widetilde{\boldsymbol{x}}$ and in the updated domain $\Omega = \widetilde{\Omega} \cup \mathcal{G}$ as $\boldsymbol{x}$. Reprinted from [175] under the terms of the Creative Commons Attribution License (CC BY).

these mesh displacements are not related to any displacement of material points in the overall simulation. The corresponding boundary conditions read

$$\boldsymbol{u}^{\mathrm{G}} \cdot \boldsymbol{n} = \overline{u}_n^{\mathrm{G}} \qquad \text{on} \quad \partial\widetilde{\Omega}^{\mathrm{G}}, \tag{4.179}$$

$$\boldsymbol{u}^{\mathrm{G}} \cdot \boldsymbol{n} = 0 \qquad \text{on} \quad \partial\widetilde{\Omega} \setminus \partial\widetilde{\Omega}^{\mathrm{G}}, \tag{4.180}$$

i.e. the displacement in surface normal direction is set to zero at all boundaries except for the growing boundary where, in the present contribution, the amount of growth is not known a-priori as assumed in [21], but results from the outflux of osteoblasts over the growing surface, see (4.161). Details on the prescription of the growth boundary conditions in surface normal direction are provided in Appendix C.2.2. After solving the boundary value problem, the nodal coordinates can be updated according to

$$\boldsymbol{x} = \widetilde{\boldsymbol{x}} + \boldsymbol{u}^{\mathrm{G}}. \tag{4.181}$$

These updated coordinates define the reference mesh for subsequent simulation steps until a new growth spurt occurs. Such new reference mesh includes all material points that exist after the growth has taken place, i.e. all material points in the pre-existing domain as well as all points in the grown region. For the latter, initial conditions have to be prescribed for the field and state variables. The particular choices made in the present contribution are discussed in Sect. 4.4.6.4, whereas Appendix C.2.3 deals with the projection of nodal values in the pre-existing domain. Since the growth surface $\partial\widetilde{\Omega}^{\mathrm{G}}$ is not necessarily aligned with an element edge after the mesh has been updated, some of the new elements may partly lie in both, the pre-existing domain $\widetilde{\Omega}$ and the grown domain $\mathcal{G}$. This may produce small errors which are decreased by choosing a sufficiently small element size in the growing regions and by decreasing the time increment, see [21].

4.4.6 Simulation of flexoelectricity-induced bone remodelling and crack healing

The initial boundary value problem addressed within the scope of this work, is described in more detail in the following after a brief recapitulation of the constitutive model employed for the cortical bone material under consideration. For the simulation of the entire remodelling process, from flexoelectric initiation to crack healing, the proposed IGA framework is adopted to capture the evolution of a microcrack in a small bone excerpt in a discretised manner as discussed in Sect. 4.4.4. Thereafter, the FEA simulation is carried out in order to investigate cell diffusion processes and surface growth as proposed in Sect. 4.4.5. Representative simulation results are presented for each step of the remodelling process.

4.4.6.1 Specification of the constitutive model

The constitutive model for the cortical bone material under investigation in this work has been introduced in Sect. 4.3.3.1. For the simulations in the present section, the constitutive relations as well as the material tensors specified therein are adopted. Accordingly, transverse isotropy is considered for the elastic material properties whereas a hexagonal symmetry structure is employed for the permittivity tensor. The flexoelectricity tensor possesses cubic symmetry. For the chemical potentials $\mu_\bullet^c$ and the corresponding material constants $\gamma_\bullet$ in relation (4.125), the set of chemical variables is redefined in terms of $\bullet \in \{\mathrm{OY}, \mathrm{MC}, \mathrm{OC}, \mathrm{MB}, \mathrm{OB}\}$.

4.4.6.2 Initial boundary value problem for the IGA simulation

In the first part of the bone remodelling simulations, the proposed IGA framework is applied to a small, rectangular sample of cortical bone. The sample of width $b = 0.8\,\mathrm{mm}$ and height $h = 0.6\,\mathrm{mm}$ features an initial crack in the size of a few micro metres, see Fig. 4.28. To be precise, the width of the crack opening is $w = 0.008\,\mathrm{mm}$ and its length l takes different values representing different discrete time steps during crack evolution. In accordance with the simulation scheme presented in Sect. 4.4.3 and visualised in Fig. 4.26, the IGA simulation is carried out several times in order to calculate the osteocyte apoptosis behaviour during these discrete time steps of a crack event. Afterwards, the results are interpolated in order to obtain a smooth distribution of osteocytes in the vicinity of the crack at the end of the crack event. A constant time increment $\Delta t = 1/8\,\mathrm{s}$ is used in the simulations in consistency with the choice made in Sect. 4.3.3.2.

As visualised in Fig. 4.28, the cortical bone sample is loaded mechanically, with a tensile load on the left and right which is prescribed in terms of Dirichlet boundary conditions. The corresponding load curve is also given in Fig. 4.28 and shows a ramped loading and unloading characteristic over a time of 5 s. Additional Dirichlet boundary conditions are prescribed on the bottom face which cannot move in vertical direction, and on the bottom left corner where the electric potential is set to zero, cf. Fig. 4.28.

For the osteocyte concentration, only initial conditions are required with a value of $c_{\mathrm{OY}}^{\mathrm{init}} = 2.5 \times 10^4\,\mathrm{mm}^{-3}$ being employed [110]. The parameters accounted for in the sink term $s_{\mathrm{OY}/e}$ (4.140) are chosen as $e_{\mathrm{crit}} = 5\,\mathrm{Vmm}^{-1}$ and $k_{\mathrm{OY},1} = 10\,\mathrm{mm}^{-3}\mathrm{s}^{-1}$. In order to accurately represent the crack evolution, a total number of 33 simulations are carried out, each considering a different time step in the evolution of the crack or, in other words, a different crack length l. Based on the final length $l_{\max} = 0.175\,\mathrm{mm}$ at the end of the crack event, the minimum crack length considered is $l_0 = \frac{1}{64}\, l_{\max}$, whereas all other investigated crack lengths can be described by $l_i = \frac{i}{32}\, l_{\max}$ with $i = 1, \ldots, 32$. The width w of the crack opening on the top surface is kept constant. In Appendix C.4.2, details on the IGA geometry of the cracked plate with different crack lengths are provided. The final discretisation for $l = l_{\max}$ is exemplary shown in Fig. 4.32 since it is also the basis for the FEA calculations which will be carried out subsequently.

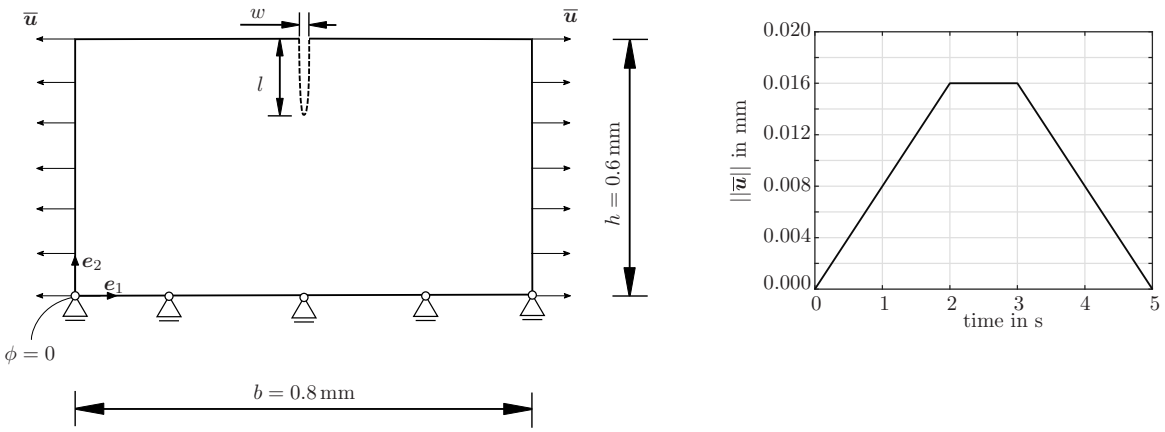

Figure 4.28: Initial boundary value problem in the IGA simulations and corresponding load curve which characterises the tensile load prescribed on the left and right boundaries of a cracked domain. Reproduced from [175] under the terms of the Creative Commons Attribution License (CC BY).

4.4.6.3 Crack evolution and osteocyte apoptosis

The presence of a mechanical load on the pre-cracked bone sample under investigation leads to an electric field in the vicinity of the crack tip due to the flexoelectric properties of the cortical bone material. This has been found experimentally in [164] and has been shown by the simulation results presented in Sect. 4.3.3.3. In Fig. 4.29, the electric field induced at different discrete time steps during crack evolution is shown for the initial boundary value problem studied in the present section. In particular, this flexoelectricity-induced electric field exceeds the value of $1\,\mathrm{Vmm}^{-1}$ in the vicinity of the crack tip and thus leads to osteocyte apoptosis [120]. Accordingly, Fig. 4.30c shows a non-homogeneous osteocyte concentration after mechanical loading, at time $t = 5\,\mathrm{s}$. In addition, the results for two intermediate steps during crack evolution are presented in Fig. 4.30a and 4.30b. In all three cases, the concentration of osteocytes has decreased significantly, namely by up to 70 % compared to the initial concentration near the crack

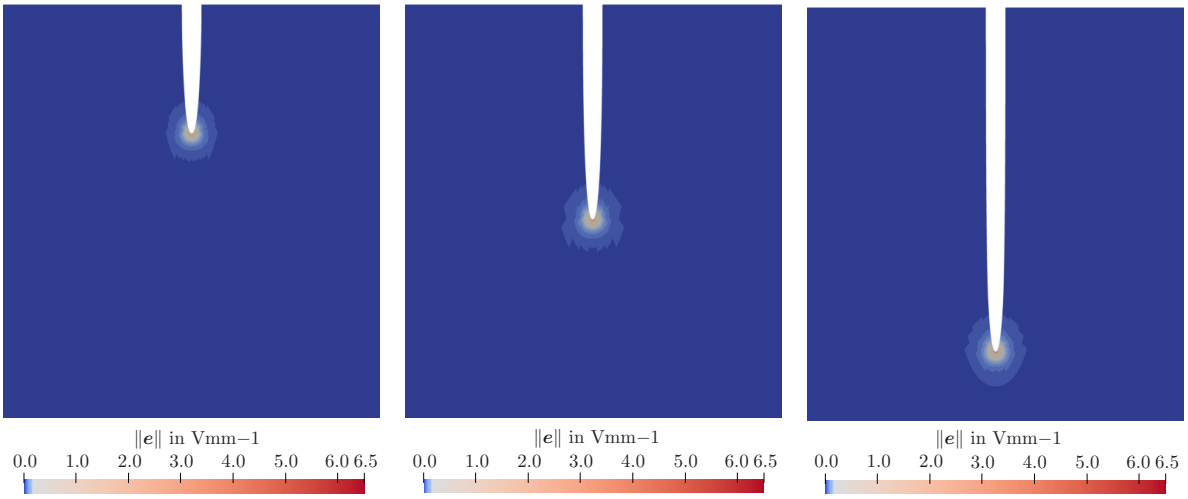

(a) Crack length $l = \frac{3}{8}\, l_{\max}$. **(b)** Crack length $l = \frac{5}{8}\, l_{\max}$. **(c)** Crack length $l = l_{\max}$.

Figure 4.29: Electric field magnitude at time $t = 2.5\,\mathrm{s}$ for different crack lengths, respectively different time steps during crack evolution. Detail view on the crack. Reprinted from [175] under the terms of the Creative Commons Attribution License (CC BY).

tip. Osteocyte apoptosis qualitatively occurs in an approximately elliptic region in front of the evolving microcrack.

Taking into account multiple simulations, each corresponding to one specific crack length or, in other words, to one time step during crack evolution, the osteocyte concentrations shown in Fig. 4.31a and 4.31b are obtained, when 16 (crack lengths $l_j = \frac{j}{16}\, l_{\max}$ with $j = 1, \ldots, 16$) and 33 (crack lengths l_i as determined in Sect. 4.4.6.2) of these time steps are considered, respectively. Therein, the resulting osteocyte concentrations c_{OY} have been projected to the crack flanks of the final geometry with $l = l_{\max}$ by mapping values to the same spatial coordinate in $\boldsymbol{e}_2$-direction and with the same distance relative to the crack flanks. It can be observed that an increasingly smooth distribution is obtained with increasing number of simulated intermediate time steps. Consequently, it is reasonable to interpolate these values in order to obtain a smooth final solution which represents a setting where the crack evolution would have been continuously tracked in time. The result after interpolation is presented in Fig. 4.31c. It shall be noted that the interpolation has been extended towards the upper surface of the domain where results are not available due to the minimal simulated crack length l_0. The resulting osteocyte distribution is used for the initialisation of the finite element analysis discussed in the following sections.

4.4.6.4 Initial boundary value problem for the FEA simulation

Based on the osteocyte concentration as a result of the IGA simulation, the proposed FEA framework is used to simulate the subsequent bone remodelling process, cf. Fig. 4.26. The initial osteocyte concentration is directly incorporated in terms of nodal

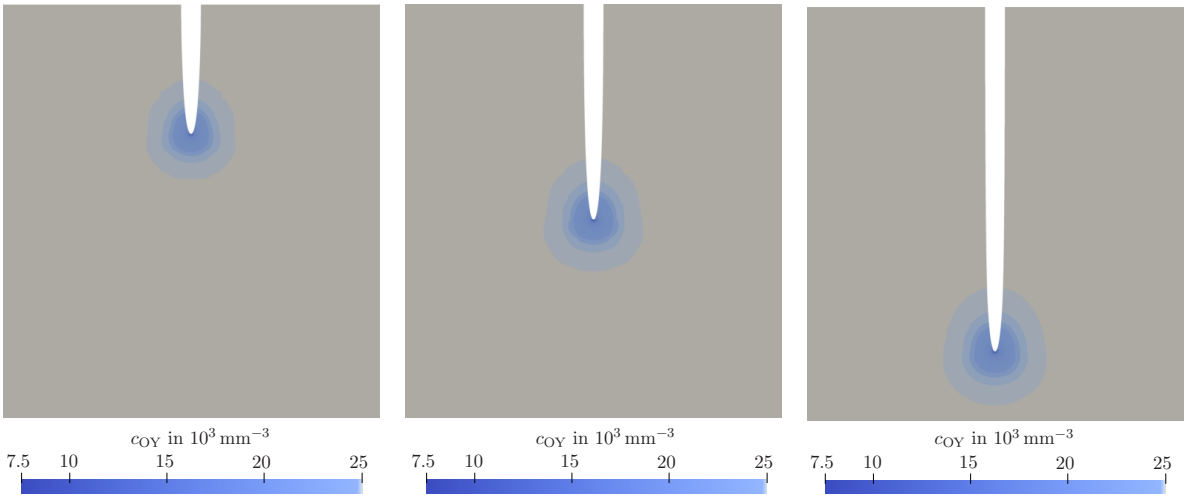

(a) Crack length $l = \frac{3}{8}\, l_{max}$. **(b)** Crack length $l = \frac{5}{8}\, l_{max}$. **(c)** Crack length $l = l_{max}$.

Figure 4.30: Osteocyte concentration at time $t = 5\,s$ for different crack lengths, respectively different time steps during crack evolution. Detail view on the crack. Reproduced from [175] under the terms of the Creative Commons Attribution License (CC BY).

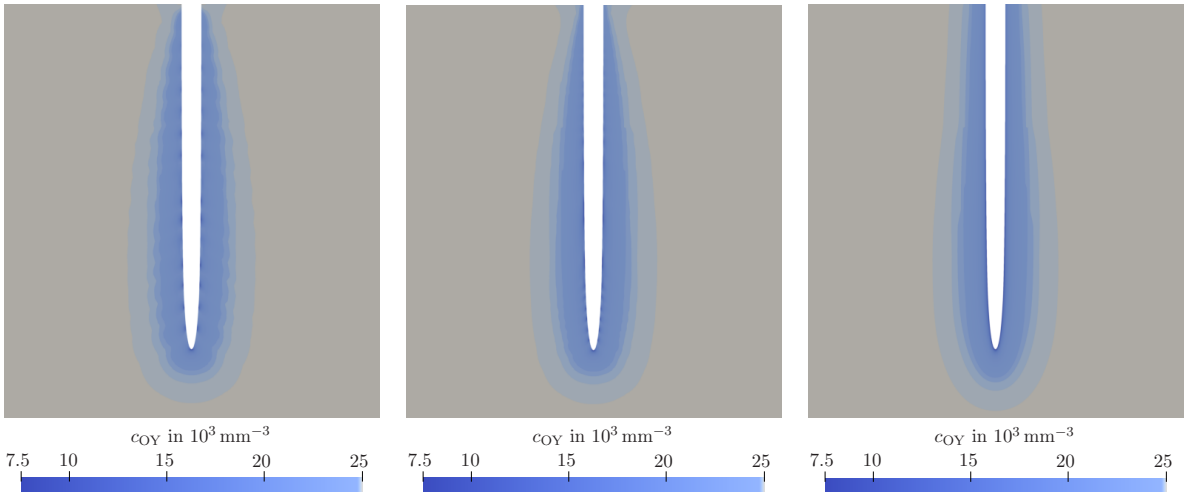

(a) Osteocyte concentration based on 16 time steps. **(b)** Osteocyte concentration based on 33 time steps. **(c)** Final osteocyte concentration after interpolation.

Figure 4.31: Convergence and interpolation of the osteocyte concentration at time $t = 5\,s$ for the final crack length. Detail view on the crack. Reproduced from [175] under the terms of the Creative Commons Attribution License (CC BY).

values determined from the interpolated data shown in Fig. 4.31c. This transfer is straightforward since the finite element discretisation of the cracked domain follows directly from the physical mesh of the IGA simulation with $l = l_{max}$, see Fig. 4.32. In the FEA framework, the time increment is $\Delta t = 1/4\,d$ and growth spurts are chosen to occur in discrete time steps $\Delta t^G = 1\,d$.

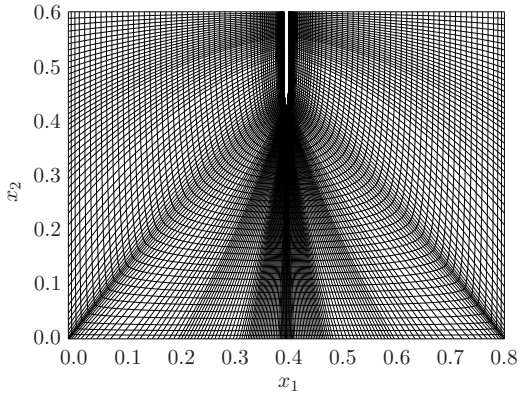

Figure 4.32: Discretisation of the bone sample including $n_{el} = 34\,986$ elements. Reproduced from [175] under the terms of the Creative Commons Attribution License (CC BY).

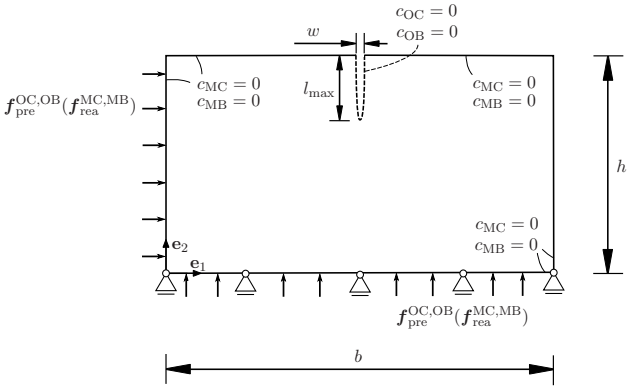

Figure 4.33: Initial boundary value problem in the FEA simulations. Reprinted from [175] under the terms of the Creative Commons Attribution License (CC BY).

The initial boundary value problem for the FEA simulation of bone remodelling is presented in Fig. 4.33. The messenger substance concentrations c_{MC} and c_{MB} are set to zero at all boundaries except for the crack flanks, in order to enable an outflux of these substances over the boundaries for signalling purposes ("infinite reservoirs"). Similarly, homogeneous Dirichlet boundary conditions are employed for the concentration of osteoclasts and osteoblasts at the crack flanks. In particular the outflux of osteoblasts is important for the prescription of surface growth. On the left-hand surface, the reaction forces of the messenger substance fields (MC, MB) are used to prescribe boundary conditions for the osteoclast and osteoblast influx according to (4.144) and (4.150). These conditions are incorporated into the finite element programme by modification of the global tangent matrix and force vectors after assembly as described in Appendix C.2.1.

Regarding the initial conditions for the simulation, all concentrations are set to zero, except for those of the osteocytes which are incorporated from the IGA results as discussed in Sect. 4.4.6.2. Moreover, additional conditions are required for the initial concentrations after each growth step, cf. Sect. 4.4.5.3. To be precise, the values of all degrees of freedom need to be initialised in the growth region where new bone material is formed. The chosen initial conditions are presented in Table 4.7. The concentration of osteocytes is set to the value of healthy bone material with $c_{OY}^{init,G} = 2.5 \times 10^4\,mm^{-3}$ being assumed in this work. Accordingly, the newly produced material is considered to be fully developed and intact. In line with this assumption, the concentrations of osteoclasts and osteoblasts are initialised to zero in the growth region since it is deduced that all of these bone cells are fully consumed by the remodelling process. For the messenger substances of both osteoclasts and osteoblasts, the concentration of their nearest neighbour in the pre-existing region is adopted after a growth spurt. The underlying

assumption is that signals are not emitted locally in a particular material point but, e.g., also by neighbouring cells.

The model parameters employed for the simulations in this work are shown in Table 4.8. Due to a lack of sufficient experimental data, these have been chosen in accordance with the knowledge regarding the underlying physical process as discussed in Sect. 4.2.

Table 4.7: Initial conditions in the newly grown material.

	$c_{\mathrm{OY}}^{\mathrm{init,G}}$	$c_{\mathrm{MC}}^{\mathrm{init,G}}$	$c_{\mathrm{MB}}^{\mathrm{init,G}}$	$c_{\mathrm{OC}}^{\mathrm{init,G}}$	$c_{\mathrm{OB}}^{\mathrm{init,G}}$
value	2.5×10^4	$\widetilde{c}_{\mathrm{MC}}$	$\widetilde{c}_{\mathrm{MB}}$	0	0
unit	mm^{-3}	mm^{-3}	mm^{-3}	mm^{-3}	mm^{-3}

Table 4.8: Model parameters employed in the FEA simulation.

	$q_{\mathrm{MC,min}}$	$q_{\mathrm{MB,min}}$	$k_{\mathrm{OY},2}$	k_{MC}	k_{MB}	k_{OC}	k_{OB}
value	0.423	248	223	5000	20	80	0.3
unit	$\mathrm{mm}^{-2}\mathrm{d}^{-1}$	$\mathrm{mm}^{-2}\mathrm{d}^{-1}$	$\mathrm{mm}^{-3}\mathrm{d}^{-1}$	$\mathrm{mm}^{-3}\mathrm{d}^{-1}$	d^{-1}	-	-

	$c_{\mathrm{OY}}^{\mathrm{init}}$	$c_{\mathrm{OB}}^{\mathrm{crit}}$	D_{MC}	D_{MB}	D_{OC}	D_{OB}	$\eta_{\parallel}$	$\eta_{\perp}$	$\eta_{\uparrow}$
value	2.5×10^4	7.5×10^2	0.03	0.03	0.03	0.03	0.3	0.2	0.5
unit	mm^{-3}	mm^{-3}	$\mathrm{mm}^2\mathrm{d}^{-1}$	$\mathrm{mm}^2\mathrm{d}^{-1}$	$\mathrm{mm}^2\mathrm{d}^{-1}$	$\mathrm{mm}^2\mathrm{d}^{-1}$	-	-	-

4.4.6.5 Bone cell diffusion and microcrack healing

Testing of the surface growth algorithm Before discussing the fully coupled problem including anisotropic bone cell diffusion, the surface growth algorithm is demonstrated in a simplified setting in which a constant osteoblast outflux is prescribed at the crack flanks and the respective surface displacement is obtained according to (4.161). Fig. 4.34 presents the results for a constant osteoblast outflux $-\overline{q}_{\mathrm{OB}} = 5\,\mathrm{mm}^{-2}\mathrm{d}^{-1}$. Over a time span of 32 d, the crack width is gradually reduced and the crack tip moves upwards in each growth spurt, cf. Fig. 4.34a-4.34b. Due to the constant prescribed flux driving the surface growth, the crack is reduced evenly from all sides. For severe growth this leads to element penetrations in the vicinity of the crack tip, as exemplarily shown in Fig. 4.34c. At this healing stage, a "classic" remeshing step (possibly including surface smoothing) is required and the moving mesh algorithm is to be re-initialised. Such an (automated) procedure will be in the focus of future work.

Numerical results with anisotropic diffusion and growth In this section, the fully coupled problem depicted in Fig. 4.33, including anisotropic diffusion of bone cells which

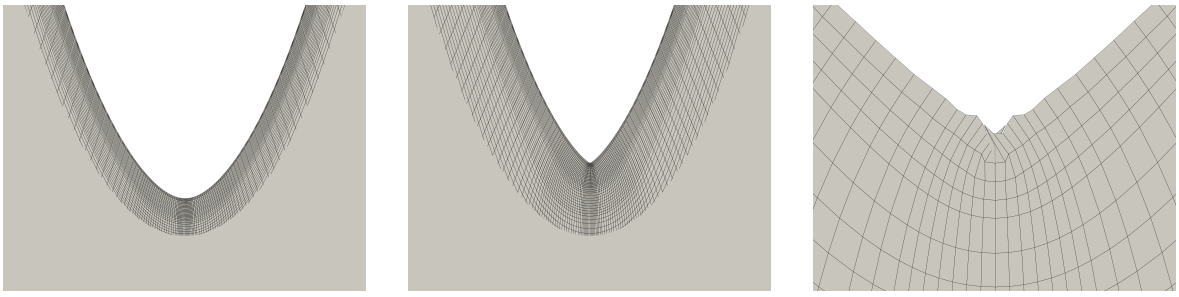

(a) Detail view after 16 days of growth.

(b) Detail view after 32 days of growth.

(c) Enlarged detail after 32 days of growth.

Figure 4.34: Surface growth in response to a constant prescribed outflux of osteoblasts over the crack flanks. The mesh after 16 and 32 days of growth is presented in detail views on the crack tip. The grey-coloured domain without element edges represents the initial domain before growth. Reprinted from [175] under the terms of the Creative Commons Attribution License (CC BY).

drives the surface growth algorithm, is studied. As a consequence of the apoptotic behaviour of osteocytes, which has been investigated by means of the isogeometric analysis framework, the finite element simulation first captures the production of messenger substances for the recruitment of osteoclasts. Fig. 4.35 reveals that these messenger substances are produced in the area of apoptosis, i.e. along the crack, and that they diffuse isotropically. At time $t = 5\,\mathrm{d}$, as shown in Fig. 4.35b, the outflux of messenger substances over the left-hand surface reaches the threshold for osteoclast recruitment. As a consequence, osteoclasts enter the domain and start migrating towards the remodelling site. Fig. 4.36 presents the concentration of osteoclasts and the corresponding cell flux direction for two different time steps. It is observable that the anisotropic diffusion tensor leads to a targeted migration towards the damaged region. The activity of osteoclasts leads to the production of new messenger substances which eventually recruit osteoblasts for further progression of the remodelling process. Fig. 4.37 presents the concentration as well as flux direction of these messenger substances at time $t = 5\,\mathrm{d}$ and $t = 36\,\mathrm{d}$ respectively. It can be observed that they are produced in locations where osteoclasts are active and that they diffuse isotropically towards the domain boundaries. The flux of messenger substances governs the recruitment of osteoblasts which enter the domain at $t = 36\,\mathrm{d}$. Afterwards, osteoblasts directly migrate towards the remodelling site due to the anisotropic diffusion tensor employed in the modelling approach. Fig. 4.38 shows the concentration and flux direction of the osteoblasts at time $t = 36\,\mathrm{d}$ and $t = 41\,\mathrm{d}$. In comparison with Fig. 4.36, it is observable that osteoblasts follow osteoclasts on their path to the remodelling site which is due to the equal anisotropic diffusion directions in the modelling approach. Since osteoblasts are responsible for the formation of new bone material, the outflux of the bone cells over the crack surfaces leads to surface growth which can be observed in Fig. 4.39. The growth mostly occurs in the region of the crack tip since a large amount of osteoblasts migrate to this area, in which osteocyte apoptosis has been most prominent. It can be observed that, in these

regions, the surface growth leads to a significant reduction of the crack area and that this reduction occurs in surface normal direction. However, similar to the academic problem discussed previously in this section, surface penetration is observed for severe growth and motivates the extension by means of a classic remeshing algorithm in future works.

For further investigation of the cell diffusion and growth behaviour within the bone sample, Appendix C.5.2 provides additional simulation results including the simultaneous recruitment of BMUs from different spatial origins. It is shown how the healing of the microcrack is influenced by the resulting changes in the cellular processes.

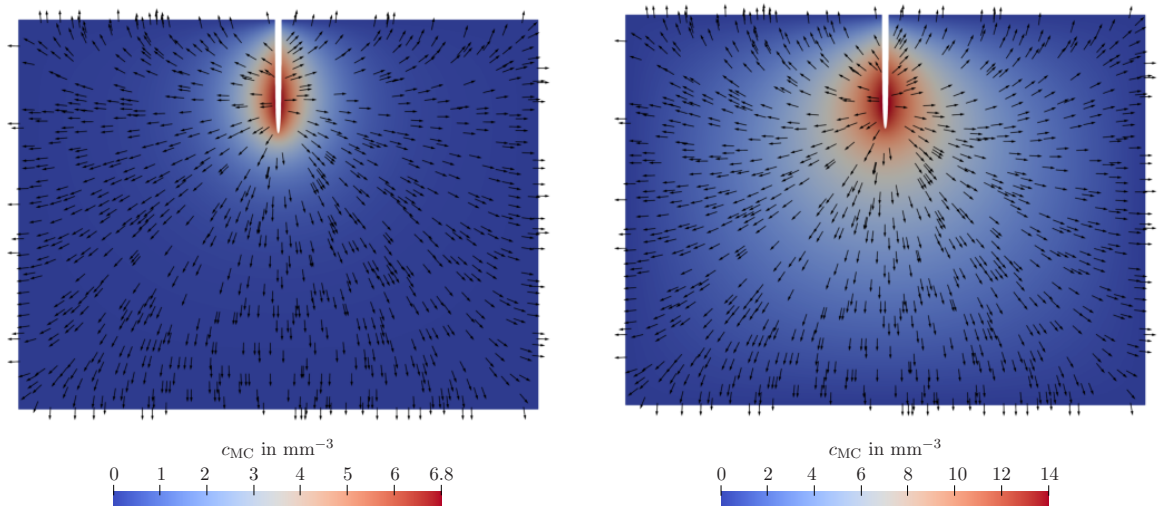

(a) Messenger substance (MC) concentration and flux after 6 hours.

(b) Messenger substance (MC) concentration and flux after 5 days.

Figure 4.35: Concentration and flux of the messenger substances for osteoclast recruitment. The contour plot presents the concentration of messenger substances c_{MC} and the glyphs indicate the direction of the corresponding flux $\boldsymbol{q}_{MC}$. Reprinted from [175] under the terms of the Creative Commons Attribution License (CC BY).

Remark 4.3. In the proposed framework, the source term (4.141) incorporates the differentiation of osteoblasts into osteocytes so as to re-increase the osteocyte concentration, i.e. to consider internal healing. Although this healing is activated in the simulations performed in this work, the influence of the source term is rather small on the time scale considered in the simulation. In order to demonstrate the impact of the source term, an academic, quasi one-dimensional example is studied. To be precise, an initially non-homogeneous concentration c_{OY} is prescribed at time $t = 0\,\mathrm{d}$ in a beam of length $L = 10\,\mathrm{mm}$. A constant influx $\overline{q}_{OB} = 3 \times 10^3\,\mathrm{mm^{-2}d^{-1}}$ is prescribed at the left-hand boundary and an isotropic diffusion coefficient $D_{OB} = 1.0\,\mathrm{mm^2d^{-1}}$ is assumed. On the right-hand boundary of the beam, homogeneous Neumann boundary conditions are considered. As the source term $s_{OY/OB}$ in the form of (4.141) (and with the constant parameters specified in Table 4.8) is activated, osteoblasts transform into osteocytes and the concentration c_{OY} approaches a homogeneous distribution at time $t = 100\,\mathrm{d}$, see Fig. 4.40.

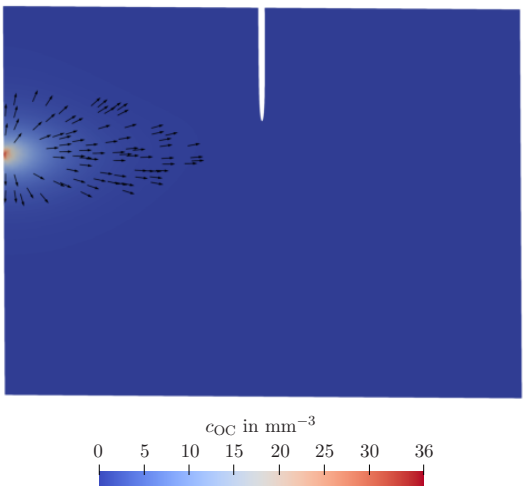

(a) Osteoclast concentration and flux after 5 days.

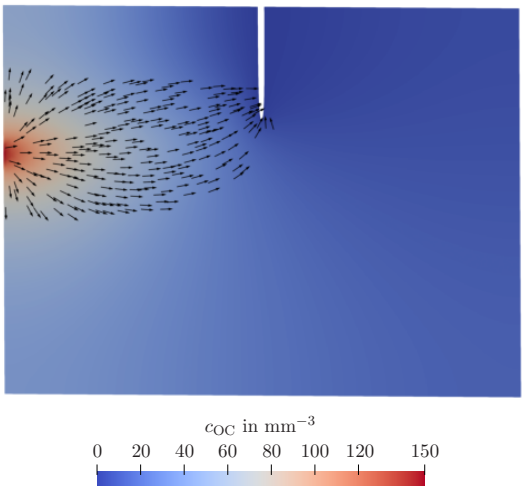

(b) Osteoclast concentration and flux after 36 days.

Figure 4.36: Concentration and flux of osteoclasts. The contour plot presents the concentration of osteoclasts c_{OC} and the glyphs indicate the direction of the corresponding flux $\boldsymbol{q}_{OC}$ in the region of interest. Reprinted from [175] under the terms of the Creative Commons Attribution License (CC BY).

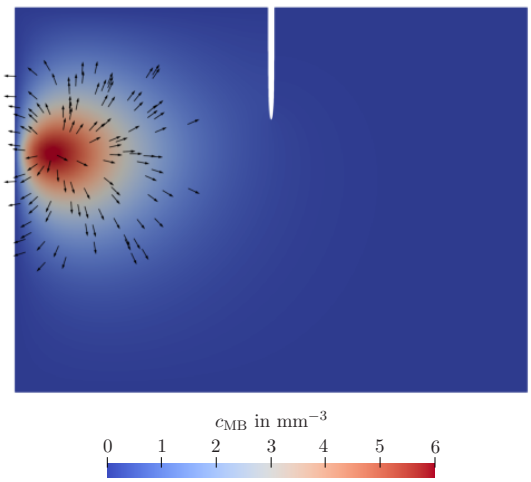

(a) Messenger substance (MB) concentration and flux after 5 days.

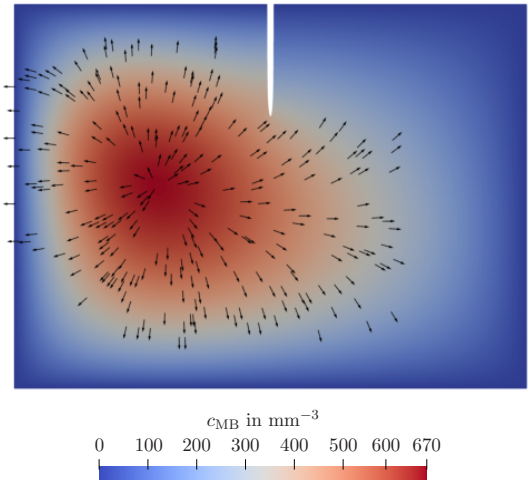

(b) Messenger substance (MB) concentration and flux after 36 days.

Figure 4.37: Concentration and flux of the messenger substances for osteoblast recruitment. The contour plot presents the concentration of messenger substances c_{MB} and the glyphs indicate the direction of the corresponding flux $\boldsymbol{q}_{MB}$ in the region of interest. Reprinted from [175] under the terms of the Creative Commons Attribution License (CC BY).

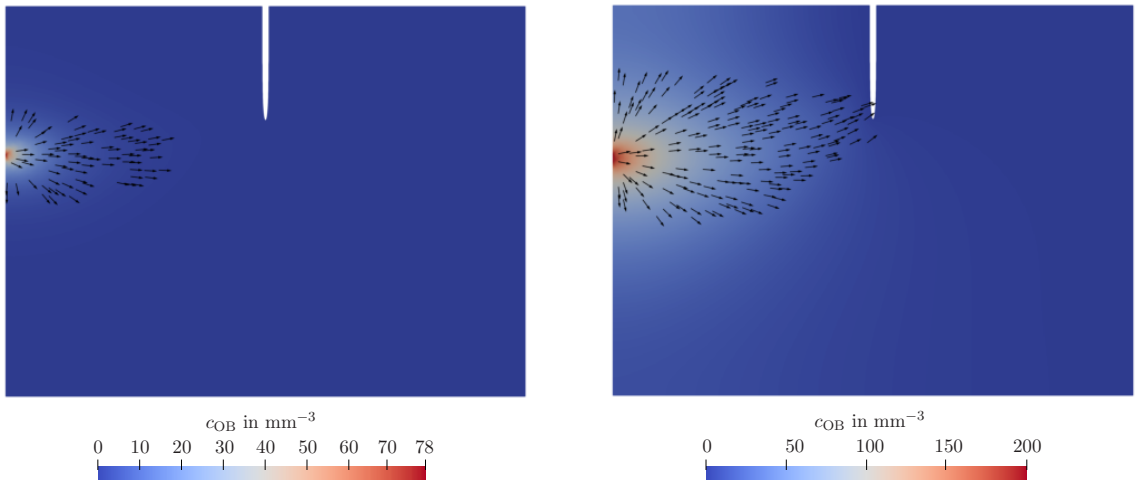

(a) Osteoblast concentration and flux after 36 days.

(b) Osteoblast concentration and flux after 40 days.

Figure 4.38: Concentration and flux of osteoblasts. The contour plot presents the concentration of osteoblasts c_{OB} and the glyphs indicate the direction of the corresponding flux $\boldsymbol{q}_{OB}$ in the region of interest. Reprinted from [175] under the terms of the Creative Commons Attribution License (CC BY).

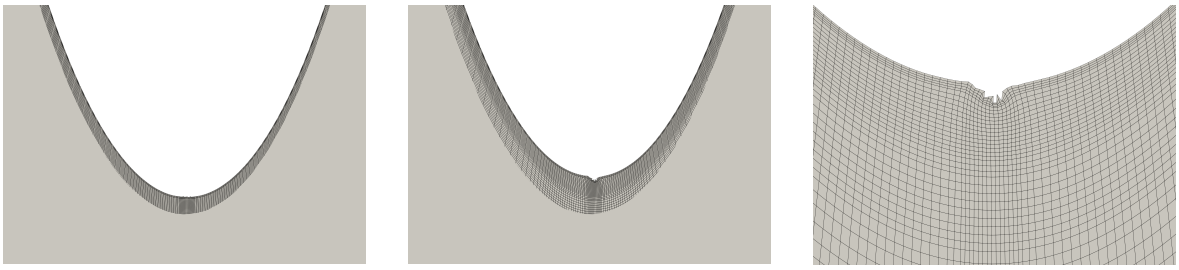

(a) Detail view on the mesh for $t = 40\,\mathrm{d}$.

(b) Detail view on the mesh for $t = 42\,\mathrm{d}$.

(c) Enlarged detail view for $t = 42\,\mathrm{d}$.

Figure 4.39: Surface growth in response to the outflux of anisotropically diffusing osteoblasts over the crack flanks. The mesh at time $t = 40\,\mathrm{d}$ and $t = 42\,\mathrm{d}$ is presented. Detail views on the crack tip region are shown. The grey coloured domain without element edges represents the initial domain for comparison. Reprinted from [175] under the terms of the Creative Commons Attribution License (CC BY).

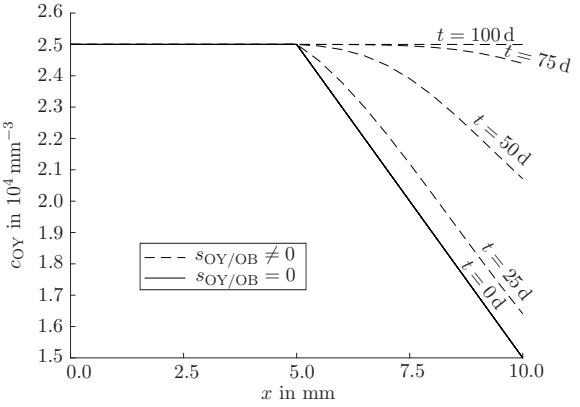

(a) Concentration of osteocytes in the beam over time. Initially, the concentration c_{OY} is constant in the left half of the beam and decreases linearly in the right half. Towards the end of the simulation, the concentration approaches a homogeneous distribution when source term $s_{\mathrm{OY/OB}}$ is activated. In the case of $s_{\mathrm{OY/OB}} = 0$, the concentration does not change over time.

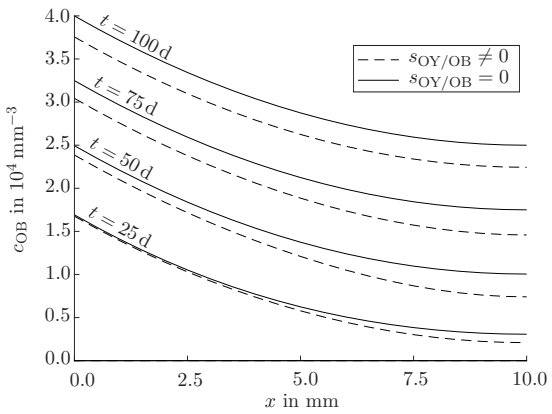

(b) Concentration of osteoblasts in the beam over time. Cells enter over the left boundary and diffuse isotropically towards the right-hand side of the beam. When source term $s_{\mathrm{OY/OB}}$ is activated, cells partly transform into osteocytes so that c_{OB} is decreased in comparison to the case with $s_{\mathrm{OY/OB}} = 0$.

Figure 4.40: Concentration of osteocytes and osteoblasts over the length of the beam at times $t \in \{0\,\mathrm{d}, 25\,\mathrm{d}, 50\,\mathrm{d}, 75\,\mathrm{d}, 100\,\mathrm{d}\}$. Reprinted from [175] under the terms of the Creative Commons Attribution License (CC BY).

C Appendix

C.1 Tangent contributions

In the following sections, the tangent contributions for both the IGA framework proposed in Sect. 4.3 as well as the combined IGA-FEA approach presented in Sect. 4.4 are derived.

C.1.1 IGA modelling approach

In the modelling approach for flexoelectric effects in cortical bone remodelling, which has been established in Sect. 4.3, the, in general, non-linear set of equations is solved monolithically by using a Newton-Raphson scheme. Accordingly, the residuals (4.115)-(4.120) are considered in a global residual vector

$$\boldsymbol{r} = \left[\boldsymbol{r}_{\boldsymbol{u}}, \boldsymbol{r}_{\phi}, \boldsymbol{r}_{\mathrm{OY}}, \boldsymbol{r}_{\mathrm{ME}}, \boldsymbol{r}_{\mathrm{OC}}, \boldsymbol{r}_{\mathrm{OB}}\right]^{\mathrm{t}} . \tag{4.182}$$

Together with the increment of the vector of unknowns

$$\boldsymbol{\varphi} = \left[\boldsymbol{u}, \phi, c_{\mathrm{OY}}, c_{\mathrm{ME}}, c_{\mathrm{OC}}, c_{\mathrm{OB}}\right]^{\mathrm{t}} \tag{4.183}$$

and iteration index k, the global system of equations takes the form

$$\boldsymbol{K}_k \cdot \Delta\boldsymbol{\varphi}_k = -\,\boldsymbol{r}_k. \tag{4.184}$$

The global stiffness matrix is obtained as

$$\boldsymbol{K} = \begin{bmatrix} \boldsymbol{K}_{\boldsymbol{uu}} & \boldsymbol{K}_{\boldsymbol{u}\phi} & \boldsymbol{0} & \boldsymbol{0} & \boldsymbol{0} & \boldsymbol{0} \\ \boldsymbol{K}_{\phi\boldsymbol{u}} & \boldsymbol{K}_{\phi\phi} & \boldsymbol{0} & \boldsymbol{0} & \boldsymbol{0} & \boldsymbol{0} \\ \boldsymbol{0} & \boldsymbol{K}_{c_{\mathrm{OY}}\phi} & \boldsymbol{K}_{c_{\mathrm{OY}}c_{\mathrm{OY}}} & \boldsymbol{0} & \boldsymbol{0} & \boldsymbol{0} \\ \boldsymbol{0} & \boldsymbol{0} & \boldsymbol{K}_{c_{\mathrm{ME}}c_{\mathrm{OY}}} & \boldsymbol{K}_{c_{\mathrm{ME}}c_{\mathrm{ME}}} & \boldsymbol{0} & \boldsymbol{0} \\ \boldsymbol{0} & \boldsymbol{0} & \boldsymbol{0} & \boldsymbol{K}_{c_{\mathrm{OC}}c_{\mathrm{ME}}} & \boldsymbol{K}_{c_{\mathrm{OC}}c_{\mathrm{OC}}} & \boldsymbol{0} \\ \boldsymbol{0} & \boldsymbol{0} & \boldsymbol{0} & \boldsymbol{K}_{c_{\mathrm{OB}}c_{\mathrm{ME}}} & \boldsymbol{0} & \boldsymbol{K}_{c_{\mathrm{OB}}c_{\mathrm{OB}}} \end{bmatrix} \tag{4.185}$$

which clearly indicates the interactions between the different field variables. Considering the symmetry of $\boldsymbol{\sigma}$, the individual contributions to the global stiffness matrix result in

$$\begin{aligned} \boldsymbol{K}_{\boldsymbol{uu}} = \mathop{\mathbf{A}}_{e=1}^{\mathrm{n_{el}}} \sum_{A=1}^{\mathrm{n_{en}}} \sum_{B=1}^{\mathrm{n_{en}}} \int_{\Omega^e} \Big[& \nabla_{\boldsymbol{x}} R^A \cdot \frac{\mathrm{d}\boldsymbol{\sigma}}{\mathrm{d}\boldsymbol{\varepsilon}} \cdot \nabla_{\boldsymbol{x}} R^B + \nabla_{\boldsymbol{x}} R^A \cdot \frac{\mathrm{d}\boldsymbol{\sigma}}{\mathrm{d}\nabla_{\boldsymbol{x}}\boldsymbol{\varepsilon}} : \nabla_{\boldsymbol{x}}\nabla_{\boldsymbol{x}} R^B \\ & + \nabla_{\boldsymbol{x}}\nabla_{\boldsymbol{x}} R^A : \frac{\mathrm{d}^{\mathrm{T}}\boldsymbol{\pi}}{\mathrm{d}\boldsymbol{\varepsilon}} \cdot \nabla_{\boldsymbol{x}} R^B \\ & + \nabla_{\boldsymbol{x}}\nabla_{\boldsymbol{x}} R^A : \frac{\mathrm{d}^{\mathrm{T}}\boldsymbol{\pi}}{\mathrm{d}\nabla_{\boldsymbol{x}}\boldsymbol{\varepsilon}} : \nabla_{\boldsymbol{x}}\nabla_{\boldsymbol{x}} R^B \Big] \mathrm{d}v \end{aligned} \tag{4.186}$$

$$\boldsymbol{K}_{\boldsymbol{u}\phi} = \mathop{\mathbf{A}}_{e=1}^{\mathrm{n_{el}}} \sum_{A=1}^{\mathrm{n_{en}}} \sum_{B=1}^{\mathrm{n_{en}}} \int_{\Omega^e} -\Big[\nabla_{\boldsymbol{x}} R^A \cdot \frac{\mathrm{d}\boldsymbol{\sigma}}{\mathrm{d}\boldsymbol{e}} \cdot \nabla_{\boldsymbol{x}} R^B + \nabla_{\boldsymbol{x}} \nabla_{\boldsymbol{x}} R^A : \frac{\mathrm{d}^{\,\mathrm{T}}\boldsymbol{\pi}}{\mathrm{d}\boldsymbol{e}} \cdot \nabla_{\boldsymbol{x}} R^B \Big] \mathrm{d}v \tag{4.187}$$

$$\boldsymbol{K}_{\phi\boldsymbol{u}} = \mathop{\mathbf{A}}_{e=1}^{\mathrm{n_{el}}} \sum_{A=1}^{\mathrm{n_{en}}} \sum_{B=1}^{\mathrm{n_{en}}} \int_{\Omega^e} \Big[\nabla_{\boldsymbol{x}} R^A \cdot \frac{\mathrm{d}\boldsymbol{d}}{\mathrm{d}\boldsymbol{\varepsilon}} \cdot \nabla_{\boldsymbol{x}} R^B + \nabla_{\boldsymbol{x}} R^A \cdot \frac{\mathrm{d}\boldsymbol{d}}{\mathrm{d}\nabla_{\boldsymbol{x}}\boldsymbol{\varepsilon}} : \nabla_{\boldsymbol{x}} \nabla_{\boldsymbol{x}} R^B \Big] \mathrm{d}v \tag{4.188}$$

$$\boldsymbol{K}_{\phi\phi} = \mathop{\mathbf{A}}_{e=1}^{\mathrm{n_{el}}} \sum_{A=1}^{\mathrm{n_{en}}} \sum_{B=1}^{\mathrm{n_{en}}} \int_{\Omega^e} -\nabla_{\boldsymbol{x}} R^A \cdot \frac{\mathrm{d}\boldsymbol{d}}{\mathrm{d}\boldsymbol{e}} \cdot \nabla_{\boldsymbol{x}} R^B \, \mathrm{d}v \tag{4.189}$$

$$\boldsymbol{K}_{c_{\mathrm{OY}}\phi} = \mathop{\mathbf{A}}_{e=1}^{\mathrm{n_{el}}} \sum_{A=1}^{\mathrm{n_{en}}} \sum_{B=1}^{\mathrm{n_{en}}} \int_{\Omega^e} R^A \frac{\mathrm{d}s_{\mathrm{OY}}}{\mathrm{d}\boldsymbol{e}} \cdot \nabla_{\boldsymbol{x}} R^B \mathrm{d}v \tag{4.190}$$

$$\boldsymbol{K}_{c_{\mathrm{OY}}c_{\mathrm{OY}}} = \mathop{\mathbf{A}}_{e=1}^{\mathrm{n_{el}}} \sum_{A=1}^{\mathrm{n_{en}}} \sum_{B=1}^{\mathrm{n_{en}}} \int_{\Omega^e} \left[-R^A \frac{\mathrm{d}s_{\mathrm{OY}}}{\mathrm{d}c_{\mathrm{OY}}} R^B + \frac{R^A R^B}{\Delta t} \right] \mathrm{d}v \tag{4.191}$$

$$\boldsymbol{K}_{c_{\mathrm{ME}}c_{\mathrm{OY}}} = \mathop{\mathbf{A}}_{e=1}^{\mathrm{n_{el}}} \sum_{A=1}^{\mathrm{n_{en}}} \sum_{B=1}^{\mathrm{n_{en}}} \int_{\Omega^e} -R^A \frac{\mathrm{d}s_{\mathrm{ME}}}{\mathrm{d}c_{\mathrm{OY}}} R^B \, \mathrm{d}v \tag{4.192}$$

$$\boldsymbol{K}_{c_{\mathrm{ME}}c_{\mathrm{ME}}} = \mathop{\mathbf{A}}_{e=1}^{\mathrm{n_{el}}} \sum_{A=1}^{\mathrm{n_{en}}} \sum_{B=1}^{\mathrm{n_{en}}} \int_{\Omega^e} \left[-\nabla_{\boldsymbol{x}} R^A \cdot \frac{\mathrm{d}\boldsymbol{q}_{\mathrm{ME}}}{\mathrm{d}\nabla_{\boldsymbol{x}} c_{\mathrm{ME}}} \cdot \nabla_{\boldsymbol{x}} R^B + \frac{R^A R^B}{\Delta t} \right] \mathrm{d}v \tag{4.193}$$

$$\boldsymbol{K}_{c_{\mathrm{OC}}c_{\mathrm{ME}}} = \mathop{\mathbf{A}}_{e=1}^{\mathrm{n_{el}}} \sum_{A=1}^{\mathrm{n_{en}}} \sum_{B=1}^{\mathrm{n_{en}}} \int_{\Omega^e} -\nabla_{\boldsymbol{x}} R^A \cdot \frac{\mathrm{d}\boldsymbol{q}_{\mathrm{OC}}}{\mathrm{d}\nabla_{\boldsymbol{x}} c_{\mathrm{ME}}} \cdot \nabla_{\boldsymbol{x}} R^B \, \mathrm{d}v \tag{4.194}$$

$$\boldsymbol{K}_{c_{\mathrm{OC}}c_{\mathrm{OC}}} = \mathop{\mathbf{A}}_{e=1}^{\mathrm{n_{el}}} \sum_{A=1}^{\mathrm{n_{en}}} \sum_{B=1}^{\mathrm{n_{en}}} \int_{\Omega^e} \left[-\nabla_{\boldsymbol{x}} R^A \cdot \frac{\mathrm{d}\boldsymbol{q}_{\mathrm{OC}}}{\mathrm{d}\nabla_{\boldsymbol{x}} c_{\mathrm{OC}}} \cdot \nabla_{\boldsymbol{x}} R^B + \frac{R^A R^B}{\Delta t} \right] \mathrm{d}v \tag{4.195}$$

$$\boldsymbol{K}_{c_{\mathrm{OB}}c_{\mathrm{ME}}} = \mathop{\mathbf{A}}_{e=1}^{\mathrm{n_{el}}} \sum_{A=1}^{\mathrm{n_{en}}} \sum_{B=1}^{\mathrm{n_{en}}} \int_{\Omega^e} -\nabla_{\boldsymbol{x}} R^A \cdot \frac{\mathrm{d}\boldsymbol{q}_{\mathrm{OB}}}{\mathrm{d}\nabla_{\boldsymbol{x}} c_{\mathrm{ME}}} \cdot \nabla_{\boldsymbol{x}} R^B \, \mathrm{d}v \tag{4.196}$$

$$\boldsymbol{K}_{c_{\mathrm{OB}}c_{\mathrm{OB}}} = \mathop{\mathbf{A}}_{e=1}^{\mathrm{n_{el}}} \sum_{A=1}^{\mathrm{n_{en}}} \sum_{B=1}^{\mathrm{n_{en}}} \int_{\Omega^e} \left[-\nabla_{\boldsymbol{x}} R^A \cdot \frac{\mathrm{d}\boldsymbol{q}_{\mathrm{OB}}}{\mathrm{d}\nabla_{\boldsymbol{x}} c_{\mathrm{OB}}} \cdot \nabla_{\boldsymbol{x}} R^B + \frac{R^A R^B}{\Delta t} \right] \mathrm{d}v \tag{4.197}$$

with the sensitivities

$$\frac{\mathrm{d}s_{\mathrm{OY}}}{\mathrm{d}\boldsymbol{e}} = -\,k_{\mathrm{OY},1} \, \exp\left(-\frac{\|\boldsymbol{e}\|}{e_{\mathrm{crit}}} \frac{c_{\mathrm{OY}}}{k_{\mathrm{OY},2}} \right) \left[\frac{1}{e_{\mathrm{crit}}} \frac{c_{\mathrm{OY}}}{k_{\mathrm{OY},2}} \right] \frac{\boldsymbol{e}}{\|\boldsymbol{e}\|}, \tag{4.198}$$

$$\frac{\mathrm{d}s_{\mathrm{OY}}}{\mathrm{d}c_{\mathrm{OY}}} = -\,k_{\mathrm{OY},1} \, \exp\left(-\frac{\|\boldsymbol{e}\|}{e_{\mathrm{crit}}} \frac{c_{\mathrm{OY}}}{k_{\mathrm{OY},2}} \right) \left[\frac{\|\boldsymbol{e}\|}{e_{\mathrm{crit}}} \frac{1}{k_{\mathrm{OY},2}} \right], \tag{4.199}$$

$$\frac{\mathrm{d}s_{\mathrm{ME}}}{\mathrm{d}c_{\mathrm{OY}}} = -\frac{k_{\mathrm{ME}}}{c_{\mathrm{OY}}^{\mathrm{init}}}, \tag{4.200}$$

$$\frac{\mathrm{d}\boldsymbol{q}_{\mathrm{ME}}}{\mathrm{d}\nabla_{\boldsymbol{x}} c_{\mathrm{ME}}} = -D_{\mathrm{ME}}\,\boldsymbol{I}, \tag{4.201}$$

$$\frac{\mathrm{d}\boldsymbol{q}_{\mathrm{OC}}}{\mathrm{d}\nabla_{\boldsymbol{x}} c_{\mathrm{OC}}} = -\boldsymbol{D}_{\mathrm{OC}}, \tag{4.202}$$

$$\frac{\mathrm{d}\boldsymbol{q}_{\mathrm{OB}}}{\mathrm{d}\nabla_{\boldsymbol{x}} c_{\mathrm{OB}}} = -\boldsymbol{D}_{\mathrm{OB}}, \tag{4.203}$$

$$\frac{\mathrm{d}\boldsymbol{q}_{\mathrm{OC}}}{\mathrm{d}\nabla_{\boldsymbol{x}} c_{\mathrm{ME}}} = -{}^{\mathrm{t}}\left[\frac{\mathrm{d}\boldsymbol{D}_{\mathrm{OC}}}{\mathrm{d}\nabla_{\boldsymbol{x}} c_{\mathrm{ME}}}\right] \cdot \nabla_{\boldsymbol{x}} c_{\mathrm{OC}}, \tag{4.204}$$

$$\frac{\mathrm{d}\boldsymbol{q}_{\mathrm{OB}}}{\mathrm{d}\nabla_{\boldsymbol{x}} c_{\mathrm{ME}}} = -{}^{\mathrm{t}}\left[\frac{\mathrm{d}\boldsymbol{D}_{\mathrm{OB}}}{\mathrm{d}\nabla_{\boldsymbol{x}} c_{\mathrm{ME}}}\right] \cdot \nabla_{\boldsymbol{x}} c_{\mathrm{OB}}. \tag{4.205}$$

The derivatives of the diffusion tensors included in (4.204)-(4.205) are

$$\frac{\mathrm{d}\boldsymbol{D}_{\mathrm{OC}}}{\mathrm{d}\nabla_{\boldsymbol{x}} c_{\mathrm{ME}}} = D_{\mathrm{OC}}\,\eta_{\uparrow}\left[\frac{1}{\|\nabla_{\boldsymbol{x}} c_{\mathrm{ME}}\|^2}\left[\boldsymbol{I} \mathbin{\overline{\otimes}} \nabla_{\boldsymbol{x}} c_{\mathrm{ME}} + \nabla_{\boldsymbol{x}} c_{\mathrm{ME}} \otimes \boldsymbol{I}\right]\right.$$
$$\left. - \frac{2}{\|\nabla_{\boldsymbol{x}} c_{\mathrm{ME}}\|^4}\left[\nabla_{\boldsymbol{x}} c_{\mathrm{ME}} \otimes \nabla_{\boldsymbol{x}} c_{\mathrm{ME}} \otimes \nabla_{\boldsymbol{x}} c_{\mathrm{ME}}\right]\right] \tag{4.206}$$

and analogously

$$\frac{\mathrm{d}\boldsymbol{D}_{\mathrm{OB}}}{\mathrm{d}\nabla_{\boldsymbol{x}} c_{\mathrm{ME}}} = \Lambda(c_{\mathrm{OC}})\,D_{\mathrm{OB}}\,\eta_{\uparrow}\left[\frac{1}{\|\nabla_{\boldsymbol{x}} c_{\mathrm{ME}}\|^2}\left[\boldsymbol{I} \mathbin{\overline{\otimes}} \nabla_{\boldsymbol{x}} c_{\mathrm{ME}} + \nabla_{\boldsymbol{x}} c_{\mathrm{ME}} \otimes \boldsymbol{I}\right]\right.$$
$$\left. - \frac{2}{\|\nabla_{\boldsymbol{x}} c_{\mathrm{ME}}\|^4}\left[\nabla_{\boldsymbol{x}} c_{\mathrm{ME}} \otimes \nabla_{\boldsymbol{x}} c_{\mathrm{ME}} \otimes \nabla_{\boldsymbol{x}} c_{\mathrm{ME}}\right]\right]. \tag{4.207}$$

The sensitivities of the stress tensors and of the dielectric displacement vector can be derived from (4.122)-(4.124) and result in

$$\frac{\mathrm{d}\boldsymbol{\sigma}}{\mathrm{d}\boldsymbol{\varepsilon}} = \mathbf{E}, \qquad \frac{\mathrm{d}\boldsymbol{\sigma}}{\mathrm{d}\nabla_{\boldsymbol{x}}\boldsymbol{\varepsilon}} = \mathbf{0}, \qquad \frac{\mathrm{d}\boldsymbol{\sigma}}{\mathrm{d}\boldsymbol{e}} = -\mathbf{e}^{\mathrm{T}}, \tag{4.208}$$

$$\frac{\mathrm{d}\boldsymbol{\pi}}{\mathrm{d}\boldsymbol{\varepsilon}} = \mathbf{0}, \qquad \frac{\mathrm{d}\boldsymbol{\pi}}{\mathrm{d}\nabla_{\boldsymbol{x}}\boldsymbol{\varepsilon}} = \mathbf{0}, \qquad \frac{\mathrm{d}\boldsymbol{\pi}}{\mathrm{d}\boldsymbol{e}} = -\boldsymbol{\mu}^{\mathrm{T}^*}, \tag{4.209}$$

$$\frac{\mathrm{d}\boldsymbol{d}}{\mathrm{d}\boldsymbol{\varepsilon}} = \mathbf{e}, \qquad \frac{\mathrm{d}\boldsymbol{d}}{\mathrm{d}\nabla_{\boldsymbol{x}}\boldsymbol{\varepsilon}} = \boldsymbol{\mu}, \qquad \frac{\mathrm{d}\boldsymbol{d}}{\mathrm{d}\boldsymbol{e}} = \boldsymbol{\chi}. \tag{4.210}$$

C.1.2 IGA-FEA modelling approach

In the combined IGA-FEA modelling approach, proposed in Sect. 4.4 for flexoelectricity-induced bone remodelling and crack healing, the system of equations is solved in two separate calculations based on the Newton-Raphson method. To be precise, the resid-

ual vectors (4.165)-(4.167) are accounted for in the proposed IGA framework whereas (4.174)-(4.178) are considered in the FEA framework that has been established for the incorporation of surface growth. The tangent contributions are thus derived separately in the following.

The tangent matrix in the global Newton scheme of the IGA simulations is obtained as

$$\boldsymbol{K} = \begin{bmatrix} \boldsymbol{K}_{\boldsymbol{u}\boldsymbol{u}} & \boldsymbol{K}_{\boldsymbol{u}\phi} & \boldsymbol{0} \\ \boldsymbol{K}_{\phi\boldsymbol{u}} & \boldsymbol{K}_{\phi\phi} & \boldsymbol{0} \\ \boldsymbol{0} & \boldsymbol{K}_{c_{\mathrm{OY}}\phi} & \boldsymbol{K}_{c_{\mathrm{OY}}c_{\mathrm{OY}}} \end{bmatrix} \tag{4.211}$$

with

$$\begin{aligned} \boldsymbol{K}_{\boldsymbol{u}\boldsymbol{u}} = \mathop{\mathsf{A}}_{e=1}^{\mathrm{n_{el}}} \sum_{A=1}^{\mathrm{n_{en}}} \sum_{B=1}^{\mathrm{n_{en}}} \int_{\Omega^e} \Big[& \nabla_{\boldsymbol{x}} R^A \cdot \frac{\mathrm{d}\boldsymbol{\sigma}}{\mathrm{d}\boldsymbol{\varepsilon}} \cdot \nabla_{\boldsymbol{x}} R^B + \nabla_{\boldsymbol{x}} R^A \cdot \frac{\mathrm{d}\boldsymbol{\sigma}}{\mathrm{d}\nabla_{\boldsymbol{x}}\boldsymbol{\varepsilon}} : \nabla_{\boldsymbol{x}}\nabla_{\boldsymbol{x}} R^B \\ & + \nabla_{\boldsymbol{x}}\nabla_{\boldsymbol{x}} R^A : \frac{\mathrm{d}^{\,\mathrm{T}}\boldsymbol{\pi}}{\mathrm{d}\boldsymbol{\varepsilon}} \cdot \nabla_{\boldsymbol{x}} R^B \\ & + \nabla_{\boldsymbol{x}}\nabla_{\boldsymbol{x}} R^A : \frac{\mathrm{d}^{\,\mathrm{T}}\boldsymbol{\pi}}{\mathrm{d}\nabla_{\boldsymbol{x}}\boldsymbol{\varepsilon}} : \nabla_{\boldsymbol{x}}\nabla_{\boldsymbol{x}} R^B \Big] \mathrm{d}v \end{aligned} \tag{4.212}$$

$$\begin{aligned} \boldsymbol{K}_{\boldsymbol{u}\phi} = \mathop{\mathsf{A}}_{e=1}^{\mathrm{n_{el}}} \sum_{A=1}^{\mathrm{n_{en}}} \sum_{B=1}^{\mathrm{n_{en}}} \int_{\Omega^e} - \Big[& \nabla_{\boldsymbol{x}} R^A \cdot \frac{\mathrm{d}\boldsymbol{\sigma}}{\mathrm{d}\boldsymbol{e}} \cdot \nabla_{\boldsymbol{x}} R^B \\ & + \nabla_{\boldsymbol{x}}\nabla_{\boldsymbol{x}} R^A : \frac{\mathrm{d}^{\,\mathrm{T}}\boldsymbol{\pi}}{\mathrm{d}\boldsymbol{e}} \cdot \nabla_{\boldsymbol{x}} R^B \Big] \mathrm{d}v \end{aligned} \tag{4.213}$$

$$\begin{aligned} \boldsymbol{K}_{\phi\boldsymbol{u}} = \mathop{\mathsf{A}}_{e=1}^{\mathrm{n_{el}}} \sum_{A=1}^{\mathrm{n_{en}}} \sum_{B=1}^{\mathrm{n_{en}}} \int_{\Omega^e} \Big[& \nabla_{\boldsymbol{x}} R^A \cdot \frac{\mathrm{d}\boldsymbol{d}}{\mathrm{d}\boldsymbol{\varepsilon}} \cdot \nabla_{\boldsymbol{x}} R^B \\ & + \nabla_{\boldsymbol{x}} R^A \cdot \frac{\mathrm{d}\boldsymbol{d}}{\mathrm{d}\nabla_{\boldsymbol{x}}\boldsymbol{\varepsilon}} : \nabla_{\boldsymbol{x}}\nabla_{\boldsymbol{x}} R^B \Big] \mathrm{d}v \end{aligned} \tag{4.214}$$

$$\boldsymbol{K}_{\phi\phi} = \mathop{\mathsf{A}}_{e=1}^{\mathrm{n_{el}}} \sum_{A=1}^{\mathrm{n_{en}}} \sum_{B=1}^{\mathrm{n_{en}}} \int_{\Omega^e} -\nabla_{\boldsymbol{x}} R^A \cdot \frac{\mathrm{d}\boldsymbol{d}}{\mathrm{d}\boldsymbol{e}} \cdot \nabla_{\boldsymbol{x}} R^B \, \mathrm{d}v \tag{4.215}$$

$$\boldsymbol{K}_{c_{\mathrm{OY}}\phi} = \mathop{\mathsf{A}}_{e=1}^{\mathrm{n_{el}}} \sum_{A=1}^{\mathrm{n_{en}}} \sum_{B=1}^{\mathrm{n_{en}}} \int_{\Omega^e} -R^A \frac{\mathrm{d}s_{\mathrm{OY}/e}}{\mathrm{d}\boldsymbol{e}} \cdot \nabla_{\boldsymbol{x}} R^B \mathrm{d}v \tag{4.216}$$

$$\boldsymbol{K}_{c_{\mathrm{OY}}c_{\mathrm{OY}}} = \mathop{\mathsf{A}}_{e=1}^{\mathrm{n_{el}}} \sum_{A=1}^{\mathrm{n_{en}}} \sum_{B=1}^{\mathrm{n_{en}}} \int_{\Omega^e} \left[R^A \frac{\mathrm{d}s_{\mathrm{OY}/e}}{\mathrm{d}c_{\mathrm{OY}}} R^B + \frac{R^A R^B}{\Delta t} \right] \mathrm{d}v. \tag{4.217}$$

Therein, symmetry of the stress tensor $\boldsymbol{\sigma}$ has been considered. The derivatives of the osteocyte sink term are

$$\frac{\mathrm{d}s_{\mathrm{OY}/e}}{\mathrm{d}\boldsymbol{e}} = k_{\mathrm{OY},1}\,\exp\left(-\frac{\|\boldsymbol{e}\|}{e_{\mathrm{crit}}}\frac{c_{\mathrm{OY}}}{k_{\mathrm{OY},2}}\right)\left[\frac{1}{e_{\mathrm{crit}}}\frac{c_{\mathrm{OY}}}{k_{\mathrm{OY},2}}\right]\frac{\boldsymbol{e}}{\|\boldsymbol{e}\|} \tag{4.218}$$

$$\frac{\mathrm{d}s_{\mathrm{OY}/e}}{\mathrm{d}c_{\mathrm{OY}}} = k_{\mathrm{OY},1}\,\exp\left(-\frac{\|\boldsymbol{e}\|}{e_{\mathrm{crit}}}\frac{c_{\mathrm{OY}}}{k_{\mathrm{OY},2}}\right)\left[\frac{\|\boldsymbol{e}\|}{e_{\mathrm{crit}}}\frac{1}{k_{\mathrm{OY},2}}\right] \tag{4.219}$$

and the non-zero sensitivities of stresses and dielectric displacements read

$$\frac{\mathrm{d}\boldsymbol{\sigma}}{\mathrm{d}\boldsymbol{\varepsilon}} = \mathsf{E}, \quad \frac{\mathrm{d}\boldsymbol{\pi}}{\mathrm{d}\boldsymbol{e}} = -\boldsymbol{\mu}^{\mathrm{T}^*}, \quad \frac{\mathrm{d}\boldsymbol{d}}{\mathrm{d}\nabla_{\boldsymbol{x}}\boldsymbol{\varepsilon}} = \boldsymbol{\mu}, \quad \frac{\mathrm{d}\boldsymbol{d}}{\mathrm{d}\boldsymbol{e}} = \boldsymbol{\chi}\,. \tag{4.220}$$

In general, special integration techniques as well as lumping techniques, including modifications of basis functions, might be necessary for dynamic contributions such as in (4.217), see e.g. [79, 117]. This similarly applies to further tangent contributions as this work proceeds. For the particular approximations chosen within the numerical examples in the present work, however, such modifications are not required.

Regarding the FEA framework, the global tangent matrix includes only chemical contributions and follows as

$$\boldsymbol{K} = \begin{bmatrix} \boldsymbol{K}_{c_{\mathrm{OY}}c_{\mathrm{OY}}} & \boldsymbol{0} & \boldsymbol{0} & \boldsymbol{0} & \boldsymbol{K}_{c_{\mathrm{OY}}c_{\mathrm{OB}}} \\ \boldsymbol{K}_{c_{\mathrm{MC}}c_{\mathrm{OY}}} & \boldsymbol{K}_{c_{\mathrm{MC}}c_{\mathrm{MC}}} & \boldsymbol{0} & \boldsymbol{0} & \boldsymbol{0} \\ \boldsymbol{0} & \boldsymbol{K}_{c_{\mathrm{OC}}c_{\mathrm{MC}}} & \boldsymbol{K}_{c_{\mathrm{OC}}c_{\mathrm{OC}}} & \boldsymbol{0} & \boldsymbol{0} \\ \boldsymbol{0} & \boldsymbol{0} & \boldsymbol{K}_{c_{\mathrm{MB}}c_{\mathrm{OC}}} & \boldsymbol{K}_{c_{\mathrm{MB}}c_{\mathrm{MB}}} & \boldsymbol{0} \\ \boldsymbol{K}_{c_{\mathrm{OB}}c_{\mathrm{OY}}} & \boldsymbol{K}_{c_{\mathrm{OB}}c_{\mathrm{MC}}} & \boldsymbol{0} & \boldsymbol{0} & \boldsymbol{K}_{c_{\mathrm{OB}}c_{\mathrm{OB}}} \end{bmatrix} \tag{4.221}$$

with

$$\boldsymbol{K}_{c_{\mathrm{OY}}c_{\mathrm{OY}}} = \mathop{\mathbf{A}}_{e=1}^{\mathrm{n_{el}}} \sum_{A=1}^{\mathrm{n_{en}}}\sum_{B=1}^{\mathrm{n_{en}}} \int_{\Omega^e} \left[-L^A\,\frac{\mathrm{d}s_{\mathrm{OY}/\mathrm{OB}}}{\mathrm{d}c_{\mathrm{OY}}}\,L^B + \frac{L^A\,L^B}{\Delta\,t}\right]\mathrm{d}v \tag{4.222}$$

$$\boldsymbol{K}_{c_{\mathrm{OY}}c_{\mathrm{OB}}} = \mathop{\mathbf{A}}_{e=1}^{\mathrm{n_{el}}} \sum_{A=1}^{\mathrm{n_{en}}}\sum_{B=1}^{\mathrm{n_{en}}} \int_{\Omega^e} -L^A\,\frac{\mathrm{d}s_{\mathrm{OY}/\mathrm{OB}}}{\mathrm{d}c_{\mathrm{OB}}}\,L^B\mathrm{d}v \tag{4.223}$$

$$\boldsymbol{K}_{c_{\mathrm{MC}}c_{\mathrm{OY}}} = \mathop{\mathbf{A}}_{e=1}^{\mathrm{n_{el}}} \sum_{A=1}^{\mathrm{n_{en}}}\sum_{B=1}^{\mathrm{n_{en}}} \int_{\Omega^e} -L^A\,\frac{\mathrm{d}s_{\mathrm{MC}}}{\mathrm{d}c_{\mathrm{OY}}}\,L^B\,\mathrm{d}v \tag{4.224}$$

$$\boldsymbol{K}_{c_{\mathrm{MC}}c_{\mathrm{MC}}} = \mathop{\mathbf{A}}_{e=1}^{\mathrm{n_{el}}} \sum_{A=1}^{\mathrm{n_{en}}}\sum_{B=1}^{\mathrm{n_{en}}} \int_{\Omega^e} \left[-\nabla_{\boldsymbol{x}}L^A\cdot\frac{\mathrm{d}\boldsymbol{q}_{\mathrm{MC}}}{\mathrm{d}\nabla_{\boldsymbol{x}}c_{\mathrm{MC}}}\cdot\nabla_{\boldsymbol{x}}L^B + \frac{L^A\,L^B}{\Delta\,t}\right]\mathrm{d}v \tag{4.225}$$

$$\boldsymbol{K}_{c_{\mathrm{OC}}c_{\mathrm{MC}}} = \mathop{\mathbf{A}}_{e=1}^{\mathrm{n_{el}}} \sum_{A=1}^{\mathrm{n_{en}}}\sum_{B=1}^{\mathrm{n_{en}}} \int_{\Omega^e} -\nabla_{\boldsymbol{x}}L^A\cdot\frac{\mathrm{d}\boldsymbol{q}_{\mathrm{OC}}}{\mathrm{d}\nabla_{\boldsymbol{x}}c_{\mathrm{MC}}}\cdot\nabla_{\boldsymbol{x}}L^B\,\mathrm{d}v \tag{4.226}$$

$$\boldsymbol{K}_{c_{\mathrm{OC}}c_{\mathrm{OC}}} = \mathop{\mathbf{A}}_{e=1}^{\mathrm{n_{el}}} \sum_{A=1}^{\mathrm{n_{en}}}\sum_{B=1}^{\mathrm{n_{en}}} \int_{\Omega^e} \left[-\nabla_{\boldsymbol{x}}L^A\cdot\frac{\mathrm{d}\boldsymbol{q}_{\mathrm{OC}}}{\mathrm{d}\nabla_{\boldsymbol{x}}c_{\mathrm{OC}}}\cdot\nabla_{\boldsymbol{x}}L^B + \frac{L^A\,L^B}{\Delta\,t}\right]\mathrm{d}v \tag{4.227}$$

$$\boldsymbol{K}_{c_{\mathrm{MB}}c_{\mathrm{OC}}} = \mathop{\mathbf{A}}_{e=1}^{\mathrm{n_{el}}} \sum_{A=1}^{\mathrm{n_{en}}} \sum_{B=1}^{\mathrm{n_{en}}} \int_{\Omega^e} -L^A \, \frac{\mathrm{d}s_{\mathrm{MB}}}{\mathrm{d}c_{\mathrm{OC}}} \, L^B \, \mathrm{d}v \tag{4.228}$$

$$\boldsymbol{K}_{c_{\mathrm{MB}}c_{\mathrm{MB}}} = \mathop{\mathbf{A}}_{e=1}^{\mathrm{n_{el}}} \sum_{A=1}^{\mathrm{n_{en}}} \sum_{B=1}^{\mathrm{n_{en}}} \int_{\Omega^e} \left[- \nabla_{\boldsymbol{x}} L^A \cdot \frac{\mathrm{d}\boldsymbol{q}_{\mathrm{MB}}}{\mathrm{d}\nabla_{\boldsymbol{x}} c_{\mathrm{MB}}} \cdot \nabla_{\boldsymbol{x}} L^B + \frac{L^A \, L^B}{\Delta \, t} \right] \mathrm{d}v \tag{4.229}$$

$$\boldsymbol{K}_{c_{\mathrm{OB}}c_{\mathrm{OY}}} = \mathop{\mathbf{A}}_{e=1}^{\mathrm{n_{el}}} \sum_{A=1}^{\mathrm{n_{en}}} \sum_{B=1}^{\mathrm{n_{en}}} \int_{\Omega^e} L^A \, \frac{\mathrm{d}s_{\mathrm{OB/OY}}}{\mathrm{d}c_{\mathrm{OY}}} \, L^B \mathrm{d}v \tag{4.230}$$

$$\boldsymbol{K}_{c_{\mathrm{OB}}c_{\mathrm{MC}}} = \mathop{\mathbf{A}}_{e=1}^{\mathrm{n_{el}}} \sum_{A=1}^{\mathrm{n_{en}}} \sum_{B=1}^{\mathrm{n_{en}}} \int_{\Omega^e} -\nabla_{\boldsymbol{x}} L^A \cdot \frac{\mathrm{d}\boldsymbol{q}_{\mathrm{OB}}}{\mathrm{d}\nabla_{\boldsymbol{x}} c_{\mathrm{MC}}} \cdot \nabla_{\boldsymbol{x}} L^B \, \mathrm{d}v \tag{4.231}$$

$$\begin{aligned} \boldsymbol{K}_{c_{\mathrm{OB}}c_{\mathrm{OB}}} = \mathop{\mathbf{A}}_{e=1}^{\mathrm{n_{el}}} \sum_{A=1}^{\mathrm{n_{en}}} \sum_{B=1}^{\mathrm{n_{en}}} \int_{\Omega^e} \Bigg[& L^A \, \frac{\mathrm{d}s_{\mathrm{OB/OY}}}{\mathrm{d}c_{\mathrm{OB}}} \, L^B - \nabla_{\boldsymbol{x}} L^A \cdot \frac{\mathrm{d}\boldsymbol{q}_{\mathrm{OB}}}{\mathrm{d}\nabla_{\boldsymbol{x}} c_{\mathrm{OB}}} \cdot \nabla_{\boldsymbol{x}} L^B \\ & + \frac{L^A \, L^B}{\Delta \, t} \Bigg] \mathrm{d}v \end{aligned} \tag{4.232}$$

and with the additional sensitivities

$$\frac{\mathrm{d}s_{\mathrm{OY/OB}}}{\mathrm{d}c_{\mathrm{OY}}} = - \, k_{\mathrm{OY},3} \, \exp\left(- \frac{c_{\mathrm{OB}}}{c_{\mathrm{OB}}^{\mathrm{crit}}} \frac{c_{\mathrm{OY}}^{\mathrm{init}} - c_{\mathrm{OY}}}{c_{\mathrm{OY}}^{\mathrm{init}}} \right) \left[\frac{c_{\mathrm{OB}}}{c_{\mathrm{OB}}^{\mathrm{crit}}} \frac{1}{c_{\mathrm{OY}}^{\mathrm{init}}} \right], \tag{4.233}$$

$$\frac{\mathrm{d}s_{\mathrm{OY/OB}}}{\mathrm{d}c_{\mathrm{OB}}} = k_{\mathrm{OY},3} \, \exp\left(- \frac{c_{\mathrm{OB}}}{c_{\mathrm{OB}}^{\mathrm{crit}}} \frac{c_{\mathrm{OY}}^{\mathrm{init}} - c_{\mathrm{OY}}}{c_{\mathrm{OY}}^{\mathrm{init}}} \right) \left[\frac{1}{c_{\mathrm{OB}}^{\mathrm{crit}}} \frac{c_{\mathrm{OY}}^{\mathrm{init}} - c_{\mathrm{OY}}}{c_{\mathrm{OY}}^{\mathrm{init}}} \right], \tag{4.234}$$

$$\frac{\mathrm{d}s_{\mathrm{MC}}}{\mathrm{d}c_{\mathrm{OY}}} = - \, \frac{k_{\mathrm{MC}}}{c_{\mathrm{OY}}^{\mathrm{init}}}, \quad \frac{\mathrm{d}s_{\mathrm{MB}}}{\mathrm{d}c_{\mathrm{OC}}} = k_{\mathrm{MB}}, \tag{4.235}$$

$$\frac{\mathrm{d}\boldsymbol{q}_{\mathrm{MC}}}{\mathrm{d}\nabla_{\boldsymbol{x}} c_{\mathrm{MC}}} = - \, D_{\mathrm{MC}} \, \boldsymbol{I}, \quad \frac{\mathrm{d}\boldsymbol{q}_{\mathrm{MB}}}{\mathrm{d}\nabla_{\boldsymbol{x}} c_{\mathrm{MB}}} = - \, D_{\mathrm{MB}} \, \boldsymbol{I}, \tag{4.236}$$

$$\frac{\mathrm{d}\boldsymbol{q}_{\mathrm{OC}}}{\mathrm{d}\nabla_{\boldsymbol{x}} c_{\mathrm{OC}}} = - \, \boldsymbol{D}_{\mathrm{OC}}, \quad \frac{\mathrm{d}\boldsymbol{q}_{\mathrm{OB}}}{\mathrm{d}\nabla_{\boldsymbol{x}} c_{\mathrm{OB}}} = - \, \boldsymbol{D}_{\mathrm{OB}}, \tag{4.237}$$

$$\frac{\mathrm{d}\boldsymbol{q}_{\mathrm{OC}}}{\mathrm{d}\nabla_{\boldsymbol{x}} c_{\mathrm{MC}}} = -D_{\mathrm{OC}}{}^{\mathrm{t}} \left[\frac{\mathrm{d}\boldsymbol{A}}{\mathrm{d}\nabla_{\boldsymbol{x}} c_{\mathrm{MC}}} \right] \cdot \nabla_{\boldsymbol{x}} c_{\mathrm{OC}}, \tag{4.238}$$

$$\frac{\mathrm{d}\boldsymbol{q}_{\mathrm{OB}}}{\mathrm{d}\nabla_{\boldsymbol{x}} c_{\mathrm{MC}}} = -D_{\mathrm{OB}}{}^{\mathrm{t}} \left[\frac{\mathrm{d}\boldsymbol{A}}{\mathrm{d}\nabla_{\boldsymbol{x}} c_{\mathrm{MC}}} \right] \cdot \nabla_{\boldsymbol{x}} c_{\mathrm{OB}} \, . \tag{4.239}$$

The derivative of structural tensor $\boldsymbol{A}$ used therein is

$$\begin{aligned} \frac{\mathrm{d}\boldsymbol{A}}{\mathrm{d}\nabla_{\boldsymbol{x}} c_{\mathrm{MC}}} = \eta_{\uparrow} \Bigg[& \frac{1}{\|\nabla_{\boldsymbol{x}} c_{\mathrm{MC}}\|^2} \left[\boldsymbol{I} \mathbin{\overline{\otimes}} \nabla_{\boldsymbol{x}} c_{\mathrm{MC}} + \nabla_{\boldsymbol{x}} c_{\mathrm{MC}} \otimes \boldsymbol{I} \right] \\ & - \frac{2}{\|\nabla_{\boldsymbol{x}} c_{\mathrm{MC}}\|^4} \left[\nabla_{\boldsymbol{x}} c_{\mathrm{MC}} \otimes \nabla_{\boldsymbol{x}} c_{\mathrm{MC}} \otimes \nabla_{\boldsymbol{x}} c_{\mathrm{MC}} \right] \Bigg]. \end{aligned} \tag{4.240}$$

C.2 Numerical aspects

C.2.1 Reaction force-driven influx boundary conditions

As discussed in Sect. 4.3.3.2 and Sect. 4.4.1.1, an influx of osteoclasts and osteoblasts is prescribed at certain boundaries in dependence of an outflux of messenger cells over the same boundaries. In the finite element scheme, this is implemented by considering linear constraints in the global equation system such that the prescribed generalised forces $\boldsymbol{f}^{\mathrm{F}}_{\mathrm{pre}}$ of the "Follower" (F) degrees of freedom are determined by the generalised reaction forces $\boldsymbol{f}^{\mathrm{L}}_{\mathrm{rea}}$ of the "Leader" (L) degrees of freedom in terms of linear relations including a constant factor $\mathcal{K}$, i.e.

$$\boldsymbol{f}^{\mathrm{F}}_{\mathrm{pre}} = \mathcal{K}\, \boldsymbol{f}^{\mathrm{L}}_{\mathrm{rea}}. \tag{4.241}$$

From the linearisation of the global residual vector

$$\boldsymbol{r}_{k+1} \approx \boldsymbol{r}_k + \Delta \boldsymbol{r} \stackrel{!}{=} \boldsymbol{0} \tag{4.242}$$

with $\boldsymbol{r}_k = \boldsymbol{f}_{\mathrm{dyn},k} + \boldsymbol{f}_{\mathrm{int},k} - \left[\boldsymbol{f}_{\mathrm{vol},k} + \boldsymbol{f}_{\mathrm{sur},k}\right]$ including, in general, all dynamic, internal, volumetric and surface forces, the "Leader" and "Follower" rows can be extracted as

$$\boldsymbol{f}^{\mathrm{L}}_{\mathrm{dyn}} + \boldsymbol{f}^{\mathrm{L}}_{\mathrm{int}} - \boldsymbol{f}^{\mathrm{L}}_{\mathrm{vol}} - \boldsymbol{f}^{\mathrm{L}}_{\mathrm{rea}} + \boldsymbol{K}^{\mathrm{L}} \cdot \Delta\boldsymbol{\varphi} - \Delta \boldsymbol{f}^{\mathrm{L}}_{\mathrm{rea}} = \boldsymbol{0}, \tag{4.243}$$

$$\boldsymbol{f}^{\mathrm{F}}_{\mathrm{dyn}} + \boldsymbol{f}^{\mathrm{F}}_{\mathrm{int}} - \boldsymbol{f}^{\mathrm{F}}_{\mathrm{vol}} - \boldsymbol{f}^{\mathrm{F}}_{\mathrm{pre}} + \boldsymbol{K}^{\mathrm{F}} \cdot \Delta\boldsymbol{\varphi} - \Delta \boldsymbol{f}^{\mathrm{F}}_{\mathrm{pre}} = \boldsymbol{0}. \tag{4.244}$$

Therein, the iteration index k is omitted for simplicity. Additionally, the equations consider the fact that in the present case, the "Leader" degrees of freedom are of Dirichlet-type, i.e. the corresponding surface force vectors are reaction forces $\boldsymbol{f}^{\mathrm{L}}_{\mathrm{rea}}$, and the "Follower" degrees of freedom are of Neumann-type, i.e. the corresponding surface force vectors are prescribed forces $\boldsymbol{f}^{\mathrm{F}}_{\mathrm{pre}}$. Rearranging (4.243) and using (4.241) yields an expression for $\boldsymbol{f}^{\mathrm{F}}_{\mathrm{pre}} + \Delta \boldsymbol{f}^{\mathrm{F}}_{\mathrm{pre}} = \mathcal{K}\left[\boldsymbol{f}^{\mathrm{L}}_{\mathrm{rea}} + \Delta \boldsymbol{f}^{\mathrm{L}}_{\mathrm{rea}}\right]$ which can be inserted into (4.244) so that

$$\boldsymbol{K}^{\mathrm{F}} \cdot \Delta\boldsymbol{\varphi} = -\boldsymbol{f}^{\mathrm{F}}_{\mathrm{dyn}} - \boldsymbol{f}^{\mathrm{F}}_{\mathrm{int}} + \boldsymbol{f}^{\mathrm{F}}_{\mathrm{vol}} + \mathcal{K}\left[\boldsymbol{K}^{\mathrm{L}} \cdot \Delta\boldsymbol{\varphi} + \boldsymbol{f}^{\mathrm{L}}_{\mathrm{dyn}} + \boldsymbol{f}^{\mathrm{L}}_{\mathrm{int}} - \boldsymbol{f}^{\mathrm{L}}_{\mathrm{vol}}\right] \tag{4.245}$$

$$\Leftrightarrow \left[\boldsymbol{K}^{\mathrm{F}} - \mathcal{K}\,\boldsymbol{K}^{\mathrm{L}}\right] \cdot \Delta\boldsymbol{\varphi} = -\boldsymbol{f}^{\mathrm{F}}_{\mathrm{dyn}} - \boldsymbol{f}^{\mathrm{F}}_{\mathrm{int}} + \boldsymbol{f}^{\mathrm{F}}_{\mathrm{vol}} + \mathcal{K}\left[\boldsymbol{f}^{\mathrm{L}}_{\mathrm{dyn}} + \boldsymbol{f}^{\mathrm{L}}_{\mathrm{int}} - \boldsymbol{f}^{\mathrm{L}}_{\mathrm{vol}}\right]. \tag{4.246}$$

To assign the constraints in the global equation system, the generalised forces in the "Follower" row are replaced by the right-hand side of (4.246) and the corresponding contributions to the stiffness matrix are replaced by the left-hand side of (4.246), respectively.

C.2.2 Growth in surface normal direction

The growth algorithm described in Sect. 4.4.5.3 requires the calculation of the surface outward normal vector of each node of the growing boundary. Since a normal vector can only be determined for a surface rather than for an individual node, the normal vectors of the adjacent element edges are calculated instead, and an averaged sum thereof is taken as reference for the nodal normal vector. This procedure is based on the derivations by [22, 92] as well as [139] where it is applied to a three-dimensional mesh.

In the two-dimensional case, the normal vectors of the two surface element edges which are connected to a point P are calculated according to

$$\boldsymbol{n}_i = \boldsymbol{r}_i \times \boldsymbol{e}_3, \quad i \in \{1, 2\} \tag{4.247}$$

with the out-of-plane direction $\boldsymbol{e}_3$, and with the vectors

$$\boldsymbol{r}_1 = \boldsymbol{x}_P - \boldsymbol{x}_Q, \quad \boldsymbol{r}_2 = \boldsymbol{x}_R - \boldsymbol{x}_P, \tag{4.248}$$

which connect the neighbouring nodes Q and R with reference node P on the surface. The normalised sum of the two resulting normal vectors $\boldsymbol{n}_1$ and $\boldsymbol{n}_2$, i.e.

$$\boldsymbol{n}_{12} = \frac{\boldsymbol{n}_1 + \boldsymbol{n}_2}{\|\boldsymbol{n}_1 + \boldsymbol{n}_2\|} \tag{4.249}$$

is then considered such that the lengths of the vectors, respectively the element edge sizes, are taken into account. Finally, an arbitrary node P_{ref} from the inside of the domain is chosen to see whether the calculated normal vector points towards the outside of the domain. If this is not the case, the orientation of the vector is switched such that the normal vector for node P reads

$$\boldsymbol{n}_P = \operatorname{sgn}\left(\boldsymbol{n}_{12} \cdot [\boldsymbol{x}_P - \boldsymbol{x}_{\mathrm{ref}}]\right) \boldsymbol{n}_{12}, \tag{4.250}$$

see Fig. 4.41.

In order to prescribe a growth boundary condition at node P in the calculated normal direction $\boldsymbol{n}_P$, a reparametrisation is carried out in the finite element framework. This enables the assignment of boundary conditions defined in a basis system which is spanned by the surface normal and tangent vectors in the underlying Cartesian basis system. To this end, the growth-related displacements of a node on $\partial\widetilde{\Omega}^{\mathrm{G}}$ are decomposed into a normal and tangential contribution as

$$\boldsymbol{u}^{\mathrm{G}} = \overline{u}_n^{\mathrm{G}}\, \boldsymbol{n} + u_s^{\mathrm{G}}\, \boldsymbol{s} \tag{4.251}$$

with normal vector $\boldsymbol{n}$ calculated from (4.250) and corresponding tangent vector $\boldsymbol{s}$. In this representation, coefficient $\overline{u}_n^{\mathrm{G}}$ is the prescribed growth displacement in normal direction,

whereas u_s^{G} remains as unknown degree of freedom and enters the global system of equations through the linear constraints resulting from (4.251).

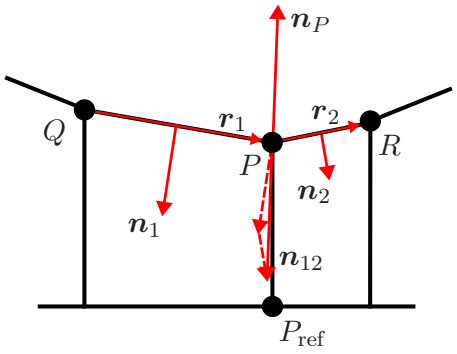

Figure 4.41: Sketch of the identification of vector $\boldsymbol{n}_P$ as the surface outward normal unit vector for node P. Reprinted from [175] under the terms of the Creative Commons Attribution License (CC BY).

C.2.3 Mapping of nodal values after growth

As discussed in Sect. 4.4.5.3, a mapping of nodal values is required between the mesh before each growth step, in the following referred to as *old* mesh, and the *updated* mesh after the growth. In this regard, it is of utmost importance to decide whether a node of the updated mesh lies in the growth region $\mathcal{G}$ of the current time step or in the region $\widetilde{\Omega}$ which already existed before the growth occurred.

For this purpose, a node $\widetilde{P}$ is identified for each node P of the updated mesh, representing the nearest neighbour of P in the old mesh. Identification of the nearest neighbour is carried out by using a k-d-tree as introduced in [19]. The k-d-tree algorithm will, however, not be further elaborated since an open-source C++ code available in the ALGLIB library, see [24], has been employed in the present work. The detected nearest neighbour $\widetilde{P}$ is then used to identify elements of the old mesh in which the new node P may be located. Accordingly, all elements $\widetilde{\Omega}_i$ which are connected to node $\widetilde{P}$ are extracted based on the connectivity list of the old mesh. These neighbouring elements and, possibly, further neighbours, e.g. in the second or third row, form the search region for the element in which the new point P may lie.

Subsequently, barycentric coordinates are used to find this particular element and to specify the precise location of point P therein. Fundamentals on barycentric coordinates can be found in [71, 140] in the context of geometric modelling and computer graphics, and a procedure to find node locations based on these coordinates has been proposed in [122, Sect. 5.2] for triangular meshes in particular. For the linear quadrilateral mesh employed in the present contribution, an algorithm based on these works is adopted

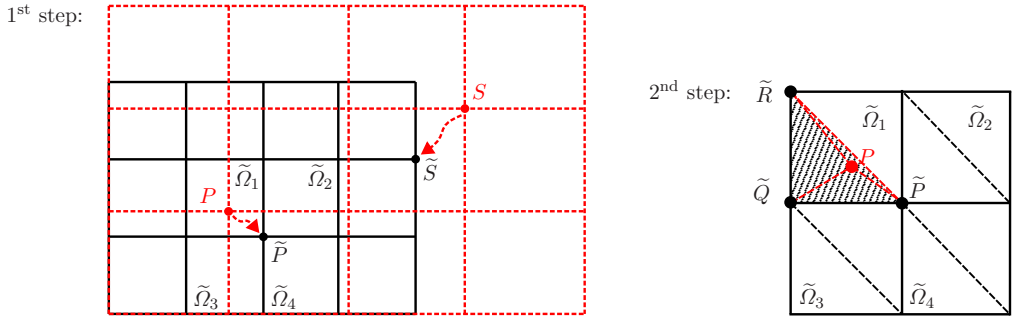

Figure 4.42: Sketch of the search algorithm for the location of points P and S of the updated mesh (red dashed lines) in the old mesh (black solid lines). 1st step: Nearest neighbour search. 2nd step: Identification of the element in the old mesh in which the new point P lies and determination of the particular location of P within this element. Reprinted from [175] under the terms of the Creative Commons Attribution License (CC BY).

by splitting each quadrilateral element into two triangles, see Fig. 4.42. The three barycentric coordinates for each of these triangles are computed as

$$\lambda_1 = \frac{\Delta_1}{\Delta_0}, \quad \lambda_2 = \frac{\Delta_2}{\Delta_0}, \quad \lambda_3 = \frac{\Delta_3}{\Delta_0}, \tag{4.252}$$

with

$$\begin{aligned} \Delta_0 &= \left\| \left[\boldsymbol{x}_{\widetilde{Q}} - \boldsymbol{x}_{\widetilde{P}} \right] \times \left[\boldsymbol{x}_{\widetilde{R}} - \boldsymbol{x}_{\widetilde{P}} \right] \right\|, \quad \Delta_1 = \left\| \left[\boldsymbol{x}_{\widetilde{R}} - \boldsymbol{x}_{\widetilde{Q}} \right] \times \left[\boldsymbol{x}_P - \boldsymbol{x}_{\widetilde{Q}} \right] \right\|, \\ \Delta_2 &= \left\| \left[\boldsymbol{x}_{\widetilde{P}} - \boldsymbol{x}_{\widetilde{R}} \right] \times \left[\boldsymbol{x}_P - \boldsymbol{x}_{\widetilde{R}} \right] \right\|, \quad \Delta_3 = \left\| \left[\boldsymbol{x}_{\widetilde{Q}} - \boldsymbol{x}_{\widetilde{P}} \right] \times \left[\boldsymbol{x}_P - \boldsymbol{x}_{\widetilde{P}} \right] \right\|. \end{aligned} \tag{4.253}$$

The cross products in (4.253) indicate that the barycentric coordinates relate the area of the original triangle $\{\widetilde{P}, \widetilde{Q}, \widetilde{R}\}$ to the area of the triangles that would be formed by replacing each of the corner points by point P, see Fig. 4.42. Depending on the resulting values of λ_i, it can be decided whether

- P lies in the triangle $\{\widetilde{P}, \widetilde{Q}, \widetilde{R}\}$ if $\lambda_i > 0 \; \forall \, i$,
- P lies on an edge of the triangle $\{\widetilde{P}, \widetilde{Q}, \widetilde{R}\}$ if one $\lambda_i = 0$,
- P lies on a corner of the triangle $\{\widetilde{P}, \widetilde{Q}, \widetilde{R}\}$ if two $\lambda_i = 0$,
- P lies outside of the triangle $\{\widetilde{P}, \widetilde{Q}, \widetilde{R}\}$ if at least one $\lambda_i < 0$.

When the element containing point P has been found, the exact location of the point is calculated by using the classic interpolation rule

$$\boldsymbol{x}_P = \sum_{A=1}^{\mathrm{n_{en}}} L^A(\boldsymbol{\xi}_P) \, \boldsymbol{x}^A \tag{4.254}$$

to solve for the coordinates $\boldsymbol{\xi}_P$ identifying the location of P in the old mesh. The mapping of nodal values between the two meshes is also performed via (4.254) by replacing the spatial coordinate vectors with the field variables and by using the computed value of $\boldsymbol{\xi}_P$. If, however, P lies outside of all elements in the search region, no projection is carried out but initial conditions are prescribed instead since the node is assumed to belong to the growth region in this case.

C.3 Proofs and analytical derivations

C.3.1 Analytical proof of non-negative osteocyte concentration

The sink term (4.83), respectively (4.140) has been proposed for the modelling of osteocyte apoptosis through flexoelectricity-induced electric fields. In order to be consistent with the physics of the underlying process, the osteocyte concentration shall not become negative which is to be ensured by this sink term, accordingly. It can be analytically shown that the proposed formulation for the sink term satisfies this requirement. For this purpose, the evolution of the osteocyte concentration in time is studied in dependence of the sink term, i.e.

$$\dot{c}_{\mathrm{OY}} = \frac{\mathrm{d}c_{\mathrm{OY}}}{\mathrm{d}t} = -k_1 \Big[1 - \exp\big(- k_2\, c_{\mathrm{OY}} \big) \Big] \tag{4.255}$$

with scalars $k_1 = k_{\mathrm{OY},1}$ and $k_2 = \|\boldsymbol{e}\| / \left[e_{\mathrm{crit}}\, k_{\mathrm{OY},2} \right]$ introduced for abbreviation of the constant expressions. In particular, $\|\boldsymbol{e}\|$ is assumed to be constant in time since the electromechanical part is considered quasi-static in this work. Moreover, the electric field is not dependent on c_{OY} in the proposed model. With these considerations at hand, the ODE (4.255) can equivalently be written as

$$\mathrm{d}t = \frac{\exp\big(k_2\, c_{\mathrm{OY}}\big)}{k_1 \left[1 - \exp\big(k_2\, c_{\mathrm{OY}}\big) \right]}\, \mathrm{d}c_{\mathrm{OY}} \tag{4.256}$$

by separation of variables, and integration on both sides of the equation yields

$$-k_1\, k_2\, [t + C] = \ln\big(1 - \exp(k_2\, c_{\mathrm{OY}})\big). \tag{4.257}$$

Successive application of the exponential function and the natural logarithm results in

$$c_{\mathrm{OY}} = \frac{1}{k_2}\, \ln(1 - \exp(-k_1\, k_2\, [t + C])) \tag{4.258}$$

and integration constant C can be obtained from the initial condition $c_{\mathrm{OY}}(t = 0) = c_{\mathrm{OY}}^{\mathrm{init}}$ taken from Table 4.4 such that

$$\ln(1 - \exp(-k_1\, k_2\, C)) = k_2\, c_{\mathrm{OY}}^{\mathrm{init}}. \tag{4.259}$$

Again, the exponential function and the natural logarithm are applied successively on both sides of the equation so that the integration constant results in

$$C = \frac{-1}{k_1\, k_2} \ln(1 - \exp(k_2\, c_{\mathrm{OY}}^{\mathrm{init}})). \tag{4.260}$$

The solution of the ODE accordingly reads

$$c_{\mathrm{OY}} = \frac{1}{k_2} \ln\Big(1 - \exp\big(-k_1\, k_2\, t\big)\left[1 - \exp\left(k_2\, c_{\mathrm{OY}}^{\mathrm{init}}\right)\right]\Big) \tag{4.261}$$

where $\exp^{a+b} = \exp^a \exp^b$ has been considered. With $k_1, k_2 \geq 0$, it can be shown that the right-hand side of (4.261) is non-negative, i.e. $c_{\mathrm{OY}} \geq 0$ holds.

C.3.2 Numerical evidence for bounded osteocyte and osteoblast concentrations

Analogously to the derivations in Appendix C.3.1, the non-negativity of the osteoblast concentration with respect to the sink term $s_{\mathrm{OY/OB}}$ is shown in this section as well as the boundedness of the osteocyte concentration with respect to the same term which acts as a source in this case. However, since this source term, respectively sink term, contains a coupling between the concentrations of osteoblasts c_{OB} and osteocytes c_{OY}, it is not straightforward to provide an analytical derivation. Instead, the equation system will be solved numerically by using a Backward-Euler scheme as in the framework proposed in Sect. 4.4.5.2, in order to show that this numerical framework produces physically sound results for the osteoblast and osteocyte concentrations with respect to $s_{\mathrm{OY/OB}}$.

The evolution of the osteoblast concentration in time is reformulated from (4.139g) by introducing constants $k_1 = k_{\mathrm{OY},2}$ and $k_2 = 1/\left[c_{\mathrm{OB}}^{\mathrm{crit}}\, c_{\mathrm{OY}}^{\mathrm{init}}\right]$, and by considering the dependence on $s_{\mathrm{OY/OB}}$ only, i.e.

$$\dot{c}_{\mathrm{OB}} = \frac{\mathrm{d}c_{\mathrm{OB}}}{\mathrm{d}t} = -k_1\left[1 - \exp\big(-k_2\, c_{\mathrm{OB}}\left[c_{\mathrm{OY}}^{\mathrm{init}} - c_{\mathrm{OY}}\right]\big)\right], \tag{4.262}$$

or, after rearranging terms,

$$\frac{\mathrm{d}c_{\mathrm{OB}}}{\mathrm{d}t} = \frac{k_1\left[1 - \exp\left(k_2\, c_{\mathrm{OB}}\left[c_{\mathrm{OY}}^{\mathrm{init}} - c_{\mathrm{OY}}\right]\right)\right]}{\exp\left(k_2\, c_{\mathrm{OB}}\left[c_{\mathrm{OY}}^{\mathrm{init}} - c_{\mathrm{OY}}\right]\right)}. \tag{4.263}$$

By employing the Backward-Euler scheme to approximate the time derivative of the osteoblast concentration on the left-hand side, the equation takes the form

$$\frac{\mathrm{d}c_{\mathrm{OB}}}{\mathrm{d}t} \approx \frac{c_{\mathrm{OB}}^{n+1} - c_{\mathrm{OB}}^{n}}{\Delta t} = \frac{k_1\left[1 - \exp\left(k_2\, c_{\mathrm{OB}}^{n+1}\left[c_{\mathrm{OY}}^{\mathrm{init}} - c_{\mathrm{OY}}^{n+1}\right]\right)\right]}{\exp\left(k_2\, c_{\mathrm{OB}}^{n+1}\left[c_{\mathrm{OY}}^{\mathrm{init}} - c_{\mathrm{OY}}^{n+1}\right]\right)} \tag{4.264}$$

and can be rewritten as

$$0 = \left[c_{\mathrm{OB}}^{n+1} - c_{\mathrm{OB}}^{n} + \Delta t\, k_1\right] \exp\left(k_2\, c_{\mathrm{OB}}^{n+1} \left[c_{\mathrm{OY}}^{\mathrm{init}} - c_{\mathrm{OY}}^{n+1}\right]\right) - \Delta t\, k_1 =: r_1. \tag{4.265}$$

By a similar procedure, the evolution of the osteocyte concentration in time (4.139c) is studied whereby the dependence on the term $s_{\mathrm{OY/OB}}$ is considered exclusively, i.e.

$$\dot{c}_{\mathrm{OY}} = \frac{\mathrm{d}c_{\mathrm{OY}}}{\mathrm{d}t} = k_1 \left[1 - \exp\left(-k_2\, c_{\mathrm{OB}} \left[c_{\mathrm{OY}}^{\mathrm{init}} - c_{\mathrm{OY}}\right]\right)\right], \tag{4.266}$$

respectively

$$\frac{\mathrm{d}c_{\mathrm{OY}}}{\mathrm{d}t} = \frac{k_1 \left[\exp\left(k_2\, c_{\mathrm{OB}} \left[c_{\mathrm{OY}}^{\mathrm{init}} - c_{\mathrm{OY}}\right]\right) - 1\right]}{\exp\left(k_2\, c_{\mathrm{OB}} \left[c_{\mathrm{OY}}^{\mathrm{init}} - c_{\mathrm{OY}}\right]\right)}. \tag{4.267}$$

Application of the Backward-Euler scheme yields

$$\frac{\mathrm{d}c_{\mathrm{OY}}}{\mathrm{d}t} \approx \frac{c_{\mathrm{OY}}^{n+1} - c_{\mathrm{OY}}^{n}}{\Delta t} = \frac{k_1 \left[\exp\left(k_2\, c_{\mathrm{OB}}^{n+1} \left[c_{\mathrm{OY}}^{\mathrm{init}} - c_{\mathrm{OY}}^{n+1}\right]\right) - 1\right]}{\exp\left(k_2\, c_{\mathrm{OB}}^{n+1} \left[c_{\mathrm{OY}}^{\mathrm{init}} - c_{\mathrm{OY}}^{n+1}\right]\right)} \tag{4.268}$$

which can be rewritten in order to obtain a residual function, hence

$$0 = \left[c_{\mathrm{OY}}^{n+1} - c_{\mathrm{OY}}^{n} - \Delta t\, k_1\right] \exp\left(k_2\, c_{\mathrm{OB}}^{n+1} \left[c_{\mathrm{OY}}^{\mathrm{init}} - c_{\mathrm{OY}}^{n+1}\right]\right) + \Delta t\, k_1 =: r_2. \tag{4.269}$$

Since (4.265) and (4.269) are non-linear and coupled equations in the unknown concentrations c_{OB}^{n+1} and c_{OY}^{n+1}, they are solved simultaneously by using a Newton-Raphson scheme with residual vector

$$\boldsymbol{r} = \begin{bmatrix} r_1 \\ r_2 \end{bmatrix} = \begin{bmatrix} \left[c_{\mathrm{OY}}^{n+1} - c_{\mathrm{OY}}^{n} - \Delta t\, k_1\right] \exp\left(k_2\, c_{\mathrm{OB}}^{n+1} \left[c_{\mathrm{OY}}^{\mathrm{init}} - c_{\mathrm{OY}}^{n+1}\right]\right) + \Delta t\, k_1 \\ \left[c_{\mathrm{OB}}^{n+1} - c_{\mathrm{OB}}^{n} + \Delta t\, k_1\right] \exp\left(k_2\, c_{\mathrm{OB}}^{n+1} \left[c_{\mathrm{OY}}^{\mathrm{init}} - c_{\mathrm{OY}}^{n+1}\right]\right) - \Delta t\, k_1 \end{bmatrix} \tag{4.270}$$

and corresponding Jacobian matrix

$$\boldsymbol{J} = \begin{bmatrix} J_{11} & J_{12} \\ J_{21} & J_{22} \end{bmatrix} \tag{4.271}$$

with

$$J_{11} = \frac{\mathrm{d}\, r_1}{\mathrm{d}\, c_{\mathrm{OY}}^{n+1}} = \left[1 - k_2\, c_{\mathrm{OB}}^{n+1} \left[c_{\mathrm{OY}}^{n+1} - c_{\mathrm{OY}}^{n} - \Delta t\, k_1\right]\right] \exp\left(k_2\, c_{\mathrm{OB}}^{n+1} \left[c_{\mathrm{OY}}^{\mathrm{init}} - c_{\mathrm{OY}}^{n+1}\right]\right) \tag{4.272}$$

$$J_{12} = \frac{\mathrm{d}\, r_1}{\mathrm{d}\, c_{\mathrm{OB}}^{n+1}} = k_2 \left[c_{\mathrm{OY}}^{\mathrm{init}} - c_{\mathrm{OY}}^{n+1}\right] \left[c_{\mathrm{OY}}^{n+1} - c_{\mathrm{OY}}^{n} - \Delta t\, k_1\right] \exp\left(k_2\, c_{\mathrm{OB}}^{n+1} \left[c_{\mathrm{OY}}^{\mathrm{init}} - c_{\mathrm{OY}}^{n+1}\right]\right) \tag{4.273}$$

$$J_{21} = \frac{\mathrm{d}\, r_2}{\mathrm{d}\, c_{\mathrm{OY}}^{n+1}} = -k_2\, c_{\mathrm{OB}}^{n+1} \left[c_{\mathrm{OB}}^{n+1} - c_{\mathrm{OB}}^{n} + \Delta t\, k_1 \right] \exp\left(k_2\, c_{\mathrm{OB}}^{n+1} \left[c_{\mathrm{OY}}^{\mathrm{init}} - c_{\mathrm{OY}}^{n+1} \right] \right) \tag{4.274}$$

$$J_{22} = \frac{\mathrm{d}\, r_2}{\mathrm{d}\, c_{\mathrm{OB}}^{n+1}} = \left[1 + k_2 \left[c_{\mathrm{OY}}^{\mathrm{init}} - c_{\mathrm{OY}}^{n+1} \right] \left[c_{\mathrm{OB}}^{n+1} - c_{\mathrm{OB}}^{n} + \Delta t\, k_1 \right] \right] \exp\left(k_2\, c_{\mathrm{OB}}^{n+1} \left[c_{\mathrm{OY}}^{\mathrm{init}} - c_{\mathrm{OY}}^{n+1} \right] \right). \tag{4.275}$$

Fig. 4.43 presents the numerical results of this system of equations by showing the concentrations of osteoblasts and osteoclasts over time. Two different initial osteocyte concentrations are considered since the initial osteocyte concentration is an outcome of the preceding IGA simulations and can vary, accordingly. In particular $c_{\mathrm{OY}}^{\mathrm{init}} = 7500\,\mathrm{mm}^{-3}$ and $c_{\mathrm{OY}}^{\mathrm{init}} = 22\,000\,\mathrm{mm}^{-3}$ are chosen since these are realistic values available in the results presented in Sect. 4.4.6.3 at different spatial locations. Moreover, different values for the osteoblast concentration at time step n are included since this value can vary in the simulations depending on the considered time step and on the model parameters. The latter are chosen as denoted in Table 4.8 in accordance with the simulations performed in Sect. 4.4.6. From Fig. 4.43a-4.43b it is observed that for $c_{\mathrm{OY}}^{\mathrm{init}} = 7500\,\mathrm{mm}^{-3}$, i.e. at locations of maximum osteocyte apoptosis in the IGA results shown in Fig. 4.30-4.31, osteoblasts differentiate into osteocytes until they approach a zero concentration. The osteocyte concentration accordingly increases, whereas a convergence to a limiting value is obtained when the availability of osteoblasts is no longer provided. Focussing on Fig. 4.43c-4.43d, a similar behaviour can be observed for $c_{\mathrm{OY}}^{\mathrm{init}} = 22\,000\,\mathrm{mm}^{-3}$, whereas in this case, the osteocyte concentration saturates earlier as it approaches the value of healthy bone material $c_{\mathrm{OY}} = 25\,000\,\mathrm{mm}^{-3}$. For rather high osteoblast concentrations such as $c_{\mathrm{OB}}^{n} = 1 \times 10^4\,\mathrm{mm}^{-3}$ and $c_{\mathrm{OB}}^{n} = 5 \times 10^3\,\mathrm{mm}^{-3}$, the differentiation of these bone cells into osteocytes is limited by the saturation of the osteocyte concentration. From a physics point of view, not all osteoblasts become embedded in the bone material in the form of osteocytes, accordingly. Instead, the remaining bone cells can still transform into bone lining cells or undergo apoptosis, which is not captured in the modelling approach.

C.4 Aspects on geometry in IGA

C.4.1 Cracked bone sample within the IGA approach

Fig. 4.44a shows the control mesh which serves as a basis for the IGA geometry of the cracked domain under consideration in Sect. 4.3.3. It is constructed using two patches which interfere at the vertical symmetry line of the domain. In Fig. 4.9, the separation of the patches is indicated by a dotted line. For each patch, a unique set of control points is defined together with corresponding weights, which are all equal to 1.0 in this

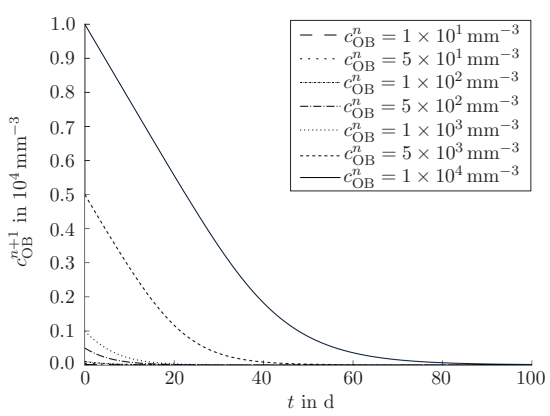

(a) Osteoblast concentration with $c_{\mathrm{OY}}^{\mathrm{init}} = 7500\,\mathrm{mm}^{-3}$.

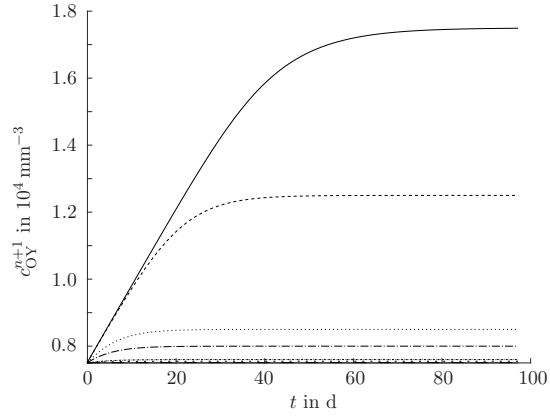

(b) Osteocyte concentration with $c_{\mathrm{OY}}^{\mathrm{init}} = 7500\,\mathrm{mm}^{-3}$.

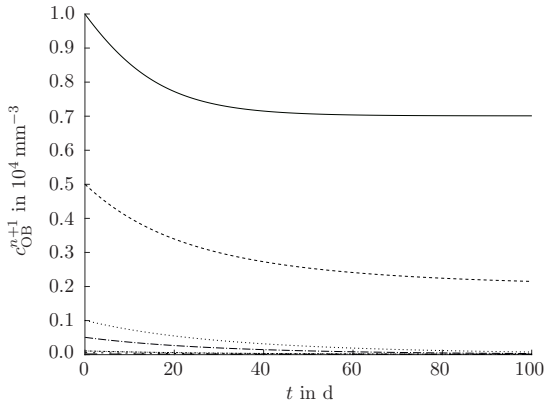

(c) Osteoblast concentration with $c_{\mathrm{OY}}^{\mathrm{init}} = 22\,000\,\mathrm{mm}^{-3}$.

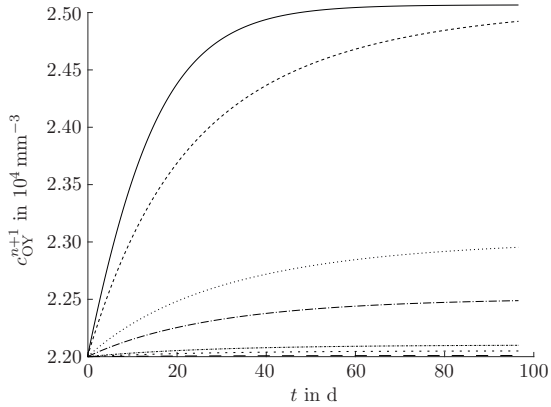

(d) Osteocyte concentration with $c_{\mathrm{OY}}^{\mathrm{init}} = 22\,000\,\mathrm{mm}^{-3}$.

Figure 4.43: Osteocyte and osteoblast concentration over time in dependence on the source, respectively sink term $s_{\mathrm{OY/OB}}$. The results include different initial osteocyte concentrations $c_{\mathrm{OY}}^{\mathrm{init}}$ as well as different osteoblast concentrations c_{OB}^{n} of the previous time step.

particular case. The number of control points is $\mathrm{n_{cp}} = \mathrm{n} \cdot \mathrm{m} = 12$ with $\mathrm{n} = 4, \mathrm{m} = 3$ for both of the two patches A and B. The control point coordinates are chosen as

$$\boldsymbol{B}^{A} = \begin{bmatrix} 0.0 & 0.0 & 0.0 & 0.4 & 0.2 & 0.2 & 0.3 & 0.4 & 0.396 & 0.396 & 0.399 & 0.4 \\ 0.6 & 0.0 & 0.0 & 0.0 & 0.6 & 0.4 & 0.25 & 0.25 & 0.6 & 0.475 & 0.425 & 0.425 \end{bmatrix}^{\mathrm{t}},$$
$$\boldsymbol{B}^{B} = \begin{bmatrix} 0.4 & 0.8 & 0.8 & 0.8 & 0.4 & 0.5 & 0.6 & 0.6 & 0.4 & 0.401 & 0.404 & 0.404 \\ 0.0 & 0.0 & 0.0 & 0.6 & 0.25 & 0.25 & 0.4 & 0.6 & 0.425 & 0.425 & 0.475 & 0.6 \end{bmatrix}^{\mathrm{t}}. \tag{4.276}$$

By repetition of the second control point in each patch the sharp corners on the lower left and right are constructed. The knot vectors are equal for both patches and read

$$\Xi = [0, 0, 0, 0.5, 1, 1, 1], \quad \mathcal{H} = [0, 0, 0, 1, 1, 1] \tag{4.277}$$

considering a polynomial degree of $p = q = 2$ within a two-dimensional setting. The resulting physical mesh is presented in Fig. 4.44b and consists of two elements in each patch. By refinement through knot insertion, cf. Sect. 2.2.2, the number of elements is increased for the simulations carried out in Sect. 4.3.3 and the mesh shown in Fig. 4.10 is obtained.

The connection between the two patches is enabled by the coinciding control points at $x_1 = 0.4$ in (4.276). Accordingly, the condition (2.28) for C^0-continuity between the patches is ensured by this choice of control points. For the simulations in this work, however, global C^1-continuity is required. Accordingly, (2.29) must be fulfilled. Due to the collinearity and equal distancing of control points across the patch interface in the geometry under consideration, cf. Fig. 4.44a, this condition is directly fulfilled with respect to the control points with the constant in (2.29) specified as $k = 1$. For the unknown fields, on the other hand, the conditions (2.28) and (2.29) are incorporated by linear constraints as described in Sect. 2.3.2.

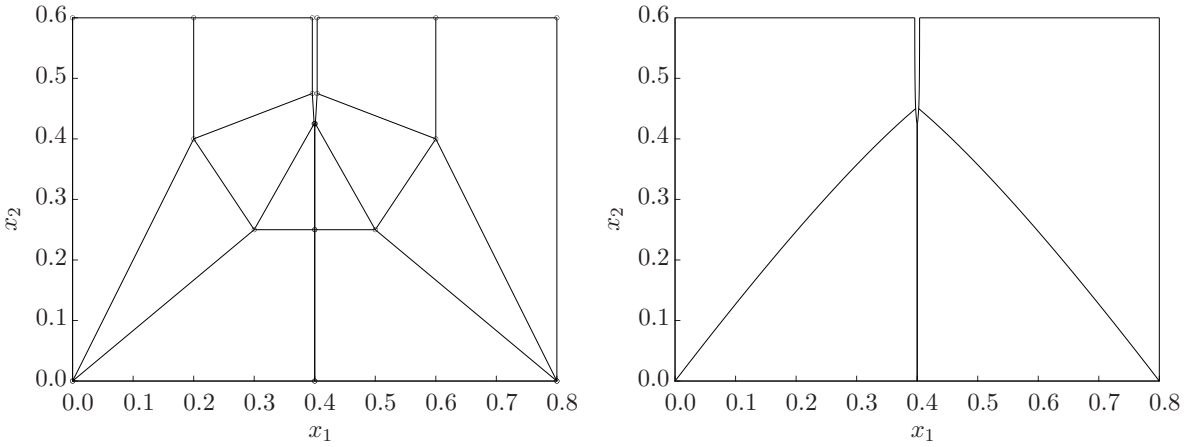

(a) Control mesh with $n_{cp} = 24$.

(b) Coarsest physical mesh with $n_{el} = 4$.

Figure 4.44: Control mesh and coarsest physical mesh of the cracked bone sample.

C.4.2 Cracked bone sample within the IGA-FEA approach

In the following, the geometric data for the IGA model is summarised for all crack lengths considered in the simulations in Sect. 4.4.6.3. The two-dimensional geometry of the cracked rectangular domain is constructed based on NURBS and consists of two patches in analogy to the geometry described in Appendix C.4.1. For the coarsest mesh, the knot vectors in the two parametric directions read

$$\Xi = [0, 0, 0, 0.5, 1, 1, 1], \quad \mathcal{H} = [0, 0, 0, 1, 1, 1] \tag{4.278}$$

for polynomial degrees $p = q = 2$ and are identical for both patches. The control points for each of the patches are

$$\boldsymbol{B}^A = \begin{bmatrix} 0.0 & 0.0 & 0.0 & 0.4 & 0.2 & 0.2 & 0.3 & 0.4 & 0.395 & 0.395 & 0.3975 & 0.4 \\ 0.6 & 0.0 & 0.0 & 0.0 & 0.6 & 0.4 & 0.25 & 0.25 & 0.6 & 0.475 & 0.425 & 0.425 \end{bmatrix}^{\mathrm{t}},$$
$$\boldsymbol{B}^B = \begin{bmatrix} 0.4 & 0.8 & 0.8 & 0.8 & 0.4 & 0.5 & 0.6 & 0.6 & 0.4 & 0.4025 & 0.405 & 0.405 \\ 0.0 & 0.0 & 0.0 & 0.6 & 0.25 & 0.25 & 0.4 & 0.6 & 0.425 & 0.425 & 0.475 & 0.6 \end{bmatrix}^{\mathrm{t}}. \tag{4.279}$$

These correspond to the geometry of the plate with maximum crack length $l_{\max} = 0.175\,\mathrm{mm}$.

Within this work, the employed crack lengths are $l_0 = 1/64\; l_{\max}$ and $l_i = i\, l_{\max}/32$ with $i = 1, \ldots, 32$. For these particular geometries, the x_2-coordinates of the control points $\boldsymbol{B}^A_{3,2}, \boldsymbol{B}^A_{3,3}, \boldsymbol{B}^A_{3,4}$ and $\boldsymbol{B}^B_{3,1}, \boldsymbol{B}^B_{3,2}, \boldsymbol{B}^B_{3,3}$ are adapted in comparison with (4.279) whereas the indices are based on the numbering defined in (2.6). The modified control points are calculated as

$$\begin{aligned} \boldsymbol{B}^A_{3,2} \cdot \boldsymbol{e}_2 &= 0.6 - \alpha_j\, l_{\max}, \quad \boldsymbol{B}^A_{3,3} \cdot \boldsymbol{e}_2 = \boldsymbol{B}^A_{3,4} \cdot \boldsymbol{e}_2 = 0.6 - \beta_j \left[0.6 - \boldsymbol{B}^A_{3,2} \cdot \boldsymbol{e}_2\right] \\ \boldsymbol{B}^B_{3,3} \cdot \boldsymbol{e}_2 &= 0.6 - \alpha_j\, l_{\max}, \quad \boldsymbol{B}^B_{3,1} \cdot \boldsymbol{e}_2 = \boldsymbol{B}^B_{3,2} \cdot \boldsymbol{e}_2 = 0.6 - \beta_j \left[0.6 - \boldsymbol{B}^B_{3,3} \cdot \boldsymbol{e}_2\right] \end{aligned} \tag{4.280}$$

for $j = 0, \ldots, 32$. Therein, scalars α_j and β_j are specified as $\alpha_0 = 1/64$, $\beta_0 = [1 + 4\,\alpha_0]\,/7$ and $\alpha_i = i/32$, $\beta_i = [1 + 4\,\alpha_i]\,/7$. The remaining control point coordinates are identical for all crack lengths. In Fig. 4.45, the corresponding control meshes are presented for the crack lengths $l \in \{\frac{3}{8}\, l_{\max}, \frac{5}{8}\, l_{\max}, l_{\max}\}$ and Fig. 4.46 shows the corresponding physical meshes without refinement. By means of knot insertion, cf. Sect. 2.2.2, the final discretisations, as presented in Fig. 4.32 for the maximum crack length, are obtained.

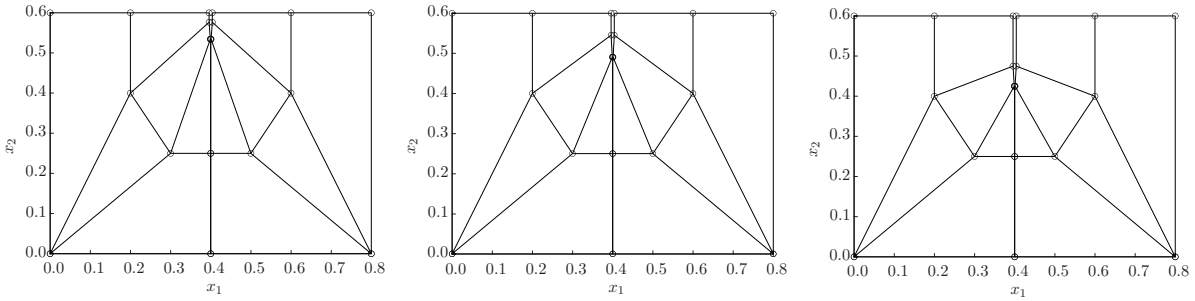

(a) Crack length $l = \frac{3}{8}\, l_{\max}$. **(b)** Crack length $l = \frac{5}{8}\, l_{\max}$. **(c)** Crack length $l = l_{\max}$.

Figure 4.45: Control meshes for different crack lengths, respectively different time steps during crack evolution with $\mathrm{n_{cp}} = 24$. Reprinted from [175] under the terms of the Creative Commons Attribution License (CC BY).

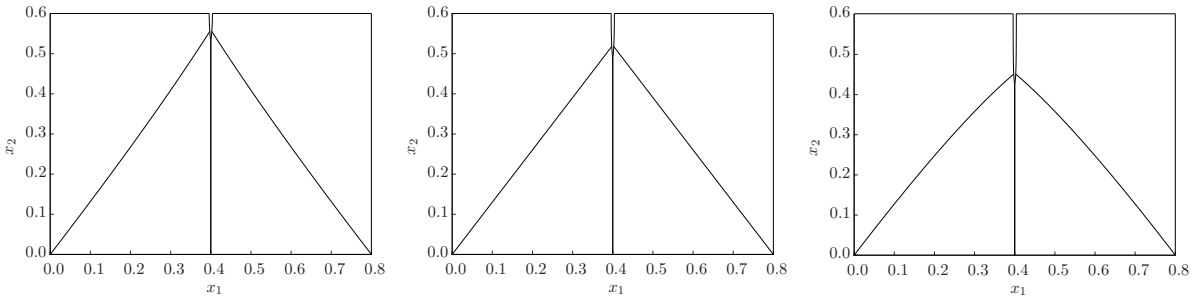

(a) Crack length $l = \frac{3}{8}\, l_{\max}$. **(b)** Crack length $l = \frac{5}{8}\, l_{\max}$. **(c)** Crack length $l = l_{\max}$.

Figure 4.46: Coarsest physical meshes for different crack lengths, respectively different time steps during crack evolution with $\mathrm{n_{el}} = 4$.

C.5 Additional results

C.5.1 Combined flexoelectric and piezoelectric remodelling initiation

In Fig. 4.19a, 4.19c and 4.19e, the electric field magnitude near the crack tip at time $t = 3\,\mathrm{s}$ is presented for the purely flexoelectric, the purely piezoelectric and the combined initiation of bone remodelling. In Fig. 4.21, the individual components of the electric field vector, i.e. e_1 and e_2, are shown for pure flexoelectricity and pure piezoelectricity in order to help explain the behaviour of the combined response. In the following, Fig. 4.47 provides a more detailed view on the results for all three cases so that the magnitude as well as the direction of the electric field can be observed in one plot each.

C.5.2 Simultaneous bone remodelling from two sides

In the bone remodelling simulations in Sect. 4.4.6.5, the boundary conditions and model parameters have been chosen in such a way that bone cells are recruited from the surrounding vasculature on the left boundary of the cracked cortical bone specimen under consideration. Active osteoclasts and osteoblasts accordingly enter the domain over the left boundary and move towards the remodelling site, i.e. to the crack to perform remodelling, respectively crack healing. Complementing these studies, additional simulations have been carried out in which the simultaneous action of bone cells from different spatial origins is considered. For this purpose, the reaction-force driven boundary conditions (4.144) and (4.150) are additionally prescribed on the right-hand surface of the cracked domain. In order to obtain a similar osteoblast outflux over the crack surfaces and, accordingly, a comparable growth behaviour with respect to the simulations in Sect. 4.4.6.5, the constant factor scaling the influx of osteoblasts is set to $k_{\mathrm{OB}} = 0.15$ within the simulations. In Fig. 4.48, the corresponding simulation results are presented in terms of the osteoclast and osteoblast diffusion. It can be observed that these cells enter from both sides of the domain and migrate towards the crack in terms of anisotropic diffusion. By this simultaneous diffusion from the left and right, the resulting osteoblast

outflux over the crack surfaces and, consequently, the growth behaviour are significantly affected. As shown in Fig. 4.49, the growth is rather symmetric in contrast to the bone formation by the one-sided bone remodelling.

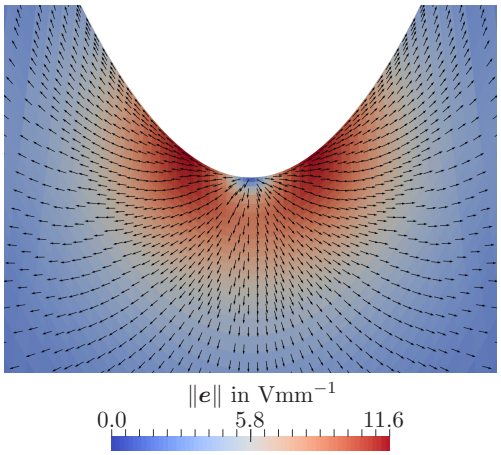

(a) Electric field at time $t = 3\,\mathrm{s}$ near the crack tip for pure flexoelectricity.

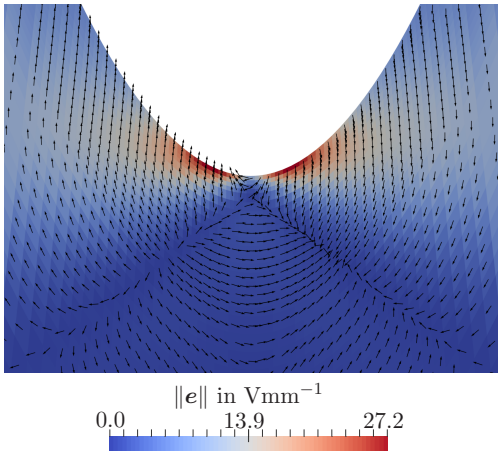

(b) Electric field at time $t = 3\,\mathrm{s}$ near the crack tip for pure piezoelectricity.

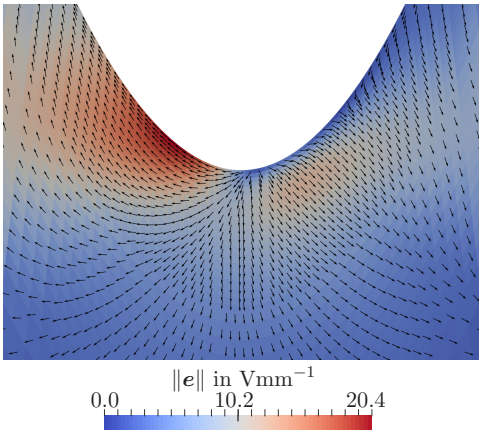

(c) Electric field at time $t = 3\,\mathrm{s}$ near the crack tip for combined flexoelectricity and piezoelectricity.

Figure 4.47: Electric field at time $t = 3\,\mathrm{s}$ near the crack tip. The plots show the results for simulations considering pure flexoelectricity, pure piezoelectricity and both effects combined. The contour plots indicate the magnitude of the electric field, whereas the glyphs show its direction. Reprinted from [174] under the terms of the Creative Commons Attribution License (CC BY).

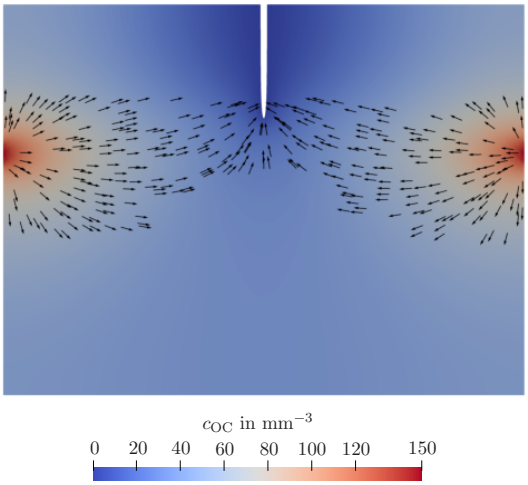

(a) Osteoclast concentration and flux from two sides.

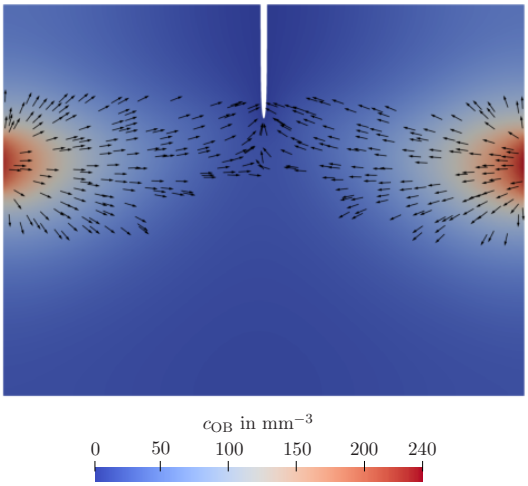

(b) Osteoblast concentration and flux from two sides.

Figure 4.48: Concentration and flux of bone cells in the simultaneous bone remodelling from two sides. The contour plots present the concentration of osteoclasts c_{OC}, respectively osteoblasts c_{OB} and the glyphs indicate the direction of the corresponding fluxes $\boldsymbol{q}_{OC}$ and $\boldsymbol{q}_{OB}$ in the region of interest.

C.6 Convergence study

Due to the spatial as well as temporal dependency of the calculations performed for the investigation of bone remodelling in this thesis, the convergence with respect to both mesh size and time increment are investigated. In particular, the IGA framework presented in Sect. 4.3 is under consideration and shall also be representative for the framework in Sect. 4.4 where an even finer mesh and the same time increment Δt is employed in the simulations.

In Fig. 4.50, the maximum magnitude of electric field present in the cortical bone specimen at maximum mechanical load ($t = 3\,\mathrm{s}$, cf. Fig. 4.9) is shown for different finite element discretisations. More specifically speaking, the number of elements in the finite element mesh is varied according to $\mathrm{n_{el}} \in \{6156, 7564, 11\,840, 16\,008\}$, whereas a constant time increment $\Delta t = 1/8\,\mathrm{s}$ is considered. Analogously, the minimum osteocyte concentration after apoptosis at time $t = 5\,\mathrm{s}$ is presented in dependence on the employed number of elements. A clear convergence can be observed in both figures with a deviation of less than 1 % between the discretisations with 11 840 and 16 008 elements.

Regarding the time increment in the numerical simulations, Fig. 4.51 includes the resulting electric field, respectively osteocyte concentration values for $\Delta t \in \{1\,\mathrm{s}, 1/2\,\mathrm{s}, 1/4\,\mathrm{s}, 1/8\,\mathrm{s}, 1/16\,\mathrm{s}\}$. For the spatial discretisation, the finest mesh including 16 008 elements is used. The maximum electric field magnitude remains almost constant in all simulations, whereas a convergence behaviour can be observed for the

minimum osteocyte concentration when sufficiently small time increments are considered. In particular, the difference between the concentration values obtained from the simulations with $\Delta t = 1/8\,\mathrm{s}$ and $\Delta t = 1/16\,\mathrm{s}$ is smaller than $1\,\%$.

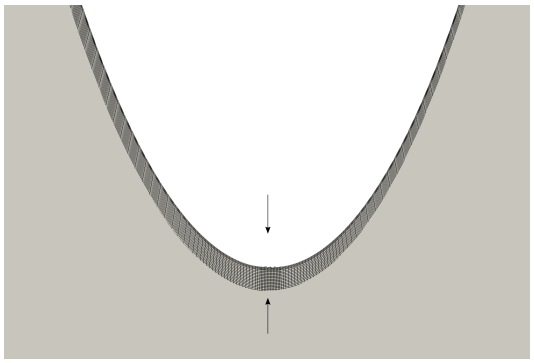

(a) Mesh after four growth steps. One-sided remodelling.

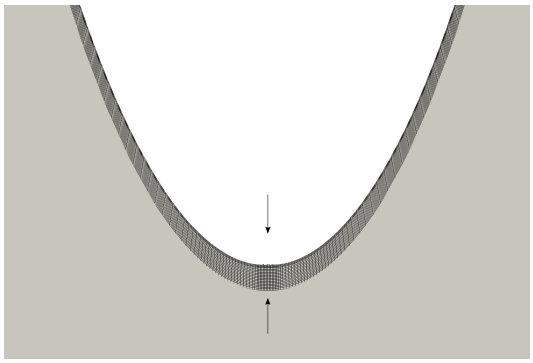

(b) Mesh after four growth steps. Two-sided remodelling.

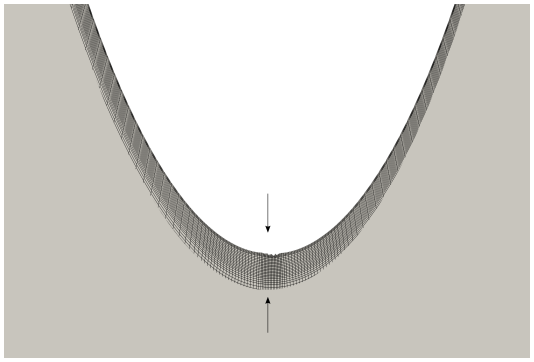

(c) Mesh after five growth steps. One-sided remodelling.

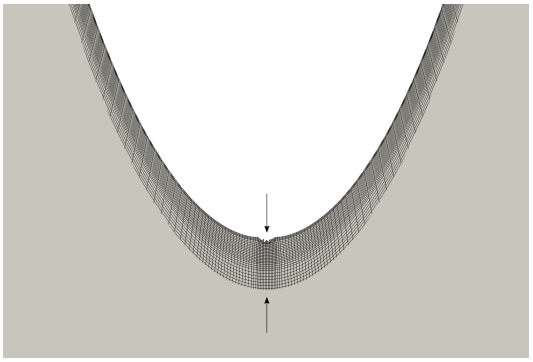

(d) Mesh after five growth steps. Two-sided remodelling.

Figure 4.49: Comparison of the surface growth behaviour in simulations with BMU progression from one, respectively two sides. Detail views on the crack tip region are shown. The grey coloured domain without element edges represents the initial domain for comparison. Arrows indicate the vertical symmetry line of the initial domain.

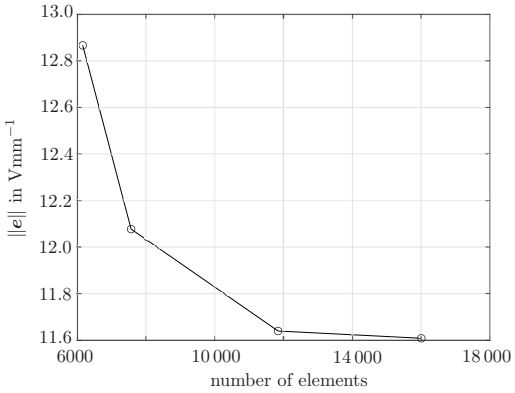

(a) Maximum electric field value at time $t = 3\,\mathrm{s}$.

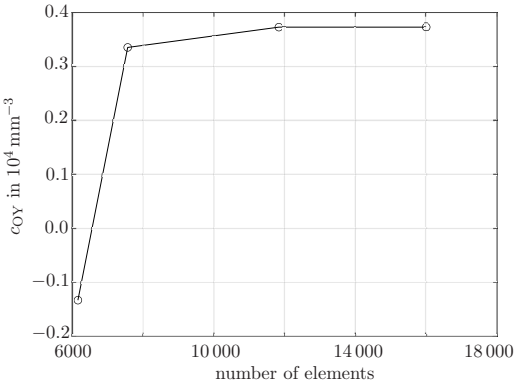

(b) Minimum osteocyte concentration at time $t = 5\,\mathrm{s}$.

Figure 4.50: Convergence behaviour of the results for simulations considering pure flexoelectricity. Four different mesh sizes are considered.

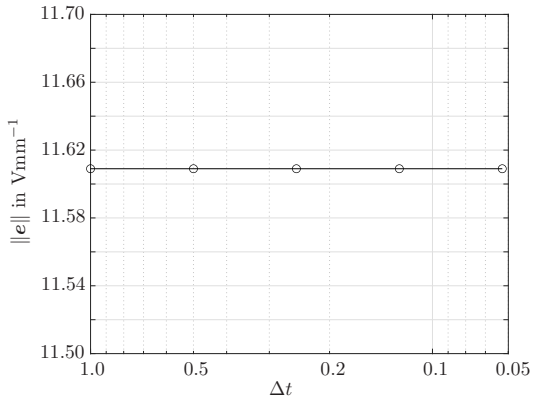

(a) Maximum electric field value at time $t = 3\,\mathrm{s}$.

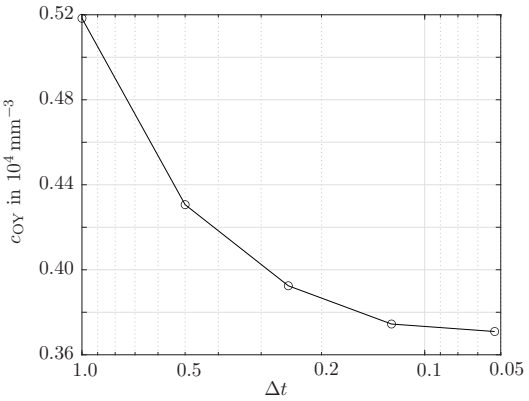

(b) Minimum osteocyte concentration at time $t = 5\,\mathrm{s}$.

Figure 4.51: Convergence behaviour of the results for simulations considering pure flexoelectricity. Five different time step sizes Δt are considered.

5 Concluding remarks

This thesis dealt with the modelling and numerical simulation of higher-gradient effects in anisotropic solids as a result of their particular microstructure. It has been shown that, within the *theory of gradient continua*, the incorporation of such higher-gradient effects leads to partial differential equations up to fourth order and, accordingly, to higher continuity requirements on the basis functions in the underlying finite element scheme. Consequently, isogeometric analysis has been employed in order to fulfil these requirements by using NURBS basis functions. In Chapter 2, a globally C^1-*continuous IGA framework* has been presented for this purpose. Therein, special techniques for imposing C^1-continuity also for complex geometries including multiple patches and repeated knots, respectively control points, are addressed. On this basis, the impact of the fibre bending stiffness on the mechanical behaviour of fibre-reinforced solids has been investigated in Chapter 3, and flexoelectricity has been studied in Chapter 4 as an initiator of remodelling and microcrack healing in cortical bone. Concluding remarks as well as an outlook to future research are subsequently provided for both topics.

Modelling of fibre-reinforced solids with fibre-bending stiffness In extension to classic structural tensor approaches for the modelling of fibre-reinforced solids which account for the tensile stiffness of the embedded fibres, a modelling approach considering the *fibre bending stiffness* has been investigated. On the basis of the couple-stress theory, the gradient of the fibre direction field has been incorporated as additional argument of the underlying stored energy density function. It has been shown that the resulting stresses and couple-stresses exhibit contributions from the *fibre curvature* within a small strain regime, whereas the *fibre stretch gradient* is additionally included under consideration of finite strains. As a further result of the employed couple-stress theory, a fourth-order partial differential equation is obtained.

By means of the globally C^1-continuous isogeometric analysis framework established in this work, this fourth-order PDE has been solved for different two-dimensional boundary value problems. For the validation of the proposed framework, a cylindrical tube subject to pure azimuthal shear has been studied since analytical solutions are available for this example. It has been shown that the numerical results obtained by isogeometric analysis are in qualitative and quantitative agreement with the analytical

solutions for both the linear and the non-linear framework up to a certain amount of deformation. In particular, an *increasingly stiff material response* has been observed upon activation of the fibre bending stiffness contributions. In the limiting case, the radial fibres in the cylindrical tube remain almost straight during deformation.

Two additional boundary value problems have been addressed by means of the proposed IGA frameworks for small, respectively finite strains in order to further examine the fibre properties. From the investigation of a bending beam as well as a notched plate under tensile load, the fibre bending stiffness has been shown to significantly affect the material response, especially when the geometric dimensions are small. Accordingly, the *size effect* included in the underlying gradient continuum theory exhibits a substantial impact on the simulation results. Moreover, the influence of the *fibre direction* has been studied, whereas the maximum resistance against bending has been obtained for fibres being aligned with the longitudinal axes of the beam-like structures under investigation. Regarding the stresses induced by the inhomogeneous deformations in the simulations, it has been found that, depending on the employed value of fibre bending stiffness, the symmetric and *skew-symmetric stress* contributions are of similar magnitude. Thus, both parts contribute significantly to the total stress response of the fibre-reinforced material.

In future works, the proposed framework shall be used for advanced constitutive modelling, such as for materials with initially curved fibres, and extended by consideration of additional deformation modes like fibre twist. Complex three-dimensional structures shall also be analysed with the proposed method.

Modelling of flexoelectricity-induced bone remodelling and microcrack healing
Targeted remodelling in cortical bone has been investigated by considering the underlying chemo-electro-mechanically coupled mechanisms contributing to the initiation as well as progression of this cell-regulated process. In particular, *flexoelectricity* has been accounted for by the incorporation of strain gradients into the underlying electric enthalpy density function in the proposed modelling approach. A thermodynamically consistent framework for flexoelectricity has been established and validated by comparison with an analytical solution for a representative boundary value problem including mechanical and electrical loading. It has been shown that the numerical simulations by the proposed isogeometric analysis scheme yield accurate results.

As a key component of the modelling approach presented in this thesis, the flexoelectricity-induced electric fields are coupled to *osteocyte apoptosis* which is known to initiate cortical bone remodelling processes. The subsequent bone cell diffusion as well as the biochemical signalling mechanisms during remodelling have been additionally accounted for in terms of (anisotropic) *diffusion equations* including specific source and sink terms that capture the physics of the underlying process.

Within the scope of this work, the initiation of bone remodelling has first been analysed in a multi-patch isogeometric analysis framework with global C^1-continuity and has been applied to a pre-cracked specimen of cortical bone. The simulation results have

revealed that the flexoelectricity-induced electric field in the vicinity of the crack tip exceeds the experimentally observed critical value for osteocyte apoptosis. Moreover, the relevance of flexoelectricity in comparison with piezoelectricity has been shown to increase on small scales due to the *size-dependency* of the flexoelectric effect. As a consequence of the electromechanical material response, cell diffusion processes are initiated through the particular modelling assumptions. To be precise, the flexoelectricity-induced osteocyte apoptosis is coupled to the *production of messenger substances* by a source term. These messenger substances *recruit osteoclastic and osteoblastic cells* from the surrounding vasculature through boundary conditions. By employing a threshold value for the influx of these bone cells, the proposed model further considers that new BMUs are most likely to originate in the Haversian or Volkmann's canal closest to the crack. After recruitment, the *targeted migration* of the bone cells towards the crack is accounted for by diffusion equations including *anisotropic evolving diffusion tensors*. More specifically speaking, a combination of the direct movement towards the crack as well as in direction of osteon alignment, i.e. a direction predetermined by the bone structure itself, has been found to be reasonable in order to imitate the migration of BMUs in real bones.

An extension of this modelling approach has additionally been presented in this thesis which captures the entire remodelling process including flexoelectric effects during crack evolution as well as the bone-forming activity of the involved bone cells under the use of a *combined IGA-FEA framework*. In the first part of the proposed framework, isogeometric analysis is employed in order to capture the flexoelectric initiation of bone remodelling. It is shown that the distribution of osteocytes within the considered bone sample changes during crack propagation due to apoptosis in the vicinity of the crack tip. Using this distribution of osteocytes as the initial osteocyte field which initiates the remodelling process, the remodelling itself is studied by the second part of the proposed framework, i.e. the finite element simulation. By using generalised Robin-type boundary conditions, the osteocyte signalling in response to the apoptosis event enables an influx of osteoclasts which migrate towards the crack in terms of anisotropic diffusion. During the resorption activity of osteoclasts, new messenger substances are released and, as they reach the domain boundaries, cause an influx of osteoblasts which similarly diffuse towards the crack. These *individual signalling mechanisms* control the timing of the process as observed in experiments. A main contribution of the proposed finite element scheme is the *surface growth* algorithm which is coupled to the diffusion of osteoblasts. A moving mesh-type approach is adopted for this purpose, and an *internal healing*, i.e. the differentiation of osteoblasts into osteocytes, is naturally accounted for by the appropriate coupling of the field equations. From the simulation results, a significant reduction of the crack width has been observed accordingly.

Overall, the proposed model provides a basis for the incorporation of the higher-order phenomenon flexoelectricity into a numerical framework for bone remodelling simulations. As experiments with bone material, especially on the micro scale and nano scale, are highly complex and difficult to conduct, this computational approach enables further investigations on the flexoelectric properties of bone and their impact on bone

remodelling processes via representative simulations. This includes, for instance, further studies on the flexoelectric coefficients and on the symmetry class of the flexoelectricity tensor in the context of cortical bone material. Besides, the proposed framework is capable of capturing the entire process of bone remodelling, from crack evolution and flexoelectricity-induced osteocyte apoptosis, to diffusion-driven crack healing. However, in order to simulate the complete closure of bone microcracks, future work shall include the consideration of further numerical techniques for severe surface growth, such as complete remeshing and additional smoothing. Moreover, appropriate contact algorithms are required in this case to avoid element penetrations. In the long run, the framework is to be extended to investigate malfunctions in the bone remodelling process which cause bone diseases such as osteoporosis.

Bibliography

[1] A. Abdollahi, C. Peco, D. Millán, M. Arroyo, and I. Arias. Computational evaluation of the flexoelectric effect in dielectric solids. *Journal of Applied Physics*, 116 (9):093502, 2014. doi:10.1063/1.4893974.

[2] A. Abdollahi, N. Domingo, I. Arias, and G. Catalan. Converse flexoelectricity yields large piezoresponse force microscopy signals in non-piezoelectric materials. *Nature Communications*, 10:1266, 2019. doi:10.1038/s41467-019-09266-y.

[3] M. Abramowitz and I. A. Stegun. *Handbook of Mathematical Functions With Formulas, Graphs, and Mathematical Tables*. U.S. Government Printing Office, Washington D.C., 10th printing edition, 1972.

[4] V. Agrawal and S. Gautam. IGA: A simplified introduction and implementation details for finite element users. *Journal of The Institution of Engineers (India): Series C*, 100:561–585, 2018. doi:10.1007/s40032-018-0462-6.

[5] I. M. Alarifi. Investigation the conductivity of carbon fiber composites focusing on measurement techniques under dynamic and static loads. *Journal of Materials Research and Technology*, 8(5):4863–4893, 2019. doi:10.1016/j.jmrt.2019.08.019.

[6] R. A. Alberty. Use of legendre transforms in chemical thermodynamics (IUPAC Technical Report). *Pure and Applied Chemistry*, 73(8):1349–1380, 2001. doi:10.1351/pac200173081349.

[7] E. Amanatidou and N. Aravas. Mixed finite element formulations of strain-gradient elasticity problems. *Computer Methods in Applied Mechanics and Engineering*, 191 (15):1723–1751, 2002. doi:10.1016/S0045-7825(01)00353-X.

[8] L. Anand. A thermo-mechanically-coupled theory accounting for hydrogen diffusion and large elastic-viscoplastic deformations of metals. *International Journal of Solids and Structures*, 48(6):962–971, 2011. doi:10.1016/j.ijsolstr.2010.11.029.

[9] E. W. Andrews, G. Gioux, P. Onck, and L. J. Gibson. Size effects in ductile cellular solids. Part II: experimental results. *International Journal of Mechanical Sciences*, 43(3):701–713, 2001. doi:10.1016/S0020-7403(00)00043-6.

[10] C. F. Arias, M. A. Herrero, L. F. Echeverri, G. E. Oleaga, and J. M. López. Bone remodeling: A tissue-level process emerging from cell-level molecular algorithms. *PLoS ONE*, 13:e0204171, 2018. doi:10.1371/journal.pone.0204171.

[11] H. Askes and E. C. Aifantis. Numerical modeling of size effects with gradient elasticity – Formulation, meshless discretization and examples. *International Journal of Fracture*, 117:347–358, 2002. doi:10.1023/A:1022225526483.

[12] T. Asmanoglo and A. Menzel. Fibre-reinforced composites with fibre-bending stiffness under azimuthal shear – Comparison of simulation results with analytical solutions. *International Journal of Non-Linear Mechanics*, 91:128–139, 2017. doi:10.1016/j.ijnonlinmec.2017.01.001.

[13] T. Asmanoglo and A. Menzel. A finite deformation continuum modelling framework for curvature effects in fibre-reinforced nanocomposites. *Journal of the Mechanics and Physics of Solids*, 107:411–432, 2017. doi:10.1016/j.jmps.2017.06.012.

[14] T. Asmanoglo and A. Menzel. A multi-field finite element approach for the modelling of fibre-reinforced composites with fibre-bending stiffness. *Computer Methods in Applied Mechanics and Engineering*, 317:1037–1067, 2017. doi:10.1016/j.cma.2017.01.003.

[15] Y. D. Bansod, M. Kebbach, D. Kluess, R. Bader, and U. van Rienen. Finite element analysis of bone remodelling with piezoelectric effects using an open-source framework. *Biomechanics and Modeling in Mechanobiology*, 20:1147–1166, 2021. doi:10.1007/s10237-021-01439-3.

[16] S. Baskaran, X. He, Y. Wang, and J. Y. Fu. Strain gradient induced electric polarization in α-phase polyvinylidene fluoride films under bending conditions. *Journal of Applied Physics*, 111(1):014109, 2012. doi:10.1063/1.3673817.

[17] A. Beheshti. Finite element analysis of plane strain solids in strain-gradient elasticity. *Acta Mechanica*, 228:3543–3559, 2017. doi:10.1007/s00707-017-1897-1.

[18] T. Bellido. Osteocyte-driven bone remodeling. *Calcified Tissue International*, 94: 25–34, 2014. doi:10.1007/s00223-013-9774-y.

[19] J. L. Bentley. Multidimensional binary search trees used for associative searching. *Communications of the ACM*, 18(9):509–517, 1975. doi:10.1145/361002.361007.

[20] V. Bentolila, T. M. Boyce, D. P. Fyhrie, R. Drumb, T. M. Skerry, and M. B. Schaffler. Intracortical remodeling in adult rat long bones after fatigue loading. *Bone*, 23(3):275–281, 1998. doi:10.1016/S8756-3282(98)00104-5.

[21] G. L. Bergel and P. Papadopoulos. A finite element method for modeling surface growth and resorption of deformable solids. *Computational Mechanics*, 68:759–774, 2021. doi:10.1007/s00466-021-02044-y.

[22] R. Berthelsen, H. Wilbuer, R. Holtermann, and A. Menzel. Computational modelling of wear – application to structured surfaces of elastoplastic tools. *GAMM-Mitteilungen*, 39(2):210–228, 2016. doi:10.1002/gamm.201610013.

[23] U. K. Bhaskar, N. Banerjee, A. Abdollahi, Z. Wang, D. G. Schlom, G. Rijnders, and G. Catalan. A flexoelectric microelectromechanical system on silicon. *Nature Nanotechnology*, 11(3):263–266, 2016. doi:10.1038/nnano.2015.260.

[24] S. Bochkanov. ALGLIB, 2022. URL `https://www.alglib.net`.

[25] J.-P. Boehler. A simple derivation of representations for non-polynomial constitutive equations in some cases of anisotropy. *ZAMM-Journal of Applied Mathematics and Mechanics/Zeitschrift für Angewandte Mathematik und Mechanik*, 59(4):157–167, 1979. doi:10.1002/zamm.19790590403.

[26] E. Brivadis, A. Buffa, B. Wohlmuth, and L. Wunderlich. Isogeometric mortar methods. *Computer Methods in Applied Mechanics and Engineering*, 284:292–319, 2015. doi:10.1016/j.cma.2014.09.012.

[27] P. R. Buenzli. Osteocytes as a record of bone formation dynamics: A mathematical model of osteocyte generation in bone matrix. *Journal of Theoretical Biology*, 364: 418–427, 2015. doi:10.1016/j.jtbi.2014.09.028.

[28] P. R. Buenzli, P. Pivonka, and D. W. Smith. Bone refilling in cortical bone multicellular units: insights into tetracycline double labelling from a computational model. *Biomechanics and Modeling in Mechanobiology*, 13:185–203, 2014. doi:10.1007/s10237-013-0495-y.

[29] E. H. Burger, J. Klein-Nulend, and T. H. Smit. Strain-derived canalicular fluid flow regulates osteoclast activity in a remodelling osteon – a proposal. *Journal of Biomechanics*, 36(10):1453–1459, 2003. doi:10.1016/S0021-9290(03)00126-X.

[30] C. L. Chan, C. Anitescu, and T. Rabczuk. Strong multipatch C1-coupling for isogeometric analysis on 2D and 3D domains. *Computer Methods in Applied Mechanics and Engineering*, 357:112599, 2019. doi:10.1016/j.cma.2019.112599.

[31] B. Chang and X. Liu. Osteon: Structure, turnover, and regeneration. *Tissue Engineering Part B: Reviews*, 28(2):261–278, 2022. doi:10.1089/ten.teb.2020.0322.

[32] K. Choi, J. L. Kuhn, M. J. Ciarelli, and S. A. Goldstein. The elastic moduli of human subchondral, trabecular, and cortical bone tissue and the size-dependency of cortical bone modulus. *Journal of Biomechanics*, 23(11):1103–1113, 1990. doi:10.1016/0021-9290(90)90003-L.

[33] M. H. V. Choy, R. M. Y. Wong, S. K. H. Chow, M. C. Li, Y. N. Chim, T. K. Li, W. T. Ho, J. C. Y. Cheng, and W. H. Cheung. How much do we know about the role of osteocytes in different phases of fracture healing? A systematic review. *Journal of Orthopaedic Translation*, 21:111–121, 2020. doi:10.1016/j.jot.2019.07.005.

[34] T. W. Clyne and D. Hull. *An Introduction to Composite Materials*. Cambridge Solid State Science Series. Cambridge University Press, Cambridge, 2nd edition, 1996. doi:10.1017/9781139050586.

[35] D. Codony, P. Gupta, O. Marco, and I. Arias. Modeling flexoelectricity in soft dielectrics at finite deformation. *Journal of the Mechanics and Physics of Solids*, 146:104182, 2021. doi:10.1016/j.jmps.2020.104182.

[36] D. Codony, A. Mocci, J. Barceló-Mercader, and I. Arias. Mathematical and computational modeling of flexoelectricity. *Journal of Applied Physics*, 130(23):231102,

2021. doi:10.1063/5.0067852.

[37] D. Codony, O. Marco, S. Fernández-Méndez, and I. Arias. An immersed boundary hierarchical B-spline method for flexoelectricity. *Computer Methods in Applied Mechanics and Engineering*, 354:750–782, 2019. doi:10.1016/j.cma.2019.05.036.

[38] K. Cordero-Edwards, H. Kianirad, C. Canalias, J. Sort, and G. Catalan. Flexoelectric fracture-ratchet effect in ferroelectrics. *Physical Review Letters*, 122:135502, 2019. doi:10.1103/PhysRevLett.122.135502.

[39] E. M. P. Cosserat and F. Cosserat. *Théorie des Corps Déformables*. A. Hermann et Fils, Paris, 1909.

[40] J. A. Cottrell, T. J. R. Hughes, and Y. Bazilevs. *Isogeometric Analysis: Toward Integration of CAD and FEA*. John Wiley & Sons, Ltd, Chichester, 2009. doi:10.1002/9780470749081.

[41] A. Creecy, J. G. Damrath, and J. M. Wallace. Control of bone matrix properties by osteocytes. *Frontiers in Endocrinology*, 11:578477, 2021. doi:10.3389/fendo.2020.578477.

[42] L. E. Cross. Flexoelectric effects: Charge separation in insulating solids subjected to elastic strain gradients. *Journal of Materials Science*, 41:53–63, 2006. doi:10.1007/s10853-005-5916-6.

[43] D. Cullinane and T. Einhorn. Chapter 2 - Biomechanics of Bone. In J. P. Bilezikian, L. G. Raisz, and G. A. Rodan, editors, *Principles of Bone Biology*, pages 17–32. Academic Press, San Diego, 2nd edition, 2002. doi:10.1016/B978-012098652-1/50104-9.

[44] M. A. Dagher and K. P. Soldatos. On small azimuthal shear deformation of fibre-reinforced cylindrical tubes. *Journal of Mechanics of Materials and Structures*, 6: 141–168, 2011. doi:10.2140/jomms.2011.6.141.

[45] M. A. Dagher and K. P. Soldatos. Pure azimuthal shear deformation of an incompressible tube reinforced by radial fibres resistant in bending. *IMA Journal of Applied Mathematics*, 79(5):848–868, 2014. doi:10.1093/imamat/hxu013.

[46] E. De Luycker, D. J. Benson, T. Belytschko, Y. Bazilevs, and M.-C. Hsu. X-FEM in isogeometric analysis for linear fracture mechanics. *International Journal for Numerical Methods in Engineering*, 87(6):541–565, 2011. doi:10.1002/nme.3121.

[47] F. Deng, Q. Deng, W. Yu, and S. Shen. Mixed finite elements for flexoelectric solids. *Journal of Applied Mechanics*, 84(8):081004, 2017. doi:10.1115/1.4036939.

[48] Q. Deng, L. Liu, and P. Sharma. Flexoelectricity in soft materials and biological membranes. *Journal of the Mechanics and Physics of Solids*, 62:209–227, 2014. doi:10.1016/j.jmps.2013.09.021.

[49] Q. Deng, S. Lv, Z. Li, K. Tan, X. Liang, and S. Shen. The impact of flexoelectricity on materials, devices, and physics. *Journal of Applied Physics*, 128(8):080902,

2020. doi:10.1063/5.0015987.

[50] J. K. Djoko, F. Ebobisse, A. T. McBride, and B. D. Reddy. A discontinuous Galerkin formulation for classical and gradient plasticity – Part 1: Formulation and analysis. *Computer Methods in Applied Mechanics and Engineering*, 196(37): 3881–3897, 2007. doi:10.1016/j.cma.2006.10.045.

[51] J. K. Djoko, F. Ebobisse, A. T. McBride, and B. D. Reddy. A discontinuous Galerkin formulation for classical and gradient plasticity. Part 2: Algorithms and numerical analysis. *Computer Methods in Applied Mechanics and Engineering*, 197 (1):1–21, 2007. doi:10.1016/j.cma.2007.06.027.

[52] X. N. Dong and X. E. Guo. The dependence of transversely isotropic elasticity of human femoral cortical bone on porosity. *Journal of Biomechanics*, 37(8):1281–1287, 2004. doi:10.1016/j.jbiomech.2003.12.011.

[53] E. F. Eriksen. Cellular mechanisms of bone remodeling. *Reviews in Endocrine and Metabolic Disorders*, 11:219–227, 2010. doi:10.1007/s11154-010-9153-1.

[54] A. C. Eringen. Linear theory of micropolar elasticity. *Journal of Mathematics and Mechanics*, 15(6):909–923, 1966.

[55] A. C. Eringen. Micropolar elastic solids with stretch. *Ari Kitabevi Matbaasi*, 24: 1–18, 1971.

[56] A. Eringen and E. Suhubi. Nonlinear theory of simple micro-elastic solids – I. *International Journal of Engineering Science*, 2(2):189–203, 1964. doi:10.1016/0020-7225(64)90004-7.

[57] J. R. Fernández, J. M. García-Aznar, and R. Martínez. Numerical analysis of a piezoelectric bone remodelling problem. *European Journal of Applied Mathematics*, 23(5):635–657, 2012. doi:10.1017/S0956792512000150.

[58] J. R. Fernández, J. M. García-Aznar, and R. Martínez. Piezoelectricity could predict sites of formation/resorption in bone remodelling and modelling. *Journal of Theoretical Biology*, 292:86–92, 2012. doi:10.1016/j.jtbi.2011.09.032.

[59] M. Ferretti, A. Madeo, F. dell'isola, and P. Boisse. Modeling the onset of shear boundary layers in fibrous composite reinforcements by second-gradient theory. *Zeitschrift für angewandte Mathematik und Physik*, 65:587–612, 2014. doi:10.1007/s00033-013-0347-8.

[60] P. Fischer, M. Klassen, J. Mergheim, P. Steinmann, and R. Müller. Isogeometric analysis of 2D gradient elasticity. *Computational Mechanics*, 47:325–334, 2011. doi:10.1007/s00466-010-0543-8.

[61] S. Forest and K. Sab. Stress gradient continuum theory. *Mechanics Research Communications*, 40:16–25, 2012. doi:10.1016/j.mechrescom.2011.12.002.

[62] D. I. Fotiadis, G. Foutsitzi, and C. V. Massalas. Wave propagation modeling in human long bones. *Acta Mechanica*, 137:65–81, 1999. doi:10.1007/BF01313145.

[63] T. A. Franz-Odendaal, B. K. Hall, and P. E. Witten. Buried alive: How osteoblasts become osteocytes. *Developmental Dynamics*, 235(1):176–190, 2006. doi:10.1002/dvdy.20603.

[64] H. M. Frost. Tetracycline-based histological analysis of bone remodeling. *Calcified Tissue Research*, 3:211–237, 1969. doi:10.1007/BF02058664.

[65] E. Fukada and I. Yasuda. On the piezoelectric effect of bone. *Journal of the Physical Society of Japan*, 12(10):1158–1162, 1957. doi:10.1143/JPSJ.12.1158.

[66] J.-F. Ganghoffer and I. Goda. A combined accretion and surface growth model in the framework of irreversible thermodynamics. *International Journal of Engineering Science*, 127:53–79, 2018. doi:10.1016/j.ijengsci.2018.02.006.

[67] J.-F. Ganghoffer, X. N. Do, and A. Ibrahimbegovic. Thermodynamic formulations of the growth of solid bodies subjected to electromechanical interactions and application to bone external and internal remodeling. *Continuum Mechanics and Thermodynamics*, 33:1567–1602, 2021. doi:10.1007/s00161-021-00986-5.

[68] J. M. García-Aznar, G. Nasello, S. Hervas-Raluy, M. Ángeles Pérez, and M. J. Gómez-Benito. Multiscale modeling of bone tissue mechanobiology. *Bone*, 151: 116032, 2021. doi:10.1016/j.bone.2021.116032.

[69] H. Ghasemi, H. S. Park, and T. Rabczuk. A level-set based IGA formulation for topology optimization of flexoelectric materials. *Computer Methods in Applied Mechanics and Engineering*, 313:239–258, 2017. doi:10.1016/j.cma.2016.09.029.

[70] I. Goda, J.-F. Ganghoffer, and G. Maurice. Combined bone internal and external remodeling based on Eshelby stress. *International Journal of Solids and Structures*, 94-95:138–157, 2016. doi:10.1016/j.ijsolstr.2016.04.036.

[71] R. Goldman. Chapter 1 - Introduction: Foundations. In *Pyramid Algorithms*, The Morgan Kaufmann Series in Computer Graphics, pages 1–43. Morgan Kaufmann Publishers, San Francisco, 2003. doi:10.1016/B978-155860354-7/50002-7.

[72] J. M. Graham, B. P. Ayati, S. A. Holstein, and J. A. Martin. The role of osteocytes in targeted bone remodeling: A mathematical model. *PloS ONE*, 8(5):e63884, 2013. doi:10.1371/journal.pone.0063884.

[73] N. Graupner, A. S. Herrmann, and J. Müssig. Natural and man-made cellulose fibre-reinforced poly(lactic acid) (PLA) composites: An overview about mechanical characteristics and application areas. *Composites Part A: Applied Science and Manufacturing*, 40(6):810–821, 2009. doi:10.1016/j.compositesa.2009.04.003.

[74] M. Groß, J. Dietzsch, and C. Röbiger. Non-isothermal energy-momentum time integrations with drilling degrees of freedom of composites with viscoelastic fiber bundles and curvature-twist stiffness. *Computer Methods in Applied Mechanics and Engineering*, 365:112973, 2020. doi:10.1016/j.cma.2020.112973.

[75] H. Ha, C. Amicucci, P. Matteini, and B. Hwang. Mini review of synthesis strategies of silver nanowires and their applications. *Colloid and Interface Science Communications*, 50:100663, 2022. doi:10.1016/j.colcom.2022.100663.

[76] K. D. Harrison and D. M. L. Cooper. Modalities for visualization of cortical bone remodeling: The past, present, and future. *Frontiers in Endocrinology*, 6:122, 2015. doi:10.3389/fendo.2015.00122.

[77] J. G. Hazenberg, T. A. Hentunen, T. J. Heino, K. Kurata, T. Lee, and D. C. Taylor. Microdamage detection and repair in bone: Fracture mechanics, histology, cell biology. *Technology and Health Care*, 17(1):67–75, 2009. doi:10.3233/THC-2009-0536.

[78] C. Hergl, C. Witt, B. Nsonga, A. Menzel, and G. Scheuermann. Electromechanical coupling in electroactive polymers – a visual analysis of a third-order tensor field. *IEEE Transactions on Visualization and Computer Graphics*, 29(12):5357–5371, 2023. doi:10.1109/TVCG.2022.3209328.

[79] T. J. R. Hughes. *The Finite Element Method – Linear Static and Dynamic Finite Element Analysis*. Prentice Hall, Inc., Englewood Cliffs, New Jersey, 1987.

[80] T. J. R. Hughes, J. A. Cottrell, and Y. Bazilevs. Isogeometric analysis: CAD, finite elements, NURBS, exact geometry and mesh refinement. *Computer Methods in Applied Mechanics and Engineering*, 194(39):4135–4195, 2005. doi:10.1016/j.cma.2004.10.008.

[81] H. Ji, S. Zhang, K. Liu, T. Wu, M. Xu, and S. Shen. Flexoelectricity in pyramid compression: decoupling from effective to intrinsic. *Journal of Physics D: Applied Physics*, 53(12):125302, 2020. doi:10.1088/1361-6463/ab5c50.

[82] G. Y. Jing, H. L. Duan, X. M. Sun, Z. S. Zhang, J. Xu, Y. D. Li, J. X. Wang, and D. P. Yu. Surface effects on elastic properties of silver nanowires: Contact atomic-force microscopy. *Physical Review B*, 73(23):235409, 2006. doi:10.1103/PhysRevB.73.235409.

[83] J. S. Kenkre and J. H. D. Bassett. The bone remodelling cycle. *Annals of Clinical Biochemistry*, 55(3):308–327, 2018. doi:10.1177/0004563218759371.

[84] S. Kogan. Piezoelectric effect during inhomogeneous deformation and acoustic scattering of carriers in crystals. *Soviet Physics - Solid State*, 5(10):2069–2070, 1964.

[85] L. Kroll, M. Meyer, W. Nendel, and M. Schormair. Highly rigid assembled composite structures with continuous fiber-reinforced thermoplastics for automotive applications. *Procedia Manufacturing*, 33:224–231, 2019. doi:10.1016/j.promfg.2019.04.027.

[86] K. Kurata, T. J. Heino, H. Higaki, and H. K. Väänänen. Bone marrow cell differentiation induced by mechanically damaged osteocytes in 3D gel-embedded culture. *Journal of Bone and Mineral Research*, 21(4):616–625, 2009.

doi:10.1359/jbmr.060106.

[87] R. S. Lakes. Experimental Methods for Study of Cosserat Elastic Solids and Other Generalized Elastic Continua. In H.-B. Mühlhaus, editor, *Continuum Models for Materials with Microstructure*, pages 1–22. Wiley, New York, 1995.

[88] B. Q. Le, V. Nurcombe, S. M. Cool, C. A. Van Blitterswijk, J. De Boer, and V. L. S. LaPointe. The components of bone and what they can teach us about regeneration. *Materials*, 11(1):14, 2018. doi:10.3390/ma11010014.

[89] H. Le Quang and Q.-C. He. The number and types of all possible rotational symmetries for flexoelectric tensors. *Proceedings of the Royal Society A: Mathematical, Physical and Engineering Sciences*, 467(2132):2369–2386, 2011. doi:10.1098/rspa.2010.0521.

[90] H. Le Quang and Q.-C. He. Compact explicit matrix representations of the flexoelectric tensor and a graphic method for identifying all of its rotation and reflection symmetries. *Journal of Applied Physics*, 129(24):244103, 2021. doi:10.1063/5.0048386.

[91] J. Le Scornec and B. Guiffard. Large curvature sensors based on flexoelectric effect in PEDOT:PSS polymer films. *ACS Materials Letters*, 5(11):2929–2941, 2023. doi:10.1021/acsmaterialslett.3c00635.

[92] J. Lengiewicz and S. Stupkiewicz. Continuum framework for finite element modelling of finite wear. *Computer Methods in Applied Mechanics and Engineering*, 205–208:178–188, 2012. doi:10.1016/j.cma.2010.12.020.

[93] X. Li, M. S. Ominsky, Q.-T. Niu, N. Sun, B. Daugherty, D. D'Agostin, C. Kurahara, Y. Gao, J. Cao, J. Gong, F. Asuncion, M. Barrero, K. Warmington, D. Dwyer, M. Stolina, S. Morony, I. Sarosi, P. J. Kostenuik, D. L. Lacey, W. S. Simonet, H. Z. Ke, and C. Paszty. Targeted deletion of the sclerostin gene in mice results in increased bone formation and bone strength. *Journal of Bone and Mineral Research*, 23(6):860–869, 2009. doi:10.1359/jbmr.080216.

[94] C. Liu, J. Wang, G. Xu, M. Kamlah, and T.-Y. Zhang. An isogeometric approach to flexoelectric effect in ferroelectric materials. *International Journal of Solids and Structures*, 162:198–210, 2019. doi:10.1016/j.ijsolstr.2018.12.008.

[95] M. S. Majdoub, P. Sharma, and T. Cagin. Enhanced size-dependent piezoelectricity and elasticity in nanostructures due to the flexoelectric effect. *Physical Review B*, 77(12):125424, 2008. doi:10.1103/PhysRevB.77.125424.

[96] S. Manolagas. Birth and death of bone cells: Basic regulatory mechanisms and implications for the pathogenesis and treatment of osteoporosis. *Endocrine Reviews*, 21:115–37, 2000. doi:10.1210/er.21.2.115.

[97] S. Mao and P. K. Purohit. Insights into flexoelectric solids from strain-gradient elasticity. *Journal of Applied Mechanics*, 81(8):081004, 2014. doi:10.1115/1.4027451.

[98] S. Mao, P. K. Purohit, and N. Aravas. Mixed finite-element formulations in piezoelectricity and flexoelectricity. *Proceedings of the Royal Society A: Mathematical, Physical and Engineering Sciences*, 472(2190):20150879, 2016. doi:10.1098/rspa.2015.0879.

[99] P. M. Mariano and L. Galano. *Fundamentals of the Mechanics of Solids*. Birkhäuser, New York, NY, 2015. doi:10.1007/978-1-4939-3133-0.

[100] R. Martin. Targeted bone remodeling involves BMU steering as well as activation. *Bone*, 40(6):1574–1580, 2007. doi:10.1016/j.bone.2007.02.023.

[101] V. S. Mashkevich and K. B. Tolpygo. Electrical, optical and elastic properties of diamond type crystals. I. *Soviet Physics - Journal of Experimental and Theoretical Physics*, 5(3):435–439, 1957.

[102] A. T. McBride, D. Davydov, and P. Steinmann. Modelling the flexoelectric effect in solids: A micromorphic approach. *Computer Methods in Applied Mechanics and Engineering*, 371:113320, 2020. doi:10.1016/j.cma.2020.113320.

[103] A. Menzel and P. Steinmann. On the comparison of two strategies to formulate orthotropic hyperelasticity. *Journal of Elasticity*, 62(3):171–201, 2001. doi:10.1023/A:1012937501411.

[104] A. Menzel and P. Steinmann. A view on anisotropic finite hyper-elasticity. *European Journal of Mechanics - A/Solids*, 22(1):71–87, 2003. doi:10.1016/S0997-7538(02)01253-6.

[105] A. Menzel and C. Witt. Extremal states and coupling properties in electroelasticity. *Philosophical Transactions of the Royal Society A: Mathematical, Physical and Engineering Sciences*, 380(2234):20210330, 2022. doi:10.1098/rsta.2021.0330.

[106] R. D. Mindlin. Micro-structure in linear elasticity. *Archive for Rational Mechanics and Analysis*, 16:51–78, 1964. doi:10.1007/BF00248490.

[107] R. D. Mindlin. Polarization gradient in elastic dielectrics. *International Journal of Solids and Structures*, 4(6):637–642, 1968. doi:10.1016/0020-7683(68)90079-6.

[108] R. D. Mindlin and H. F. Tiersten. Effects of couple-stresses in linear elasticity. *Archive for Rational Mechanics and Analysis*, 11(1):415–448, 1962. doi:10.1007/BF00253946.

[109] R. D. Mindlin and N. N. Eshel. On first strain-gradient theories in linear elasticity. *International Journal of Solids and Structures*, 4:109–124, 1968. doi:10.1016/0020-7683(68)90036-X.

[110] A. M. Mohamed. An overview of bone cells and their regulating factors of differentiation. *The Malaysian Journal of Medical Sciences*, 15:4–12, 2008.

[111] M. Mohammadkhah, D. Marinkovic, M. Zehn, and S. Checa. A review on computer modeling of bone piezoelectricity and its application to bone adaptation and regeneration. *Bone*, 127:544–555, 2019. doi:10.1016/j.bone.2019.07.024.

[112] S. S. Moosa, M. H. R. Shaikh, M. Khwaja, S. A. H. Shaikh, F. B. Siddiqui, S. R. H. Daimi, S. D. Hiware, E. E. Ismail, and Y. Begum. Sexual dimorphic parameters of femur: a clinical guide in orthopedics and forensic studies. *Journal of Medicine and Life*, 14(6):762–768, 2022. doi:10.25122/jml-2021-0022.

[113] J. D. Murray. Mathematical Biology. I. An Introduction. In *Interdisciplinary Applied Mathematics*. Springer, New York, 3rd edition, 2002. doi:10.1007/b98868.

[114] S. Nemat-Nasser and M. Hori. Section 3 - Linearly Elastic Solids. In *Micromechanics: Overall Properties of Heterogeneous Materials*, volume 37 of *North-Holland Series in Applied Mathematics and Mechanics*, pages 67–83. North-Holland, Amsterdam, 1993. doi:10.1016/B978-0-444-89881-4.50010-4.

[115] B. H. Nguyen, X. Zhuang, and T. Rabczuk. NURBS-based formulation for nonlinear electro-gradient elasticity in semiconductors. *Computer Methods in Applied Mechanics and Engineering*, 346:1074–1095, 2019. doi:10.1016/j.cma.2018.08.026.

[116] D. L. Nguyen, D. J. Kim, G. S. Ryu, and K. T. Koh. Size effect on flexural behavior of ultra-high-performance hybrid fiber-reinforced concrete. *Composites Part B: Engineering*, 45(1):1104–1116, 2013. doi:10.1016/j.compositesb.2012.07.012.

[117] T.-H. Nguyen, R. R. Hiemstra, S. Eisenträger, and D. Schillinger. Towards higher-order accurate mass lumping in explicit isogeometric analysis for structural dynamics. *Computer Methods in Applied Mechanics and Engineering*, 417:116233, 2023. doi:10.1016/j.cma.2023.116233.

[118] V. P. Nguyen, P. Kerfriden, M. Brino, S. P. A. Bordas, and E. Bonisoli. Nitsche's method for two and three dimensional NURBS patch coupling. *Computational Mechanics*, 53:1163–1182, 2014. doi:10.1007/s00466-013-0955-3.

[119] J. W. Nunziato and S. C. Cowin. A nonlinear theory of elastic materials with voids. *Archive for Rational Mechanics and Analysis*, 72:175–201, 1979. doi:10.1007/BF00249363.

[120] R. Núñez-Toldrà, F. Vasquez-Sancho, N. Barroca, and G. Catalan. Investigation of the cellular response to bone fractures: Evidence for flexoelectricity. *Scientific Reports*, 10:254, 2020. doi:10.1038/s41598-019-57121-3.

[121] R. Owen and G. C. Reilly. In vitro models of bone remodelling and associated disorders. *Frontiers in Bioengineering and Biotechnology*, 6:134, 2018. doi:10.3389/fbioe.2018.00134.

[122] S. J. Owen, D. R. White, and T. J. Tautges. Facet-based surfaces for 3D mesh generation. In N. Chrisochoides, editor, *Proceedings of the 11th International Meshing Roundtable*, pages 297–311, 2002.

[123] S.-A. Papanicolopulos, A. Zervos, and I. Vardoulakis. A three-dimensional C1 finite element for gradient elasticity. *International Journal for Numerical Methods in Engineering*, 77(10):1396–1415, 2009. doi:10.1002/nme.2449.

[124] A. M. Parfitt. The mechanism of coupling: a role for the vasculature. *Bone*, 26 (4):319–323, 2000. doi:10.1016/S8756-3282(00)80937-0.

[125] A. M. Parfitt. Chapter 36 - Skeletal Heterogeneity and the Purposes of Bone Remodeling: Implications for the Understanding of Osteoporosis. In R. Marcus, D. Feldman, D. W. Dempster, M. Luckey, and J. A. Cauley, editors, *Osteoporosis*, pages 855–872. Academic Press, San Diego, 4th edition, 2013. doi:10.1016/B978-0-12-415853-5.00036-4.

[126] G. R. Paul, A. Malhotra, and R. Müller. Mechanical stimuli in the local in vivo environment in bone: Computational approaches linking organ-scale loads to cellular signals. *Current Osteoporosis Reports*, 16(4):395–403, 2018. doi:10.1007/s11914-018-0448-6.

[127] N. Petrov, S. Pollack, and R. Blagoeva. A discrete model for streaming potentials in a single osteon. *Journal of Biomechanics*, 22(6):517–521, 1989. doi:10.1016/0021-9290(89)90002-X.

[128] L. Piegl and W. Tiller. A menagerie of rational B-spline circles. *IEEE Computer Graphics and Applications*, 9(5):48–56, 1989. doi:10.1109/38.35537.

[129] L. Piegl and W. Tiller. The NURBS Book. In *Monographs in Visual Communications*. Springer, Berlin and Heidelberg, 1995. doi:10.1007/978-3-642-97385-7.

[130] D. Pienkowski and S. R. Pollack. The origin of stress-generated potentials in fluid-saturated bone. *Journal of Orthopaedic Research*, 1(1):30–41, 1983. doi:10.1002/jor.1100010105.

[131] D. K. Rajak, D. D. Pagar, R. Kumar, and C. I. Pruncu. Recent progress of reinforcement materials: a comprehensive overview of composite materials. *Journal of Materials Research and Technology*, 8(6):6354–6374, 2019. doi:10.1016/j.jmrt.2019.09.068.

[132] Y. Rhee, M. R. Allen, K. Condon, V. Lezcano, A. C. Ronda, C. Galli, N. Olivos, G. Passeri, C. A. O'Brien, N. Bivi, L. I. Plotkin, and T. Bellido. PTH receptor signaling in osteocytes governs periosteal bone formation and intracortical remodeling. *Journal of Bone and Mineral Research*, 26(5):1035–1046, 2010. doi:10.1002/jbmr.304.

[133] I. Romero, E. M. Andrés, and Ángel Ortiz-Toranzo. Variational updates for general thermo-chemo-mechanical processes of inelastic solids. *Computer Methods in Applied Mechanics and Engineering*, 385:114013, 2021. doi:10.1016/j.cma.2021.114013.

[134] M. D. Ryser, N. Nigam, and S. V. Komarova. Mathematical modeling of spatio-temporal dynamics of a single bone multicellular unit. *Journal of Bone and Mineral Research*, 24(5):860–870, 2009. doi:10.1359/jbmr.081229.

[135] M. D. Ryser, S. V. Komarova, and N. Nigam. The cellular dynamics of bone remodeling: A mathematical model. *SIAM Journal on Applied Mathematics*, 70

(6):1899–1921, 2010. doi:10.1137/090746094.

[136] K. Sab, F. Legoll, and S. Forest. Stress gradient elasticity theory: Existence and uniqueness of solution. *Journal of Elasticity*, 123:179–201, 2016. doi:10.1007/s10659-015-9554-1.

[137] M. B. Schaffler and O. D. Kennedy. Osteocyte signaling in bone. *Current Osteoporosis Reports*, 10:118–125, 2012. doi:10.1007/s11914-012-0105-4.

[138] R. Schenk and H. Willenegger. Zur Histologie der primären Knochenheilung. *Langenbecks Archiv für klinische Chirurgie*, 308:440–452, 1964. doi:10.1007/BF01576559.

[139] M. Schewe, H. Wilbuer, and A. Menzel. Simulation of wear and effective friction properties of microstructured surfaces. *Wear*, 464-465:203491, 2021. doi:10.1016/j.wear.2020.203491.

[140] P. J. Schneider and D. Eberly. Geometric Tools for Computer Graphics. In *The Morgan Kaufmann Series in Computer Graphics*. Morgan Kaufmann Publishers, San Francisco, 2002. doi:10.1016/B978-1-55860-594-7.X5000-0.

[141] J. Schulte, M. Dittmann, S. R. Eugster, S. Hesch, T. Reinicke, F. dell'Isola, and C. Hesch. Isogeometric analysis of fiber reinforced composites using Kirchhoff-Love shell elements. *Computer Methods in Applied Mechanics and Engineering*, 362:112845, 2020. doi:10.1016/j.cma.2020.112845.

[142] Z. Sha, X. Cheng, M. S. Islam, P. Sangkarat, W. Chang, S. A. Brown, S. Wu, J. Zhang, Z. Han, S. Peng, and C. H. Wang. Synergistically enhancing the electrical conductivity of carbon fibre reinforced polymers by vertical graphene and silver nanowires. *Composites Part A: Applied Science and Manufacturing*, 168:107463, 2023. doi:10.1016/j.compositesa.2023.107463.

[143] N. D. Sharma, C. M. Landis, and P. Sharma. Piezoelectric thin-film superlattices without using piezoelectric materials. *Journal of Applied Physics*, 108(2):024304, 2010. doi:10.1063/1.3443404.

[144] S. Sharma, R. Kumar, and R. Vaish. Universal converse flexoelectricity in dielectric materials via varying electric field direction. *International Journal of Smart and Nano Materials*, 12(1):107–128, 2021. doi:10.1080/19475411.2021.1880491.

[145] K. B. Shingare and S. Naskar. Analytical solution for static and dynamic analysis of graphene-based hybrid flexoelectric nanostructures. *Journal of Composites Science*, 5(3):74, 2021. doi:10.3390/jcs5030074.

[146] L. Shu, X. Wei, T. Pang, X. Yao, and C. Wang. Symmetry of flexoelectric coefficients in crystalline medium. *Journal of Applied Physics*, 110(10):104106, 2011. doi:10.1063/1.3662196.

[147] L. Shu, R. Liang, Z. Rao, L. Fei, S. Ke, and Y. Wang. Flexoelectric materials and their related applications: A focused review. *Journal of Advanced Ceramics*, 8:

153–173, 2019. doi:10.1007/s40145-018-0311-3.

[148] N. A. Sims and T. J. Martin. Coupling signals between the osteoclast and osteoblast: How are messages transmitted between these temporary visitors to the bone surface? *Frontiers in Endocrinology*, 6:41, 2015. doi:10.3389/fendo.2015.00041.

[149] R. C. Smith. 2. Model Development for Ferroelectric Compounds. In *Frontiers in Applied Mathematics: Smart Material Systems*, pages 43–137. Society for Industrial and Applied Mathematics, Philadelphia, 2005. doi:10.1137/1.9780898717471.ch2.

[150] K. P. Soldatos. Second-gradient plane deformations of ideal fibre-reinforced materials: Implications of hyper-elasticity theory. *Journal of Engineering Mathematics*, 68:99–127, 2010. doi:10.1007/s10665-009-9353-4.

[151] A. J. M. Spencer. *Deformations of Fibre-reinforced Materials*. Oxford Science Research Papers. Clarendon Press, Oxford, 1972.

[152] A. J. M. Spencer. Continuum Theory of the Mechanics of Fibre-Reinforced Composites. In *CISM International Centre for Mechanical Sciences (CISM, volume 282)*. Springer, Vienna, 1984. doi:10.1007/978-3-7091-4336-0.

[153] A. J. M. Spencer and K. P. Soldatos. Finite deformations of fibre-reinforced elastic solids with fibre bending stiffness. *International Journal of Non-Linear Mechanics*, 42(2):355–368, 2007. doi:10.1016/j.ijnonlinmec.2007.02.015.

[154] D. J. Steigmann. Theory of elastic solids reinforced with fibers resistant to extension, flexure and twist. *International Journal of Non-Linear Mechanics*, 47(7): 734–742, 2012. doi:10.1016/j.ijnonlinmec.2012.04.007.

[155] D. J. Steigmann. Effects of Fiber Bending and Twisting Resistance on the Mechanics of Fiber-reinforced Elastomers. In L. Dorfmann and R. W. Ogden, editors, *Nonlinear Mechanics of Soft Fibrous Materials*, pages 269–305. Springer, Vienna, 2015. doi:10.1007/978-3-7091-1838-2_6.

[156] H. Suemasu, A. Kondo, K. Itatani, and A. Nozue. A probabilistic approach to the toughening mechanism in short-fiber-reinforced ceramic-matrix composites. *Composites Science and Technology*, 61(2):281–288, 2001. doi:10.1016/S0266-3538(00)00211-6.

[157] E. S. Suhubi and A. C. Eringen. Nonlinear theory of micro-elastic solids – II. *International Journal of Engineering Science*, 2(4):389–404, 1964. doi:10.1016/0020-7225(64)90017-5.

[158] C. Tekoglu, L. J. Gibson, T. Pardoen, and P. R. Onck. Size effects in foams: Experiments and modeling. *Progress in Materials Science*, 56(2):109–138, 2011. doi:10.1016/j.pmatsci.2010.06.001.

[159] T. Q. Thai, T. Rabczuk, and X. Zhuang. A large deformation isogeometric approach for flexoelectricity and soft materials. *Computer Methods in Applied Mechanics and Engineering*, 341:718–739, 2018. doi:10.1016/j.cma.2018.05.019.

[160] A. Todoroki, H. Shiomi, Y. Mizutani, and Y. Suzuki. Electrical shorting between the carbon-fiber cloth electrodes of structural capacitors with a glass-fiber cloth separator. *Open Journal of Composite Materials*, 4(3):140–147, 2014. doi:10.4236/ojcm.2014.43016.

[161] R. A. Toupin. Elastic materials with couple-stresses. *Archive for Rational Mechanics and Analysis*, 11(1):385–414, 1962. doi:10.1007/BF00253945.

[162] R. A. Toupin. The elastic dielectric. *Journal of Rational Mechanics and Analysis*, 5(6):849–915, 1956.

[163] A. Tripathy, B. Saravanakumar, S. Mohanty, S. K. Nayak, and A. Ramadoss. Comprehensive review on flexoelectric energy harvesting technology: Mechanisms, device configurations, and potential applications. *ACS Applied Electronic Materials*, 3(7):2898–2924, 2021. doi:10.1021/acsaelm.1c00267.

[164] F. Vasquez-Sancho, A. Abdollahi, D. Damjanovic, and G. Catalan. Flexoelectricity in bones. *Advanced Materials*, 30(9):1705316, 2018. doi:10.1002/adma.201705316.

[165] J. Ventura, D. Codony, and S. Fernández-Méndez. A C0 interior penalty finite element method for flexoelectricity. *Journal of Scientific Computing*, 88:88, 2021. doi:10.1007/s10915-021-01613-w.

[166] R. Voide, P. Schneider, M. Stauber, P. Wyss, M. Stampanoni, U. Sennhauser, G. H. van Lenthe, and R. Müller. Time-lapsed assessment of microcrack initiation and propagation in murine cortical bone at submicrometer resolution. *Bone*, 45 (2):164–173, 2009. doi:10.1016/j.bone.2009.04.248.

[167] Z. Wang, S. Rudraraju, and K. Garikipati. A three dimensional field formulation, and isogeometric solutions to point and line defects using Toupin's theory of gradient elasticity at finite strains. *Journal of the Mechanics and Physics of Solids*, 94:336–361, 2016. doi:10.1016/j.jmps.2016.03.028.

[168] J. P. Webb. Imposing linear constraints in finite-element analysis. *Communications in Applied Numerical Methods*, 6(6):471–475, 1990. doi:10.1002/cnm.1630060607.

[169] J. Wei, M. Liao, A. Ma, Y. Chen, Z. Duan, X. Hou, M. Li, N. Jiang, and J. Yu. Enhanced thermal conductivity of polydimethylsiloxane composites with carbon fiber. *Composites Communications*, 17:141–146, 2020. doi:10.1016/j.coco.2019.12.004.

[170] C. Witt, T. Kaiser, and A. Menzel. An isogeometric finite element approach to fibre-reinforced composites with fibre bending stiffness. *Archive of Applied Mechanics*, 91(2):643–672, 2021. doi:10.1007/s00419-020-01754-8.

[171] C. Witt, T. Kaiser, and A. Menzel. A finite deformation isogeometric finite element approach to fibre-reinforced composites with fibre bending stiffness. *Journal of*

Engineering Mathematics, 128(1):15, 2021. doi:10.1007/s10665-021-10117-3.

[172] C. Witt. Isogeometric higher gradient finite element formulations. Master's thesis, Institute of Mechanics, TU Dortmund University, Germany, 2019.

[173] C. Witt, T. Kaiser, and A. Menzel. On the incorporation of curvature effects into the isogeometric analysis of fibre-reinforced solids. *Proceedings in Applied Mathematics and Mechanics*, 21(1):e202100185, 2021. doi:10.1002/pamm.202100185.

[174] C. Witt, T. Kaiser, and A. Menzel. Modelling and numerical simulation of remodelling processes in cortical bone: An IGA approach to flexoelectricity-induced osteocyte apoptosis and subsequent bone cell diffusion. *Journal of the Mechanics and Physics of Solids*, 173:105194, 2023. doi:10.1016/j.jmps.2022.105194.

[175] C. Witt, T. Kaiser, and A. Menzel. An IGA-FEA model for flexoelectricity-induced healing of microcracks in cortical bone. *Computer Methods in Applied Mechanics and Engineering*, 425:116919, 2024. doi:10.1016/j.cma.2024.116919.

[176] N. K. Wittig, M. Østergaard, J. Palle, T. E. K. Christensen, B. L. Langdahl, L. Rejnmark, E.-M. Hauge, A. Brüel, J. S. Thomsen, and H. Birkedal. Opportunities for biomineralization research using multiscale computed X-ray tomography as exemplified by bone imaging. *Journal of Structural Biology*, 214(1):107822, 2022. doi:10.1016/j.jsb.2021.107822.

[177] J. Yvonnet and L. P. Liu. A numerical framework for modeling flexoelectricity and Maxwell stress in soft dielectrics at finite strains. *Computer Methods in Applied Mechanics and Engineering*, 313:450–482, 2017. doi:10.1016/j.cma.2016.09.007.

[178] Q. S. Zheng. Theory of representations for tensor functions – A unified invariant approach to constitutive equations. *Applied Mechanics Reviews*, 47(11):545–587, 1994. doi:10.1115/1.3111066.

[179] W. Zheng, B. Luo, and Y. Wang. Compressive and tensile properties of reactive powder concrete with steel fibres at elevated temperatures. *Construction and Building Materials*, 41:844–851, 2013. doi:10.1016/j.conbuildmat.2012.12.066.

[180] X. Zhuang, B. H. Nguyen, S. S. Nanthakumar, T. Q. Tran, N. Alajlan, and T. Rabczuk. Computational modeling of flexoelectricity – A review. *Energies*, 13(6):1326, 2020. doi:10.3390/en13061326.

[181] F. Ziegler. *Mechanics of Solids and Fluids*. Springer, New York, NY, 2nd edition, 1995. doi:10.1007/978-1-4612-0805-1.

Publication series of the Institute of Mechanics

published to date:

2010/01 Palnau, V.: Implementierung eines netzfreien Diskretisierungsverfahrens und seine Anwendung auf die Scherbandanalyse.
ISBN 978-3-921823-51-4

2010/02 Klusemann, B.: Application of homogenization methods and crystal plasticity to the modeling of heterogeneous materials of technological interest.
ISBN 978-3-921823-53-8

2011/01 Hortig, C.: Local and non-local thermomechanical modeling and finite-element simulation of high-speed cutting.
ISBN 978-3-921823-54-5

2011/02 Parvizian, F.: Modeling of microstructure evolution in aluminum alloys during hot extrusion.
ISBN 978-3-921823-56-9

2011/03 Noman, M.: Characterization and model identification for the simulation of the forming behavior of ferritic steels.
ISBN: 978-3-921823-55-2

2011/04 Kayser, T.: Characterization of microstructure in aluminum alloys based on electron backscatter diffraction.
ISBN: 978-3-921823-57-6

2011/05 Bargmann, S.: Computational modeling of material behavior on different scales based on continuum mechanics.
ISBN: 978-3-921823-58-3

2013/01 Waffenschmidt, T.: Modelling and simulation of adaptation and degradation in anisotropic biological tissues.
ISBN: 978-3-921823-61-3

2015/01 Ostwald, R.: Modelling and simulation of phase-transformations in elastoplastic polycrystals.
ISBN: 978-3-921823-66-8

2016/01 Subramanian, M.: Phenomenological modelling and simulation of ferroelectric ceramics.
ISBN: 978-3-921823-74-3

2016/02 Clausmeyer, T.: Evolution of plastic anisotropy in metals.
ISBN: 978-3-921823-76-7

2017/01 Holtermann, R.: Computational multiscale modelling of grinding processes.
ISBN: 978-3-921823-86-6

2017/02 Bartels, A.: Modelling of evolving microstructures at different scales.
ISBN: 978-3-921823-93-4

2017/03 Dusthakar Kumar Rao, D. K.: Computational modelling of single and polycrystalline ferroelectric materials.
ISBN 978-3-921823-94-1

2019/01 Buckmann, K.: Microstructure evolution in functional magnetic materials.
ISBN 978-3-947323-09-8

2019/02 Kaiser, T.: Computational modelling of non-simple and anisotropic materials.
ISBN 978-3-947323-14-2

2019/03 Heitbreder, T.: Modelling of material interfaces at different length scales.
ISBN 978-3-947323-18-0

2020/01 Berthelsen, R.: Computational homogenisation of thermomechanical problems.
ISBN 978-3-947323-19-7

2020/02 Sievers, C.: Describing the macroscopic behavior of surfaces based on atomistic models.
ISBN 978-3-947323-24-1

2022/01 Rose, L.: Optimisation based parameter identification using optical field measurements.
ISBN 978-3-947323-31-9

2023/01 Langenfeld, K.: Continuum modeling of brittle and ductile damage: theory and computational frameworks.
ISBN 978-3-947323-41-8

2023/02 Schulte, R.: Parameter identification approaches with application to different classes of materials.
ISBN 978-3-947323-45-6

2023/03 Kaiser, T.: Multiscale multiphysics material modelling.
ISBN 978-3-947323-46-3

2024/01 Noll, I.: Thermomechanical modelling and simulation of laser powder bed fusion processes.
ISBN 978-3-947323-49-4

2024/02 Witt, C.: Isogeometric analysis of anisotropic mechanical and electromechanical higher-gradient continua.
ISBN 978-3-947323-50-0